Thomas Huber, M. Eng

Multi-Decade GaN Power Amplifiers in Common-Source and Cascode Topology

DOCTORAL THESIS

to achieve the university degree of

Doktor der technischen Wissenschaften

submitted to

Graz University of Technology

Supervisor

Univ.-Prof. Dipl.-Ing. Dr. techn. MBA, Wolfgang Bösch

Institute of Microwave and Photonic Engineering (IHF)

PD Dr. techn., Rüdiger Quay
Fraunhofer Institute for Applied Solid State Physics (IAF)

Graz, December 2019

This document was written with L_YX (Version 2.3.3) and compiled with pdfLaTeX and BibTeX. The program L_YX uses LaTeX as backend processor. The document template is based on the KOMA script.

Affidavit

I declare that I have authored this thesis independently, that I have not used other than the declared sources/resources, and that I have explicitly indicated all material which has been quoted either literally or by content from the sources used. The text document uploaded to TUGRAZonline is identical to the present doctoral thesis.

_____   _____
            Date   Signature

To my sister Barbara

Acknowledgments

Abstract

State-of-the-art measurement equipment —i.e. signal generators, spectrum and network analyzers— demands for very high frequencies up to the millimeter wave range, maintaining high linearity, large dynamic range and low noise contribution. Due to that fact, broadband power amplifiers —as key elements in high-end measurement equipment— with highest RF performance, are necessary to fulfill the new standards (i.e. 5G) and their high requirements. There are only two kind of power amplifier (PA) topologies to achieve a multi-decade frequency bandwidth and there are only some octave bandwidth PA topologies. Furthermore, semiconductors with high band-gaps —i.e. gallium nitride (GaN)— are needed to fabricate high-end transistors. Using the cascode (CC) topology as basic circuit in PAs instead of the common-source (CS) topology, is a common technique to improve the RF performance of broadband PAs. Despite the superior behavior of the CC topology, there are some disadvantages especially in multi-decade PA designs which should not be neglected. The increased power compression degradation over frequency is one of them. Therefore the main goal of this thesis is to understand this RF response and addressing it by developing a new concept that replaces the constant stabilization capacitor (CSC) by a variable adjustable stabilization capacitor (VASC) with a certain small-signal and large-signal behavior.

As the semiconductor GaN is more and more used nowadays to process high electron mobility transistors (HEMTs) to gain high output power (P_{out}) at very high frequencies, the superior performance of the GaN-HEMT technology is demonstrated and compared to other semiconductor technologies. In this thesis a GaN-HEMT technology is used with a gate-length (l_g) of 200 nm. Furthermore, the functionality is explained and a short overview about the small-signal, large-signal as well as the noise modeling is given.

To get an in-depth understanding of the CC topology and its advantages and disadvantages in broadband PAs —using the GaN-HEMT technology—, the functionality of the CC is explained and the small-signal, large-signal and noise key parameters are derived and compared with the common-source stage (CSS). The comparison helps to get a comprehension of the power compression degradation at higher frequencies of the CC topology in multi-decade PAs. This RF behavior is mainly caused by the transconductance compression of the common-gate stage (CGS) at higher frequencies especially if the CC designs are small-signal optimized.

In the first main chapter a new concept —using a CC with a VASC— is developed and presented to improve the RF behavior of the CC topology in multi-decade PAs. The VASC enables to improve and adjust several key-parameters of the PA using the CC topology, like the small-signal gain ($\underline{S}_{21}$), power compression and linearity. Several realization structures of the VASC are presented and compared with each other to show the trade-offs.

In the second main chapter, the trade-offs of the CC topology compared to the CS topology as well as the improvement due to the new concept are verified by small-signal and large-signal measurements of several developed feedback amplifiers (FBAs) achieving state-of-the-art performance by using the GaN-HEMT technology. The FBA using the CC topology (CC-FBA), either the bandwidth can be improved by 40 % (CC-FBA-IB) or the gain can be improved by 1–2 dB and the P_{out} at lower frequencies by 3 dB (CC-FBA-IG). While on the one hand, the CC-FBA-IB using the new concept —one diode, direction: down— (CC-FBA-IB-D1D) shows the best dynamic behavior to adjust the $\underline{S}_{21}$, on the other hand the new concept using two anti-parallel diodes (CC-FBA-IB-D2) has a superior linearity performance in a certain frequency and power level range.

Contents

List of Figures

List of Tables

Abbreviations

2DEG	**2**-**d**imensional **e**lectron **g**as
3H-SiC	**si**licon **c**arbide (lattice composed of pure cubic bonds, stacking sequence: ABC)
4G	**4**th **g**eneration
4H-SiC	**si**licon **c**arbide (lattice composed of one-half cubic bonds and one-half hexagonal bonds, stacking sequence: ABCB)
5G	**5**th **g**eneration
6H-SiC	**si**licon **c**arbide (lattice composed of two-thirds cubic bonds and one-third hexagonal bonds, stacking sequence: ABCACB)
AC	**a**lternating **c**urrent
Al_2O_3	sapphire
AlN	**al**uminum **n**itride
AlGaAs	**al**uminum **ga**llium **ar**senide
AlGaN	**al**uminum **ga**llium **n**itride
CC	**c**as**c**ode
CC-FBA	**c**as**c**ode **f**eed**b**ack **a**mplifier
CC-FBA-IB	**c**as**c**ode **f**eed**b**ack **a**mplifier with **i**mproved **b**andwidth
CC-FBA-IG	**c**as**c**ode **f**eed**b**ack **a**mplifier with **i**mproved **g**ain
CC-FBA-IB-D1D	**c**as**c**ode **f**eed**b**ack **a**mplifier with **i**mproved **b**andwidth using a VASC: one varactor **d**iode (direction: **d**own)
CC-FBA-IB-D2	**c**as**c**ode **f**eed**b**ack **a**mplifier with **i**mproved **b**andwidth using a VASC: two varactor **d**iodes in parallel (direction: up&down)
CG	**c**ommon-**g**ate
CGS	**c**ommon-**g**ate **s**tage
CS	**c**ommon-**s**ource
CSC	**c**onstant **s**tabilization **c**apacitor
CSS	**c**ommon-**s**ource **s**tage
DC	**d**irect **c**urrent
D	**d**rain contact
D_i	intrinsic **d**rain contact
DPA	**d**istributed **p**ower **a**mplifiers
EHF	**e**xtremely **h**igh **f**requency

FBA	**feedb**ack **a**mplifier
FET	**f**ield **e**ffect **t**ransistors
FM	**f**requency **m**odulation
G	**g**ate contact
G-	inverse-hybrid
GaAs	**ga**llium **ar**senide
GaN	**ga**llium **n**itride
Ge	**ge**rmanium
G_i	intrinsic **g**ate contact
GPS	**g**lobal **p**ositioning **s**ystem
H-	**h**ybrid
HBT	**h**etero **b**ipolar **t**ransistor
HEMT	**h**igh electron **m**obility **t**ransistor
HF	**h**igh **f**requency
HFET	**h**igh **f**ield **e**ffect **t**ransistor
IEEE	**i**nstitut of **e**lectrical and **e**lectronics **e**ngineers
ITU	**I**nternational **T**elecommunication **U**nion
InP	**in**dium **p**hosphide
LDMOS	**l**ateral **d**iffused **m**etal **o**xide **s**emiconductor
LSM	**l**arge-**s**ignal **m**odel
LTE	**l**ong-**t**erm **e**volution standard
LTE+	**l**ong-**t**erm **e**volution standard advanced
MGWS	**m**ultiple **g**igabit **w**ireless **s**ystem
MIM	**m**etal-**i**nsulator-**m**etal
MMIC	**m**onolithic **m**icrowave **i**ntegrated **c**ircuit
MODFET	**mo**dulation **d**oped **f**ield **e**ffect **t**ransistor
NLSC	**n**on-**l**inear **s**tabilization **c**apacitor
PA	**p**ower **a**mplifier
RF	**r**adio **f**requency
RFID	**r**adio **f**requency **id**entification
S	**s**ource contact
S-	**s**cattering
SHF	**s**uper **h**igh **f**requency
S_i	intrinsic **s**ource contact
SDHT	**s**electively-**d**oped **h**eterojunction **t**ransistor

Si	**si**licon
SiC	**si**licon **c**arbide
SMD	**s**urface **m**ounted **d**evice
SOA	**s**afe-**o**perating-**ar**ea
SSM	**s**mall-**s**ignal **m**odel
TEGFET	**t**wo-dimensional **e**lectron **g**as **f**ield **e**ffect **t**ransistor
TFR	**t**hin-**f**ilm **r**esistor
TWA	**t**raveling-**w**ave **a**mplifier
UHF	**u**ltra **h**igh **f**requency
VASC	**v**ariable **a**djustable **s**tabilization **c**apacitor
VHF	**v**ery **h**igh **f**requency
WLAN	**w**ireless **l**ocal **a**rea **n**etwork
Y-	admittance
Z-	impedance

Notation and Formula Symbols

Notation

In this work instantaneous-, direct-, and alternating- currents, voltages and powers are distinguished by using a certain notation of symbols. These kind of notations are based on [1] and use the following pattern for symbols:

- Small letters for symbols are used for instantaneous time dependent quantities (i.e. $i(t)$, $v(t)$).
  - Small letters for indexes for periodic alternating quantities (only alternating components, i.e. $i_{ds}(t)$, $v_{ds}(t)$).
  - Capital letters for indexes for periodic non alternating quantities (impulse quantities, i.e. $i_{DS}(t)$, $v_{DS}(t)$)
- Capital letters for symbols are used for constant time independent quantities (i.e. I, V).
  - Small letters for indexes for mean averages periodic alternating quantities and for quantities in the frequency domain (i.e. I_{ds}, V_{ds}, $\underline{I}_{ds}$, $\underline{V}_{ds}$).
  - Capital letters for constant direct quantities (i.e. I_{DS}, V_{DS}).
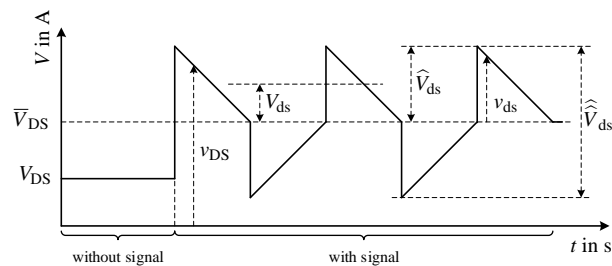
Figure 0.0.1: Illustration of notations for time dependent and time independent quantities [1].

Formula Symbols

Variable	Unit	Description
$1OCP$	W	1 dB output compression point
$1ICP$	W	1 dB input compression point
$\underline{\mathbf{A}}$	$\begin{pmatrix} - & \Omega \\ S & - \end{pmatrix}$	chain matrix ($ABCD$ matrix) of a two-port network
a_1, a_2	$\sqrt{W}$	incident power wave at port one and two
B	Hz	bandwidth
b_1, b_2	$\sqrt{W}$	reflected power wave at port one and two
B_{cor}	S	correlation susceptance

Variable	Unit	Description
B_s	S	source susceptance
$B_\mathrm{s,opt}$	S	optimum source susceptance
$Comp$	−	gain compression
C	−	criticalness factor
c_0, c_1	−	fitting constants of the transfered short circuit output admittance of CSS
$C_\mathrm{DC\text{-}block}$	F	DC blocking capacitance
C_ds	F	large-signal drain-source capacitance
		small-signal drain-source capacitance
$C_\mathrm{ds,eff}$	F	recalculated small-signal drain-source capacitance
$C_\mathrm{ds1}, C_\mathrm{ds2}$	F	small-signal drain-source capacitance of CSS and CGS respectively
$C_\mathrm{ds2,eff}$	F	recalculated small-signal drain-source capacitance of CGS
C_fp	F	parallel feedback capacitance
$C_\mathrm{fp,ext}$	F	external parallel feedback capacitance
C_gd	F	large-signal gate-drain capacitance
		small-signal gate-drain capacitance
$C_\mathrm{gd,eff}$	F	recalculated small-signal gate-drain capacitance
$C_\mathrm{gd1}, C_\mathrm{gd2}$	F	small-signal gate-drain capacitance of CSS and CGS respectively
$C_\mathrm{gd2,eff}$	F	recalculated small-signal gate-drain capacitance of CGS
C_gs	F	large-signal gate-source capacitance
		small-signal gate-source capacitance
$C_\mathrm{gs,eff}$	F	recalculated large-signal gate-source capacitance
		recalculated small-signal gate-source capacitance
$C_\mathrm{gs,0}$	F	DC part of the large-signal gate-source capacitance
$C_\mathrm{gs,1}$	$\frac{\mathrm{F}}{\mathrm{V}}$	linear part of the large-signal gate-source capacitance
$C_\mathrm{gs,2}$	$\frac{\mathrm{F}}{\mathrm{V}^2}$	cubic part of the large-signal gate-source capacitance
$C_\mathrm{gs\|gd}$	F	gate to source and drain capacitance
$C_\mathrm{gs1}, C_\mathrm{gs2}$	F	small-signal gate-source capacitance of CSS and CGS respectively
$C_\mathrm{gs2,eff}$	F	recalculated small-signal gate-source capacitance of CGS
C_l	F	load capacitance of the VASC of the CS-FBA-IB-D1D
$C_\mathrm{m1}, C_\mathrm{m2}$	F	capacitance of the first and second input matching network respectively
C_pds	F	pad drain-source capacitance

Variable	Unit	Description
C_{pgd}	F	pad gate-drain capacitance
C_{pgs}	F	pad gate-source capacitance
$C_{\mathrm{RF\text{-}Short}}$	F	RF short capacitance
$C_{\mathrm{sg,ext}}$	F	external source-gate capacitance
C_{st}	F	stabilization capacitance (capacitance of the CSC)
$C_{\mathrm{st,var}}$	F	variable adjustable stabilization capacitance (capacitance of the VASC)
C_{th}	$\frac{\mathrm{W\cdot s}}{\mathrm{K}}$	thermal capacitance
E	$\frac{\mathrm{V}}{\mathrm{m}}$	electric field strength
	J	energy
E_{BR}	$\frac{\mathrm{V}}{\mathrm{m}}$	breakdown field strength
E_{c}	J	conduction band energy
E_{g}	J	band-gap energy
E_{f}	J	Fermi level
E_{g1}	J	band-gap energy of first semiconductor
E_{g2}	J	band-gap energy of second semiconductor
E_{v}	J	valance band energy
F	–	noise factor
f	Hz	frequency
f_{∞}	Hz	frequency pole
$f_{\infty 1}$, $f_{\infty 2}$	Hz	first and second frequency pole
f_0	Hz	frequency zero
f_{01}, f_{02}, f_{03}, f_{04}	Hz	first, second, third and fourth frequency zero
f_{c}	Hz	cut-off frequency
F_{min}	–	minimum noise factor
f_{t}	Hz	transition frequency
Gain	–	large-signal gain
normalized *Gain*	–	normalized large-signal gain
G_{cor}	S	correlation conductance
g_{ds}	S	small-signal drain-source conductance
G_{m}	S	large-signal trans-conductance of the voltage controlled current source
g_{m}	S	small-signal trans-conductance of the voltage controlled current source
$\underline{g}_{\mathrm{m}}$	S	small-signal trans-impedance of the voltage controlled current source

Variable	Unit	Description
G_m	S	large-signal trans-conductance of the voltage controlled current source
$G_\mathrm{m,0}$	S	DC part of the large-signal trans-conductance of the voltage controlled current source
$G_\mathrm{m,1}$	$\frac{\mathrm{S}}{\mathrm{V}}$	linear part of the large-signal trans-conductance of the voltage controlled current source
$G_\mathrm{m,2}$	$\frac{\mathrm{S}}{\mathrm{V}^2}$	cubic part of the large-signal trans-conductance of the voltage controlled current source
$g_\mathrm{m,eff}$	S	recalculated small-signal trans-conductance of the voltage controlled current source
$\underline{g}_\mathrm{m,eff}$	S	recalculated small-signal trans-impedance of the voltage controlled current source
g_m1, g_m2	S	small-signal trans-conductance of the voltage controlled current source of CSS and CGS respectively
$g_\mathrm{m2,eff}$	S	recalculated small-signal trans-conductance of the voltage controlled current source of CGS
G_n	S	equivalent noise conductance of uncorrelated part of noise current source
g_n	S	equivalent noise conductance of noise current source
GP	m	gate periphery (total size of the HEMT)
G_s	S	source conductance
$G_\mathrm{s,opt}$	S	optimum source conductance
$\underline{\mathbf{H}} = \begin{pmatrix} \underline{H}_{11} & \underline{H}_{12} \\ \underline{H}_{21} & \underline{H}_{22} \end{pmatrix}$	$\begin{pmatrix} \Omega & - \\ - & \mathrm{S} \end{pmatrix}$	hybrid matrix of a two-port network
$\underline{H}_{11}$	Ω	short circuit input impedance
$\underline{H}_{12}$	–	open circuit voltage retro-activity
$\underline{H}_{21}$	–	short circuit current gain
$\underline{H}_{22}$	S	open circuit output admittance
$HD2$	W	harmonic distortion second order
$HD3$	W	harmonic distortion third order
I	A	time independent current in the time domain
$\underline{I}$	A	time independent current in the frequency domain
i	A	instantaneous time dependent current
$\underline{I}_1$	A	current at port one of a two-port network
$\underline{I}_2$	A	current at port two of a two-port network
I_DS, I_ds	A	drain-source current
$I_\mathrm{DS,MAX}$	A	maximum drain-source current

Variable	Unit	Description
$\widehat{I}_{\mathrm{ds,max}}$	A	maximum drain-source current peak amplitude
I_{DSQ}	A	drain-source current at a certain quiescent point
I_{gd}	A	gate-drain current
$I_{\mathrm{GS}}, I_{\mathrm{gs}}$	A	gate-source current
$I_{\mathrm{GS1}}, I_{\mathrm{GS2}}$	A	gate-source current of CSS and CGS respectively
I_{max}	A	maximum current
$IMD2$	W	inter-modulation distortion second order
$IMD3$	W	inter-modulation distortion third order
$\underline{I}_{\mathrm{n}}$	A	noise current
$\underline{I}_{\mathrm{n,d}}$	A	thermal channel noise current
$\underline{I}_{\mathrm{n,d1}}, \underline{I}_{\mathrm{n,d2}}$	A	thermal channel noise current of CSS and CGS respectively
$\underline{I}_{\mathrm{n,d,Ziel}}$	A	thermal channel noise current of Van der Ziel's noise model
$\underline{I}_{\mathrm{n,g}}$	A	induced gate noise current
$\underline{I}_{\mathrm{n,g1}}, \underline{I}_{\mathrm{n,g2}}$	A	induced gate noise current of CSS and CGS
$\underline{I}_{\mathrm{n,g,Ziel}}$	A	induced gate noise current of Van der Ziel's noise model
$\underline{I}_{\mathrm{n,uc}}$	A	noise current of uncorrelated part of noise current source
$\underline{I}_{\mathrm{n1}}$	A	noise current at port one of a two-port network
$\underline{I}_{\mathrm{n2}}$	A	noise current at port two of a two-port network
$IP3$	W	third order intercept point
$I_{\mathrm{pot.}}$	A	average current through a potential barrier
I_{th}	W	thermal current
K_{f}	–	fitting constant for flicker noise
k	–	stability factor Rollett
L_{bw}	H	bondwire inductance
L_{d}	H	feeding drain inductance
L_{fp}	H	parallel feedback inductance
L_{g}	H	feeding gate inductance
l_{g}	m	gate-length
$L_{\mathrm{m1}}, L_{\mathrm{m2}}$	H	inductance of first and second input matching network respectively
L_{m3}	H	inductance of output matching network
LSB	Hz	large-signal bandwidth
L_{s}	H	feeding source inductance
MAG	–	maximum available gain

Variable	Unit	Description
MSG	–	maximum stable gain
$MTTF$	s	mean time to failure
N	–	number of electrons during trap life time
	$\frac{1}{m^3}$	doping concentration
n	–	variable
N_1	$\frac{1}{m^3}$	doping concentration of first semiconductor
N_2	$\frac{1}{m^3}$	doping concentrations of second semiconductor
NF	dB	noise figure
NF_{min}	dB	minimum noise figure
NGF	–	number of gate finger
n_s	$\frac{1}{m^2}$	sheet carrier density
$OIP3$	W	output inter-modulation point third order
$P1dB$	W	1 dB compression point
P_{DC}	W	DC power
P_{DISS}	W	dissipation power
$P_{DISS,MAX}$	W	maximum dissipation power
P_{in}	W	input power
PAE	%	power added efficiency
$P_{n,av}$	W	available thermal noise power
P_{out}	W	output power
$P_{out,1tone}$	W	output power of a one tone signal
$P_{out,max}$	W	maximum output power
P_{sat}	W	saturated output power
$Q(V,I)$	(V, A)	quiescent point of transistor defined by voltage and current
$Q_1(V,I)$, $Q_2(V,I)$	(V, A)	quiescent point of transistor defined by voltage and current of the CSS and CGS respectively
R_{att}	Ω	attenuation resistance
R_{cor}	Ω	correlation resistance
R_d	Ω	feeding drain resistance
R_{ds}	Ω	large-signal drain-source resistance
r_{ds}	Ω	small-signal drain-source resistance
$r_{ds,eff}$	Ω	recalculated small-signal drain-source resistance
r_{ds1}, r_{ds2}	Ω	small-signal drain-source resistance of CSS and CGS respectively
$r_{ds2,eff}$	Ω	recalculated small-signal drain-source resistance of CGS

Variable	Unit	Description
r_{fgd}	Ω	small-signal gate-drain feedback resistance
r_{fgs}	Ω	small-signal gate-source feedback resistance
R_{fp}	Ω	parallel feedback resistance
R_{fs}	Ω	series feedback resistance
R_{g}	Ω	feeding gate resistance
R_{gd}	Ω	large-signal gate-drain resistance
r_{gd}	Ω	small-signal gate-drain resistance
$r_{\text{gd,eff}}$	Ω	recalculated small-signal gate-drain resistance
R_{gs}	Ω	large-signal gate-source resistance
r_{gs}	Ω	small-signal gate-source resistance
$r_{\text{gs,eff}}$	Ω	recalculated small-signal gate-source resistance
R_{l}	Ω	load resistance of the VASC of the CS-FBA-IB-D1D
R_{n}	Ω	equivalent noise resistance of noise voltage source
r_{n}	Ω	equivalent noise resistance of uncorrelated part of noise voltage source
R_{on}	Ω	on-resistance
R_{s}	Ω	feeding source resistance, source resistance
$R_{\text{s,opt}}$	Ω	optimum source resistance
R_{st}	Ω	stabilization resistance
R_{th}	$\frac{\text{K}}{\text{W}}$	thermal resistance
$\underline{\mathbf{S}} = \begin{pmatrix} \underline{S}_{11} & \underline{S}_{12} \\ \underline{S}_{21} & \underline{S}_{22} \end{pmatrix}$	$\begin{pmatrix} - & - \\ - & - \end{pmatrix}$	scattering matrix of a two-port network
$\underline{S}_{11}$	$-$	input port reflection coefficient
$\underline{S}_{12}$	$-$	reverse transmission coefficient (isolation)
$\underline{S}_{21}$	$-$	forward transmission coefficient (small-signal gain)
$\underline{S}_{22}$	$-$	output port reflection coefficient
S_{n}	$\frac{\text{W}}{\text{Hz}}$	power spectral density
$S_{\text{n,f}}$	$\frac{\text{A}^2}{\text{Hz}}$	normalized current power spectral density of flicker noise
$S_{\text{n,gr}}$	$\frac{\text{V}^2}{\text{Hz}}$	normalized voltage power spectral density of generation-recombination noise
$S_{\text{n,shot}}$	$\frac{\text{A}^2}{\text{Hz}}$	normalized current power spectral density of shot noise
SNR	$-$	signal-to-noise ratio
SSB	Hz	small-signal bandwidth
T	K	temperature
T_0	K	ambient temperature

Variable	Unit	Description
T_d	K	temperature of small-signal drain-source resistor in Pospieszalski's noise model
T_g	K	temperature of small-signal gate-source resistor in Pospieszalski's noise model
T_j	K	junction temperature (channel temperature)
$T_{j,max1}$, $T_{j,max2}$	K	maximum junction temperature of CSS and CGS respectively
U	–	unilateral power gain, Mason's invariant
UGW	m	unit gate-width
V	V	time independent voltage in the time domain
$\underline{V}$	V	time independent voltage in the frequency domain
v	V	instantaneous time dependent voltage
$\underline{V}_1$	V	voltage at port one of a two-port network
		voltage at the gate-source capacitor
$\underline{V}_2$	V	voltage at port two of a two-port network
		voltage at the gate-source capacitor of the CGS of the CC
V_{BR}	V	breakdown voltage
V_{BR1}, V_{BR2}	V	breakdown voltage of CSS and CGS respectively
v_d	$\frac{m}{s}$	electron drift velocity
$v_{d,sat}$	$\frac{m}{s}$	saturated electron drift velocity
$v_{d,max}$	$\frac{m}{s}$	maximum electron drift velocity
V_{DD}	V	supply voltage
V_{DS}, V_{ds}	V	drain-source voltage
$\widehat{\widehat{V}}_{ds}$	V	drain-source voltage swing
$V_{DS,MAX}$	V	maximum drain-source voltage
$\widehat{V}_{ds,max}$	V	maximum drain-source voltage peak amplitude
V_{ds1}, V_{ds2}	V	drain-source voltage of CSS and CGS respectively
v_g	V	gate voltage
V_{GD}	V	gate-drain voltage
V_{GS}, $\underline{V}_{gs}$, v_{gs}	V	gate-source voltage
$\widehat{V}_{gs}$	V	gate-source voltage peak amplitude
$\widehat{\widehat{V}}_{gs}$	V	gate-source voltage swing
V_{GSD}	V	gate-source-drain voltage (source and drain have the same voltage potential)
V_{gdc}	V	gate-drain voltage at the large-signal gate-drain capacitor

Variable	Unit	Description
V_{gsc}	V	gate-source voltage at the large-signal gate-source capacitor
V_{KNEE}	V	knee voltage
V_{KNEE1}, V_{KNEE2}	V	knee voltage of CSS and CGS respectively
$\underline{V}_{\text{n}}$	V	noise voltage
$\underline{V}_{\text{n,uc}}$	V	noise voltage of uncorrelated part of noise voltage source
$\underline{V}_{\text{n1}}$	V	noise voltage at port one of a two-port network
$\underline{V}_{\text{n2}}$	V	noise voltage at port two of a two-port network
v_{s}	V	source voltage
v_{sg}	V	source-gate voltage
V_{VASC}	V	quiescent voltage at the VASC (one diode)
V_{VASC1}, V_{VASC2}	V	first and second quiescent voltage at the VASC (two diodes)
x	m	distance
$\underline{X}_{\text{cor}}$	Ω	correlation reactance
$\underline{X}_{\text{s}}$	Ω	source reactance
$\underline{X}_{\text{s,opt}}$	Ω	optimum source reactance
y	m	distance
$\underline{\mathbf{Y}} = \begin{pmatrix} \underline{Y}_{11} & \underline{Y}_{12} \\ \underline{Y}_{21} & \underline{Y}_{22} \end{pmatrix}$	$\begin{pmatrix} \text{S} & \text{S} \\ \text{S} & \text{S} \end{pmatrix}$	admittance matrix of a two-port network
$\underline{Y}_{11}$	S	short circuit input admittance
$\underline{Y}_{12}$	S	short circuit reverse trans-admittance
$\underline{Y}_{21}$	S	short circuit trans-admittance
$\underline{Y}_{22}$	S	short circuit output admittance
$\underline{Y}_{\text{cor}}$	S	correlation admittance
$\underline{Y}_{\text{ds}}$	S	drain-source admittance
$\underline{Y}_{\text{ds1}}$, $\underline{Y}_{\text{ds2}}$	S	drain-source admittance of CSS and CGS respectively
$\underline{Y}_{\text{ds2,eff}}$	S	recalculated drain-source admittance of CGS
$\underline{Y}_{\text{gd}}$	S	gate-drain admittance
$\underline{Y}_{\text{gd1}}$, $\underline{Y}_{\text{gd2}}$	S	gate-drain admittance of CSS and CGS respectively
$\underline{Y}_{\text{gd2,eff}}$	S	recalculated gate-drain admittance of CGS
$\underline{Y}_{\text{gs}}$	S	gate-source admittance
$\underline{Y}_{\text{gs1}}$, $\underline{Y}_{\text{gs2}}$	S	gate-source admittance of CSS and CGS respectively
$\underline{Y}_{\text{gs2,eff}}$	S	recalculated gate-source admittance of CGS
$\underline{Y}_{\text{s}}$	S	source admittance

Variable	Unit	Description
$\underline{Y}_{\text{s,opt}}$	S	optimum source admittance
$\underline{Y}_{\text{st}}$	S	stabilization admittance
z	m	distance
$\underline{Z}_{11}$	Ω	open circuit input impedance
$\underline{Z}_{12}$	Ω	open circuit reverse trans-impedance
$\underline{Z}_{21}$	Ω	open circuit trans-impedance
$\underline{Z}_{22}$	Ω	open circuit output impedance
$\underline{Z}_{\text{cor}}$	Ω	correlation impedance
$\underline{Z}_{\text{fs}}$	Ω	series feedback impedance
$\underline{Z}_{\text{fp}}$	Ω	parallel feedback impedance
$\underline{Z}_{\text{gs}}$	Ω	gate-source impedance
$\underline{Z}_{\text{in}}$	Ω	input impedance
$\underline{Z}_{\text{in,max}}$	Ω	maximum input impedance
$\underline{Z}_{\text{load}}$	Ω	load impedance
$\underline{Z}_{\text{load,opt}}$	Ω	optimum load impedance
$\underline{Z}_{\text{load1}}, \underline{Z}_{\text{load2}}$	Ω	load impedance of CSS and CGS respectively
$\underline{Z}_{\text{s}}$	Ω	source impedance
$\underline{Z}_{\text{s,opt}}$	Ω	optimum source impedance

Greek letters

Variable	Unit	Description
α_f	–	fitting constant for flicker noise
β_f	–	fitting constant for flicker noise
$\underline{\gamma}$	–	correlation coefficient (correlation between two noise sources)
η	–	stability factor Venkateswaran
η_{drain}	%	drain efficiency (output efficiency)
$\eta_{power-added}$	%	power added efficiency
η_{true}	%	true efficiency
λ	$\frac{W}{m \cdot K}$	thermal conductivity
μ	–	distance from the center of the Smith chart to the nearest output (load) stability circle
μ'	–	distance from the center of the Smith chart to the nearest input (source) stability circle
μ_n	$\frac{m^2}{V \cdot s}$	electron mobility
τ	s	transit time of electrons in the channel
τ_{eff}	s	recalculated transit time of electrons in the channel
τ_t	s	trap life time
ϕ_B	V	Schottky barrier height
χ	J	electron affinity
χ_1	J	electron affinity of first semiconductor material
χ_2	J	electron affinity of second semiconductor material
ω	$rad \cdot Hz$	angular frequency

Physical constants

$e = 1.602176565 \cdot 10^{-19} \, C$ elementary electric charge

$h = 6.626068 \cdot 10^{-34} \, J \cdot s$ Planck constant

$k = 1.3806503 \cdot 10^{-23} \, \frac{J}{K}$ Boltzmann constant

Mathematical constant

$\pi = 3.14159265\ldots$ pi

1 Introduction

Motivation

The amount of the electronic data exchange has increased significantly the last decades and become a permanent part of the modern human society. Semiconductors can be found in almost every electronic device. Even in the household, there are more and more electronic devices communicating with each other to facilitate the human life. Besides the telecommunication, the automobile industry is another big motor which boosts the development of semiconductor technologies. The dream of autonomous driving is no longer science fiction.

While the mobile communication standard of the fourth generation (4G), which is based on the long-term evolution standard (LTE) and LTE-Advanced (LTE+), further expands and has already —even if not area-covering yet— established in most countries, the fifth generation (5G) is available in some areas around the world. 5G addresses the engineering demands like the higher data rate (peak data rate tens of $\frac{\text{Gbit}}{\text{s}}$), lower latency (below $1\,\text{ms}$ to enable real-time applications) and lower energy costs (which would increase by 100x due to 100x higher data rate as in 4G) [2]. To deal with the necessity of the higher data rate and the lower latency the RF channel bandwidth has to be increased. Since the frequency spectrum is already very occupied at microwave frequencies (up to the centimeter wave range) and more and more frequency bands are required to transfer data from one point to another, the only way to face this problem is to expand the spectrum to the millimeter wave (mmWave) range. Fig. 1.0.1 illustrates the radar and the International Telecommunication Union (ITU) frequency bands and their fields of application at different frequency ranges.
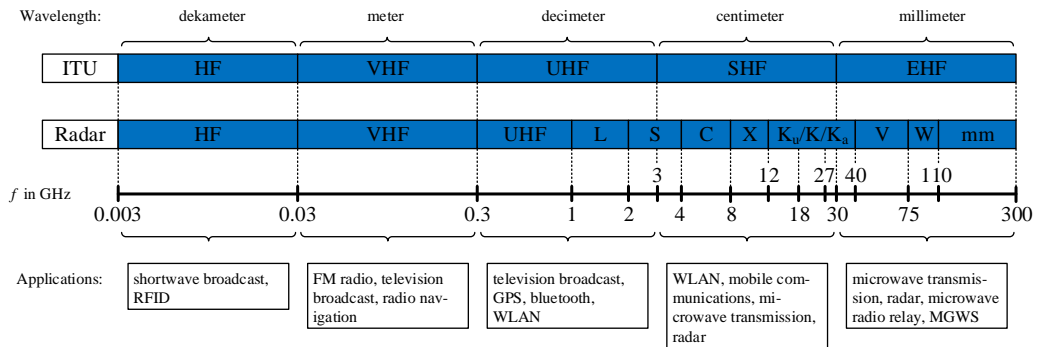
Figure 1.0.1: Radar and ITU frequency ranges and the corresponding letter designations [3–6].

To be capable of developing and measuring state-of-the-art devices —fulfilling the new standards and their strict requirements— the measurement equipment demands for high output power and high linearity over a multi-decade frequency spectrum. The GaN technology is very suited to realize broadband PAs to meet the challenges regarding P_{out} and linearity.

Cascodes in Broadband Power Amplifiers

The CC topology is a very old technique [7, 8], to improve the frequency performance of broadband PAs compared to the CS topology (i.e. bandwidth, P_{out}). The last few years common-gate (CG) models and CC models were developed for the HEMT to adapt the CC technique to the GaN-HEMT technology. More and more multi-decade PAs were already published using the GaN-HEMT technology in

combination with the CC topology (i.e. [9–16], [17, Table 5]). However, besides the advantages of the CC topology in multi-decade PAs, there are a few disadvantages like the degraded power compression at the band edge. The power degradation mainly occurs in small-signal optimized designs due to the effect that it is not possible to achieve a simultaneous power match over the complete frequency range which is related to the theory presented in [18–25]. Due to the fact that in most cases the bandwidth is of more importance in multi-decade PAs, the compression behavior degrades at higher frequencies. It is a trade-off between power match at the band edge and achieving the maximum cut-off frequency (f_c) in multi-decade amplifier designs.

This thesis addresses the advantages and disadvantages of the CC topology compared to the CS topology. The main focus of this thesis is a new proposed solution to improve the RF behavior of the CC topology, i.e. to deal with the power compression degradation of the CC topology at higher frequencies in multi-decade PAs. A new concept will be presented —based on [26–29]— which is adopted to a CC-FBA using the GaN-HEMT technology. Three possible applications of the new concept are developed and explained to improve the RF performance of multi-decade PAs which is underlined by small-signal and large-signal measurements of several designed CC-FBAs.

Thesis Summary

In Ch. 2 certain small- and large-signal parameters are explained and summarized. The small-signal definitions comprises small parts of the four-pole theory and noise four-pole theory. Small-signal definitions like the maximum stable gain (MSG), the transition frequency (f_t) and the unilateral power gain (U) will be explained and their dependencies will be shown. Large-signal parameters like the 1 dB output compression point ($1OCP$) and output inter-modulation point third order ($OIP3$), will we explained and illustrated.

Ch. 3 comprises the GaN-HEMT technology and modeling. First, the properties of GaN are compared with other semiconductor materials —silicon (Si), gallium arsenide (GaAs), diamond and so on— to point out the superior performance. Afterwards, the operation and physical structure of the GaN-HEMT will be explained and described. Furthermore, the small- and large-signal model of Jutzi [30] and the noise model of Van der Ziel [31] is presented and explained.

At the beginning of Ch. 4, the functionality of the CSS and classical CC is explained. Afterwards, certain small-signal parameters of the CSS and the CC are determined. Due to the fact that the CGS of the classical CC is modified nowadays —especially using the GaN technology— the modified CC is investigated and the small-signal dependencies are listed. At the end the large-signal parameters like the maximum output power ($P_{out,max}$) of the CSS and the CC are determined.

In Ch. 5 certain small- and large-signal parameters of the CSS and the CC are compared with each other to show the advantages and disadvantages of the CC. Furthermore, the influence of the stabilization capacitor is elaborated to show the difference between classical CC and modified CC. At the end the advantages and disadvantages of the CC compared to the CSS are summarized.

In the following main Ch. 6 a new concept is presented to realize the modified CGS which is used nowadays in CCs to improve the performance in broadband PAs. The general principle of the new concept is explained at the beginning. Afterwards, three applications are presented in detail to improve certain parameters of the CGS. Moreover, different realizations of the new concept are compared with each other to point out the advantages and disadvantages. At the end a short summary of the new concept is given.

In the second main Ch. 7 the performance of several designed FBAs are shown. At the beginning two kind of multi-decade PAs are explained. Afterwards the results of two designed FBAs in CS and CC topology are illustrated and compared with each other to point out the trade-off between the CSS and the CC in broadband PAs. Furthermore the performance of several designed CC-FBAs are compared with each other to highlight the performance of different applications and realizations of the new concept.

In the last Ch. 8 the key findings of the thesis are summarized and discussed. New ideas are suggested to achieve further improvements of the new concept in broadband PAs using the CC topology.

2 Definitions

In this chapter a short summary is given about the most important small- and large-signal parameters and how they are defined. On the one hand small-signal definitions like *MSG*, f_t and U will be explained and on the other hand large-signal parameters like 1*OCP*, *OIP*3 and harmonics will be illustrated and explained.

2.1 Four-Pole Theory

The electrical behavior of a linear two-port network (i.e. amplifier, filter, attenuator) can be described by mathematical expressions and equations, depending on currents, voltages and power waves at the input and the output of the network, shown in Fig. 2.1.1.

Figure 2.1.1: (a) General two-port network with currents and voltages and (b) the equivalent power waves [32].

There are different representations of a two-port network, reflected by i.e. impedance-parameters (Z-), admittance (Y-), hybrid (H-) or scattering (S-) parameters, which can be determined by measurement and calculation. While the Z-, Y- and H-parameters describe ratios of currents and/or voltages to each other, the S-parameters (scattering parameters) represent ratios of power waves, which have many advantages in the high frequency domain [32]. The S-parameters are given by

$$\begin{pmatrix} \underline{b}_1 \\ \underline{b}_2 \end{pmatrix} = \begin{pmatrix} \underline{S}_{11} = \frac{\underline{b}_1}{\underline{a}_1}\big|_{\underline{a}_2=0} & \underline{S}_{12} = \frac{\underline{b}_1}{\underline{a}_2}\big|_{\underline{a}_1=0} \\ \underline{S}_{21} = \frac{\underline{b}_2}{\underline{a}_1}\big|_{\underline{a}_2=0} & \underline{S}_{22} = \frac{\underline{b}_2}{\underline{a}_2}\big|_{\underline{a}_1=0} \end{pmatrix} \begin{pmatrix} \underline{a}_1 \\ \underline{a}_2 \end{pmatrix}. \tag{2.1.1}$$

In the following Y-parameters (admittance parameters), H-parameters (hybrid parameters) and their relation are presented, mainly obtained from [32], due to the fact that they are mainly used in this thesis. The Y-parameters and H-parameters can be calculated by

$$\begin{pmatrix} \underline{I}_1 \\ \underline{I}_2 \end{pmatrix} = \begin{pmatrix} \underline{Y}_{11} = \frac{\underline{I}_1}{\underline{V}_1}\big|_{\underline{V}_2=0} & \underline{Y}_{12} = \frac{\underline{I}_1}{\underline{V}_2}\big|_{\underline{V}_1=0} \\ \underline{Y}_{21} = \frac{\underline{I}_2}{\underline{V}_1}\big|_{\underline{V}_2=0} & \underline{Y}_{22} = \frac{\underline{I}_2}{\underline{V}_2}\big|_{\underline{V}_1=0} \end{pmatrix} \begin{pmatrix} \underline{V}_1 \\ \underline{V}_2 \end{pmatrix} \tag{2.1.2}$$

and

$$\begin{pmatrix} \underline{V}_1 \\ \underline{I}_2 \end{pmatrix} = \begin{pmatrix} \underline{H}_{11} = \frac{\underline{V}_1}{\underline{I}_1}\big|_{\underline{V}_2=0} & \underline{H}_{12} = \frac{\underline{V}_1}{\underline{V}_2}\big|_{\underline{I}_1=0} \\ \underline{H}_{21} = \frac{\underline{I}_2}{\underline{I}_1}\big|_{\underline{V}_2=0} & \underline{H}_{22} = \frac{\underline{I}_2}{\underline{V}_2}\big|_{\underline{I}_1=0} \end{pmatrix} \begin{pmatrix} \underline{I}_1 \\ \underline{V}_2 \end{pmatrix}. \tag{2.1.3}$$

The Y-parameters can be recalculated to the H-parameters and vice versa by

$$\underline{\mathbf{Y}} = \begin{pmatrix} \frac{1}{\underline{H}_{11}} & -\frac{\underline{H}_{12}}{\underline{H}_{11}} \\ \frac{\underline{H}_{21}}{\underline{H}_{11}} & \frac{\det(\underline{\mathbf{H}})}{\underline{H}_{11}} \end{pmatrix} \qquad\qquad \underline{\mathbf{H}} = \begin{pmatrix} \frac{1}{\underline{Y}_{11}} & -\frac{\underline{Y}_{12}}{\underline{Y}_{11}} \\ \frac{\underline{Y}_{21}}{\underline{Y}_{11}} & \frac{\det(\underline{\mathbf{Y}})}{\underline{Y}_{11}} \end{pmatrix} . \tag{2.1.4}$$

2.2 Small-Signal Key Parameters

Small-signal parameters are used to characterize the linear electrical performance of microwave devices, circuits and systems. A very good overview about the different power gains in FBAs was given in 1992 by Gupta [33] and will be summarized in the following.

Rollett's Stability Factor

Obtained from [34–36], in 1962 Venkateswaran [37] and Rollett [38, 39] presented that the critical-ness factor (C) published by Linvill et al. [40, 41] remains unchanged, expressing the stability factor (Venkateswaran's η, Rollett's k) as the reverse of C by the Z-, Y-, H- and inverse-hybrid (G-) parameters. The Rollett criterion is expressed by

$$k = \frac{2 \cdot \Re\{\underline{Y}_{11}\}\Re\{\underline{Y}_{22}\} - \Re\{\underline{Y}_{12}\underline{Y}_{21}\}}{|\underline{Y}_{12}\underline{Y}_{21}|} > 1 \tag{2.2.1}$$

and

$$\Re\{\underline{Y}_{11}\} > 0 \tag{2.2.2}$$
$$\Re\{\underline{Y}_{22}\} > 0 , \tag{2.2.3}$$

where $\underline{Y}_{ij}$ either $\underline{Z}_{ij}$, $\underline{H}_{ij}$ or $\underline{G}_{ij}$. If the Rollett criterion eq. (2.2.1)–eq. (2.2.3) and the Rollet proviso —two-port network is intrinsic stable at any passive load at the input and output of the network (network has no right half-plane poles)— is fulfilled, the two-port network is unconditionally stable. In [42], the Rollett stability criterion was recalculated in terms of S-parameters by Kurokawa to

$$k = \frac{1 + |\det(\underline{\mathbf{S}})|^2 - |\underline{S}_{11}|^2 - |\underline{S}_{22}|^2}{2 \cdot |\underline{S}_{12}||\underline{S}_{21}|} > 1 \tag{2.2.4}$$

and

$$|\det(\underline{\mathbf{S}})| < 1 . \tag{2.2.5}$$

Further suited stability factors presented in [43] which give the distance from the center of the Smith chart to the nearest output (load) stability circle and input (source) stability circle are μ and μ' respectively expressed by

$$\mu = \frac{1 - |\underline{S}_{11}|^2}{|\underline{S}_{22} - \underline{S}_{11}^* \det(\underline{\mathbf{S}})| + |\underline{S}_{21}||\underline{S}_{12}|} > 1 \tag{2.2.6}$$

and

$$\mu' = \frac{1 - |\underline{S}_{22}|^2}{|\underline{S}_{11} - \underline{S}_{22}^* \det(\underline{\mathbf{S}})| + |\underline{S}_{21}||\underline{S}_{12}|} > 1 . \tag{2.2.7}$$

Maximum Available Gain

The definition of the maximum available gain (*MAG*), also called maximum available power gain, goes back to the 50s [44]. The *MAG* is achieved, if the input and output of a two-port network are simultaneously matched to the source and load respectively within the limits of the stability condition (positive resistive part of the input and output impedance of the two-port network for arbitrary passive input and output terminations). Rollett expresses the *MAG* in [38] in terms of the stability factor k by

$$MAG = \left|\frac{\underline{Y}_{21}}{\underline{Y}_{12}}\right| \left(k - \sqrt{k^2 - 1}\right) \tag{2.2.8}$$

for $k > 1$, where $\underline{Y}_{ij}$ either $\underline{Z}_{ij}$, $\underline{H}_{ij}$ or $\underline{G}_{ij}$. Later one, in [42], the *MAG* was recalculated in terms of the S-parameters to

$$MAG = \left|\frac{\underline{S}_{21}}{\underline{S}_{12}}\right| \left(k - \sqrt{k^2 - 1}\right) . \tag{2.2.9}$$

Maximum Stable Gain

In [45], the *MSG*, also named maximum stable power gain, referenced to [46], was derived by Rollett to

$$MSG = \left|\frac{\underline{Y}_{21}}{\underline{Y}_{12}}\right| \tag{2.2.10}$$

for $k \leq 1$.

Unilateral Power Gain

In 1954 [47], Mason introduced U, also known as Mason's invariant, as a figure of merit of an active device. By using a lossless reciprocal passive network, the active device is unilateralized (no further reverse transmission of the output to the input of the active device). Afterwards the source and load impedance are chosen in such a way, that the gain is maximized. Mason determined U to

$$U = \frac{|\underline{Y}_{21} - \underline{Y}_{12}|^2}{4 \cdot (\Re\{\underline{Y}_{11}\}\Re\{\underline{Y}_{22}\} - \Re\{\underline{Y}_{12}\}\Re\{\underline{Y}_{21}\})} , \tag{2.2.11}$$

where $\underline{Y}_{ij}$ either $\underline{Z}_{ij}$, $\underline{H}_{ij}$ or $\underline{G}_{ij}$. In [48], the U was recalculated, in terms of S-parameters, to

$$U = \frac{|\underline{S}_{21} - \underline{S}_{12}|^2}{\det\left(\mathbf{1} - \overline{\mathbf{S}} \cdot \mathbf{S}\right)} . \tag{2.2.12}$$

Maximum Oscillation Frequency

The maximum oscillation frequency ($f_{\max}$) is related to U of an active device. $f_{\max}$ is the frequency at which U gets equal one:

$$U\left(f = f_{\max}\right) = 1 . \tag{2.2.13}$$

In [49, 50], $f_{\max}$ was mentioned the first time. Due to the fact that $f_{\max}$ is a single value it is often used as a key parameter to benchmark different semiconductor technologies with each other and to show the progress of the active device technology.

Transition Frequency

Another important key parameter of active devices to compare different foundry processes with each other is f_t. The idea of the internal cut-off frequency f_t was first presented in [51] which was the result of informal discussions on IRE-AIEE Task Group 28.4.8 on Transistor Internal Parameters of Pritchard with his colleagues. f_t is defined as the frequency at which the magnitude of $\underline{H}_{21}$ of the active device is unity:

$$|\underline{H}_{21}\left(f = f_t\right)| = 1 . \tag{2.2.14}$$

f_t is also known as a measure of the current-gain bandwidth product of an active device and also sometimes named beta cut-off frequency as in [52].

2.3 Large-Signal Key Parameters

Large-signal parameters are used to characterize the non-linear electrical performance of microwave devices, circuits and systems. A very good overview about the most important large-signal key parameters can be found in [53]. Some of the large-signal key parameters for PA in class A operation, mainly obtained from [53], will be summarized in this section.

Efficiency

There are different definitions of the efficiency of PAs. Efficiency is a figure of merit how much direct current (DC) power (P_{DC}) is converted into P_{out} and how less dissipation power (P_{DISS}) is generated. The most common definition of the efficiency is the power added efficiency ($\eta_{power-added}$ or PAE) which is given by

$$\eta_{power-added} = 100\% \cdot \left(\frac{P_{out} - P_{in}}{P_{DC}} \right) = PAE \; , \tag{2.3.1}$$

considering the input power (P_{in}) of the PA. The PAE is used in this thesis to determine the overall efficiency of designed PAs. Output efficiency, also called drain efficiency (η_{drain}), is another frequently used definition expressed by

$$\eta_{drain} = 100\% \cdot \left(\frac{P_{out}}{P_{DC}} \right) \; . \tag{2.3.2}$$

η_{drain} is very similar to the PAE, if the overall gain is very high. Therefore in a hole system amplifier —including several stages— the η_{drain} is rather sufficient. However, for single stages with low gain η_{drain} is not suited. The true efficiency (η_{true}) is used very seldom and is given by

$$\eta_{true} = 100\% \cdot \left(\frac{P_{out}}{P_{DC} + P_{in}} \right) \; , \tag{2.3.3}$$

which represents the total efficiency of the PA. It can be directly mapped to the P_{DISS}:

$$P_{DISS} = \frac{P_{out}}{1 - \eta_{true}} \; . \tag{2.3.4}$$

Gain Compression and Saturated Output Power

Gain compression (power compression) is a fundamental behavior of PAs in class A operation (explanation of the different PA operation classes —i.e. A, AB, B, C, D/E/F—can be found in [53]). The gain compression ($Comp$) and the normalized $Gain$ are defined by

$$Comp = \frac{1}{\text{normalized } Gain} \qquad\qquad Comp_{dB} = -\text{normalized } Gain_{dB} \tag{2.3.5}$$

$$= \frac{P_{out,SS}}{P_{out,LS}} \qquad\qquad\qquad = P_{out,SS,dB} - P_{out,LS,dB} \; , \tag{2.3.6}$$

where $P_{out,SS}$ is P_{out} for low input power (P_{in}) and $P_{out,LS}$ is P_{out} in large-signal operation. In case of low P_{in} (small-signal condition is valid), the P_{out} can be written as

$$P_{out} = P_{in} \cdot |\underline{S}_{21}| \qquad\qquad P_{out,dBm} = P_{in,dBm} + |\underline{S}_{21}|_{dB} \; . \tag{2.3.7}$$

However, at larger P_{out} the eq. (2.3.7) is no longer valid and have to be modified to

$$P_{out} = P_{in} \cdot \underbrace{\frac{|\underline{S}_{21}|}{Comp}}_{Gain} \qquad\qquad P_{out,dBm} = P_{in,dBm} + \underbrace{|\underline{S}_{21}|_{dB} - Comp_{dB}}_{Gain_{dB}} \; . \tag{2.3.8}$$

Fig. 2.3.1 shows a typical compression behavior of the P_{out} versus P_{in}. The 1 dB compression point ($P1dB$) illustrated in Fig. 2.3.1 is used among other things as a figure of merit to highlight the linearity characteristic of a PA. The $1OCP$ refers the $P1dB$ to the output and the 1 dB input compression point ($1ICP$) refers the $P1dB$ to the input of the PA. However it is very common in practice, that the $1OCP$ is identified with the $P1dB$, which is also done in this thesis. In general the saturated output power (P_{sat}) of a PA is usually achieved at a *Comp* of about 3–5 dB, which depends among other things on the semiconductor technology, i.e. GaAs: $P_{sat} = P_{out}(Comp_{dB} \approx 3\,dB)$ and GaN: $P_{sat} = P_{out}(Comp_{dB} \approx 5\,dB)$. At higher compression the P_{out} can even degrade due to the higher P_{DISS} which results in a higher junction temperature (T_j) of the active device.
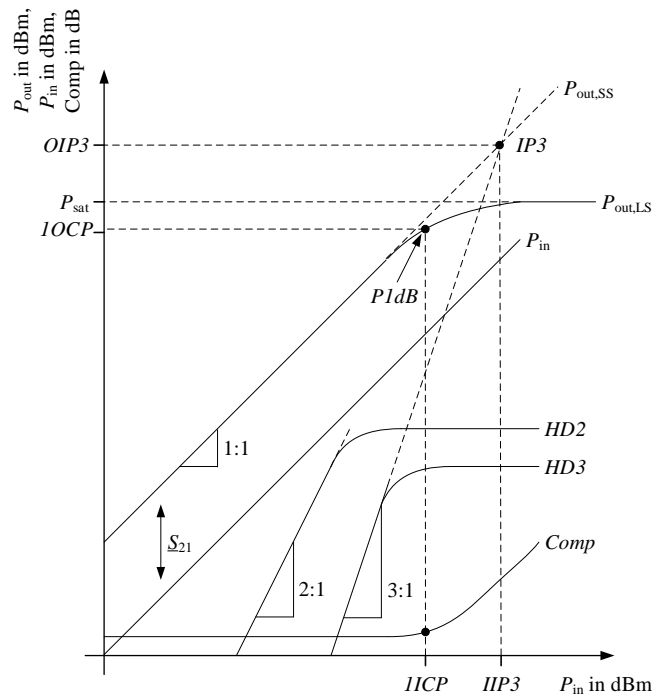
Figure 2.3.1: Typical power compression of a PA in class A operation [53].

Harmonic Distortion and Inter-Modulation Distortion

Due to the fact, that the active device is non-linear in large-signal operation, the useful input signal is distorted. As a result undesirable signals arise at frequencies which are integral multiples of the fundamental signal. These higher frequency terms are called harmonics and can be very annoying in microwave systems, since they can i.e. interleave with neighborhood telecommunication channels which are often very close next to each other to utilize the entire bandwidth. The second harmonic distortion ($HD2$) and the third harmonic distortion ($HD3$), whose power levels are usually expressed relative to the fundamental tone in dBc, are typically the most critical harmonics. However, at certain applications higher harmonics can be very important as well. Fig. 2.3.2 illustrated a typical spectrum of a distorted signal.

Another very important distortion is the inter-modulation distortion. This kind of distortion occurs in a non-linear circuit if the input signal consists of multiple frequencies. Each signal at a certain frequency at the input itself creates harmonics, but two signals with different frequencies at the input generate inter-modulation products which are the sum and the differences of all useful signals and harmonics. Fig. 2.3.2 shows some possible combinations of only two useful signals of a non-linear circuit. It can be seen that the frequency of the inter-modulation distortion third order ($IMD3$) is very close to the fundamental tones. This is one of the main disadvantages of inter-modulation terms compared to harmonics. Due to the fact that the harmonics are typically far away from the fundamental tone, they can be filtered out in narrow-band PAs with a following low-pass filter. However, the $IMD3$ terms are mainly in-band

and therefore it is very difficult to get rid off these terms. The inter-modulation distortion is typically specified by the third oder intercept point (*IP3*), illustrated in Fig. 2.3.1, as a figure of merit to point out the linearity of a PA. The *IP3* referring to the output (*OIP3*) can be expressed by

$$OIP3 = P_{\text{out,1tone}} \cdot \sqrt{\frac{P_{\text{out,1tone}}}{IMD3}} \qquad\qquad OIP3_{\text{dBm}} = P_{\text{out,1tone,dBm}} + \frac{IMD3_{\text{dBc}}}{2} \ . \qquad (2.3.9)$$

Furthermore, Cripps derived a relationship between the 1*OCP* and the *OIP3* to [54, Ch 9]

$$OIP3 = 1OCP \cdot \left(\frac{1}{1 - 10^{-0.05}} \right) \qquad\qquad OIP3 = 1OCP + \underbrace{10 \lg \left(\frac{1}{1 - 10^{-0.05}} \right)}_{\approx 9.6\,\text{dB}}, \qquad (2.3.10)$$

which can be used as a rule-of-thumb to predict the *OIP3* from the *P1dB* without any measurements of the *IMD3*.
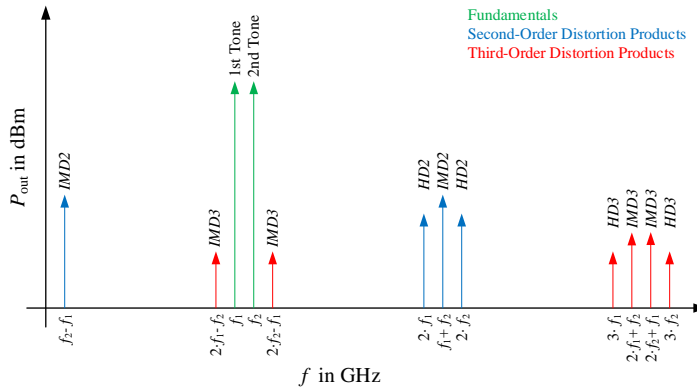
Figure 2.3.2: Typical power spectrum at the output of a PA in class A operation stimulated by a 2-tone signal [53].

2.4 Noise Theory

2.4.1 Noise Mechanisms

The following brief summary of noise types is based on the very good overview about the most common noise sources which can be found in [55] and was summarized in [6]. Fig. 2.4.1 illustrates the noise power spectrum of the most common noise sources.
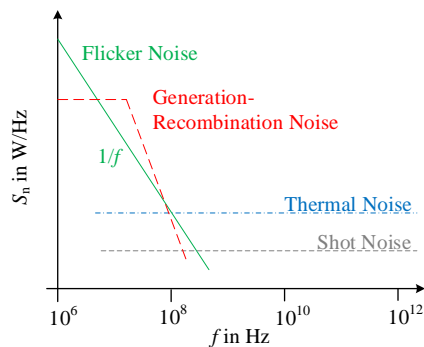
Figure 2.4.1: Power spectrum of flicker noise, generation–recombination noise, shot noise and thermal noise [6].

Thermal Noise

Thermal noise which is generated by random motion of charge carriers in a conductor was first studied in [56] by Johnson and later mathematically explained in [57] by Nyquist:

$$P_{n,av} = \left[\frac{1}{2}hf + \frac{hf}{\exp\left(\frac{hf}{kT}\right) - 1} \right] B \tag{2.4.1}$$

$$\approx kTB . \tag{2.4.2}$$

$P_{n,av}$, h, f, k, T and B are the available thermal noise power, Planck constant, frequency, Boltzmann constant, temperature and bandwidth respectively. The approximation is valid for frequencies up to $\approx 100\,\text{GHz}$.

Shot Noise

Shot noise was first introduced in [58] by Schottky in vacuum tubes which is generated by the discontinuous current composed of a forced DC current and randomly charges hopping over a potential barrier. The normalized current power spectral density of shot noise ($S_{n,shot}$) can be expressed by [55]

$$S_{n,shot} = 2e \left| I_{pot.} \right| , \tag{2.4.3}$$

where e and $I_{pot.}$ are the elementary electric charge and the average current through a potential barrier respectively.

Flicker Noise

In [59] and [60] flicker noise was discovered by Johnson and interpreted by Schottky respectively. Flicker noise has a slope inverse to the frequency due to that fact it gets dominant at low frequencies. Very common names besides the flicker noise are also $\frac{1}{f}$-noise or pink noise. The normalized current power spectral density of flicker noise $S_{n,f}$ can be expressed by [61]

$$S_{n,f}(f) = \frac{K_f I^{\beta_f}}{f^{\alpha_f}} , \tag{2.4.4}$$

where K_f, α_f and β_f are fitting parameters which are close to unity.

Generation–Recombination Noise

The noise spectrum of the generation–recombination noise which is caused by electron and/or hole traps and recombination centers can be described by [55]

$$S_{n,gr}(f) = 4\overline{\Delta N^2} \frac{\tau_t}{1 + \omega^2 \tau_t^2} , \tag{2.4.5}$$

where $S_{n,gr}$, τ_t, $\overline{\Delta N^2}$ and ω are the normalized voltage power spectral density of generation-recombination noise, trap life time, variance of number of electrons (N) emitted during τ_t and angular frequency respectively.

2.4.2 Noise Four-Pole Theory

The following overview of the noise four-pole theory is mainly obtained from [62] and was summarized in [6]. The noise four-pole theory can be handled in a similar way as the four-pole theory. The noise behavior of a noisy two-port, shown in Fig. 2.4.2, can be described by mathematical expressions and equations as well [62]:

$$\underline{V}_1 = \underline{Z}_{11}\underline{I}_1 + \underline{Z}_{12}\underline{I}_2 + \underline{V}_{n1} \qquad\qquad \underline{I}_1 = \underline{Y}_{11}\underline{V}_1 + \underline{Y}_{12}\underline{V}_2 + \underline{I}_{n1} \tag{2.4.6}$$

$$\underline{V}_2 = \underline{Z}_{21}\underline{I}_1 + \underline{Z}_{22}\underline{I}_2 + \underline{V}_{n2} \qquad\qquad \underline{I}_2 = \underline{Y}_{21}\underline{V}_1 + \underline{Y}_{22}\underline{V}_2 + \underline{I}_{n2} . \tag{2.4.7}$$
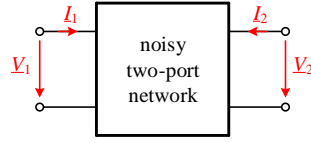
Figure 2.4.2: Two-port network with internal noise sources [62].

In [62], Rothe and Dahlke introduced three representations to model noise in two-port networks, shown in Fig. 2.4.3:

1. Two correlated noise voltage sources at the input with $\underline{V}_{n1}$ and output with $\underline{V}_{n2}$ of the noiseless two-port network.
2. Two correlated noise current sources at the input with $\underline{I}_{n1}$ and output with $\underline{I}_{n2}$ of the noiseless two-port network.
3. Two correlated noise sources at the input:
   a) One noise voltage source with $\underline{V}_n$ and
   b) one noise current source with $\underline{I}_n$.
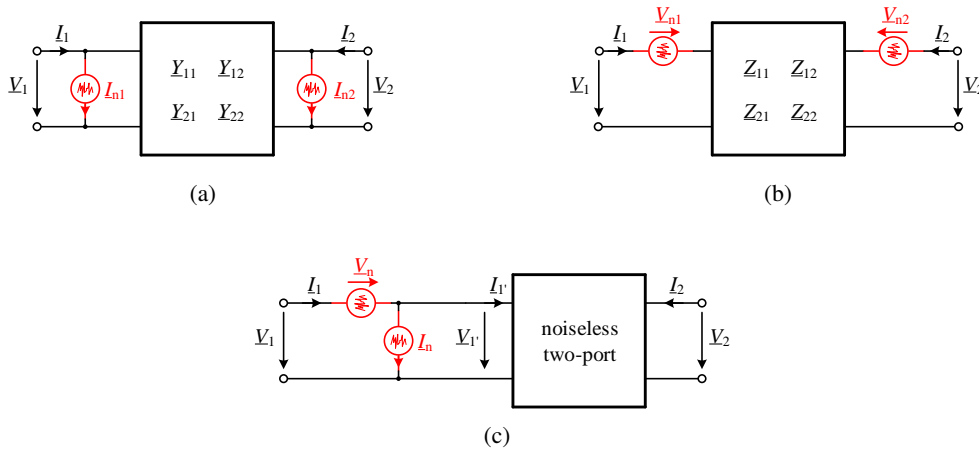
Figure 2.4.3: (a) Noiseless two-port network with two correlated noise current sources. (b) Noiseless two-port network with two correlated noise voltage sources. (c) Noiseless two-port network with correlated noise voltage and noise current source [6, 62].

The last noise representation of noisy two-port networks, shown in Fig. 2.4.3c has the superior advantage over the other representations that the noise calculation is independent of the circuit elements of the two-port network, because they are referring to the output of the network. The two noise sources are described by [62]

$$\overline{|\underline{V}_n|^2} = 4kT_0B \cdot R_n \tag{2.4.8}$$

$$\overline{|\underline{I}_n|^2} = 4kT_0B \cdot g_n \tag{2.4.9}$$

and are correlated with correlation coefficient $\underline{\gamma}$:

$$\underline{\gamma} = \frac{\overline{\underline{V}_n^* \underline{I}_n}}{\sqrt{\overline{|\underline{V}_n|^2} \cdot \overline{|\underline{I}_n|^2}}} \ . \tag{2.4.10}$$

R_n and g_n are the equivalent noise resistance and noise conductance of $\underline{V}_n$ and $\underline{I}_n$ respectively. Furthermore, two correlated noise sources can be recalculated into two uncorrelated noise sources using a correlation impedance ($\underline{Z}_{cor}$) or a correlation admittance ($\underline{Y}_{cor}$), shown in Fig. 2.4.4.
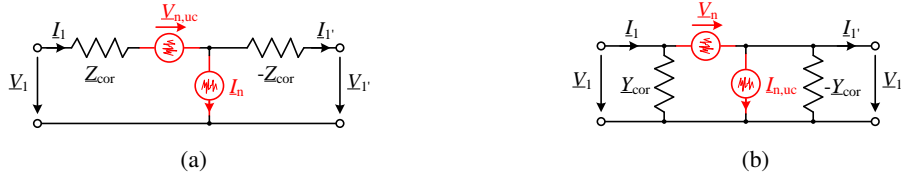
Figure 2.4.4: Noiseless two-port network with two uncorrelated noise sources. (a) T-presentation. (b) PI-presentation [6, 62].

Recalculated noise sources with $\overline{\left|\underline{V}_{\mathrm{n,uc}}\right|^2}$ and $\overline{\left|\underline{I}_{\mathrm{n,uc}}\right|^2}$ and corresponding $\underline{Z}_{\mathrm{cor}}$ and $\underline{Y}_{\mathrm{cor}}$ can be derived to [6, 62]

$$\overline{\left|V_{\mathrm{n,uc}}\right|^2} = 4kT_0B \cdot r_{\mathrm{n}} \qquad\qquad \underline{Z}_{\mathrm{cor}} = \frac{\overline{\underline{I}_{\mathrm{n}}^*\underline{V}_{\mathrm{n}}}}{\overline{\left|\underline{I}_{\mathrm{n}}\right|^2}} = \underline{\gamma}\sqrt{\frac{R_{\mathrm{n}}}{g_{\mathrm{n}}}} \qquad (2.4.11)$$

$$\overline{\left|I_{\mathrm{n,uc}}\right|^2} = 4kT_0B \cdot G_{\mathrm{n}} \qquad\qquad \underline{Y}_{\mathrm{cor}} = \frac{\overline{\underline{V}_{\mathrm{n}}^*\underline{I}_{\mathrm{n}}}}{\overline{\left|\underline{V}_{\mathrm{n}}\right|^2}} = \underline{\gamma}\sqrt{\frac{g_{\mathrm{n}}}{R_{\mathrm{n}}}} \; . \qquad (2.4.12)$$

One of the most important noise parameters of two-port networks which characterize noise behavior are the noise factor (F) and the minimum noise factor (F_{min}). F and F_{min} expressed logarithmically by $NF = 10\log(F)$ and $NF_{\mathrm{min}} = 10\log(F_{\mathrm{min}})$ are called noise figure (NF) and minimum noise figure (NF_{min}), respectively. F reflects the noise increase due to the noisy two-port network to the useful signal, which was first defined by Friis in [63] as the ratio of the signal-to-noise ratio (SNR) at the input and output of the two-port network. F_{min} is the minimum F, which can be achieved for optimum noise matching at the input of the two-port network. F and F_{min} can be calculated to [6, 62]

$$F = F_{\mathrm{min}} + \frac{g_{\mathrm{n}}}{R_{\mathrm{s}}}\left|\underline{Z}_{\mathrm{s}} - \underline{Z}_{\mathrm{s,opt}}\right|^2 \qquad\qquad F_{\mathrm{min}} = 1 + 2g_{\mathrm{n}}\left(R_{\mathrm{s,opt}} + R_{\mathrm{cor}}\right) \qquad (2.4.13)$$

$$F = F_{\mathrm{min}} + \frac{R_{\mathrm{n}}}{G_{\mathrm{s}}}\left|\underline{Y}_{\mathrm{s}} - \underline{Y}_{\mathrm{s,opt}}\right|^2 \qquad\qquad F_{\mathrm{min}} = 1 + 2R_{\mathrm{n}}\left(G_{\mathrm{s,opt}} + G_{\mathrm{cor}}\right) \; , \qquad (2.4.14)$$

with optimum source impedance ($\underline{Z}_{\mathrm{s,opt}} = R_{\mathrm{s,opt}} + jX_{\mathrm{s,opt}}$)

$$R_{\mathrm{s,opt}} = \sqrt{\frac{r_{\mathrm{n}}}{g_{\mathrm{n}}} + R_{\mathrm{cor}}^2} = \sqrt{\frac{R_{\mathrm{n}}}{g_{\mathrm{n}}} - X_{\mathrm{cor}}^2} \qquad\qquad X_{\mathrm{s,opt}} = -X_{\mathrm{cor}} \; , \qquad (2.4.15)$$

optimum source admittance ($\underline{Y}_{\mathrm{s,opt}} = G_{\mathrm{s,opt}} + jB_{\mathrm{s,opt}}$)

$$G_{\mathrm{s,opt}} = \sqrt{\frac{G_{\mathrm{n}}}{R_{\mathrm{n}}} + G_{\mathrm{cor}}^2} = \sqrt{\frac{g_{\mathrm{n}}}{R_{\mathrm{n}}} - B_{\mathrm{cor}}^2} \qquad\qquad B_{\mathrm{s,opt}} = -B_{\mathrm{cor}} \qquad (2.4.16)$$

and source impedance ($\underline{Z}_{\mathrm{s}} = R_{\mathrm{s}} + jX_{\mathrm{s}}$) and source admittance ($\underline{Y}_{\mathrm{s}} = G_{\mathrm{s}} + jB_{\mathrm{s}}$).

In eq. (2.4.13) and eq. (2.4.14) it can be seen, that equivalent noise conductance of noise current source (g_{n}) and equivalent noise resistance of noise voltage source (R_{n}) determine the degradation of F if the optimum noise matching at the input of the two-port network is not fulfilled.

3 GaN-HEMT Technology and Modeling

This chapter points out on the one hand the advantages of the GaN-HEMT technology by comparing it with other semiconductor technologies and shows on the other hand how GaN-HEMTs can be modeled. The chapter starts by comparing the key properties of GaN semiconductor with other semiconductors and explain afterwards the functionality of the HEMT to highlight the superiority of the GaN-HEMT technology —combining the GaN material with the HEMT structure— over other technologies.

3.1 GaN-HEMT Technology

The following information in this section is mainly based on the very good overview about the superior performance of the GaN-HEMT technology which can be found in [30, 64, 65] and was briefly summarized in [6], adding additionally state-of-the-art performance.

3.1.1 GaN Semiconductor

Due to the large community and the cheap manufacturing costs, the semiconductor Si is used in a wide range of applications. In the last decades, the Si semiconductor development, i.e. lateral diffused metal oxide semiconductor (LDMOS) proceed significantly. In 2002 Olsson [66] presented a maximum power density of Si-LDMOS transistors of $1\frac{W}{mm}$ and $2\frac{W}{mm}$ at $3.2\,GHz$ and $1\,GHz$, respectively. In 2018 Theeuwen [67] published a $3\,dB$ output power density of a modern Si-LDMOS technology between $1.6\frac{W}{mm}$ at $\approx 2\,GHz$ and around $1\frac{W}{mm}$ at $12\,GHz$. Since the band-gap energy (E_g) of Si is rather low compared to other semiconductors, shown in Table 3.1.1, the only possibility to increase the power density at higher frequencies is the use of another semiconductor with higher E_g. The GaAs semiconductor is widespread nowadays, due to the higher E_g and very high electron mobility (μ_n). As a result GaAs semiconductor technology is very suited to achieve high power (capable of higher power density) and high gain at higher frequencies.

Comparing the semiconductors in Table 3.1.1, diamond is the most promising material due to the very large E_g —resulting in a high breakdown field strength (E_{BR}) and high breakdown voltage (V_{BR})—, saturated electron drift velocity ($v_{d,sat}$) and thermal conductivity (λ). However, using diamond as a commercial semiconductor technology, several issues have to be addressed and solved (i.e. homogeneous doping concentration or competitive reasonable device fabrication regarding costs and performance) as reported in [68] and [69]. At the present day, the semiconductor GaN with moderate high E_g (much higher than Si or GaAs) is used with silicon carbide (SiC) as a substrate to maintain a good thermal interconnection. There are different crystal structures of SiC (i.e. 4H-SiC, 6H-SiC) with different material properties as explained in [70]. An alternative to the expensive SiC substrate in combination with the GaN offers the Si substrate, which is more and more used for base station PAs because costs play a dominate role. However, the performance suffers a little bit. Table 3.1.1 highlights the advantage of GaN semiconductor compared to common Si or GaAs semiconductor.

Table 3.1.1: Comparison of physical and electrical properties of different semiconductor materials: Si, germanium (Ge), GaAs, SiC, GaN, aluminum gallium nitride (AlGaN), aluminum nitride (AlN), indium phosphide (InP) and diamond.

Semi-conductor	μ_n $(\frac{cm^2}{mV \cdot s})$	$v_{d,max}$ $(\frac{cm}{\mu s})$	$v_{d,sat}$ $(\frac{cm}{\mu s})$	E_g (eV)	E_{BR} $(\frac{MV}{cm})$	λ $(\frac{W}{cm \cdot K})$
Si	1.2[71]–1.5[72]	10[73]	10[72]	1.1[72], 1.12[74,75]	0.25[71]–0.3[72]	1.3[74,75]–1.5[72]
Ge	3.9[74,75]	6[76]		0.661[74,75]	0.1[74,75]	0.58[74,75]
InP	5.4[74,75]	25[77]	9[77]	1.34[78], 1.344[74,75]	0.45[78]–0.5[74,75]	0.67[78]–0.68[74,75]
GaAs	6.5[71]–8.5[72]	19[77]–22[73]	8[77]–12[73]	1.424[74,75]–1.43[72]	0.25[71]–0.6[72]	0.46[72]–0.55[74,75]
3H-SiC	0.3[75,79]–1.0[72]	N/A	22[72]–25[75,80]	2.2[72]–2.36[75,79,81]	1.3[78]–2.0[75,82]	4[78]–7[75,79]
4H-SiC	0.7[75,83]–1.14[72]	22[73]	18[73]–20[72]	3.25[75,83]–3.3[73]	2.2[84,85]–3.5[78]	4[78]–7[75,79]
6H-SiC	0.33[75,83]–0.8[73,85]	19[73]	15[73]	2.86[78]–3.03[84,86]	2.5[84,85]–4.0[73]	4[78]–7[75,79]
GaN	0.9[71]–1.25[72]	25[71]–28[73]	15[73]–20[73]	3.4[78]–3.45[72]	2.0[78]–4.0[85]	1.1[75,79]–1.5[73]
AlGaN	0.15[85]	30[78]	17[78]	4.1[85]	5.9[85]	0.4[85]
AlN	0.425[85]	N/A	N/A	6.2[85]	16.6[85]	2.9[85]–3.0[72]
Diamond	1.9[73]–2.0[72]	27[72]	19[73]	5.45[72]–5.6[78]	5.0[78]–10.0[72]	6[74,75]–30[78]

Fig. 3.1.1 illustrates v_d of different semiconductor technologies versus the electric field. Due to the fact that $v_{d,sat}$ of the GaN is much better compared to the Si and $v_{d,max}$ is reached at higher electric fields compared to the GaAs, the GaN offers a superior performance in applications which require high power at microwave frequencies.
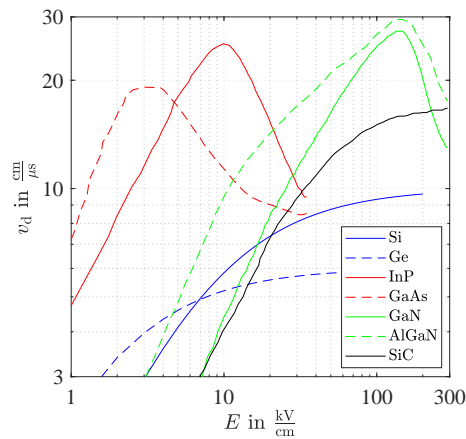
Figure 3.1.1: Electron drift velocity (v_d) of Si (sim.), Ge (sim.), InP, GaAs, GaN and SiC [74, 75, 77, 78, 87–89].

3.1.2 HEMT

In [90, 91] Anderson investigated and presented the improved properties of a Ge/GaAs heterojunction. Based on the aluminum gallium arsenide / gallium arsenide (AlGaAs/GaAs) heterojunction, in 1980 a new kind of field effect transistor (FET) was presented in [92], called HEMT. Nowadays several abbreviations exist which describe the HEMT:

- high field effect transistor (HFET)
- modulation doped field effect transistor (MODFET)
- two-dimensional electron gas field effect transistor (TEGFET)
- selectively-doped heterojunction transistor (SDHT)

3.1.2.1 Operation

Basic idea of the HEMT:

- Use of a heterojunction between two different semiconductors to build a highly conducting channel in the undoped part of the semiconductor which is controlled by an external voltage.

Common properties of the two different semiconductors to build a heterojunction:

- different band-gap energies: E_{g1} and E_{g2}
- different electron affinities (χ): χ_1 and χ_2
- different doping concentrations (N): N_1 and N_2

Fig. 3.1.2 shows an AlGaN/GaN heterojunction of a modern GaN-HEMT. Compared to other heterojunctions the AlGaN/GaN heterojunction does not necessarily need an additional doped layer in heterojunction to build a conducting channel in the GaN layer due to the spontaneous polarization (high ionic bond with Ga atoms) and the piezoelectric polarization (lattice mismatch between the AlGaN and GaN layer) as stated in [93].
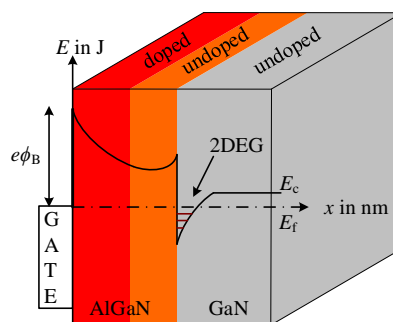
Figure 3.1.2: Heterojunction of GaN-HEMT [6, 65, 94].

Functionality of the heterojunction on the basis of Fig. 3.1.2:

- Due to different electron affinities χ_1 and χ_2, a spike ($\Delta E_c = \chi_2 - \chi_1$) occurs in conduction band energy (E_c) along the x-axes. Since the spike is very sharp and narrow, electrons can occupy only certain energy levels. As a result, if the Fermi level (E_c) is above E_c at the spike location, only a very focused 2-dimensional electron gas (2DEG) arises [95].
- The hole current which has a lower mobility than the electron current is suppressed by the additional discontinuity $\Delta E_v = E_{g1} - E_{g2} - \Delta E_c$ in the valance band energy (E_v) along the x-axes which lead to a much faster active device.
- Increasing the gate voltage above the pinch-off ($E_c < E_f$) the 2DEG arises. The amount of electrons along the y-axes can be controlled by the gate voltage.

3.1.2.2 Physical Structure

One of the first GaN-HEMT devices was published in [96] using a sapphire (Al_2O_3) substrate. Fig. 3.1.3 shows a simplified typical physical structure of an AlGaN/GaN-HEMT with five common layers [94]:

- Nucleation Layer:
  - Reducing the lattice mismatch between buffer layer and substrate if necessary (different lattice constant of buffer layer and substrate).
- Buffer Layer:
  - Serving as an insulator for non-insulating substrates.
  - Forming the heterojunction with the AlGaN semiconductor. The conducting channel is formed in the buffer layer.
- Spacer Layer:
  - To form the heterojunction with donor layer and buffer layer.
  - Responsible to keep a certain distance between the doped supply layer and the 2DEG in the buffer layer to avoid any mobility degradation.
- Carrier Supply Layer / Donor Layer:
  - Forming heterojunction with spacer layer and buffer layer.
  - Providing electrons to the 2DEG in the buffer layer.
- Substrate:
  - Serving as a epitaxy layer of the device structure.
  - Thermal connection to the outside of the active device to get rid of the dissipated power.
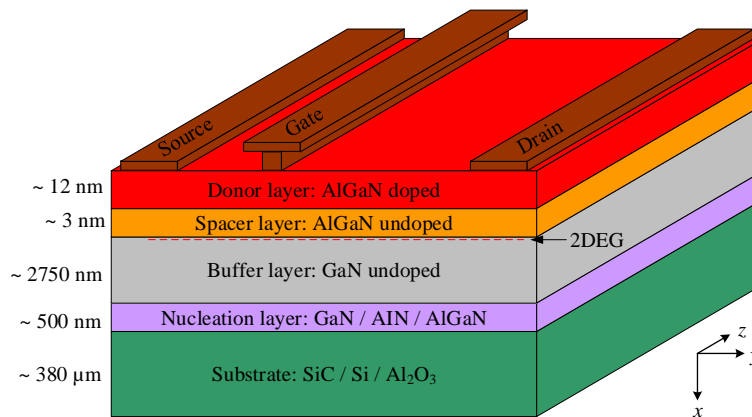
Figure 3.1.3: Physical structure of GaN-HEMT [6, 65, 94].

Table 3.1.2 shows the advantages and disadvantages of different substrates for the GaN-HEMT.

Table 3.1.2: Properties of different substrates for the GaN-HEMT [6, 30, 94, 97].

		Al_2O_3	Si	SiC[*]	Diamond
RF Performance	P_{out}	↓	0	↑	↑↑
	f	0	↓	↑	↑↑
Thermal Conductivity		↓	0	↑	↑↑
Price		0	↓	↑	↑↑

[*] 4H-SiC

3.1.3 GaN-HEMT Power Amplifiers

In this subsection the advantages of the GaN-HEMT technology are summarized and an overview is given regarding power performance versus frequency of different semiconductor technologies.

Key advantages of the GaN-HEMT technology:

Fig. 3.1.4 illustrates the advantages of the GaN-HEMT technology on physical, device and system level.
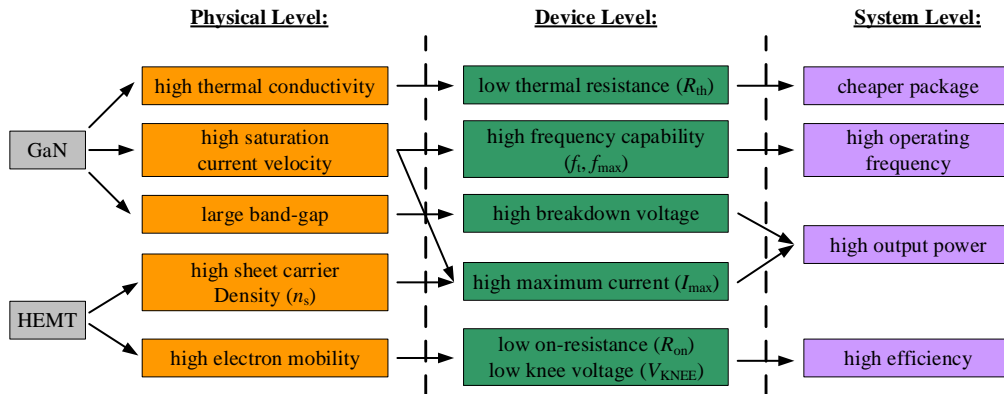
Figure 3.1.4: Advantages of GaN-HEMT PAs [64, 65, 98].

Advantages of GaN-HEMT technology on device level:

- low R_{th}: $\propto \lambda$
- high f_t and high f_{max}: $\propto v_{d,sat}$
- high V_{BR}: $\propto E_g$
- high I_{max}: $\propto (v_{d,sat}, n_s)$
- low R_{on} and low V_{KNEE}: $\propto \frac{1}{\mu_n}$

Advantage of GaN-HEMT technology on system level:

- cheaper package due to lower R_{th}
- higher operating frequency due to higher f_t and f_{max}
- higher output power due to higher I_{max} and higher V_{BR}
- higher efficiency due to lower V_{KNEE}

Overview of power performance versus frequency of different semiconductor technologies:

Fig. 3.1.5 highlights the higher power-bandwidth product compared to other semiconductor technologies.
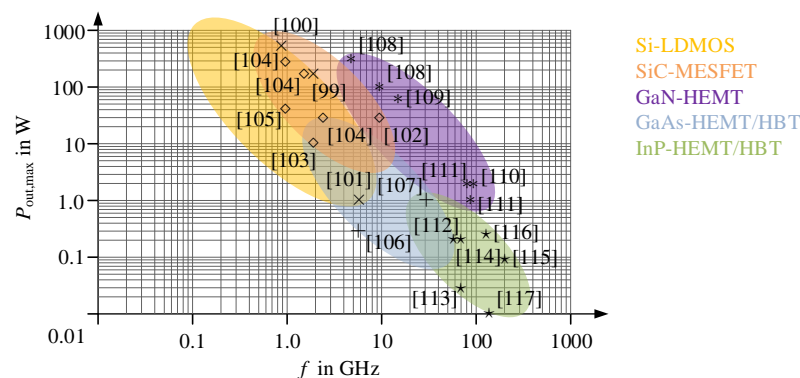
Figure 3.1.5: Field of application for different semiconductors [6]: Si ($\times$); [99–101], SiC ($\diamond$); [102–105], GaAs ($+$); [106, 107], GaN ($\ast$); [108–111], InP ($\star$); [112–117].

3.2 GaN-HEMT Modeling

[53, 118] give a good overview about modeling of transistors for microwave circuits and will be briefly summarized in the following. Non-linear models —including linear models as well— of transistors can be divided in various ways:

1. How is the model derived:

    a) physical parameters (i.e. geometry, fundamental transport of electrons)
    b) measurements / empirical observed characteristics (i.e. DC currents and voltages, S-parameters)

2. Which technique is used to solve the equations of the model:

    a) analytical (closed, unique solution)
    b) numerical (approximation)
    c) black box (table-based, artificial neural networks)

3. Which type of performance is predicted by the model:

    a) Small-signal performance
    b) Large-signal performance
    c) Noise performance
    d) Thermal behavior

The most important models for circuit designers are the small-signal model (SSM), large-signal model (LSM) and noise model of a transistor to be able to simulate RF performance of a complete microwave system (i.e. a matched amplifier). These models are usually implemented as physical parameter models (coefficients of the analytical equations of the model have a physical significance: physically / analytical-model) and compact models (dealing with resistors, capacitors, inductors and voltage or current controlled current sources which have a physical significance). Fig. 3.2.1 reflects the method to determine the parameters of the SSM, LSM and noise model suggested by [118].
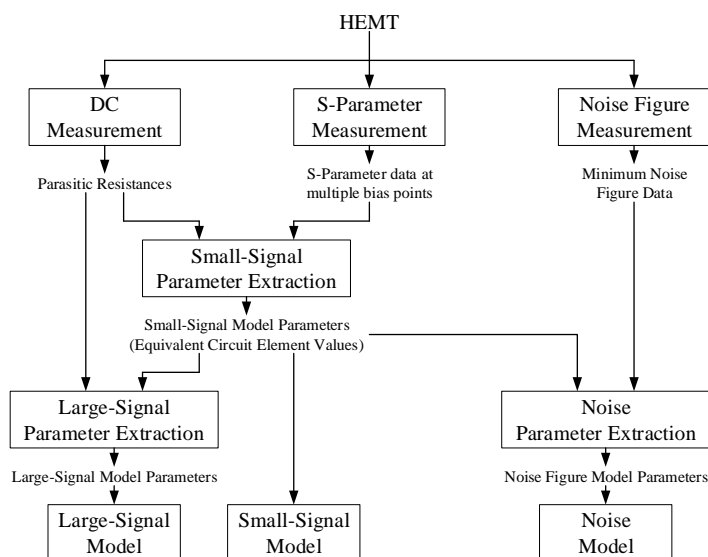
Figure 3.2.1: Algorithm of parameter extraction of SSM, LSM and noise model [118].

3.2.1 Small-Signal Modeling

Fig. 3.2.2 illustrates the SSM of a CSS which is very similar to the presented SSM-CSS in [30]. The used parameters can be extracted using the methods suggested in [119–122]. The SSM consists of the inner shell (intrinsic transistor) which is modeled by the following elements:

- An active element:
  voltage controlled current source with the small-signal trans-impedance ($\underline{g}_\mathrm{m} = g_\mathrm{m}\exp\left(-j\omega\tau\right)$), where g_m is the small-signal trans-conductance and τ is the transit time of electrons in the channel of the HEMT
- A gate-source path: impedance depending on small-signal gate-source capacitance (C_gs), resistance (r_gs) and feedback resistance (r_fgs)
- An feedback path: impedance with small-signal gate-drain capacitance (C_gd), resistance (r_gd) and feedback resistance (r_fgd)
- Drain-source path: impedance with small-signal drain-source capacitance (C_ds) and resistance (r_ds)

The intrinsic elements depend on the quiescent point as well as on the device size. The outer shell which only depends on the device size, consists of the feedings impedances

- $j\omega L_\mathrm{g} + R_\mathrm{g}$, $j\omega L_\mathrm{s} + R_\mathrm{s}$, $j\omega L_\mathrm{d} + R_\mathrm{d}$ and

of the pad capacitors between gate and source, drain and source and gate and drain (C_pgs, C_pds and C_pgd). L_g, L_s, L_d and R_g, R_s, R_d are the feeding gate, source and drain inductances and resistances respectively. Since C_ds was determined to $1\,\mathrm{fF}$ it was neglected in the original model presented by [30].
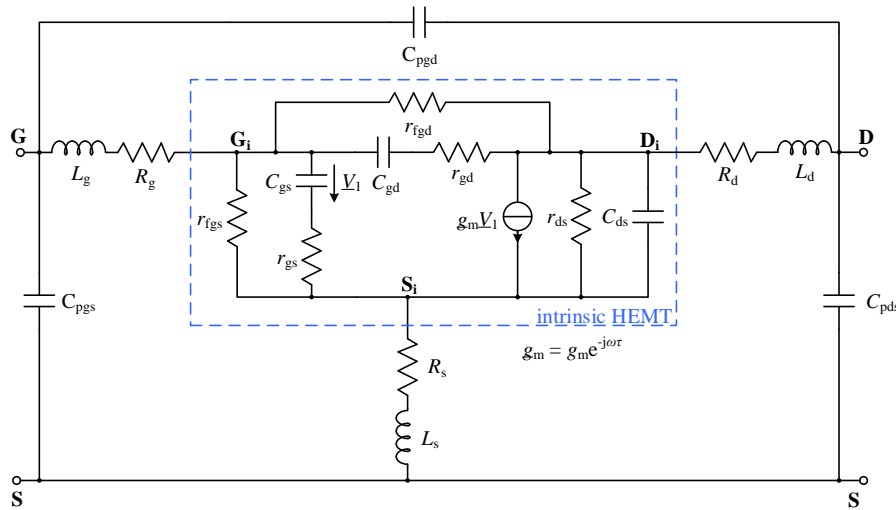
Figure 3.2.2: SSM of the GaN-HEMT [6, 30].

3.2.2 Large-Signal Modeling

Fig. 3.2.3 illustrates the LSM of a CSS —similar to the presented figure in [30]—, which is based on the SSM-CSS, shown in Fig. 3.2.2. The large-signal gate-source capacitor with capacitance $C_\mathrm{gs}\left(V_\mathrm{GS}, V_\mathrm{GD}\right)$, large-signal gate-drain capacitor with capacitance $C_\mathrm{gd}\left(V_\mathrm{GS}, V_\mathrm{GD}\right)$ and drain-source current $I_\mathrm{ds}\left(V_\mathrm{GS}, V_\mathrm{GD}\right)$ reflect the non-linearity of the active device. The Schottky diodes between gate-source and gate-drain is modeled by the currents I_gs and I_gd respectively.
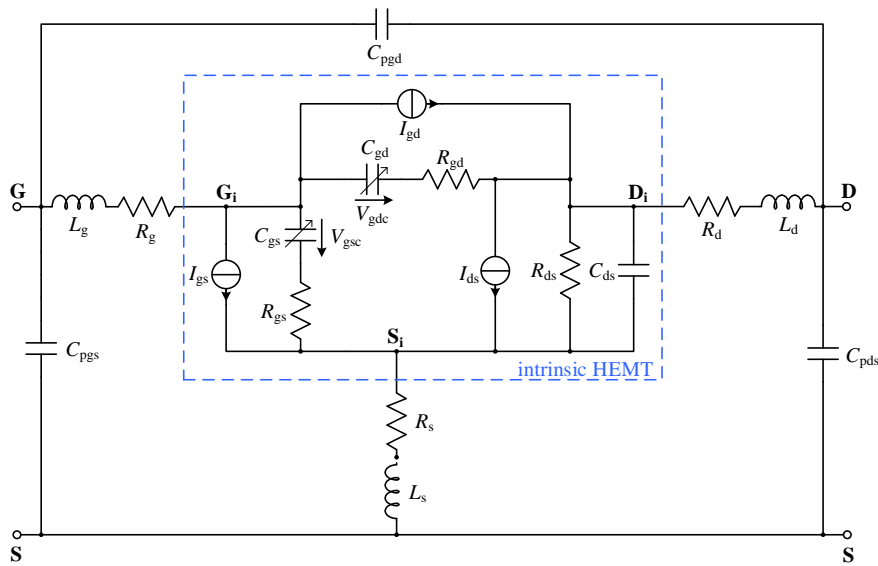
Figure 3.2.3: LSM of the GaN-HEMT [6, 30].

Fig. 3.2.4 reflects the self heating (due to the high power dissipation) of the GaN-HEMT, which is modeled by a thermal

- resistor with resistance R_{th},
- capacitor with capacitance C_{th} and
- current source with current I_{th}.

I_{th} represents the static heat dissipation from the channel in the GaN-HEMT. The thermal resistor with resistance R_{th} describes the power transfer from the channel to the backside of the active device and together with the thermal capacitor with capacitance C_{th} they model the time delay of the power transfer. The voltage drop at thermal resistor and capacitor —with resistance R_{th} and capacitance C_{th}— reflects the temperature increase of the channel temperature and as a result of T_j.
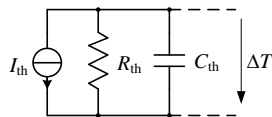
Figure 3.2.4: Modeling of the temperature change of the channel temperature [6, 30].

3.2.3 Noise Modeling

GaN-HEMTs has several different kind of noise sources like thermal noise, shot noise, generation–recombination noise and flicker noise. The most dominant noise source in GaN-HEMTs at moderate and high frequencies is the thermal noise generated in the conductive channel. A very good overview about the reasons why additional noise occurs in the channel was given by Liechti in his paper [123] and was summarized by [6]. Some of these reasons are the modulation effect [124], the hot electron effect [125, 126], the intervalley scattering noise [127] and the high field diffusion noise [128–130]. There are two main fundamental noise models of FETs in the literature:

- Van der Ziel's (Pucel's) noise model [31, 124]:
  The model consists of two correlated noise sources, one at the input and one at the output of the transistor. Fig. 3.2.5 shows the original noise model of Van der Ziel (Pucel) which is used in a similar manner in this thesis.

- Pospieszalski's noise model [131]:
  The model consists of two uncorrelated noise sources represented by the thermal noise of the internal gate-source resistor and drain-source resistor with the thermal temperatures T_g and T_d (T_d is much higher than room temperature).

There are several modifications of these two fundamental noise models i.e. presented by Fukui [132], Podell [133], Klapproth et. al. [134] and Danneville et. al. [135]. Furthermore, with respect to GaN-HEMTs, in [136] an improved noise modeling technique can be found.
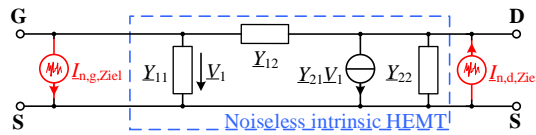
Figure 3.2.5: Noise model of Van der Ziel for FETs [6, 31].

Further information about the different noise mechanisms and the noise models are summarized in [6].

4 Cascode

The name cascode was first mentioned by Hunt and Hickman in 1939 [7]. One of the first amplifiers using CCs can be found in [8], which was designed by Wallmann et al. in 1948. Nowadays, to achieve high-end performance in PA systems, CCs become a standard part to achieve this goal. In [10, 12, 13, 16, Table 5], CCs are used to show the superior performance compared to other amplifier topologies and to achieve state-of-the-art performance.

This chapter explains the functionality of the CSS and the classical CC (obtained from [1] and adapted for HEMTs). Furthermore the modified CC is explained due to the fact that it is more used nowadays. To point out later on the advantages and disadvantages of the classical CC, of the modified CC and of the single CSS in Ch. 5, certain small- and large-signal parameters are derived and their dependencies are explained.

4.1 Functionality

4.1.1 Classical Cascode

The basic structure of the classical CC is shown in Fig. 4.1.1. In general the CC consists of two stages:

- The first stage comprises a transistor in CS configuration. The stage behaves like a voltage controlled current source and offers a high input impedance and a high output impedance.
- The second stage comprises a transistor in CG configuration. The stage behaves like current controlled current source and offers a low input impedance and a high output impedance.

As a result the CC behaves like a voltage controlled current source and offers a high input impedance and a high output impedance.
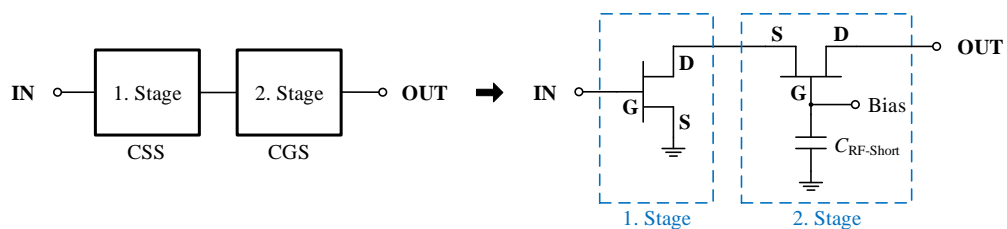
Figure 4.1.1: Schematic of the classical CC [98].

The functionality of the classical CC can be split into the DC operation and the AC operation:

- DC operation:
  - The quiescent point of the CC can be adjusted by three DC voltages. One at the gate of the CSS, one at the gate of the CGS and one at the drain of the CGS.
  - For equal device sizes of the CSS and the CGS, the DC drain-source current (I_{DS}) is the same in both devices as well as the gate-source voltage (V_{GS}) at the CSS and at the CGS.
- AC operation:
  - The input voltage swing at the CSS controls the drain-source current of the CSS. If the capacitor at the gate of the CGS with capacitance $C_{RF-Short}$ acts as a short to GND in the desired frequency range, the voltage gain of the CSS is equal one. Therefore, the input and output voltage swing of

the CSS are the same. Since the output voltage —the drain-source voltage (V_{ds})— of the CSS is very small and the drain-source current I_{ds} is high, the load line of the CSS is very steep.

– The current gain of the CGS is equal one. As a result, the output current I_{ds}, controlled by the input voltage of the CC, is very similar to the single CSS. However, due to the suppression of the Miller-effect [137] the bandwidth of the CC is significantly increased.

To minimize any parasitics between the CSS and the CGS dual-gate transistors are used as CCs to achieve better performance at very high frequencies. One disadvantage is the thermal aspect. Due to the fact that the two active cells are very close to each other the channel temperature increases.

4.1.2 Modified Cascode

Using CCs in broadband PAs, especially using the GaN technology, Fraysse et al. have shown in [138], that adding an additional stabilization capacitor with a certain stabilization capacitance (C_{st}) and a stabilization resistor with a certain stabilization resistance (R_{st}) in the gate path of the CGS of the CC has some key advantages:

- The resistor with R_{st} improves the stability of the CC up to a certain frequency.
- The capacitor with C_{st} improves the stability of the CC and improve the power transfer from the CSS to the CGS by optimizing the load impedance. Since the additional stabilization capacitor acts as a frequency independent voltage divider the optimized power transfer as well as the improved stability is frequency independent.

For simplicity most of the later calculations and considerations of the modified CGS neglect the stabilization resistor with R_{st}. The principle structure of the modified CC is shown Fig. 4.1.2.
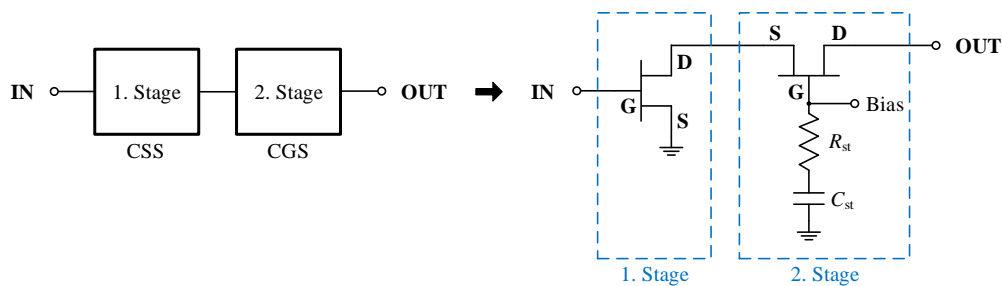
Figure 4.1.2: Schematic of the modified CC [98].

Regarding the functionality of the modified CC, the DC operation is equal to the classical C. However, the AC operation differs compared to the classical CC due to the stabilization capacitor and resistor in the gate path of the CGS of the CC:

- Due to the additional stabilization capacitor with C_{st}, which acts as a frequency independent voltage divider, the input and output voltage swing of the CSS are no longer equal.
- The input impedance of the CGS increases with decreasing C_{st}.
- As the input impedance of the CGS increases, the voltage gain of the CSS increases as well. As a result the load line becomes flatter and the power transfer from the CSS to the CGS increases.
- The Miller-effect increases due to the increasing input impedance of the CGS, which lowers the usable bandwidth.

To show the performance of the classical and the modified CC and to compare them later with the single CSS, the small-signal parameters will be investigated and shown in the following section.

4.2 Small-Signal Parameters

4.2.1 Y-Parameters of the Common-Source Stage

Since the CSS acts as a voltage controlled current source with high input and output impedance the Y-parameters are well suited to show the small-signal characteristic. Fig. 4.2.1 shows the simplified SSM of the CSS which comprises

- a voltage controlled current source with current $g_\mathrm{m}\underline{V}_1$,
- an input capacitor with capacitance C_gs,
- a feedback capacitor with capacitance C_gd and
- an output impedance depending on r_ds and C_ds.
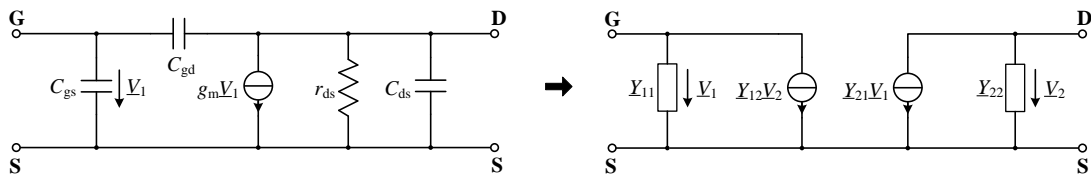
Figure 4.2.1: Simplified SSM of the CSS [98].

Using the simplified SSM of the CSS, shown in Fig. 4.2.1, the Y-parameters of the CSS can be calculated to

$$\underline{Y}_{11,\mathrm{CSS}} = j\omega\left(C_\mathrm{gs} + C_\mathrm{gd}\right) \tag{4.2.1}$$

$$\underline{Y}_{12,\mathrm{CSS}} = -j\omega C_\mathrm{gd} \tag{4.2.2}$$

$$\underline{Y}_{21,\mathrm{CSS}} = g_\mathrm{m} - j\omega C_\mathrm{gd} \tag{4.2.3}$$

$$\underline{Y}_{22,\mathrm{CSS}} = \frac{1}{r_\mathrm{ds}} + j\omega\left(C_\mathrm{ds} + C_\mathrm{gd}\right) . \tag{4.2.4}$$

The following properties of the Y-parameters of the CSS can be determined:

- The $\left|\underline{Y}_{11,\mathrm{CSS}}\right|$ and $\left|\underline{Y}_{12,\mathrm{CSS}}\right|$ increases with frequency (input impedance and isolation decreases).
- The $\left|\underline{Y}_{21,\mathrm{CSS}}\right|$ and $\arg\left(\underline{Y}_{21,\mathrm{CSS}}\right)$ increases at higher frequencies.
- The $\left|\underline{Y}_{22,\mathrm{CSS}}\right|$ and $\arg\left(\underline{Y}_{22,\mathrm{CSS}}\right)$ increases at higher frequencies and $\left|\underline{Y}_{22,\mathrm{CSS}}\right|$ is limited by $\frac{1}{r_\mathrm{ds}}$ at low frequencies (output impedance decreases).

Further information about the Y-parameters of the CSS can be found in Appendix A.1. To determine and investigate the Y-parameters of the CC, the H-parameters of the CGS are derived in the following subsection.

4.2.2 H-Parameters of the Common-Gate Stage

4.2.2.1 H-Parameters of the Classical Common-Gate Stage

Since the CGS acts as a current controlled current source with low input impedance and high output impedance the H-parameters are well suited to show the small-signal characteristic. Fig. 4.2.1 shows the simplified SSM of the CGS which comprises the same small-signal elements as the CSS.
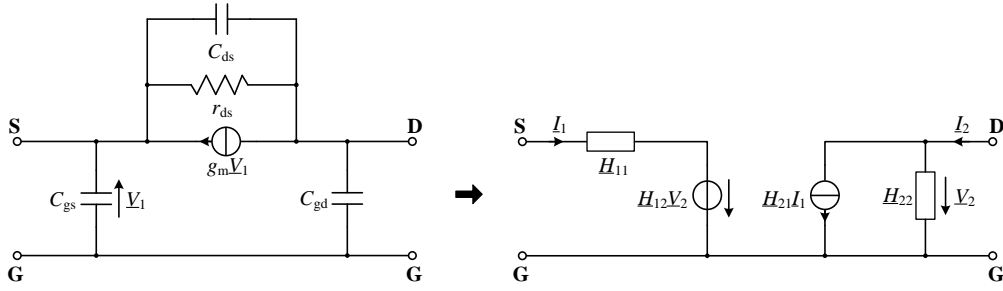
Figure 4.2.2: Simplified SSM of the classical CGS [98].

Using the simplified SSM of the CGS, shown in Fig. 4.2.2, the H-parameters of the CGS can be calculated to

$$\underline{H}_{11,\mathrm{CGS}} = \frac{r_{\mathrm{ds}}}{1 + g_{\mathrm{m}}r_{\mathrm{ds}}}\left(1 + j\omega\cdot\ldots\right) \tag{4.2.5}$$

$$\underline{H}_{12,\mathrm{CGS}} = \frac{1}{1 + g_{\mathrm{m}}r_{\mathrm{ds}}}\left(1 + j\omega\cdot\ldots\right) \tag{4.2.6}$$

$$\underline{H}_{21,\mathrm{CGS}} = -\left(1 + j\omega\cdot\ldots\right) \tag{4.2.7}$$

$$\underline{H}_{22,\mathrm{CGS}} = j\omega C_{\mathrm{gd}} + j\omega\left(\frac{C_{\mathrm{gs}}}{1 + g_{\mathrm{m}}r_{\mathrm{ds}}}\right)\left(1 + j\omega\cdot\ldots\right) . \tag{4.2.8}$$

The following properties of the H-parameters of the CGS can be determined:

- The $\left|\underline{H}_{11,\mathrm{CGS}}\right|$ and $\left|\underline{H}_{12,\mathrm{CGS}}\right|$ increases at higher frequencies (input impedance increases and isolation degrades).
- The $\left|\underline{H}_{21,\mathrm{CGS}}\right| = 1$ and decreases at higher frequencies.
- The $\left|\underline{H}_{22,\mathrm{CGS}}\right|$ increases with frequency (output impedance decreases).

4.2.2.2 H-Parameters of the Modified Common-Gate Stage

Fig. 4.2.3 shows the simplified SSM of the modified CGS. Fig. 4.2.3a shows the modified CGS which comprises the same small-signal elements as the CSS with the additional stabilization capacitor with C_{st} and Fig. 4.2.3b shows the recalculated modified CGS (considering C_{st}).

(a) Modified CGS with stabilization capacitor with C_{st}.

(b) Recalculated modified CGS (considering C_{st}).
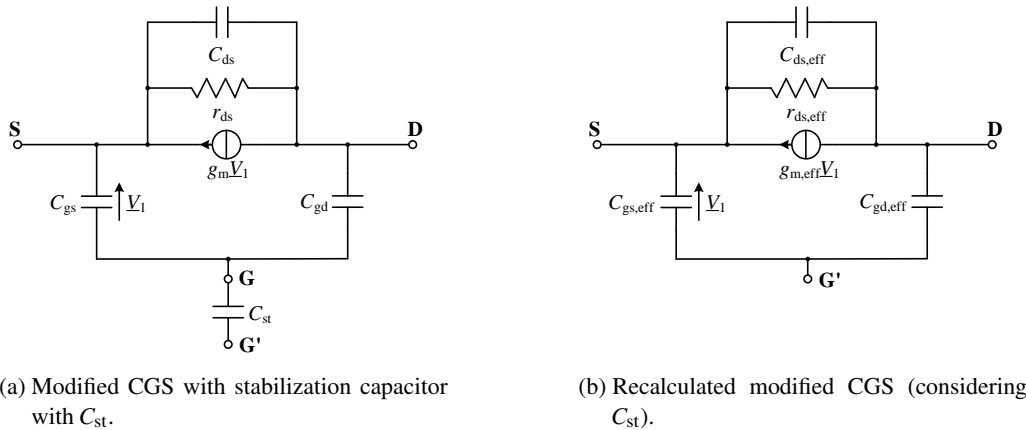
Figure 4.2.3: Simplified SSM of the modified CGS.

Using the simplified SSM of the modified CGS, shown in Fig. 4.2.3a, the effective small-signal elements

of the modified CGS (considering C_{st}), shown in Fig. 4.2.3b can be expressed by

$$C_{\text{gs,eff}} = C_{\text{gs}} \cdot \frac{C_{\text{st}}}{C_{\text{st}} + C_{\text{gs}} + C_{\text{gd}}} \qquad\qquad r_{\text{gs,eff}} = 0 \qquad\qquad (4.2.9)$$

$$C_{\text{gd,eff}} = C_{\text{gd}} \cdot \frac{C_{\text{st}}}{C_{\text{st}} + C_{\text{gs}} + C_{\text{gd}}} \qquad\qquad r_{\text{gd,eff}} = 0 \qquad\qquad (4.2.10)$$

$$C_{\text{ds,eff}} = C_{\text{ds}} + \frac{C_{\text{gs}}C_{\text{gd}}}{C_{\text{st}} + C_{\text{gs}} + C_{\text{gd}}} \qquad r_{\text{ds,eff}} = r_{\text{ds}} \cdot \frac{C_{\text{st}} + C_{\text{gs}} + C_{\text{gd}}}{C_{\text{st}} + C_{\text{gs}} + C_{\text{gd}}\left(1 + g_{\text{m}}r_{\text{ds}}\right)} \qquad (4.2.11)$$

$$g_{\text{m,eff}} = g_{\text{m}} \cdot \frac{C_{\text{st}}}{C_{\text{st}} + C_{\text{gs}} + C_{\text{gd}}} \qquad\qquad \tau_{\text{eff}} = 0 \,. \qquad\qquad (4.2.12)$$

It can be noticed that all recalculated small-signal elements, eq. (4.2.9)–eq. (4.2.9), decrease with decreasing C_{st}, except C_{ds} which increases with decreasing C_{st}. Using the recalculated small-signal parameters, the following properties of the H-parameters of the modified CGS can be determined:

- The $\left|\underline{H}_{11,\text{CGS}}\right|$ increases with decreasing C_{st} (input impedance increases). A maximum short circuit impedance of

$$\left|\underline{H}_{11,\text{CGS}}\left(C_{\text{st}} \to 0\right)\right| = r_{\text{ds}} \cdot \frac{C_{\text{gs}} + C_{\text{gd}}}{C_{\text{gs}} + C_{\text{gd}}\left(1 + g_{\text{m}}r_{\text{ds}}\right)} \qquad\qquad (4.2.13)$$

  can be reached.
- The $\left|\underline{H}_{12,\text{CGS}}\right|$ increases with decreasing C_{st} (isolation degrades).
- The $\left|\underline{H}_{21,\text{CGS}}\right|$ is almost unchanged at low frequencies with decreasing C_{st}. However, the $\left|\underline{H}_{21,\text{CGS}}\right|$ increases slightly at higher frequencies with decreasing C_{st}.
- The open circuit output capacitance ($\frac{\underline{H}_{22,\text{CGS}}}{j\omega}$) decreases with decreasing C_{st} (output impedance increases).

Further information about the H-parameters of the classical and modified CGS can be found in Appendix B.1. Additionally, in Appendix B.1.3, Table B.1.1 and Table B.1.2 show the change of the H-parameters (magnitude, poles and zeros) of the CGS depending on C_{st}.

4.2.3 Y-Parameters of the Cascode

4.2.3.1 Y-Parameters of the Classical Cascode

Since the CC acts as a voltage controlled current source with high input and output impedance the Y-parameters are well suited to show the small-signal characteristic. Fig. 4.2.4 shows the simplified small-signal model of the CC which consists of the CSS and the CGS. Both stages have the same device size.
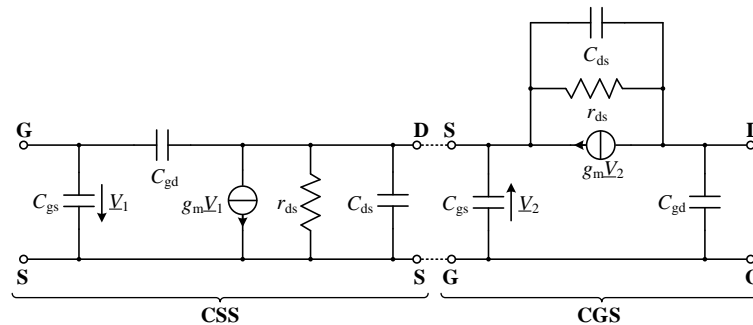
Figure 4.2.4: Simplified SSM of the classical CC [98].

Using the simplified small-signal model of the CC, shown in Fig. 4.2.4, the Y-parameters of the CC can be calculated to

$$\underline{Y}_{11,\text{CC}} = j\omega \left(C_{\text{gs}} + C_{\text{gd}} \right) + j\omega C_{\text{gd}} \left(\frac{g_{\text{m}} r_{\text{ds}}}{2 + g_{\text{m}} r_{\text{ds}}} \right) (1 + j\omega \cdot \ldots) \tag{4.2.14}$$

$$\underline{Y}_{12,\text{CC}} = -j\omega C_{\text{gd}} \frac{1}{(2 + g_{\text{m}} r_{\text{ds}})} (1 + j\omega \cdot \ldots) \tag{4.2.15}$$

$$\underline{Y}_{21,\text{CC}} = g_{\text{m}} \left(\frac{1 + g_{\text{m}} r_{\text{ds}}}{2 + g_{\text{m}} r_{\text{ds}}} \right) (1 + j\omega \cdot \ldots) \tag{4.2.16}$$

$$\underline{Y}_{22,\text{CC}} = j\omega C_{\text{gd}} + j\omega \left(\frac{C_{\text{gs}}}{1 + g_{\text{m}} r_{\text{ds}}} \right) (1 + j\omega \cdot \ldots) + \frac{1}{r_{\text{ds}} (2 + g_{\text{m}} r_{\text{ds}})} (1 + j\omega \cdot \ldots) . \tag{4.2.17}$$

The following properties of the Y-parameters of the CC can be determined:

- The $\left| \underline{Y}_{11,\text{CC}} \right|$ and $\left| \underline{Y}_{12,\text{CC}} \right|$ increases with frequency (input impedance and isolation decreases).
- The $\left| \underline{Y}_{21,\text{CC}} \right|$ increases at higher frequencies.
- The $\left| \underline{Y}_{22,\text{CC}} \right|$ increases at higher frequencies and is limited by $\frac{1}{r_{\text{ds}}(2 + g_{\text{m}} r_{\text{ds}})}$ at low frequencies (output impedance decreases).

If the relationship $g_{\text{m}} r_{\text{ds}} \gg 1$ is valid, which is valid for the most processes, the Y-parameters of the CC can be approximated by

$$\underline{Y}_{11,\text{CC}} \approx j\omega \left(C_{\text{gs}} + 2 \cdot C_{\text{gd}} \right) (1 + j\omega \cdot \ldots) \tag{4.2.18}$$

$$\underline{Y}_{12,\text{CC}} \approx -j\omega \frac{C_{\text{gd}}}{g_{\text{m}} r_{\text{ds}}} (1 + j\omega \cdot \ldots) \tag{4.2.19}$$

$$\underline{Y}_{21,\text{CC}} \approx g_{\text{m}} (1 + j\omega \cdot \ldots) \tag{4.2.20}$$

$$\underline{Y}_{22,\text{CC}} \approx j\omega C_{\text{gd}} + j\omega \frac{C_{\text{gs}}}{g_{\text{m}} r_{\text{ds}}} (1 + j\omega \cdot \ldots) + \frac{g_{\text{ds}}}{g_{\text{m}} r_{\text{ds}}} (1 + j\omega \cdot \ldots) . \tag{4.2.21}$$

4.2.3.2 Y-Parameters of the Modified Cascode

Fig. 4.2.5 shows the simplified SSM of the modified CC. Fig. 4.2.5a shows the modified CC stage which comprises the same small-signal elements as the classical CC with the additional stabilization capacitor with C_{st} and Fig. 4.2.5b shows the modified CC with the recalculated modified CGS (considering C_{st}).

(a)
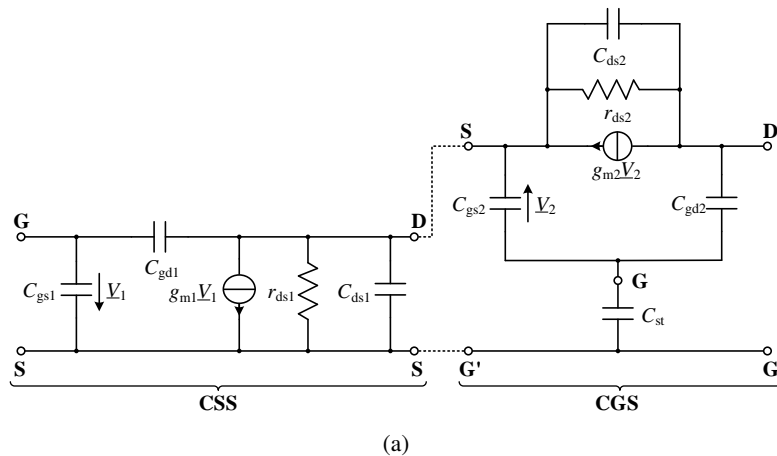
Figure 4.2.5: Simplified SSM of the modified CC. (a) With stabilization capacitor with C_{st}.
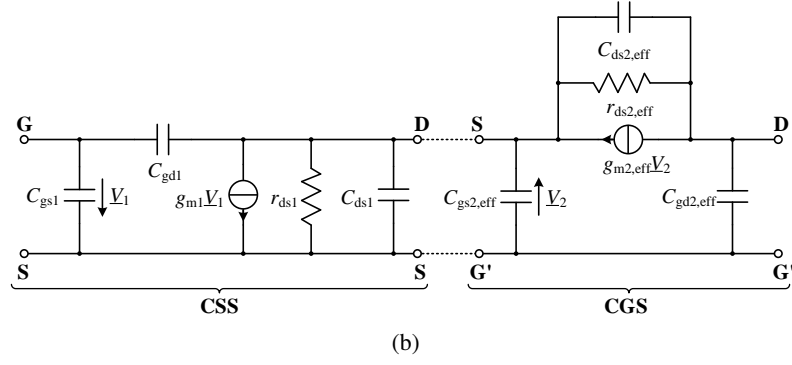
Figure 4.2.5: (Continued..) Simplified SSM of the modified CC. (b) With recalculated modified CGS (considering C_{st}).

Using eq. (4.2.9)–eq. (4.2.9) to calculate the H-parameters of the CGS and using the Y-parameters of the CSS, the Y-parameters of the modified CC can be calculated with eq. (C.1.1)–eq. (C.1.4). The Y-parameters can be expressed by

$$\underline{Y}_{11,\text{CC}} = j\omega \left(C_{\text{gs1}} + C_{\text{gd1}} \right) + j\omega C_{\text{gd1}} \left(\frac{g_{\text{m1}} \left[r_{\text{ds1}} \parallel r_{\text{ds2,eff}} \right]}{1 + g_{\text{m2,eff}} \left[r_{\text{ds1}} \parallel r_{\text{ds2,eff}} \right]} \right) \left(1 + j\omega \cdot \ldots \right) \tag{4.2.22}$$

$$\underline{Y}_{12,\text{CC}} = -j\omega C_{\text{gd1}} \frac{1}{\left(1 + \frac{r_{\text{ds2,eff}}}{r_{\text{ds1}}} + g_{\text{m2,eff}} r_{\text{ds2,eff}} \right)} \left(1 + j\omega \cdot \ldots \right) \tag{4.2.23}$$

$$\underline{Y}_{21,\text{CC}} = g_{\text{m1}} \frac{\left(1 + g_{\text{m2,eff}} r_{\text{ds2,eff}} \right)}{\left(1 + \frac{r_{\text{ds2,eff}}}{r_{\text{ds1}}} + g_{\text{m2,eff}} r_{\text{ds2,eff}} \right)} \left(1 + j\omega \cdot \ldots \right) \tag{4.2.24}$$

and

$$\underline{Y}_{22,\text{CC}} = j\omega C_{\text{gd2}} + j\omega \left(\frac{C_{\text{gs2}}}{1 + g_{\text{m2,eff}} r_{\text{ds2,eff}}} \right) \left(1 + j\omega \cdot \ldots \right)$$
$$+ \frac{1}{\left(r_{\text{ds1}} + r_{\text{ds2,eff}} \right) \left(1 + g_{\text{m2,eff}} \left[r_{\text{ds1}} \parallel r_{\text{ds2,eff}} \right] \right)} \left(1 + j\omega \cdot \ldots \right) . \tag{4.2.25}$$

The following properties of the Y-parameters of the modified CC can be determined:

- The $\left| \underline{Y}_{11,\text{CC}} \right|$ increases due to the increase of $\underline{H}_{11,\text{CGS}}$ (Miller-effect increases => input impedance decrease). For $C_{\text{st}} \to 0$, $\underline{Y}_{11,\text{CC}}$ can be expressed by

$$\underline{Y}_{11,\text{CC}} = j\omega \left(C_{\text{gs1}} + C_{\text{gd1}} \right) + j\omega C_{\text{gd1}} \left(g_{\text{m1}} \left[r_{\text{ds1}} \parallel r_{\text{ds2,eff}} \right] \right) \left(1 + j\omega \cdot \ldots \right) . \tag{4.2.26}$$

- The $\left| \underline{Y}_{12,\text{CC}} \right|$ increases due to the increase of the $\underline{H}_{12,\text{CGS}}$ (isolation degrades). For $C_{\text{st}} \to 0$, the $\underline{Y}_{12,\text{CC}}$ can be expressed by

$$\underline{Y}_{12,\text{CC}} = -j\omega C_{\text{gd1}} \frac{1}{\left(1 + \frac{r_{\text{ds2,eff}}}{r_{\text{ds1}}} \right)} \left(1 + j\omega \cdot \ldots \right) . \tag{4.2.27}$$

- The $\left| \underline{Y}_{21,\text{CC}} \right|$ decreases due to the increase of the $\underline{H}_{11,\text{CGS}}$ (degraded mismatch between $\underline{Y}_{22,\text{CSS}}$ and $\underline{H}_{11,\text{CGS}}$). For $C_{\text{st}} \to 0$, the $\underline{Y}_{21,\text{CC}}$ can be expressed by

$$\underline{Y}_{21,\text{CC}} = g_{\text{m1}} \frac{1}{\left(1 + \frac{r_{\text{ds2,eff}}}{r_{\text{ds1}}} \right)} \left(1 + j\omega \cdot \ldots \right) . \tag{4.2.28}$$

- The $\left|\underline{Y}_{22,\mathrm{CC}}\right|$ increases due to the increase of the $\underline{H}_{12,\mathrm{CGS}}$ (output impedance decrease). For $C_{\mathrm{st}} \to 0$, the $\underline{Y}_{22,\mathrm{CC}}$ can be expressed by

$$\underline{Y}_{22,\mathrm{CC}} = \frac{1}{(r_{\mathrm{ds1}} + r_{\mathrm{ds2,eff}})} + j\omega \left(C_{\mathrm{ds1}} + C_{\mathrm{gd1}}\right) \left(\frac{r_{\mathrm{ds1}} - [r_{\mathrm{ds1}} \parallel r_{\mathrm{ds2,eff}}]}{r_{\mathrm{ds1}} + r_{\mathrm{ds2,eff}}}\right) + (j\omega)^2 \cdot (\ldots) \ . \quad (4.2.29)$$

Further information about the Y-parameters of the CC and their derivations can be found in Appendix C.1 and Appendix C.1.1 respectively.

4.3 Large-Signal Parameters

4.3.1 Maximum Output Power

The $P_{\mathrm{out,max}}$ of the active device in CS configuration, shown in Fig. 4.3.1, depends on different factors [1, 30, 53, 54]:

- The $P_{\mathrm{out,max}}$ depends on the quiescent point $Q(V_{\mathrm{DS}}, I_{\mathrm{DS}})$ of the amplifier, which limits the maximum *PAE* of the amplifier.
- The V_{BR} and V_{KNEE} of the active device limits the drain-source voltage swing $(\widehat{V}_{\mathrm{ds}})$ and as a result $P_{\mathrm{out,max}}$.
- Furthermore, the $P_{\mathrm{out,max}}$ is limited by the maximum I_{DS} which is limited by the maximum allowed DC gate-source current (I_{GS}).
- Another very import point is the maximum allowed T_{j} which defines the life time —i.e. the mean time to failure ($MTTF$)— of the device.
- At the end, the most limiting factor of the $P_{\mathrm{out,max}}$ is the load impedance ($\underline{Z}_{\mathrm{load}}$) at the output.
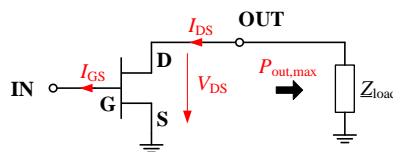
Figure 4.3.1: CSS with load impedance [98].

Assuming the CSS in class A operation, the efficiency is equal to $PAE = 50\%$. If the output of the CSS is matched to the optimum $\underline{Z}_{\mathrm{load}}$ ($\underline{Z}_{\mathrm{load,opt}}$), $P_{\mathrm{out,max}}$ can be achieved to

$$P_{\mathrm{out,max,CSS}} = \frac{1}{2} \cdot \widehat{V}_{\mathrm{ds,max}} \widehat{I}_{\mathrm{ds,max}} \quad (4.3.1)$$

$$= \frac{1}{8} \cdot (V_{\mathrm{BR}} - V_{\mathrm{KNEE}}) I_{\mathrm{DS,MAX}} \ . \quad (4.3.2)$$

Fig. 4.3.2 shows the output I-V characteristic and the safe-operating-area (SOA), for $\frac{P_{\mathrm{DISS,MAX}}}{GP} \leq 7\,\frac{\mathrm{W}}{\mathrm{mm}}$, of an active device in CS configuration using a certain foundry process.
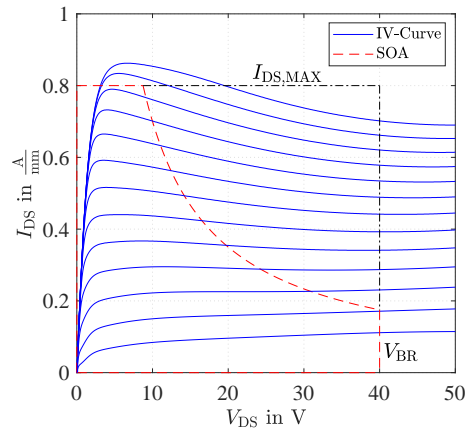
Figure 4.3.2: I-V characteristic of the CSS.

The $P_{\text{out,max}}$ of the active device in CC configuration, shown in Fig. 4.3.3, can be split into two cases:

- The gate of the CGS is shorten to GND by a high blocking capacitance $C_{\text{RF-Short}}$ for the classical CC, shown in Fig. 4.3.3a.
- The value of stabilization capacitor C_{st} ($C_{\text{RF-Short}}$) is in the same range as the intrinsic C_{gs} of the CGS for the modified CC, shown in Fig. 4.3.3b.
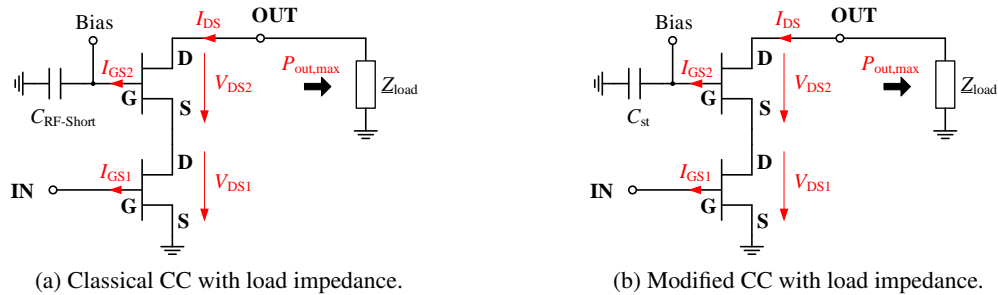
(a) Classical CC with load impedance.

(b) Modified CC with load impedance.

Figure 4.3.3: Classical and modified CC with load impedance [98]. (a) Classical CC. (b) Modified CC.

Assuming the CSS and the CGS in class A operation, the *PAE* of the CC is equal to $PAE = 50\%$. The $P_{\text{out,max}}$ of the CC is the sum of the $P_{\text{out,max}}$ of the CSS and the CGS. $P_{\text{out,max}}$ is given by

$$P_{\text{out,max,CC}} = P_{\text{out,max,CSS}} + P_{\text{out,max,CGS}} \tag{4.3.3}$$

$$= \frac{1}{2} \cdot \left(\widehat{V}_{\text{ds,max,CSS}} + \widehat{V}_{\text{ds,max,CGS}} \right) \widehat{I}_{\text{ds,max,CC}} \tag{4.3.4}$$

$$= \frac{1}{8} \cdot n \cdot (V_{\text{BR}} - V_{\text{KNEE}}) I_{\text{DS,MAX}} \tag{4.3.5}$$

$$\leq 2 \cdot P_{\text{out,max,CSS}} \tag{4.3.6}$$

with

$$n = 1.1\text{--}2 \, , \tag{4.3.7}$$

assuming a optimal $\underline{Z}_{\text{load}}$ at the output of the CGS.

For the classical CC the input impedance of the CGS is very low. Since the input impedance of the CGS is the load impedance of the CSS, the output of the CSS is not matched properly to achieve the $P_{\text{out,max}}$ of the CSS. As a result, the $P_{\text{out,max}}$ of the CC is limited due to the low input impedance of the CGS. Therefore,

factor n for the classical CC is far below two. Using the modified CC, the input impedance ($\underline{Z}_{\text{in}}$) of the CGS can be increased by lowering C_{st}, shown in Fig. 4.3.4. Fig. 4.3.4a and Fig. 4.3.4b shows the $\left|\underline{H}_{11,\text{CGS}}\right|$ and $\left|\underline{Z}_{\text{in,CGS}}\right|$ respectively depending on C_{st} for a certain foundry process. $\left|\underline{H}_{11,\text{CGS}}\left(\underline{Z}_{\text{load}}=0\right)\right|$, $\left|\underline{Z}_{\text{in,CGS}}\left(f=1\,\text{GHz}\right)\right|$
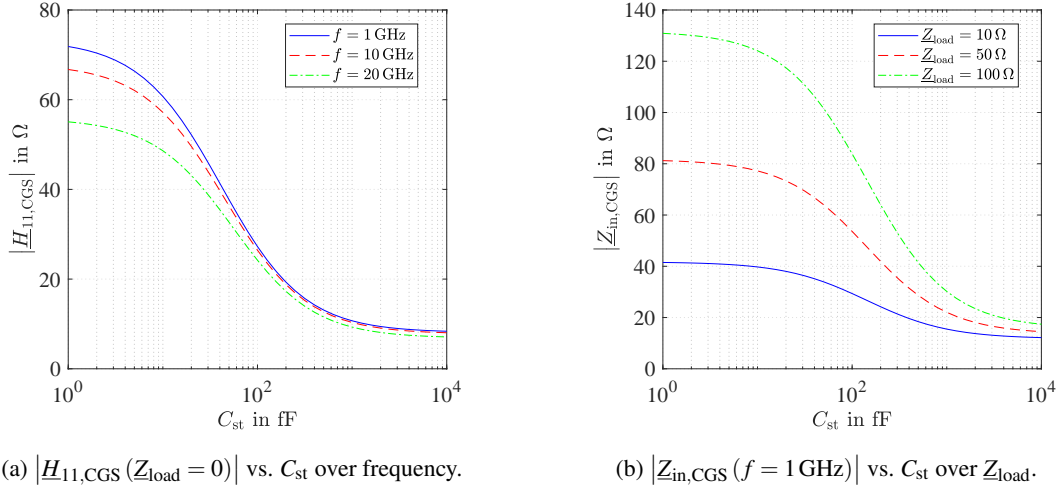
(a) $\left|\underline{H}_{11,\text{CGS}}\left(\underline{Z}_{\text{load}}=0\right)\right|$ vs. C_{st} over frequency.   (b) $\left|\underline{Z}_{\text{in,CGS}}\left(f=1\,\text{GHz}\right)\right|$ vs. C_{st} over $\underline{Z}_{\text{load}}$.

Figure 4.3.4: (a) and (b) $\left|\underline{H}_{11,\text{CGS}}\right|$ and $\left|\underline{Z}_{\text{in,CGS}}\right|$ vs. C_{st}, respectively, of the modified CGS.

$\underline{Z}_{\text{in,CGS}}$ can be expressed by

$$\underline{Z}_{\text{in,CGS}} = \underline{H}_{11,\text{CGS}} - \frac{\underline{H}_{21,\text{CGS}}\underline{H}_{12,\text{CGS}}\underline{Z}_{\text{load}}}{1 + \underline{H}_{22,\text{CGS}}\underline{Z}_{\text{load}}} \ . \tag{4.3.8}$$

For $C_{\text{st}} \to 0$, using the simplified SSM of the CGS, shown in Fig. 4.2.3, a maximum $\underline{Z}_{\text{in,CGS}}$ (load impedance of the CSS) of

$$\underline{Z}_{\text{in,max,CGS}}\left(C_{\text{st}} \to 0, f \to 0\right) = r_{\text{ds}} \cdot \frac{C_{\text{gs}} + C_{\text{gd}}}{C_{\text{gs}} + C_{\text{gd}}\left(1 + g_{\text{m}}r_{\text{ds}}\right)} + \underline{Z}_{\text{load}} \tag{4.3.9}$$

can be reached at low frequencies. Due to this fact the power transfer from the CSS to the CGS increases and as a result the overall P_{out} of the modified CC increases as well. A factor n up to two can be achieved depending on the process.

4.3.2 Power Compression

Power compression and, as a result, the non-linearity is one of the key-characteristics in class A PAs. For larger P_{in} the output signal starts to compress and even clips at a certain P_{in} [53]. Fig. 4.3.5 shows the simplified LSM of the CSS which reflects the most important intrinsic elements depending on the voltage swing. Elements of the active device which change in large-signal condition:

- the voltage controlled current source with large-signal trans-conductance $G_{\text{m}}\left(V_{\text{GS}},V_{\text{GD}}\right)$
- the input capacitor with large-signal gate-source capacitance $C_{\text{gs}}\left(V_{\text{GS}},V_{\text{GD}}\right)$
- the feedback capacitor with large-signal gate-drain capacitance $C_{\text{gd}}\left(V_{\text{GS}},V_{\text{GD}}\right)$

As $C_{\text{gd}}\left(V_{\text{GS}},V_{\text{GD}}\right)$ has only a minor influence on the large-signal behavior, the voltage dependency is often neglected. Main elements which change with voltage swing are the $G_{\text{m}}\left(V_{\text{GS}},V_{\text{GD}}\right)$ and $C_{\text{gs}}\left(V_{\text{GS}},V_{\text{GD}}\right)$. Moreover, the voltage V_{GS} has a higher impact on the elements compared to the voltage V_{GD}.
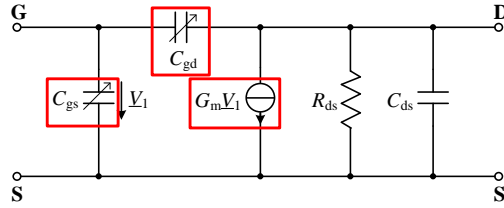
Figure 4.3.5: Simplified LSM of the CSS [98].

The large-signal $C_{\mathrm{gs}}\left(\widehat{\widehat{V}}_{\mathrm{gs}}\right)$ as well as the $G_{\mathrm{m}}\left(\widehat{\widehat{V}}_{\mathrm{gs}}\right)$ degrades with higher voltage swing ($\widehat{\widehat{V}}_{\mathrm{gs}}$) in class A PAs. Due to the fact, that in general the matching networks are passive and that voltage is independent, the optimum load can not be offered over the entire frequency and input power range. As a result the large-signal gain degrades as $G_{\mathrm{m}}\left(\widehat{\widehat{V}}_{\mathrm{gs}}\right)$ degrades with higher voltage swing. The lower large-signal $C_{\mathrm{gs}}\left(\widehat{\widehat{V}}_{\mathrm{gs}}\right)$ —with higher voltage swing $\widehat{\widehat{V}}_{\mathrm{gs}}$— can have a positive or negative behavior on the performance of the PA. Both effects significantly depend on the design of PAs and are more pronounced in broadband PAs as the matching has to be done over a wide frequency range.

The most important changes of the large-signal Y-parameters of the CSS in class A operation are summarized in the following:

- The $\left|\underline{Y}_{11,\mathrm{CSS}}\right|$ —expressed by eq. (4.2.1)— decreases with higher $\widehat{\widehat{V}}_{\mathrm{gs}}$ due to the fact that the large-signal $C_{\mathrm{gs}}\left(\widehat{\widehat{V}}_{\mathrm{gs}}\right)$ decreases with higher voltage swing $\widehat{\widehat{V}}_{\mathrm{gs}}$ (effective input impedance increases).
- The $\left|\underline{Y}_{21,\mathrm{CSS}}\right|$ —expressed by eq. (4.2.3)— decreases with higher $\widehat{\widehat{V}}_{\mathrm{gs}}$ due to the degradation of $G_{\mathrm{m}}\left(\widehat{\widehat{V}}_{\mathrm{gs}}\right)$ which decreases also with higher $\widehat{\widehat{V}}_{\mathrm{gs}}$.

In PAs using the CC topology, the second stage is in CG configuration, therefore the large-signal dependent parameters are twice as much as the single CSS. Since the second stage is in CG configuration the large-signal behavior is different. The most important changes of the large-signal H-parameters of the CGS in class A operation are summarized in the following:

- The $\left|\underline{H}_{11,\mathrm{CGS}}\right|$ and $\left|\underline{H}_{12,\mathrm{CGS}}\right|$ —expressed by eq. (4.2.5) and eq. (4.2.6)— increases at low frequencies with higher $\widehat{\widehat{V}}_{\mathrm{gs}}$ due to the degradation of $G_{\mathrm{m}}\left(\widehat{\widehat{V}}_{\mathrm{gs}}\right)$ which decreases with higher $\widehat{\widehat{V}}_{\mathrm{gs}}$ (input impedance increases and isolation degrades).
- The $\left|\underline{H}_{21,\mathrm{CGS}}\right|$ —expressed by eq. (4.2.7)— is independent at low frequencies with respect to the higher $\widehat{\widehat{V}}_{\mathrm{gs}}$. However, at higher frequencies the $\underline{H}_{21,\mathrm{CGS}}$ will suffer due to the degradation of the pole, explained in detail in Sec. 5.2.2.

4.4 Summary

In Sec. 4.1 the functionality of the classical CC and the modified CC were explained. Furthermore in Sec. 4.2 and Sec. 4.3, certain small- and large-signal parameters of the CSS and the CC were derived and their dependencies explained. It was shown, that the stabilization capacitor with C_{st} has a huge influence on the performance of the CC:

- Small-signal behavior:
  The Miller-effect increases with decreasing C_{st}, which results in a lower $\underline{Y}_{11,\mathrm{CC}}$, but a larger $\underline{Y}_{12,\mathrm{CC}}$. As a result the useful bandwidth of CCs in broadband PAs degrades.
- Large-signal behavior:
  A decreasing C_{st} increases the input impedance of the CGS. Because the input impedance of the CGS is the load impedance of the CSS, the power transfer from the CSS to the CGS significantly depends on C_{st}. Due to that fact, the overall P_{out} of the CC can be increased by changing C_{st} in the right manner.

5 Comparison of Common-Source Stage and Cascode

In this chapter the small- and large-signal parameters of the CSS and the CC are compared with each other to point out the advantages and disadvantages of the CC in broadband PAs. It was assumed that the CSS and the CGS have the same device size when the simplified SSM is used. The derivation and their dependencies of certain small- and large-signal parameters of the CSS and the CC can be found in the previous Ch. 4 and in Appendix A–Appendix C.

5.1 Small-Signal Parameters

5.1.1 Y-Parameters

Due to the fact the CSS as well as the CC acts as a voltage controlled current source with high input and output impedance the Y-parameters are well suited to compare both topologies. Table 5.1.1 oppose the general valid Y-parameters of the CSS and the CC.

Table 5.1.1: Y-parameters of the CSS and the CC [98].

	Common-Source Stage	Cascode
$\underline{Y}_{11}$	$\underline{Y}_{11,\mathrm{CSS}}$	$\underline{Y}_{11,\mathrm{CSS}} - \frac{\underline{H}_{11,\mathrm{CGS}}\underline{Y}_{12,\mathrm{CSS}}\underline{Y}_{21,\mathrm{CSS}}}{1+\underline{Y}_{22,\mathrm{CSS}}\underline{H}_{11,\mathrm{CGS}}}$
$\underline{Y}_{12}$	$\underline{Y}_{12,\mathrm{CSS}}$	$\underline{Y}_{12,\mathrm{CSS}} \cdot \left(\frac{\underline{H}_{12,\mathrm{CGS}}}{1+\underline{Y}_{22,\mathrm{CSS}}\underline{H}_{11,\mathrm{CGS}}} \right)$
$\underline{Y}_{21}$	$\underline{Y}_{21,\mathrm{CSS}}$	$\underline{Y}_{21,\mathrm{CSS}} \cdot \left(\frac{-\underline{H}_{21,\mathrm{CGS}}}{1+\underline{Y}_{22,\mathrm{CSS}}\underline{H}_{11,\mathrm{CGS}}} \right)$
$\underline{Y}_{22}$	$\underline{Y}_{22,\mathrm{CSS}}$	$\underline{H}_{22,\mathrm{CGS}} + \underline{Y}_{22,\mathrm{CSS}} \cdot \left(\frac{-\underline{H}_{12,\mathrm{CGS}}\underline{H}_{21,\mathrm{CGS}}}{1+\underline{Y}_{22,\mathrm{CSS}}\underline{H}_{11,\mathrm{CGS}}} \right)$

Comparing the Y-parameters of both topologies in Table 5.1.1, the following properties can be determined:

- Due to the fact that the $\Im\left\{\underline{Y}_{12,\mathrm{CSS}}\right\} < 0$ the imaginary part of the last term of $\underline{Y}_{11,\mathrm{CC}}$ is positive:

$$\Im\left\{ \frac{\underline{Y}_{12,\mathrm{CSS}}\underline{Y}_{21,\mathrm{CSS}}\underline{H}_{11,\mathrm{CGS}}}{1+\underline{Y}_{22,\mathrm{CSS}}\underline{H}_{11,\mathrm{CGS}}} \right\} > 0 \,. \tag{5.1.1}$$

As a result the $\Im\left\{\underline{Y}_{11,\mathrm{CC}}\right\} > \Im\left\{\underline{Y}_{11,\mathrm{CSS}}\right\}$ (larger short circuit input capacitance). Additionally it can be seen that the impedance mismatch

$$1+\underline{Y}_{22,\mathrm{CSS}}\underline{H}_{11,\mathrm{CGS}} \tag{5.1.2}$$

between the CSS and the CC plays an important part. In general the $\left|\underline{Y}_{22,\mathrm{CSS}}\underline{H}_{11,\mathrm{CGS}}\right|$ degrades for larger impedance mismatch due to the fact that the $\underline{Y}_{22,\mathrm{CSS}} < \frac{1}{\underline{H}_{11,\mathrm{CGS}}}$. Therefore, the magnitude of eq. (5.1.2) decreases with decreasing match and as a result the Miller-effect [137] reduces.

- The $\left|\underline{Y}_{12,\mathrm{CC}}\right| < \left|\underline{Y}_{12,\mathrm{CSS}}\right|$ (larger isolation) because $\left|\underline{H}_{12,\mathrm{CGS}}\right| \leq 1$ and the magnitude of the mismatch between the CSS and the CGS —expressed by eq. (5.1.2)— is always larger one. In case of improved impedance match between the CSS and the CC the isolation even increases.

- The $\underline{Y}_{21,\text{CC}}$ is defined by the product of the $\underline{Y}_{21,\text{CSS}}$ and $\underline{H}_{21,\text{CGS}}$ divided by the mismatch eq. (5.1.2). Due to the fact that $\left|\underline{H}_{21,\text{CGS}}\right| \leq 1$ at low frequencies, degrades at high frequencies and the magnitude of the mismatch eq. (5.1.2) is greater one, the $\underline{Y}_{21,\text{CC}}$ is always lower compared to the $\underline{Y}_{21,\text{CSS}}$. In case of matching the output impedance of the CSS to the input impedance of the CGS the $\underline{Y}_{21,\text{CC}}$ deteriorates further over the complete frequency range.
- The $\underline{Y}_{22,\text{CC}}$ is defined by the sum of the $\underline{H}_{22,\text{CGS}}$ and $\underline{Y}_{22,\text{CSS}}$ multiplied by

$$\left(\frac{-\underline{H}_{12,\text{CGS}}\underline{H}_{21,\text{CGS}}}{1+\underline{Y}_{22,\text{CSS}}\underline{H}_{11,\text{CGS}}}\right) . \tag{5.1.3}$$

In general the first summand $\underline{H}_{22,\text{CGS}}$ is much smaller than the $\underline{Y}_{22,\text{CSS}}$ because the output capacitance is dominated by the feedback capacitance C_{gd} of the CGS which is much smaller compared to C_{ds}. Due to the isolation $\underline{H}_{12,\text{CGS}}$ and the mismatch eq. (5.1.2), the $\underline{Y}_{22,\text{CSS}}$ has only a small proportion of the $\underline{Y}_{22,\text{CC}}$. Therefore, the $\underline{Y}_{22}$ of the CC is much smaller compared to the CSS (smaller short circuit output capacitance and larger short circuit output resistance).

Using the simplified SSM of the CSS and the classical CC, shown in Fig. 4.2.1 and Fig. 4.2.4 respectively, Table 5.1.2 opposes the determined Y-parameters of the CSS and the classical CC. Table 5.1.3 opposes the Y-parameters of the CSS and the modified CC using the simplified SSM shown in Fig. 4.2.5 for $C_{\text{st}} \to 0$.

Table 5.1.2: Y-parameters of the CSS and the classical CC using the simplified SSM [98].

	Common-Source Stage	Classical Cascode
$\underline{Y}_{11}$	$j\omega\left(C_{\text{gs}}+C_{\text{gd}}\right)$	$j\omega\left(C_{\text{gs}}+C_{\text{gd}}\right) + j\omega C_{\text{gd}}\left(\frac{g_{\text{m}}r_{\text{ds}}}{2+g_{\text{m}}r_{\text{ds}}}\right)\left(1+j\omega\cdot\ldots\right)$
$\underline{Y}_{12}$	$-j\omega C_{\text{gd}}$	$-j\omega C_{\text{gd}}\frac{1}{(2+g_{\text{m}}r_{\text{ds}})}\left(1+j\omega\cdot\ldots\right)$
$\underline{Y}_{21}$	$g_{\text{m}}\left(1+j\omega\cdot\ldots\right)$	$g_{\text{m}}\left(\frac{1+g_{\text{m}}r_{\text{ds}}}{2+g_{\text{m}}r_{\text{ds}}}\right)\left(1+j\omega\cdot\ldots\right)$
$\underline{Y}_{22}$	$\frac{1}{r_{\text{ds}}}+j\omega\left(C_{\text{ds}}+C_{\text{gd}}\right)$	$j\omega C_{\text{gd}}+j\omega\left(\frac{C_{\text{gs}}}{1+g_{\text{m}}r_{\text{ds}}}\right)\left(1+j\omega\cdot\ldots\right)+\frac{1}{r_{\text{ds}}(2+g_{\text{m}}r_{\text{ds}})}\left(1+j\omega\cdot\ldots\right)$

Table 5.1.3: Y-parameters of the CSS and the modified CC ($C_{\text{st}} \to 0$) using the simplified SSM.

	Common-Source Stage	Modified Cascode
$\underline{Y}_{11}$	$j\omega\left(C_{\text{gs1}}+C_{\text{gd1}}\right)$	$j\omega\left(C_{\text{gs1}}+C_{\text{gd1}}\right) + j\omega C_{\text{gd1}}\left(g_{\text{m1}}\left[r_{\text{ds1}}\parallel r_{\text{ds2,eff}}\right]\right)\left(1+j\omega\cdot\ldots\right)$
$\underline{Y}_{12}$	$-j\omega C_{\text{gd1}}$	$-j\omega C_{\text{gd1}}\frac{1}{\left(1+\frac{r_{\text{ds2,eff}}}{r_{\text{ds1}}}\right)}\left(1+j\omega\cdot\ldots\right)$
$\underline{Y}_{21}$	$g_{\text{m1}}\left(1+j\omega\cdot\ldots\right)$	$g_{\text{m1}}\frac{1}{\left(1+\frac{r_{\text{ds2,eff}}}{r_{\text{ds1}}}\right)}\left(1+j\omega\cdot\ldots\right)$
$\underline{Y}_{22}$	$\frac{1}{r_{\text{ds1}}}+j\omega\left(C_{\text{ds1}}+C_{\text{gd1}}\right)$	$\frac{1}{\left(r_{\text{ds1}}+r_{\text{ds2,eff}}\right)}+j\omega\left(C_{\text{ds1}}+C_{\text{gd1}}\right)\left(\frac{r_{\text{ds1}}-\left[r_{\text{ds1}}\parallel r_{\text{ds2,eff}}\right]}{r_{\text{ds1}}+r_{\text{ds2,eff}}}\right)+\left(j\omega\right)^{2}\cdot\left(\ldots\right)$

Comparing the Y-parameters of the CSS, the classical CC and the modified CC with each other, shown in in Table 5.1.2 and in Table 5.1.3, the following properties can be determined:

- The short circuit input capacitance of the CSS is slightly smaller compared to the classical CC. However, the short circuit input capacitance of the modified CC increases with increasing C_{st} due to the Miller-effect [137]. As a result the short circuit input capacitance of the modified CC can be significantly larger compared to the classical CC.
- The isolation $\underline{Y}_{12}$ of the classical CC is much larger (by a factor of $\approx g_{\text{m}}r_{\text{ds}}$) compared to the CSS. Decreasing the stabilization capacitance C_{st} of the modified CC the isolation degrades significantly. For $C_{\text{st}} \to 0$ the isolation of the modified CC remains slightly better compared to the CSS.

- $\underline{Y}_{21}$ of the CSS and the classical CC is very similar. However, $\underline{Y}_{21}$ of the modified CC is much lower due to the frequency independent voltage divider which consists of the gate-source capacitor with C_{gs} and the stabilization capacitor with C_{st} of the CGS. Decreasing C_{st} decreases $\underline{Y}_{21}$ of the modified CC.
- Comparison of $\underline{Y}_{22}$ of the CSS and the CC can be split into real part and imaginary part:
  - Because the feedback capacitor with capacitance C_{gd} is usually much smaller than C_{ds} of an active device, the short circuit output capacitance of the CSS is much larger compared to the classical CC. Although the isolation of the modified CGS decreases with decreasing C_{st} the short circuit output capacitance of the modified CC can be significantly reduced, due to the lower effective capacitances of the modified CGS.
  - The short circuit output resistance of the classical CC is much larger (by a factor of $\approx g_m r_{ds}$) compared to the CSS due to the isolation of the CGS. Decreasing C_{st} of the modified CC, the isolation degrades significantly and for $C_{st} \to 0$ the short circuit output resistance is only slightly larger compared to the CSS.

5.1.2 Maximum Stable Gain

The *MSG* is an attractive figure of merit which illustrates a certain gain bandwidth product of active device cells. Therefore, the *MSG* calculated by eq. (2.2.10) can be used to compare the CSS and the CC with each other. Table 5.1.4 opposes the general valid *MSG* of the CSS and the CC.

Table 5.1.4: *MSG* of the CSS and the CC [98].

Common-Source Stage	Cascode
$\dfrac{\underline{Y}_{21,\text{CSS}}}{\underline{Y}_{12,\text{CSS}}}$	$\dfrac{\underline{Y}_{21,\text{CSS}}}{\underline{Y}_{12,\text{CSS}}} \cdot \left(-\dfrac{\underline{H}_{21,\text{CGS}}}{\underline{H}_{12,\text{CGS}}} \right)$

Comparing the *MSG* of both topologies in Table 5.1.4, it can be seen that the improvement of the CC is defined by the *MSG* of the CGS. Applying the simplified SSM of the classical CGS and the modified CGS, shown in Fig. 4.2.2 and Fig. 4.2.3 respectively, Table 5.1.5 shows the improvement of the classical CC and the modified CC compared to the CSS.

Table 5.1.5: *MSG* of the classical CGS and modified CGS using the simplified SSM [98].

	Classical Common-Gate Stage	Modified Common-Gate Stage
MSG_{CGS}	$\left(1 + g_m r_{ds}\right)\left\|\dfrac{1 + j\frac{f}{f_{01}}}{1 + j\frac{f}{f_{\infty 1}}}\right\|$	$\dfrac{C_{gs} + \left(C_{st} + C_{gd}\right)\left(1 + g_m r_{ds}\right)}{C_{st} + C_{gs} + C_{gd}\left(1 + g_m r_{ds}\right)}\left\|\dfrac{1 + j\frac{f}{f_{02}}}{1 + j\frac{f}{f_{\infty 2}}}\right\|$
Zero f_0	$\dfrac{1}{2\pi} \cdot \dfrac{1 + g_m r_{ds}}{r_{ds} C_{ds}}$	$\dfrac{1}{2\pi} \cdot \dfrac{C_{gs} + \left(C_{st} + C_{gd}\right)\left(1 + g_m r_{ds}\right)}{r_{ds}\left(C_{ds}\left[C_{st} + C_{gs} + C_{gd}\right] + C_{gd} C_{gs}\right)}$
Pole f_∞	$\dfrac{1}{2\pi} \cdot \dfrac{1}{r_{ds} C_{ds}}$	$\dfrac{1}{2\pi} \cdot \dfrac{C_{st} + C_{gs} + C_{gd}\left(1 + g_m r_{ds}\right)}{r_{ds}\left(C_{ds}\left[C_{st} + C_{gs} + C_{gd}\right] + C_{gd} C_{gs}\right)}$

Examining the *MSG* of the classical CGS and the modified CGS, shown in Table 5.1.5, the following properties can be determined:

- Properties of the classical CC:
  - The *MSG* of the classical CGS is > 1 over the complete frequency range. As a result the *MSG* of the classical CC is larger compared to the *MSG* of the CSS.
  - The improvement of the classical CC amounts to $1 + g_m r_{ds}$ at low frequencies and starts to degrade above the cut-off frequency $f_{\infty 1}$.

- Properties of the modified CC:
  - The *MSG* of the modified CGS is smaller than the classical CGS but is also > 1 over the entire frequency range, except $C_{st} = 0$. As a result the *MSG* of the modified CC is larger than the *MSG* of the CSS.
  - Decreasing C_{st} of the modified CGS results in a reduction of the *MSG* but it remains > 1. Moreover, the cut-off frequency $f_{\infty 2}$ is shifted to higher frequencies if the in-equation

$$C_{gs} < C_{ds} \cdot g_m r_{ds} \tag{5.1.4}$$

  is valid. As a result the overall *MSG* of the modified CC is improved in a wider frequency range.
  - For $C_{st} \to 0$ the *MSG* of the modified CGS is $= 1$ one over the entire frequency range. Pole and zero of the modified CGS cancel each other for $C_{st} \to 0$. As a result the *MSG* of the CSS and the modified CC are equal.

Further information about the derivation of the *MSG* of the CSS, the CGS and the CC can be found in Appendix A.2, Appendix B.2 and Appendix C.2 respectively.

5.1.3 Transition Frequency and Maximum Oscillation Frequency

The two important figure of merits f_t and f_{max} are usually quoted by foundries to compare their processes with other foundries processes and to show their superior high frequency device performance. These figure of merits which are normally related to compare different processes can also be used to oppose the CSS with the CC. In 1975 [139] Asai et al. have already shown that dual-gate devices (similar to CC devices) are better in the lower frequency range and that single-gate devices are more attractive at higher frequencies. Chen et al. in 1999 [140] and Green et al. in 2000 [141] approximated the $\underline{H}_{21}$ and, as a result, f_t of the CC by

$$\underline{H}_{21,CC} \approx \frac{1}{j \frac{f}{f_{c,CSS}} \left(1 + j \frac{f}{f_{c,CGS}} \right)} \tag{5.1.5}$$

to show the degradation of the transition frequency. The $f_{c,CSS}$ and $f_{c,CGS}$ refer to the cut-off frequencies of the $\underline{H}_{21}$ of the CSS and the CGS. Based on eq. (5.1.5), the lower f_t is only caused by the $f_{c,CGS}$. Among other things, a second degradation effect which cannot be neglected nowadays in modern CC designs is determined in the following.

5.1.3.1 Transition Frequency

Due to the fact that the f_t and $\underline{H}_{21}$ are linked together by eq. (2.2.14), it makes sense to examine the difference between $\underline{H}_{21}$ of the CSS and the CC because the comparison can be done in an easier way. $\underline{H}_{21}$ of the CC can be calculated by eq. (2.1.4). Table 5.1.6 compares the general valid $\underline{H}_{21}$ of the CSS and the CC.

Table 5.1.6: $\underline{H}_{21}$ of the CSS and the CC [98].

Common-Source Stage	Cascode
$\dfrac{\underline{Y}_{21,CSS}}{\underline{Y}_{11,CSS}}$	$\dfrac{\underline{Y}_{21,CSS}}{\underline{Y}_{11,CSS}} \cdot \left(\dfrac{-\underline{H}_{21,CGS}}{1 + \underline{H}_{22,CSS}\underline{H}_{11,CGS}} \right)$

Comparing $\underline{H}_{21}$ of both topologies in Table 5.1.6, the following properties can be determined:

- The $\underline{H}_{21,CC}$ is the multiplication of the $\underline{H}_{21,CSS}$ and $\underline{H}_{21,CGS}$ divided by the mismatch

$$1 + \underline{H}_{11,CGS}\underline{H}_{22,CSS} \tag{5.1.6}$$

  of the CSS and the CGS.

- The $\left|\underline{H}_{21,\text{CC}}\right| < \left|\underline{H}_{21,\text{CSS}}\right|$ because $\left|\underline{H}_{21,\text{CGS}}\right| \leq 1$ and the magnitude of the mismatch eq. (5.1.6) is always larger one. As a result $f_{\text{t,CC}} < f_{\text{t,CSS}}$.

The reason of the smaller $\underline{H}_{21,\text{CC}}$ can be split into two degradation effects:

- Degradation of the $\underline{H}_{21,\text{CGS}}$.
- Matching between the CSS and the CGS expressed by eq. (5.1.6).

Applying the simplified SSM of the CSS, the classical CGS and the modified CGS, shown in Fig. 4.2.1, Fig. 4.2.2 and Fig. 4.2.3 respectively, Table 5.1.7 shows the degradation of the classical CC and the modified CC compared to the CSS.

Table 5.1.7: Degradation effects of the $\underline{H}_{21}$ of the classical CC and the modified CC ($C_{\text{st}} \to 0$) compared to the CSS using the simplified SSM.

	Classical Cascode	Modified Cascode
$\underline{H}_{21,\text{CGS}}$	$-\dfrac{\left(1+j\frac{f}{f_{01}}\right)}{\left(1+j\frac{f}{f_{\infty 1}}\right)}$	$-\dfrac{\left(1+j\frac{f}{f_{01}}\right)}{\left(1+j\frac{f}{f_{\infty 1}}\right)} = -1$
Zero f_{01}	$\dfrac{1}{2\pi} \cdot \dfrac{1+g_m r_{ds}}{r_{ds} C_{ds}}$	$\dfrac{1}{2\pi} \cdot \dfrac{1}{r_{ds2,\text{eff}} C_{ds2,\text{eff}}}$
Pole $f_{\infty 1}$	$\dfrac{1}{2\pi} \cdot \dfrac{1+g_m r_{ds}}{r_{ds}\left(C_{gs}+C_{ds}\right)}$	$\dfrac{1}{2\pi} \cdot \dfrac{1}{r_{ds2,\text{eff}} C_{ds2,\text{eff}}}$
$\dfrac{1}{1+\underline{H}_{22,\text{CSS}}\underline{H}_{11,\text{CGS}}}$	$\dfrac{1+g_m r_{ds}}{2+g_m\left(1+\frac{C_{gd}}{C_{gs}+C_{gd}}\right)r_{ds}} \dfrac{\left(1+j\frac{f}{f_{02}}\right)}{\left(1+j\frac{f}{f_{\infty 2}}\right)}$	$\dfrac{1}{1+\left(\frac{1}{r_{ds1}}+g_{m1}\left[\frac{C_{gd1}}{C_{gs1}+C_{gd1}}\right]\right)r_{ds2,\text{eff}}} \dfrac{\left(1+j\frac{f}{f_{02}}\right)}{\left(1+j\frac{f}{f_{\infty 2}}\right)}$
Zero f_{02}	$\dfrac{1}{2\pi} \cdot \dfrac{1+g_m r_{ds}}{r_{ds}\left(C_{gs}+C_{ds}\right)}$	$\dfrac{1}{2\pi} \cdot \dfrac{1}{r_{ds2,\text{eff}} C_{ds2,\text{eff}}}$
Pole $f_{\infty 2}$	$\dfrac{1}{2\pi} \cdot \dfrac{2+g_m\left(1+\frac{C_{gd}}{C_{gs}+C_{gd}}\right)}{C_{gs}+2\cdot C_{ds}+C_{gd}\left(1-\frac{C_{gd}}{C_{gs}+C_{gd}}\right)}$	$\dfrac{1}{2\pi} \cdot \dfrac{\frac{1}{\left(r_{ds1}\|r_{ds2,\text{eff}}\right)}+g_{m1}\left(\frac{C_{gd1}}{C_{gs1}+C_{gd1}}\right)}{\left(C_{ds2,\text{eff}}+C_{ds1}+C_{gd1}\left[1-\frac{C_{gd1}}{C_{gs1}+C_{gd1}}\right]\right)}$

Examining the degradation effects of $\underline{H}_{21}$ of the classical CC and the modified CC, shown in Table 5.1.7, the following properties can be determined:

- Properties of the classical CC:
  - The mismatch between the CSS and the CGS is very high and as a result the magnitude of the mismatch eq. (5.1.6) is very low which can be expressed by

$$1+\left(\frac{g_m r_{ds}}{1+g_m r_{ds}}\right)\left(\frac{C_{gd}}{C_{gs}+C_{gd}}\right)+\frac{1}{1+g_m r_{ds}} \approx 1 \tag{5.1.7}$$

  at low frequencies.
  - The cut-off frequency $f_{\infty 2}$ shown in Table 5.1.7 which can be approximated by

$$f_{\infty 2} = \frac{1}{2\pi} \cdot \frac{g_m}{C_{gs}+2\cdot C_{ds}+C_{gd}} \tag{5.1.8}$$

  defines the frequency where the mismatch starts to decrease —magnitude of the mismatch eq. (5.1.6) increases—.
  - The mismatch eq. (5.1.6) stops to degrade at cut-off frequency f_{02} shown in Table 5.1.7 expressed by

$$f_{02} = \frac{1}{2\pi} \cdot \frac{1+g_m r_{ds}}{r_{ds}\left(C_{gs}+C_{ds}\right)} . \tag{5.1.9}$$

  Although the cut-off frequency $f_{\infty 1}$ of the $\underline{H}_{21,\text{CGS}}$ is equal to the cut-off frequency f_{02}, shown in Table 5.1.7, $\underline{H}_{21,\text{CC}}$ degrades further.

The degradation effect of $\underline{H}_{21}$ of the classical CC is dominated at medium frequencies ($f_{\infty 2}$–f_{02}) by the mismatch between the CSS and the classical CGS. At higher frequencies ($f_{02} = f_{\infty 1} < f < f_{01}$) $\underline{H}_{21}$ of the classical CC is further degraded by the degradation of $\underline{H}_{21,\text{CGS}}$. As a result both degradation effects lead to a lower $f_{\text{t,CC}}$ compared to $f_{\text{t,CSS}}$. In Fig. 5.1.1 the degradation of f_{t} of the classical CC is plotted varying C_{gd} and C_{ds}. The overall degradation of f_{t} of the classical CC is at least $> 20\,\%$.

- Properties of the modified CC:
  - Mismatch between the CSS and the modified CGS decreases with decreasing C_{st}. As a result magnitude of mismatch eq. (5.1.6) increases which can be expressed by

$$1 + \left(\frac{1}{r_{\text{ds1}}} + g_{\text{m1}} \left[\frac{C_{\text{gd1}}}{C_{\text{gs1}} + C_{\text{gd1}}} \right] \right) \left(\frac{r_{\text{ds2}}}{1 + g_{\text{m2}} r_{\text{ds2}}} \right) \approx 1\text{--}2 \qquad (5.1.10)$$

    at low frequencies. Therefore, the $\underline{H}_{21,\text{CC}}$ suffers due to improved match between the CSS and the modified CGS.
  - The cut-off frequency f_{02} shown in Table 5.1.7 is slightly shifted to lower frequencies depending on the process parameters (assuming that the in-eq. 5.1.4 is valid).
  - The cut-off frequency f_{01} and $f_{\infty 1}$ of $\underline{H}_{21}$ of the modified CGS shown in Table 5.1.7 decreases with decreasing C_{st} and cancel each other for $C_{\text{st}} \to 0$.

Mismatch between the CSS and the modified CGS is the dominated degradation effect of $\underline{H}_{21}$ of the modified CC from DC up to the cut-off frequency f_{02}. The degradation effect increases with decreasing C_{st}. Due to the fact that the cut-off frequency f_{01} and $f_{\infty 1}$ of $\underline{H}_{21}$ of the modified CGS decrease and nearing each other with decreasing C_{st}, $\underline{H}_{21}$ of the modified CC at higher frequencies ($f_{02} = f_{\infty 1} < f < f_{01}$) is the minor part of the overall degradation effect of $\underline{H}_{21}$ of the modified CC.

Therefore, both degradation effects are still responsible, except $C_{\text{st}} \to 0$, for the degradation of $\underline{H}_{21}$ of the modified CC and as a result of the lower $f_{\text{t,CC}}$ compared to the $f_{\text{t,CSS}}$. The degradation effect of $\underline{H}_{21}$ of the classical CC is dominated at medium frequencies ($f_{\infty 2}$–f_{02}) by the mismatch between the CSS and the classical CGS. At higher frequencies ($f > f_{02} = f_{\infty 1}$) $\underline{H}_{21}$ of the classical CC is further degraded by the degradation of $\underline{H}_{21}$ of the classical CGS. As a result both degradation effects lead to a lower $f_{\text{t,CC}}$ compared to the $f_{\text{t,CSS}}$. Assuming $C_{\text{gd}} = C_{\text{ds}} = 0$ the degradation of f_{t} of the modified CC is plotted in Fig. 5.1.2 varying C_{st} and R_{st}. Due to the fact that the assumption $C_{\text{gd}} = C_{\text{ds}} = 0$ is not fulfilled, in reality as a first approximation both degradations Fig. 5.1.1 and Fig. 5.1.2 can be multiplied to maintain the overall degradation of the modified CC.
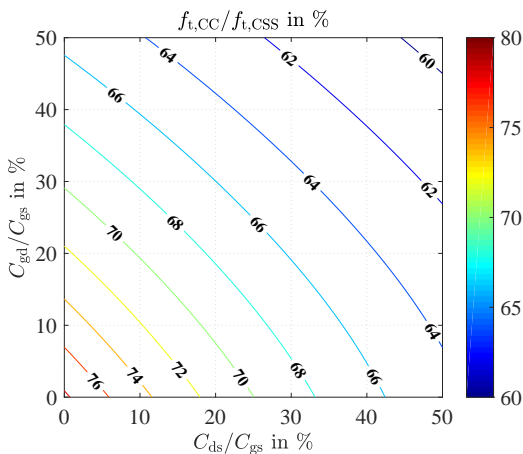
Figure 5.1.1: Degradation of the f_{t} of the classical CC.
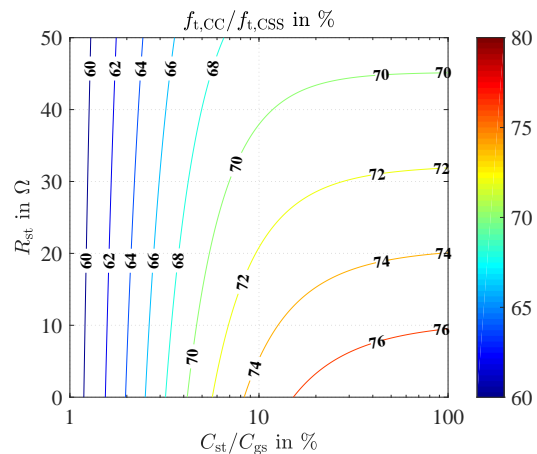
Figure 5.1.2: Degradation of the f_{t} of the modified CC.

Fig. 5.1.3 shows the simulated and measured $\underline{H}_{21}$ of the CSS and the CC using the 250 nm AlGaN/GaN technology at the Fraunhofer Institute for Applied Solid-State Physics (Fraunhofer IAF). The gate pe-

riphery (*GP*) —total size of the HEMT— of the CSS is 1 mm, which is the number of gate finger (*NGF*) times the unit gate-width (*UGW*). The CSS and the CGS of the CC have the same *GP*, which is equal to the single CSS. C_{st} and R_{st} of the CGS are chosen to 22 Ω and 2.4 pF respectively.
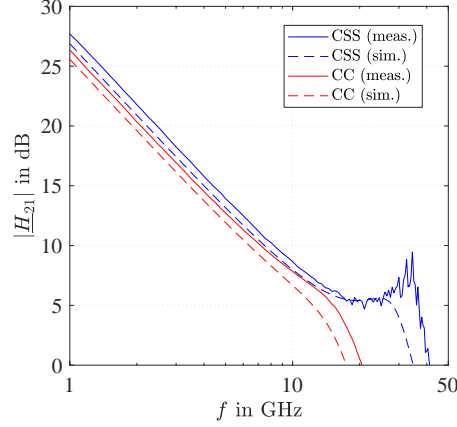
Figure 5.1.3: Measured (solid lines) and simulated (dashed lines) $|\underline{H}_{21}|$ of the CSS (blue) and the modified CC (red) at $V_{\text{DS}} = 20\,\text{V}$ and $I_{\text{DSQ}} = 100\,\text{mA}$.

As shown in Fig. 5.1.3 the $\underline{H}_{21,\text{CC}}$ is lower than the $\underline{H}_{21,\text{CSS}}$ over the complete frequency range. In the range of 1–10 GHz, $\underline{H}_{21,\text{CC}}$ is $\approx 86\,\%$ of the $\underline{H}_{21,\text{CSS}}$. Due to the fact that the degradation is constant in this frequency range, this effect can be traced back to the mismatch between the CSS and the CGS. At higher frequencies the degradation of $\underline{H}_{21,\text{CC}}$ increases due to the decreasing of $\underline{H}_{21,\text{CGS}}$. Based on the curve progression of $\underline{H}_{21,\text{CC}}$, f_{t} of each circuit topology results to

$$f_{\text{t,CSS}} \approx 30\,\text{GHz} \tag{5.1.11}$$
$$f_{\text{t,CC}} \approx 17\,\text{GHz}. \tag{5.1.12}$$

Therefore, the f_{t} of the CC is only $\approx 57\,\%$ of the CSS.

Further information about the derivation of $\underline{H}_{21,\text{CSS}}$ and $\underline{H}_{21,\text{CC}}$ can be found in Appendix A.3 and Appendix C.3 respectively.

5.1.3.2 Maximum Oscillation Frequency

In most RF applications the f_{max} is more important than the f_{t} as stated in [142]. Like the $\underline{H}_{21}$ and f_{t} are linked together, the *U* and f_{max} are also linked together given by eq. (2.2.13). The *U* can be calculated by eq. (2.2.11). Table 5.1.8 compares the general valid *U* of the CSS and the CC under two assumptions:

- Neglecting of $\underline{Y}_{12}$ of the CSS: $\underline{Y}_{12,\text{CSS}} = 0$
- Neglecting of the mismatch between the CSS and the CGS: $\left|\underline{Y}_{22,\text{CSS}}\underline{H}_{11,\text{CGS}}\right| \ll 1$

Table 5.1.8: Approximated *U* of the CSS and the CC.

Common-Source Stage	Cascode
$\dfrac{\left|\underline{Y}_{21,\text{CSS}}\right|^2}{4\cdot\left(\Re\{\underline{Y}_{11,\text{CSS}}\}\Re\{\underline{Y}_{22,\text{CSS}}\}\right)}$	$\dfrac{\left|\underline{Y}_{21,\text{CSS}}\underline{H}_{21,\text{CGS}}\right|^2}{4\cdot\left(\Re\{\underline{Y}_{11,\text{CSS}}\}\Re\{\underline{H}_{22,\text{CGS}}-\underline{Y}_{22,\text{CSS}}\underline{H}_{12,\text{CGS}}\underline{H}_{21,\text{CGS}}\}\right)}$

Comparing the approximated *U* of the CSS and the CC shown in Table 5.1.6, the ratio of *U* between the

CSS and the CC can be calculated to

$$ratio_U = \frac{U_{CC}}{U_{CSS}} \tag{5.1.13}$$

$$= \left| \underline{H}_{21,CGS} \right|^2 \cdot \frac{\Re\left\{\underline{Y}_{22,CSS}\right\}}{\Re\left\{\underline{H}_{22,CGS}\right\} - \Re\left\{\underline{Y}_{22,CSS}\underline{H}_{12,CGS}\underline{H}_{21,CGS}\right\}} \cdot \tag{5.1.14}$$

Examining the eq. (5.1.14), two terms can be identified which show the improvement and degradation of U of the CC compared to the CSS:

- First term is the $\underline{H}_{21,CGS}$. Due to the fact that the $\underline{H}_{21}$ decreases at higher frequencies eq. (5.1.14) decreases also and as a result the U of the CC.
- Second term is the ratio of the $\Re\{\underline{Y}_{22}\}$ of the CSS and the CC. Due to the fact that the $\Re\{\underline{Y}_{22}\}$ of the CC is much smaller compared to the CSS which was already shown in Sec. 5.1.1 the U of the CC is much larger compared to the CSS.

Using the simplified SSM of the classical CC and the modified CC, shown in Fig. 4.2.4 and Fig. 4.2.5 respectively, the identified terms in eq. (5.1.14) can be further investigated with respect to the intrinsic small-signal elements of the CC, shown in Table 5.1.9.

Table 5.1.9: $\underline{H}_{21,CGS}$ and real part of $\underline{Y}_{22} \approx x_1 + x_2$ of the classical and modified CC ($C_{st} \to 0$).

	Classical Cascode	Modified Cascode
$\left\|\underline{H}_{21,CGS}\right\|^2$	$\left\|\dfrac{\left(1+j\frac{f}{f_0}\right)}{\left(1+j\frac{f}{f_\infty}\right)}\right\|^2$	1
$x_1 = \Re\left\{\underline{H}_{22,CGS}\right\}$	$\omega^2 C_{gs} r_{ds} \dfrac{(C_{gs}-C_{ds}g_m r_{ds})}{(1+g_m r_{ds})^2} \dfrac{1}{\left\|1+j\frac{f}{f_\infty}\right\|^2}$	0
$x_2 = -\Re\left\{\underline{Y}_{22,CSS}\underline{H}_{12,CGS}\underline{H}_{21,CGS}\right\}$	$\dfrac{g_{ds}}{1+g_m r_{ds}} \dfrac{1}{\left\|1+j\frac{f}{f_\infty}\right\|^4} \left(1+c_0\omega^2+c_1\omega^4\right)$	$\dfrac{1}{r_{ds1}}$
Zero f_0	$\dfrac{1}{2\pi} \cdot \dfrac{1+g_m r_{ds}}{r_{ds}C_{ds}}$	$\dfrac{1}{2\pi} \cdot \dfrac{1}{r_{ds2,eff}C_{ds2,eff}}$
Pole f_∞	$\dfrac{1}{2\pi} \cdot \dfrac{1+g_m r_{ds}}{r_{ds}\left(C_{gs}+C_{ds}\right)}$	$\dfrac{1}{2\pi} \cdot \dfrac{1}{r_{ds2,eff}C_{ds2,eff}}$

Comparing the $\underline{H}_{21}$ of the classical and modified CGS and approximated $\Re\{\underline{Y}_{22}\}$ of the classical and modified CC in Table 5.1.9, the following properties can be determined:

- Properties of the classical CC:
  - The eq. (5.1.14) degrades by $20\,dB$ per decade above the cut-off frequency f_∞ which can be approximated by

$$f_\infty = \frac{1}{2\pi} \cdot \frac{g_m}{C_{gs}+C_{ds}} \tag{5.1.15}$$

  for $g_m r_{ds} \gg 1$ due to the decreasing $\underline{H}_{21}$ of the CGS.
  - The $\Re\{\underline{Y}_{22}\}$ of the CC can be split into two parts:
    * The real part of the transfered $\underline{Y}_{22}$ of the CSS to the output of the CGS can be approximated by

$$-\Re\left\{\underline{Y}_{22,CSS}\underline{H}_{12,CGS}\underline{H}_{21,CGS}\right\} = \frac{g_{ds}}{1+g_m r_{ds}} \frac{1}{\left|1+j\frac{f}{f_\infty}\right|^4} \tag{5.1.16}$$

    neglecting higher frequency terms.

* The $\Re\{\underline{H}_{22}\}$ of the CGS can be expressed by

$$\Re\{\underline{H}_{22,\mathrm{CGS}}\} = \omega^2 C_{\mathrm{gs}} r_{\mathrm{ds}} \frac{\left(C_{\mathrm{gs}} - C_{\mathrm{ds}} g_{\mathrm{m}} r_{\mathrm{ds}}\right)}{\left(1 + g_{\mathrm{m}} r_{\mathrm{ds}}\right)^2} \frac{1}{\left|1 + j\frac{f}{f_\infty}\right|^2} \ .$$

If the in-eq. 5.1.4 is valid, the $\Re\{\underline{H}_{22,\mathrm{CGS}}\} < 1$.
Considering only the real part of the transfered $\underline{Y}_{22}$ of the CSS to the output of the CGS it can be already seen that the $\Re\{\underline{Y}_{22}\}$ of the classical CC is much lower (by a factor of $\approx g_{\mathrm{m}} r_{\mathrm{ds}}$) compared to the CSS and even decreases above the cut-off frequency f_∞ which compensates the degradation of the $\underline{H}_{21}$ of the CGS. Due to the fact that the $\Re\{\underline{H}_{22,\mathrm{CGS}}\} < 1$ —valid using the GaN-HEMT technology— and increases with frequency, the $\Re\{\underline{Y}_{22}\}$ of the classical CC decreases further. As a result the U of the classical CC is much larger (by a factor of $\approx g_{\mathrm{m}} r_{\mathrm{ds}}$) compared to the CSS. This improvement of the U of the classical CC leads to a higher $f_{\max}$ in contrast to the CSS.
* Properties of the modified CC:
  - The cut-off frequency f_0 and f_∞ of the $\underline{H}_{21}$ of the modified CGS shown in Table 5.1.9 decreases with decreasing C_{st} and cancel each other for $C_{\mathrm{st}} \to 0$. As a result the degradation of the U of the modified CC due to the $\underline{H}_{21}$ of the modified CGS disappears for $C_{\mathrm{st}} \to 0$.
  - The $\Re\{\underline{Y}_{22}\}$ of the modified CC can be split into two parts:
    * The real part of the transfered $\underline{Y}_{22}$ of the CSS to the output of the modified CGS increases with decreasing C_{st} and results to

$$-\Re\{\underline{Y}_{22,\mathrm{CSS}}\underline{H}_{12,\mathrm{CGS}}\underline{H}_{21,\mathrm{CGS}}\} = \frac{1}{r_{\mathrm{ds1}}} \tag{5.1.17}$$

    for $C_{\mathrm{st}} \to 0$.
    * The $\Re\{\underline{H}_{22}\}$ of the CGS tends to zero for $C_{\mathrm{st}} \to 0$.
  As a result the improvement of the U of the modified CC compared to the CSS decreases significantly by decreasing C_{st}. Therefore, the $f_{\max}$ of the modified CC decreases also.

Fig. 5.1.4 shows the measured MSG, the measured MAG and the simulated and measured U of the CSS and the CC using the 250 nm AlGaN/GaN technology at the Fraunhofer IAF. The GP of the CSS is 1 mm. The CSS and the CGS of the CC have the same GP, which is equal to the single CSS. C_{st} and R_{st} of the CGS are chosen to 22 Ω and 2.4 pF respectively.
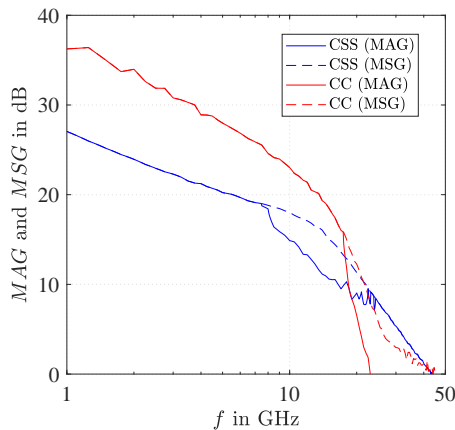
(a) Measured MAG (solid lines) and MSG (dashed lines) of the CSS (blue) and the CC (red) [98].
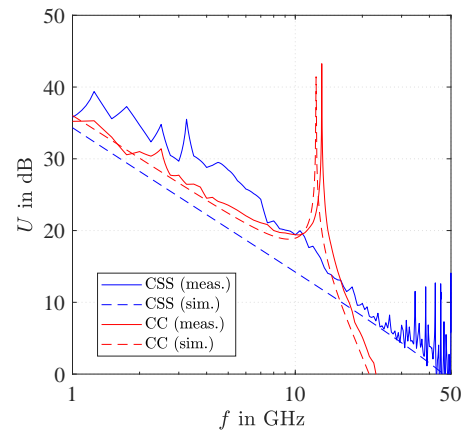
(b) Measured (solid lines) and simulated (dashed lines) U of the CSS (blue) and the CC (red).

Figure 5.1.4: MSG, MAG and U of the CSS and the CC at $V_{\mathrm{DS}} = 20\,\mathrm{V}$ and $I_{\mathrm{DSQ}} = 100\,\mathrm{mA}$.

Fig. 5.1.4a shows the larger MSG and MAG of the CC compared to the CSS up to a frequency of $\approx$ 17 GHz. At higher frequencies the MAG of the CC decreases significantly and becomes even lower

than the *MAG* of the CSS. As a result the $f_{\mathrm{max,CSS}}$ is higher compared to the $f_{\mathrm{max,CC}}$. This behavior is mainly caused by the additional series resistor with resistance R_{st} which was neglected in the previous theory. Nevertheless, the general frequency characteristic of the *MAG* matches with the simulation results presented in [13], which compares the CC and the CS cell.

Moreover, the series resistor with resistance R_{st} leads to a negative U of the CC, shown in Fig. 5.1.4b. The passive behavior of the active device, due to the unilateralization of the active device, exists up to a frequency of $\approx 13\,\mathrm{GHz}$. At higher frequencies the U of the CC decreases by $40\,\mathrm{dB}$ per decade. Based on measured curves of the U, shown in Fig. 5.1.4b, the f_{max} of each topology results to

$$f_{\mathrm{max,CSS}} \approx 48\,\mathrm{GHz} \tag{5.1.18}$$
$$f_{\mathrm{max,CC}} \approx 23\,\mathrm{GHz}\,. \tag{5.1.19}$$

f_{max} of the CC is only $\approx 48\,\%$ of the CSS. This behavior is mainly caused by R_{st} and C_{st}. However, the CC can be re-designed for very high frequencies using a certain value of R_{st} and C_{st} to achieve a higher f_{max} than the CSS.

Further information about the derivation of the U of the CC can be found in Appendix C.4. Moreover, additional information about the $\underline{H}_{22}$ of the CGS considering a stabilization capacitor with C_{st} and a stabilization resistor with R_{st} can be found in Appendix B.3.

5.1.4 Noise

Besides the small-signal gain and the maximum operating frequency of an active device, the noise performance is another very important key-parameter in PAs. In [13, 143], the noise performance of the CSS and the CC are compared. The following information are obtained from [143] and are summarized in this subsection. Fig. 5.1.5 shows the noise model of the CSS, based on Van der Ziel's noise model for FETs presented in [31].
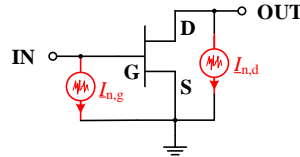
Figure 5.1.5: CSS with noise sources [31, 143].

The noise model in Fig. 5.1.5 comprises the following two correlated noise currents:

- $\underline{I}_{\mathrm{n,d}}$ represents the thermal channel noise of the conducting channel of the FET.
- $\underline{I}_{\mathrm{n,g}}$ represents the induced gate noise, which is caused by the capacitive coupling between the channel noise and the gate of the FET.

Using the noise representation shown in Fig. 2.4.3c, the equivalent input noise sources with $\underline{I}_{\mathrm{n}}$ and $\underline{V}_{\mathrm{n}}$ of the CSS can be calculated to [143]

$$\underline{I}_{\mathrm{n,CSS}} = \frac{\underline{Y}_{11,\mathrm{CSS}}}{\underline{Y}_{21,\mathrm{CSS}}}\underline{I}_{\mathrm{n,d}} - \underline{I}_{\mathrm{n,g}} \tag{5.1.20}$$

$$\underline{V}_{\mathrm{n,CSS}} = \frac{1}{\underline{Y}_{21,\mathrm{CSS}}}\underline{I}_{\mathrm{n,d}}\,. \tag{5.1.21}$$

The correlation factor γ can be calculated by using the eq. (2.4.10).

Fig. 5.1.6 shows the CC with four noise sources, since the CC consists of two stages, the CSS and the CGS. The two noise sources of each stage (CSS, CGS) are correlated with each other due to the fact that they have the same noise origin.

(a) CC with four noise current sources.   (b) CC with recalculated noise sources.
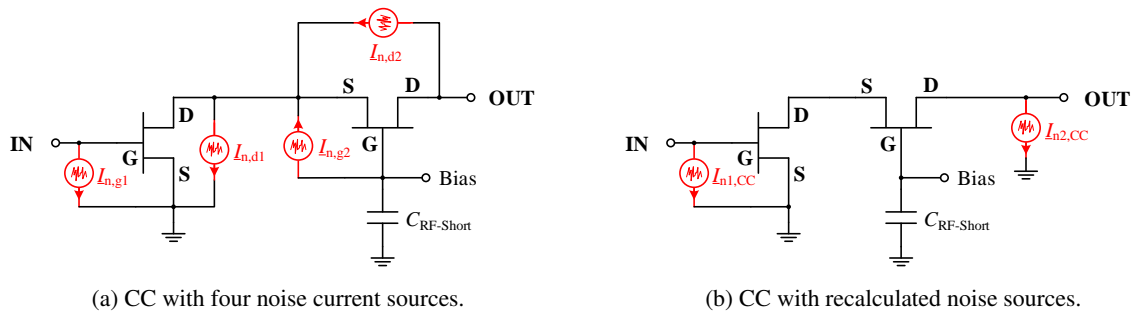
Figure 5.1.6: CC with noise sources [98].

The four noise sources of the CC shown in Fig. 5.1.6a can be recalculated into two noise sources, one at the input and one at the output of the CC shown in Fig. 5.1.6b. The equivalent noise sources with $\underline{I}_{\text{n1,CC}}$ and $\underline{I}_{\text{n2,CC}}$ can be determined to

$$\underline{I}_{\text{n1,CC}} = \underline{I}_{\text{n,g1}} + \frac{\underline{Y}_{12,\text{CSS}} \underline{H}_{11,\text{CGS}}}{1 + \underline{Y}_{22,\text{CSS}} \underline{H}_{11,\text{CGS}}} \left(-\underline{I}_{\text{n,d1}} + \underline{I}_{\text{n,g2}} + \underline{I}_{\text{n,d2}} \right) \tag{5.1.22}$$

$$\underline{I}_{\text{n2,CC}} = \underline{I}_{\text{n,d2}} + \frac{\underline{H}_{21,\text{CGS}}}{1 + \underline{Y}_{22,\text{CSS}} \underline{H}_{11,\text{CGS}}} \left(-\underline{I}_{\text{n,d1}} + \underline{I}_{\text{n,g2}} + \underline{I}_{\text{n,d2}} \right) . \tag{5.1.23}$$

Inserting eq. (5.1.22) and eq. (5.1.23) into eq. (5.1.20) and eq. (5.1.21), the equivalent input noise sources with $\underline{I}_{\text{n}}$ and $\underline{V}_{\text{n}}$ of the CC, using the noise representation shown in Fig. 2.4.3c, can be calculated to [143]

$$\underline{I}_{\text{n,CC}} = \underline{I}_{\text{n,CSS}} - \frac{\underline{Y}_{11,\text{CSS}}}{\underline{Y}_{21,\text{CSS}}} \left(\underline{I}_{\text{n,g2}} + \left[1 + \frac{1 + \underline{H}_{22,\text{CSS}} \underline{H}_{11,\text{CGS}}}{\underline{H}_{21,\text{CGS}}} \right] \underline{I}_{\text{n,d2}} \right) \tag{5.1.24}$$

$$\underline{V}_{\text{n,CC}} = \underline{V}_{\text{n,CSS}} - \frac{1}{\underline{Y}_{21,\text{CSS}}} \left(\underline{I}_{\text{n,g2}} + \left[1 + \frac{1 + \underline{Y}_{22,\text{CSS}} \underline{H}_{11,\text{CGS}}}{\underline{H}_{21,\text{CGS}}} \right] \underline{I}_{\text{n,d2}} \right) . \tag{5.1.25}$$

The degradation of the noise parameters of the CC can be seen by comparing the recalculated input noise parameters of the CSS, eq. (5.1.20) and eq. (5.1.21), and the CC, eq. (5.1.24) and eq. (5.1.25), with each other. The $\left| \underline{I}_{\text{n,CC}} \right|$ and $\left| \underline{V}_{\text{n,CC}} \right|$ is always higher than the $\left| \underline{I}_{\text{n,CSS}} \right|$ and $\left| \underline{V}_{\text{n,CSS}} \right|$, respectively due to the additional noise current sources of the CGS. The influence of the CGS on the recalculated input noise parameters is summarized in the following:

- Ideal CGS ($\underline{H}_{11,\text{CGS}} \to 0$, $\underline{H}_{21,\text{CGS}} \to -1$):
    - The thermal channel noise of the CGS represented by $\underline{I}_{\text{n,d2}}$ has no effect on the noise parameters.
    - The induced gate noise of the CGS represented by $\underline{I}_{\text{n,g2}}$ dominates compared to $\underline{I}_{\text{n,d2}}$ and increases at higher frequencies. As a result the noise parameters of the CC become worse at higher frequencies compared to the CSS.
- Non-ideal CGS ($\underline{H}_{11,\text{CGS}} > 0$, $\underline{H}_{21,\text{CGS}} > -1$):
    - Noise parameters of the CC and the CSS are equal in case of a noiseless CGS.
    - If the CGS becomes non-ideal, the $\underline{I}_{\text{n,d}}$ of the CGS gets more dominant.
    - The noise of the CGS are reduced by the correlation between $\underline{I}_{\text{n,g1}}$ and $\underline{I}_{\text{n,g2}}$ depending on $\underline{H}_{11,\text{CGS}}$ and $\underline{H}_{21,\text{CGS}}$.
    - Usage of a stabilization capacitor with C_{st} in case of a modified CGS worsens the noise parameters, since the CGS becomes even more non-ideal (higher $\underline{H}_{11,\text{CGS}}$).

Further information regarding the recalculated noise sources can be found in Appendix C.5 including a stabilization capacitor with C_{st}.

5.2 Large-Signal Parameters

5.2.1 Maximum Output Power

Like the *MSG*, f_t, f_{max} are key parameters to describe the small-signal performance of an active device, the $P_{out,max}$ is an important large-signal figure of merit to emphasize the large-signal performance of an active device. In [10, 12, 144, 145, Table 5] the CC topology shows a superior behavior regarding the $P_{out,max}$ in contrast to the CS topology. As already mentioned in Sec. 4.3.1 the $P_{out,max}$ depends on different factors. Table 5.2.1 opposes the parameters which have an influence on the $P_{out,max}$ of the CSS and the CC.

Table 5.2.1: Parameters which have an influence on the $P_{out,max}$ of the CSS and the CC.

		Common-Source Stage	Cascode
	Quiescent Point	$Q\left(V_{DS}, I_{DS}\right)$	$Q_1\left(V_{DS1}, I_{DS}\right), Q_2\left(V_{DS2}, I_{DS}\right)$
$\widehat{V}_{ds,max}$	Breakdown Voltage	V_{BR}	$V_{BR1} + V_{BR2}$
	Knee Voltage	V_{KNEE}	$V_{KNEE1} + V_{KNEE2}$
$\widehat{I}_{ds,max}$	Maximum DC Current I_{GS}	I_{GS}	I_{GS1}, I_{GS2}
	Maximum T_j	$T_{j,max}$	$T_{j,max1}, T_{j,max2}$
	Load Impedance	$\underline{Z}_{load}$	$\underline{Z}_{load1}, \underline{Z}_{load2}$

Comparing the parameters shown in Table 5.2.1 of the CSS and the CC, the following properties can be determined:

- Quiescent point of the single CSS and the CC can be chosen equal. As a result the maximum *PAE* of both topologies does not differ from each other.
- $\widehat{V}_{ds,max}$ of the CC which depends on the V_{BR} and the V_{KNEE} of each stage is much higher compared to the CSS due to the fact that the $V_{BR,CC} = 2 \cdot V_{BR,CSS}$.
- $\widehat{I}_{ds,max}$ of both topologies are equal because the same I_{ds} of the CSS flows through the CGS of the CC.
- $T_{j,max}$ of the CSS and the CC are defined by the process and are equal to each other. However, to achieve the same T_j and as a result the same *MTTF* of each single active device, the backside temperature of the CC has to be sightly smaller due to the thermal coupling between the CSS and the CGS (especially in dual-gate FETs). Another possibility is to reduce the power density of the CC which results in a reduced P_{out}.
- The $\underline{Z}_{load,opt}$ of both topologies are very different since the overall $\underline{Z}_{load}$ of the CC is a combination of the $\underline{Z}_{load}$ of the CSS and the $\underline{Z}_{load}$ of the CGS. In case of the classical CC the $\underline{Z}_{load}$ of the CSS is very low and as a result the maximum allowed V_{ds} is not used which leads to a lower output power. The modified CC increases the $\underline{Z}_{load}$ with decreasing C_{st} which improves the power transfer from the CSS to the CGS.

As a result, the CC can achieve a higher P_{out} in contrast to the CSS especially using the modified CC. Further advantages of the CC due to the higher V_{BR} and higher P_{out} can be found in Sec. 5.3

5.2.2 Power Compression

Power compression is a fundamental characteristic of PAs. As mentioned in the previous Sec. 4.3.2 the intrinsic large-signal elements $G_m\left(V_{GS}, V_{GD}\right)$, $C_{gs}\left(V_{GS}, V_{GD}\right)$ and $C_{gd}\left(V_{GS}, V_{GD}\right)$ reflect the compression of an amplifier in a first approximation using the simplified LSM shown in Fig. 4.3.5. The compression also depends on the $\underline{Z}_{load}$ at the output of an amplifier. Matching networks to achieve the $P_{out,max}$ differs from networks to achieve maximum bandwidth and gain. It is a trade-off between maximum bandwidth

and power match. In optimized small-signal matched designs it is not possible to achieve simultaneously a power match over the complete frequency range which can be traced back to the theory stated in [18–25]. Improving the small-signal RF-performance of multi-decade broadband PAs —i.e. traveling-wave amplifiers (TWAs) or FBAs— by using CCs to increase the bandwidth, the compression point usually decreases over frequency and deteriorates significantly near the band edge. This large-signal behavior in multi-decade PAs using the CC topology can be detected in several different papers in literature ([11, 13, 15, 16, 143, 144, 146, 147] using the GaN technology), as well as in commercial products ([148–150] using the GaAs technology), illustrated in Fig. 5.2.1.
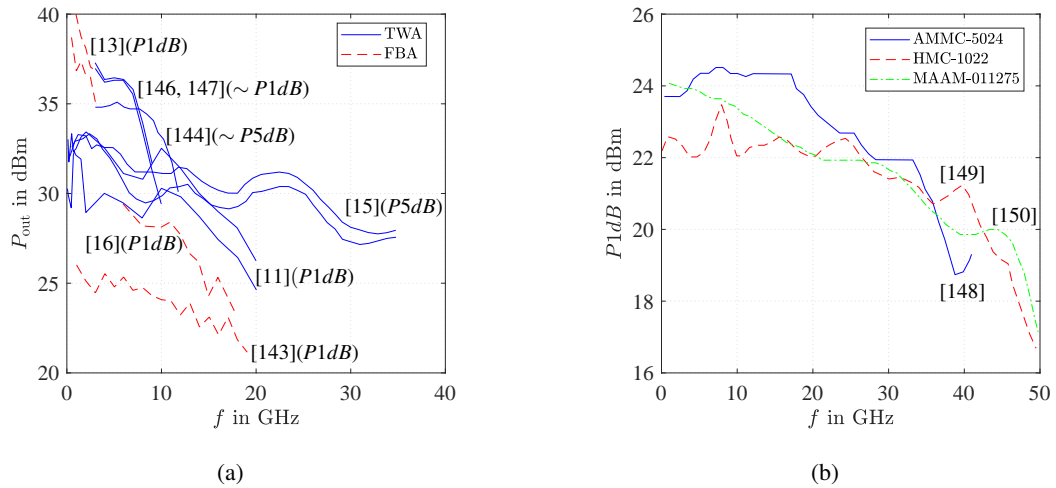
Figure 5.2.1: Power compression versus frequency of multi-decade GaN PAs in CC topology [11, 13, 15, 16, 143, 144, 146–151]. (a) Publications. (b) Commercial products.

Compared to the CC topology the $P1dB$ characteristic of the CS amplifier is usually very flat over the complete bandwidth. In this subsection the main origin of the power degradation of CCs in broadband PAs is explained and illustrated based on the simulation results of a broadband FBA in CS and CC topology.

5.2.2.1 Compression of the Common-Source Stage

Considering a G_m compression of the CSS and the CGS (neglecting the non-linearity of the capacitors with C_{gs} and C_{gd}), Fig. 5.2.2 shows the $\widehat{V}_{gs}$ at the input of the CSS of the CS-FBA and the CC-FBA. Fig. 5.2.3 shows the gain of the CC topology for different G_m compression values of the CSS. Both topologies (CS-FBA, CC-FBA) have similar input voltage swings at the CSS (Fig. 5.2.2), which are almost constant over frequency. In conjunction with having equal CS devices with the same bias conditions in both designs, the G_m compression of the CSS is similar and independent of frequency. Lowering the G_m compression of the CSS by reducing the non-linearity of the G_m curve, the gain (Fig. 5.2.3) and, as a result, $P1dB$ increases. The gain improvement is almost constant over the complete frequency range. Therefore $P1dB$ is also constant.
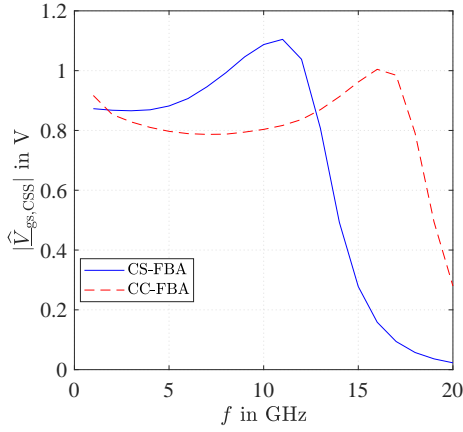
Figure 5.2.2: $\widehat{V}_{\text{gs,CSS}}$ of the CS-FBA and CC-FBA [98].
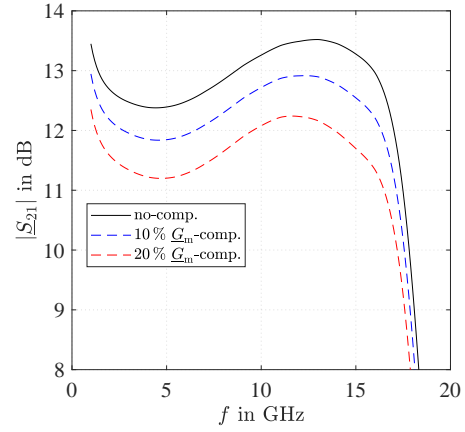
Figure 5.2.3: $|\underline{S}_{21}|$ of the CC-FBA for different G_m compressions of the CSS [98].

5.2.2.2 Compression of the Common-Gate Stage

Fig. 5.2.4 shows the $\widehat{V}_{\text{gs}}$ of the CGS, which is almost constant over the complete bandwidth. This fact leads to the conclusion that the G_m compression of the CGS is also independent of frequency. Fig. 5.2.5 shows the gain of the CC topology for different G_m compression values of the CGS. Lowering the G_m compression of the CGS by reducing the non-linearity of the G_m curve, the gain and as a result the $P1dB$ increases slightly at low frequencies but significantly at higher frequencies.
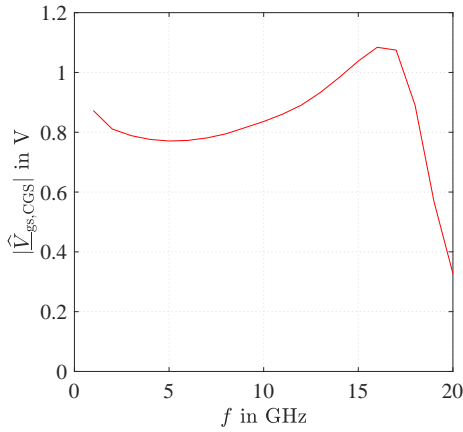
Figure 5.2.4: $\widehat{V}_{\text{gs,CGS}}$ of the CC-FBA [98].
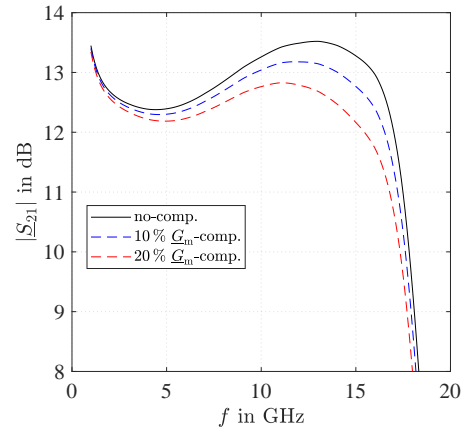
Figure 5.2.5: $|\underline{S}_{21}|$ of the CC-FBA for different G_m compressions of the CGS [98].

Therefore, besides the load mismatch of the CSS, the compression of the CGS is one of the main reasons for the decreasing $P1dB$ at high frequencies in optimized small-signal matched CC designs. Of course the exact behavior of the compression depends on the exact compression and the design itself. However, achieving a large bandwidth and simultaneously small-signal matching, the $P1dB$ of the CC topology typically degrades at higher frequencies. If the G_m compression can be reduced by reducing the non-linearity of the G_m curve of the CGS of the CC topology, the $P1dB$ will improve at higher frequencies. A new concept which deals with this problem is presented in Ch. 6.

5.3 Summary

In Sec. 5.1 and Sec. 5.2 certain small- and large-signal parameters and their behavior of the CSS and the CC were opposed and are summarized in the following:

- Small-signal parameters: Y-parameters, MSG, $\underline{H}_{21}$ (linked to f_t), U (linked to f_{max}) and $\underline{I}_n$, $\underline{V}_n$
- Large-signal parameters: $P_{out,max}$ and power compression

Key findings:

Fig. 5.3 illustrates the advantages and disadvantages of the CC topology compared to the CSS on the device level and the system level.
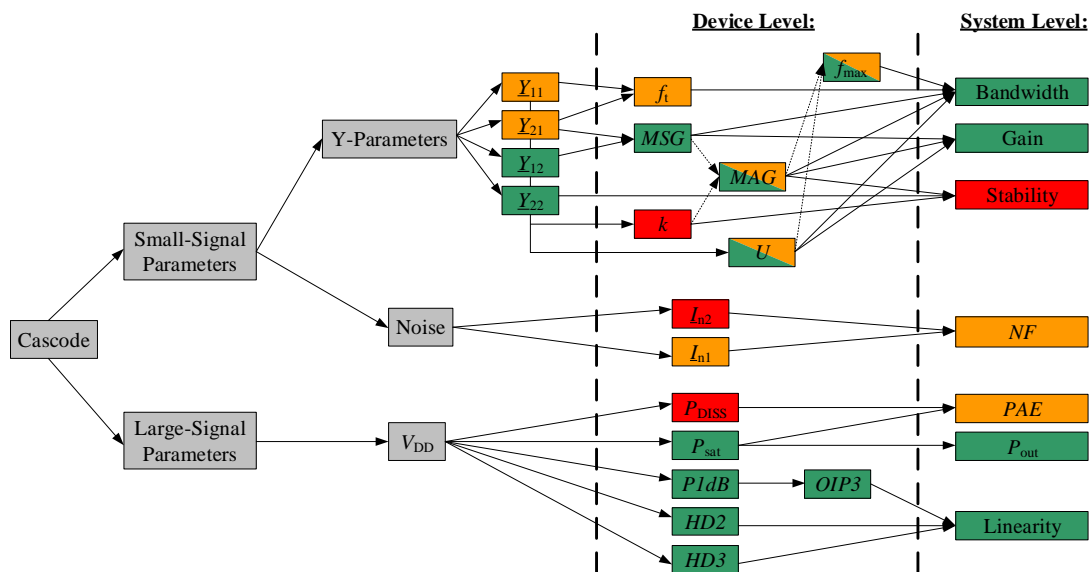
Figure 5.3.1: Advantages and disadvantages of the CC [13, 98].

Key advantages of the CC compared to the CSS:

- Small-signal gain and/or the overall bandwidth, i.e. of an broadband PA, can be significantly increased using the CC topology in contrast to the CSS. It is always a trade-off between bandwidth and gain improvement.
- Due to the higher V_{BR} the CC topology will offer a higher P_{out} compared to the CSS. As a result of the higher P_{out} the linearity improves as well due to the higher back-off. Therefore certain figure of merits increase like $HD2$, $HD3$, $P1dB$ and so on. Since the $OIP3$ and the $P1dB$ are linked together, expressed by eq. (2.3.10), the inter-modulation behavior improves also.

Key disadvantages of the CC compared to the CSS:

- Due to the fact that the conditional stability region of the MSG of the CCs is wider, the stability is more critical compared to the CSS.
- Although the P_{out} increases due to the higher allowed supply voltage, the PAE suffers a little bit since the P_{out} does not increase by the maximum theoretically possible factor.
- Furthermore, the reason of power degradation of CCs in broadband PAs at higher frequencies were discussed in-depth, which has its origin in the CGS of the CC cell.
- On the device level, the equivalent input noise expressed by $\underline{I}_n$ and $\underline{V}_n$ of the CC are worse. However, on the system level the noise performance of a broadband PA using CCs can be improved:
  - If the noise of the PA is dominated by the feedback resistance, the noise performance of the CC topology at the same gain is better compared to the CS topology.
  - If the internal noise is the dominant part of the noise of the PA, the noise performance of the CS topology is better compared to the CC topology.

6 New Cascode Concept

In this chapter a new concept is presented which can be used in CC designs, i.e. broadband PAs using a CC. This new concept is based on [26, 27] and has a similar structure to [28, 29]. However the functionality of the proposed concept is completely different. Three possibilities are introduced and explained in detail how this new concept can be used in broadband PAs. First the general principle of the new technique is explained. Afterwards advantage and disadvantage of the new concept are discussed depending on the realization of the new concept. At the end of this chapter a short summary is given to point out the advantages and disadvantages of the new concept to give some key findings.

6.1 General Principle

Using CCs in broadband PAs, an additional stabilization capacitor with C_{st} and stabilization resistor with R_{st} are added in the gate path of the CGS of the CC [138]. The additional stabilization capacitor with C_{st} acts as a frequency independent voltage divider. As a result the effective $\underline{g}_m$ is reduced, which can be expressed at low frequencies by eq. (4.2.12):

$$\underline{g}_{m,eff} = g_m \cdot \left(\frac{C_{st}}{C_{st} + C_{gs} + C_{gd}} \right) . \tag{6.1.1}$$

Due to the fact that the effective C_{gs}, C_{gd} and C_{ds} is also changed, which can be seen in eq. (4.2.9)– eq. (4.2.11), the electrical behavior of the CGS is very different to the classical CGS. Therefore, the stabilization capacitor with C_{st} can be used to change the electrical performance of the CGS in a certain manner to achieve a required electrical behavior. However, if the C_{st} is chosen, the value is fixed in the modified CC and as a result the electrical behavior.

The new concept replaces the CSC with C_{st}, shown in Fig. 6.1.1a, by a VASC with $C_{st,var}$, shown in Fig. 6.1.1b. This new technique allows to change the electrical behavior of the CGS by changing the absolute value as well as the electrical characteristic (capacitive voltage-dependency) of the $C_{st,var}$, i.e. by an external voltage.
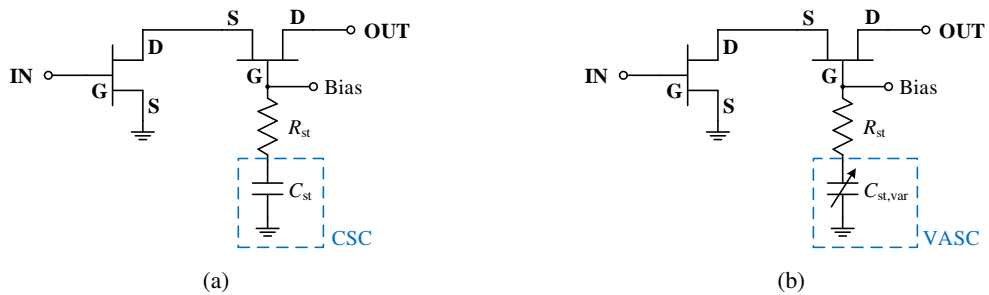
Figure 6.1.1: Modified CC with (a) a CSC and (b) a VASC [98].

The $C_{st,var}$ has influence on small-signal performance of the CGS and therefore of the CC. The large-signal operation of the CC depends on the absolute value and on the electrical characteristic of the $C_{st,var}$ of the VASC. Therefore this technique allows to improve and modify three fundamental key-parameters of broadband PAs using a CC:

- Controlling the $\underline{S}_{21}$ at higher frequencies.
- Improving the compression behavior ($P1dB$).
- Improving the linearity ($HD2$, $HD3$, $OIP3$).

The improvement depends on capacitive voltage-dependency of the $C_{\text{st,var}}$ of the VASC. The following section shows different possibilities to realize a VASC with different voltage-dependencies to point out the advantages and disadvantages.

6.2 Implementation

The VASC can be realized i.e. by a varactor diode. In case that a varactor diode is not available in every process a transistor can also be used as a varactor diode to realize a VASC (i.e. in [152] a HEMT is used as an anti-series varactor diode which achieves a tuning ratio of 4.7 and a maximum quality factor of 130). In general the following advantages and disadvantages can be obtained using a varactor diode or a transistor as a VASC:

- Advantage:
  - simple circuit design
  - gain and stability can be controlled at high frequencies
  - automatic gain control is possible
  - no change of class operation of the broadband PA
- Disadvantage:
  - additional harmonics are generated due to nonlinear capacitance $C_{\text{st,var}}$
  - higher gain reduces stability
  - additional noise due to the active device
  - additional bias is needed
  - a DC blocking capacitor is needed on-chip (size of cap can be relatively large, depending on the lower cut-off frequency)

Fig. 6.2.1b shows the gate to source and drain capacitance $C_{\text{gs}\|\text{gd}}$ (sum of the parallel capacitances C_{gs} and C_{gd}) of a certain transistor, depending on the applied DC voltage. Since the value of the capacitance can be adjusted by the DC voltage, the transistor behaves like a varactor diode, shown in Fig. 6.2.1a. The large-signal behavior regarding the harmonics differs for different DC quiescent points.

(a) Single transistor as a varactor diode.

(b) Voltage dependency of $C_{\text{gs}\|\text{gd}}$.
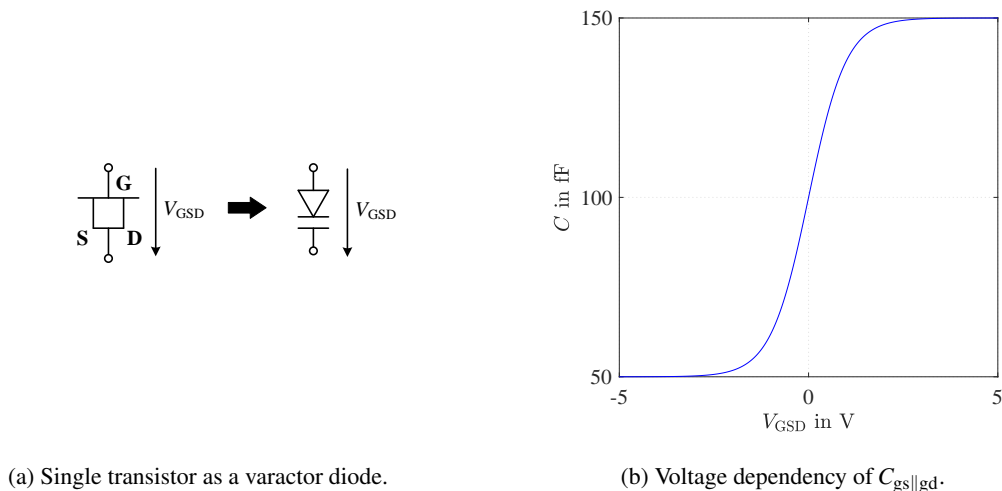
Figure 6.2.1: Single transistor as VASC.

To achieve a certain voltage dependency of the $C_{\text{st,var}}$ and to keep the circuit complexity simple, two varactor diodes (realized by two transistors) can be interconnected in different ways with each other.

There are several possibilities to arrange one or two varactor diodes to achieve a certain behavior of the VASC with $C_{st,var}$. In Fig. 6.2.2–Fig. 6.2.9 the principle arrangements and the corresponding circuit realization (schematic and layout) of the VASC are shown. It can be seen in case of two diodes the realization of the VASC gets a little bit more complicated to bias the two diodes independently of each other.

(a) Principle realization of VASC.

(b) Detailed schematic of VASC.
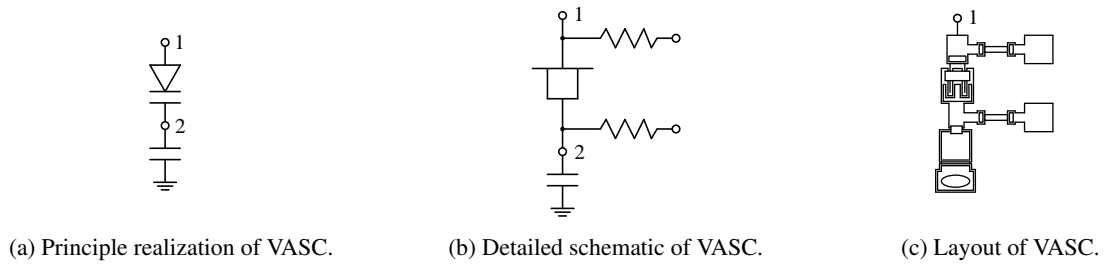
(c) Layout of VASC.

Figure 6.2.2: (a) Principle arrangement and the corresponding circuit realization, (b) schematic and (c) layout of one varactor diode (direction: down) as VASC.

(a) Principle realization of VASC.

(b) Detailed schematic of VASC.
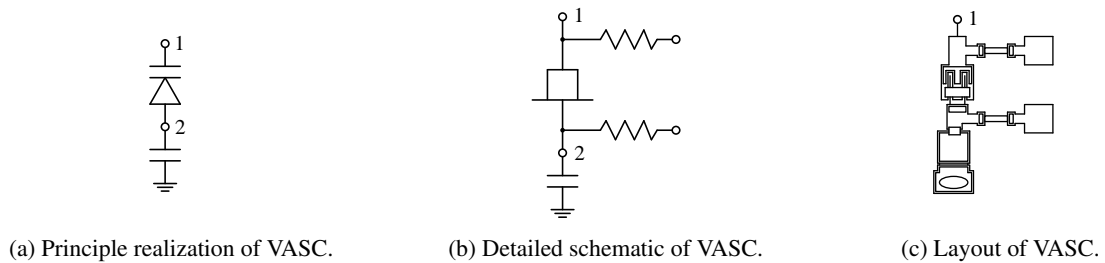
(c) Layout of VASC.

Figure 6.2.3: (a) Principle arrangement and the corresponding circuit realization, (b) schematic and (c) layout of one varactor diode (direction: up) as VASC.

(a) Principle realization of VASC.

(b) Detailed Schematic of VASC.
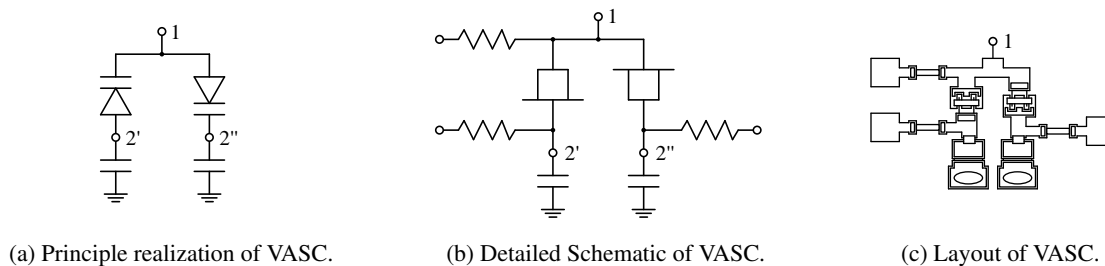
(c) Layout of VASC.

Figure 6.2.4: (a) Principle arrangement and the corresponding circuit realization, (b) schematic and (c) layout of two varactor diodes in parallel (direction: up&down) as VASC.

(a) Principle realization of VASC.

(b) Detailed Schematic of VASC.
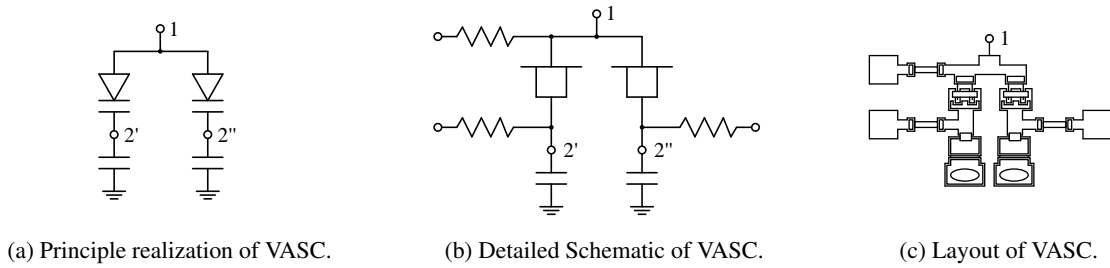
(c) Layout of VASC.

Figure 6.2.5: (a) Principle arrangement and the corresponding circuit realization, (b) schematic and (c) layout of two varactor diodes in parallel (direction: down&down) as VASC.

(a) Principle realization of VASC.

(b) Detailed Schematic of VASC.
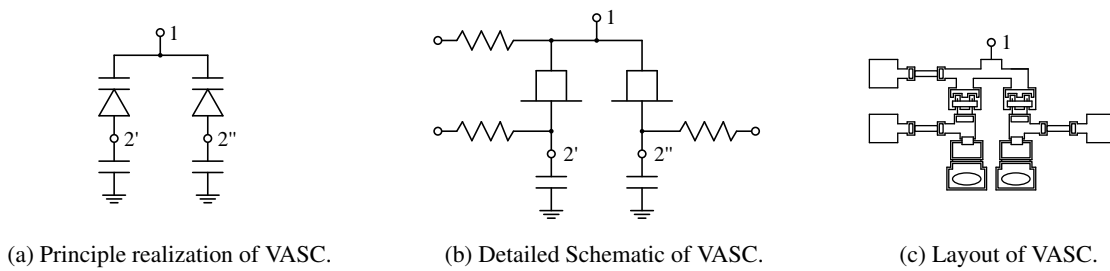
(c) Layout of VASC.

Figure 6.2.6: (a) Principle arrangement and the corresponding circuit realization, (b) schematic and (c) layout of two varactor diodes in parallel (direction: up&up) as VASC.

(a) Principle realization of VASC.

(b) Detailed Schematic of VASC.
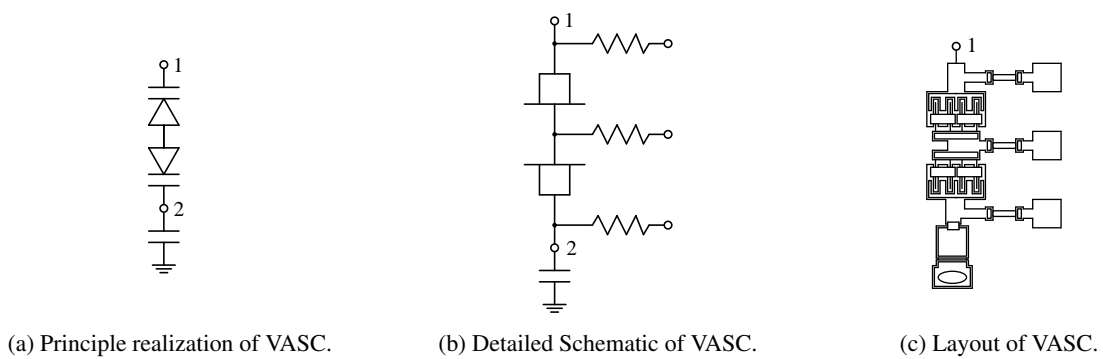
(c) Layout of VASC.

Figure 6.2.7: (a) Principle arrangement and the corresponding circuit realization, (b) schematic and (c) layout of two varactor diodes in series (direction: up&down) as VASC.

(a) Principle realization of VASC.

(b) Detailed Schematic of VASC.
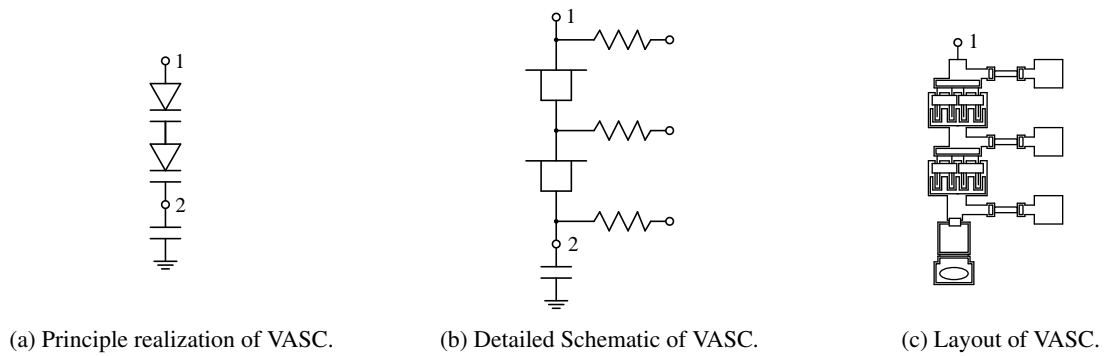
(c) Layout of VASC.

Figure 6.2.8: (a) Principle arrangement and the corresponding circuit realization, (b) schematic and (c) layout of two varactor diodes in series (direction: down&down) as VASC.

(a) Principle realization of VASC.

(b) Detailed Schematic of VASC.
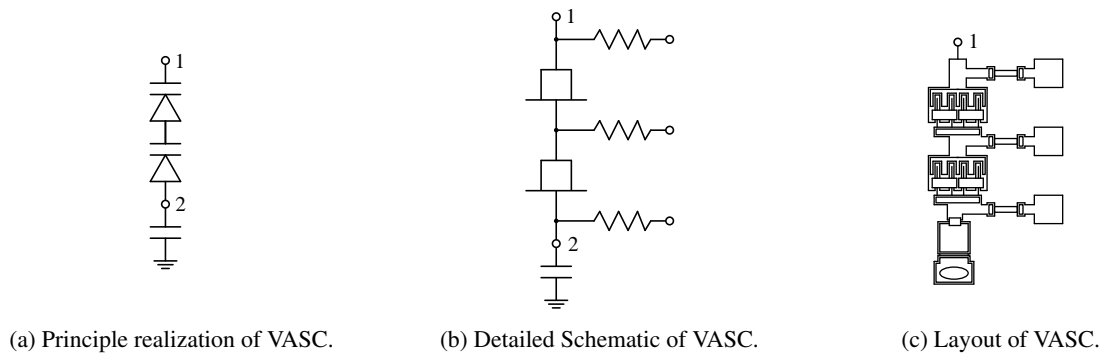
(c) Layout of VASC.

Figure 6.2.9: (a) Principle arrangement and the corresponding circuit realization, (b) schematic and (c) layout of two varactor diodes in series (direction: up&up) as VASC.

The voltage dependency of the $C_{st,var}$ is fixed for the single diode, shown in Fig. 6.2.10 and Fig. 6.2.11. However for the two diodes the voltage dependency can be adjusted by the applied DC voltage. Fig. 6.2.12, Fig. 6.2.14 and Fig. 6.2.16 show different voltage dependencies for different DC quiescent points for two diodes in parallel. The second and third derivative of $C_{st,var}$ for two diodes in parallel are shown in Fig. 6.2.13, Fig. 6.2.15 and Fig. 6.2.17. The voltage dependencies for different DC quiescent points for two diodes in series are illustrated in Fig. 6.2.18, Fig. 6.2.20 and Fig. 6.2.22. The second and third derivative of $C_{st,var}$ for two series diodes are shown in Fig. 6.2.19, Fig. 6.2.21 and Fig. 6.2.23.

(a) Varactor arrangement.

(b) Voltage dependency of $C_{st,var}$.

(c) First and second derivative of $C_{st,var}$.
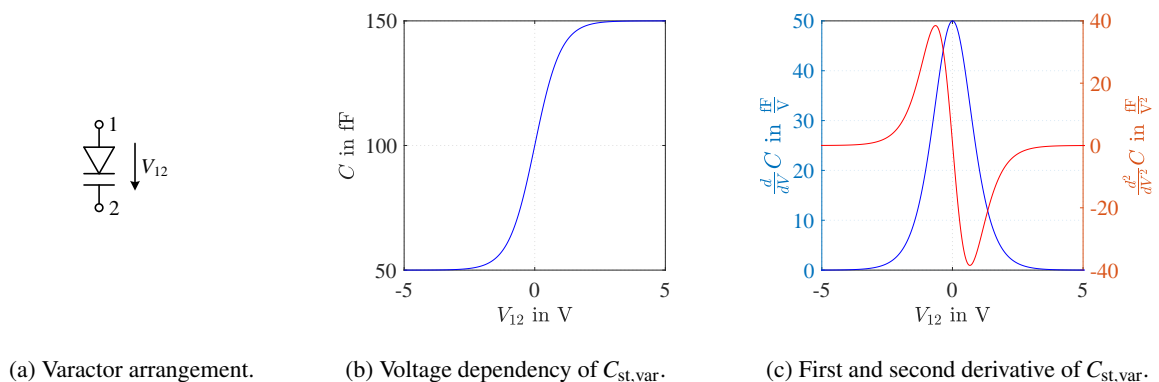
Figure 6.2.10: (a) Principle arrangement, (b) the corresponding voltage dependency and (c) the corresponding first and second derivative of one varactor diode (direction: down) as VASC.

(a) Varactor arrangement.   (b) Voltage dependency of $C_{st,var}$.   (c) First and second derivative of $C_{st,var}$.
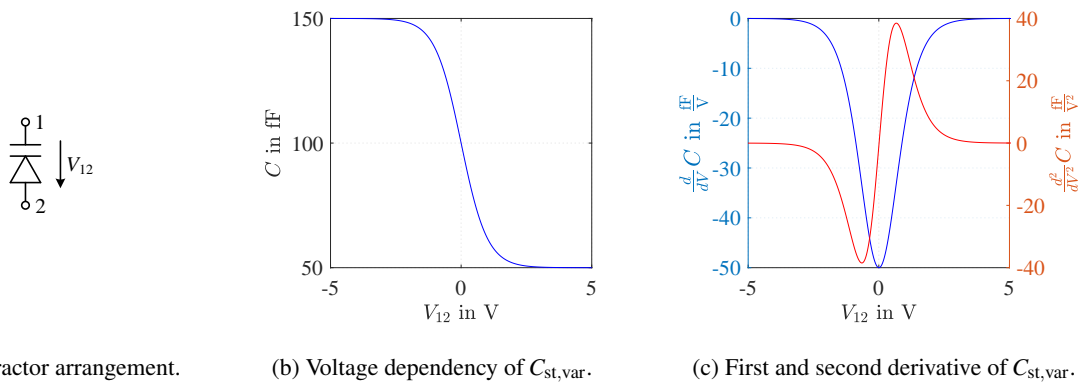
Figure 6.2.11: (a) Principle arrangement, (b) the corresponding voltage dependency and (c) the corresponding first and second derivative of one varactor diode (direction: up) as VASC.

(a) Varactor arrangement.   (b) Certain quiescent points of VASC.   (c) Voltage dependency of $C_{st,var}$.
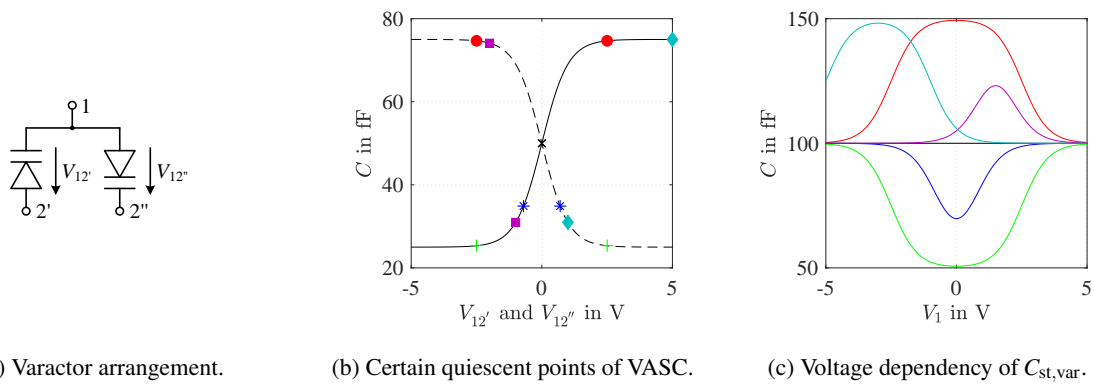
Figure 6.2.12: (a) Principle arrangement, (b) certain quiescent points and (c) the corresponding voltage dependency of two varactor diodes in parallel (direction: up&down) as VASC.

(a) Certain quiescent points of VASC.   (b) First derivative of $C_{st,var}$.   (c) Second derivative of $C_{st,var}$.
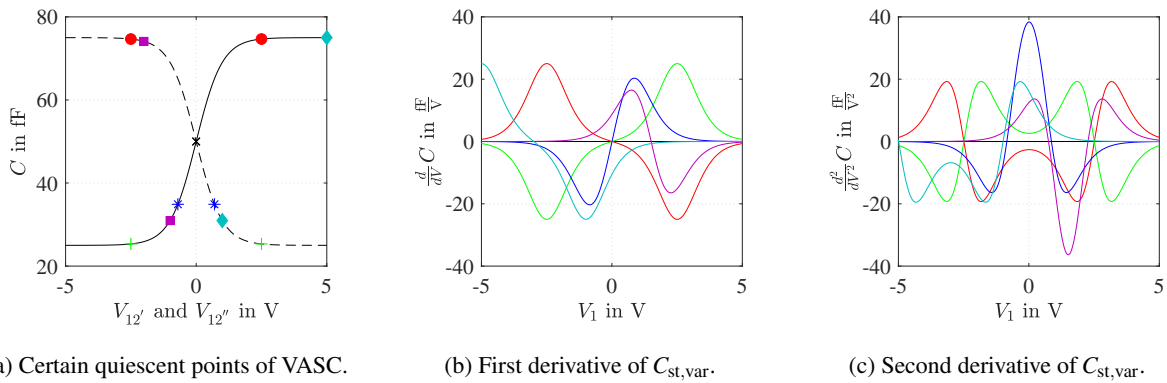
Figure 6.2.13: (a) Certain quiescent points and the corresponding (b) first derivative and (c) second derivative of two varactor diodes in parallel (direction: up&down) as VASC.

(a) Varactor arrangement.

(b) Certain quiescent points of VASC.

(c) Voltage dependency of $C_{\mathrm{st,var}}$.
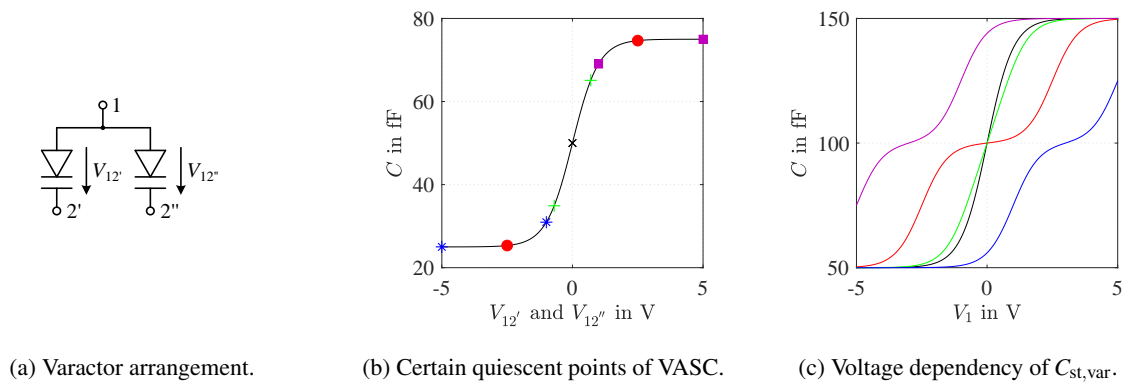
Figure 6.2.14: (a) Principle arrangement, (b) certain quiescent points and (c) the corresponding voltage dependency of two varactor diodes in parallel (direction: down&down) as VASC.

(a) Certain quiescent points of VASC.

(b) First derivative of $C_{\mathrm{st,var}}$.

(c) Second derivative of $C_{\mathrm{st,var}}$.
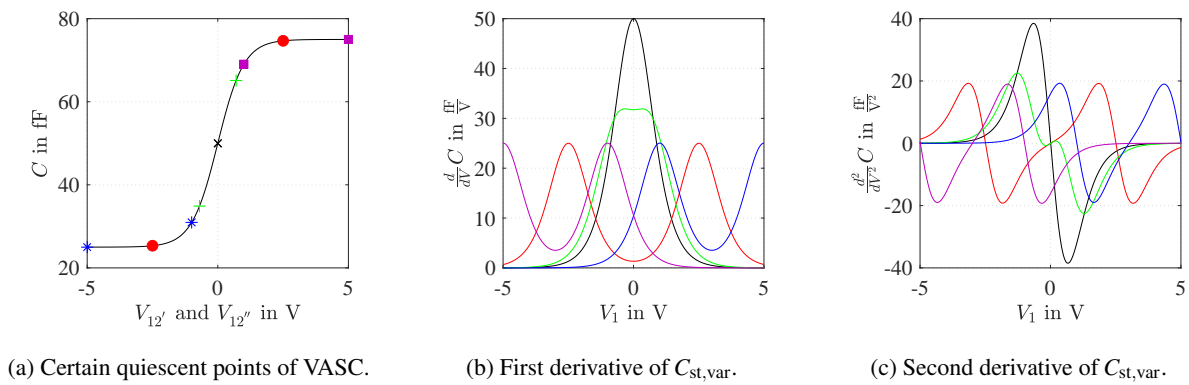
Figure 6.2.15: (a) Certain quiescent points and the corresponding (b) first derivative and (c) second derivative of two varactor diodes in parallel (direction: down&down) as VASC.

(a) Varactor arrangement.

(b) Certain quiescent points of VASC.

(c) Voltage dependency of $C_{\mathrm{st,var}}$.
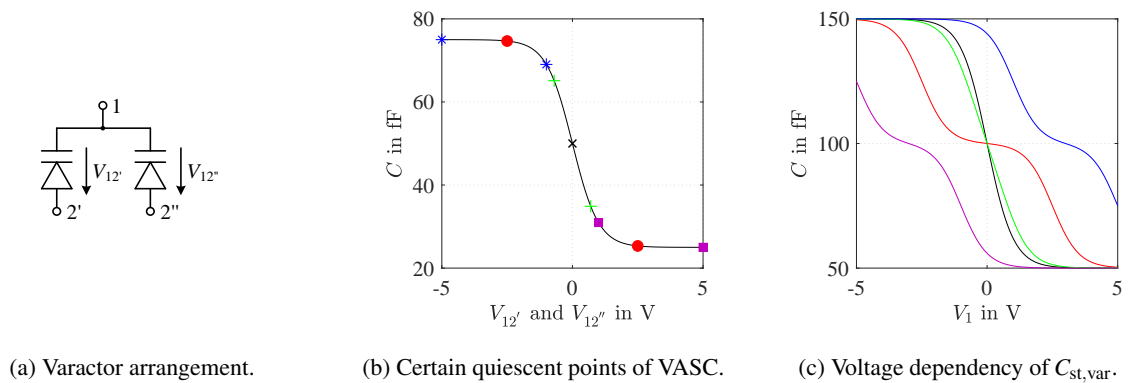
Figure 6.2.16: (a) Principle arrangement, (b) certain quiescent points and (c) the corresponding voltage dependency of two varactor diodes in parallel (direction: up&up) as VASC.

(a) Certain quiescent points of VASC.

(b) First derivative of $C_{st,var}$.

(c) Second derivative of $C_{st,var}$.
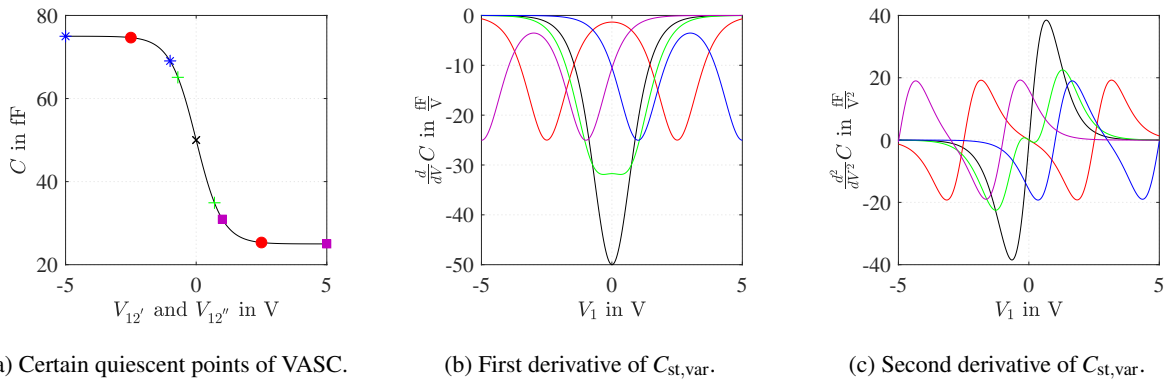
Figure 6.2.17: (a) Certain quiescent points and the corresponding (b) first derivative and (c) second derivative of two varactor diodes in parallel (direction: up&up) as VASC.

(a) Varactor arrangement.

(b) Certain quiescent points of VASC.

(c) Voltage dependency of $C_{st,var}$.
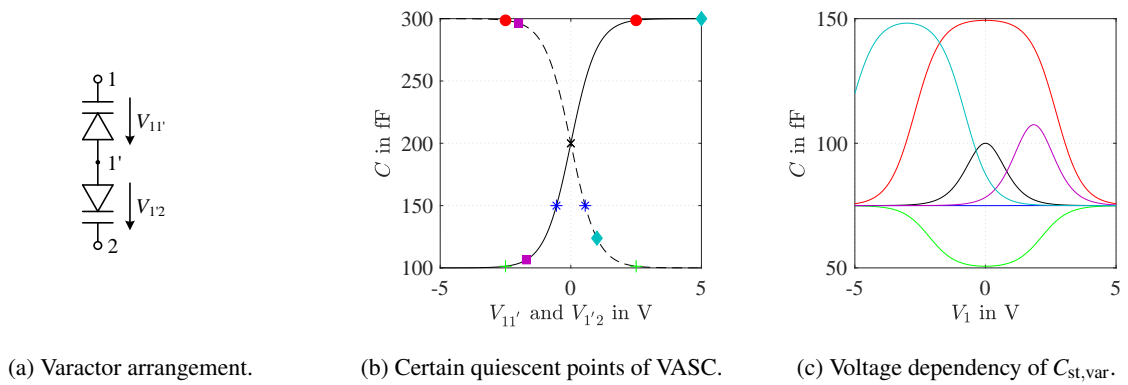
Figure 6.2.18: (a) Principle arrangement, (b) certain quiescent points and (c) the corresponding voltage dependency of two varactor diodes in series (direction: up&down) as VASC.

(a) Certain quiescent points of VASC.

(b) First derivative of $C_{st,var}$.

(c) Second derivative of $C_{st,var}$.
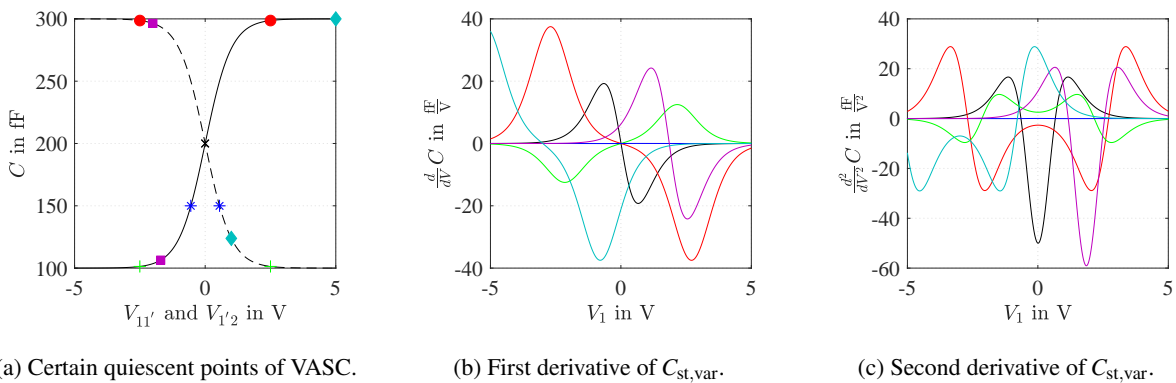
Figure 6.2.19: (a) Certain quiescent points and the corresponding (b) first derivative and (c) second derivative of two varactor diodes in series (direction: up&down) as VASC.

(a) Varactor arrangement.

(b) Certain quiescent points of VASC.

(c) Voltage dependency of $C_{st,var}$.
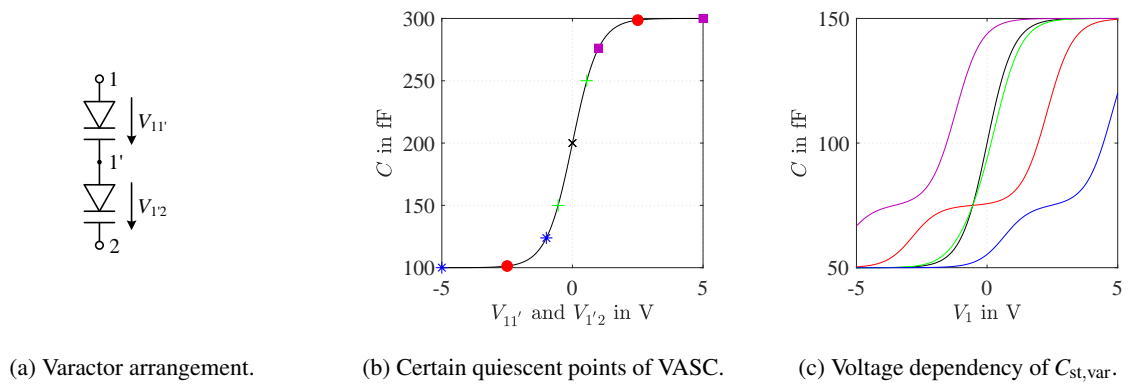
Figure 6.2.20: (a) Principle arrangement, (b) certain quiescent points and (c) the corresponding voltage dependency of two varactor diodes in series (direction: down&down) as VASC.

(a) Certain quiescent points of VASC.

(b) First derivative of $C_{st,var}$.

(c) Second derivative of $C_{st,var}$.
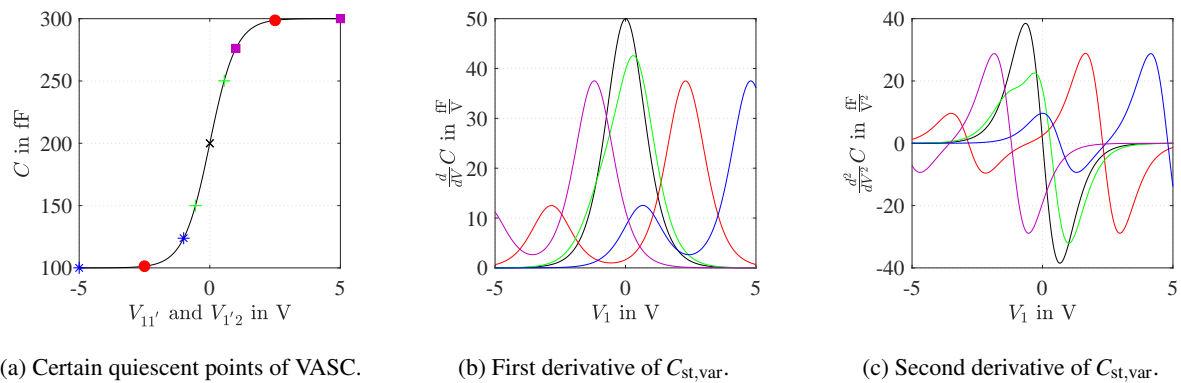
Figure 6.2.21: (a) Certain quiescent points and the corresponding (b) first derivative and (c) second derivative of two varactor diodes in series (direction: down&down) as VASC.

(a) Varactor arrangement.

(b) Certain quiescent points of VASC.

(c) Voltage dependency of $C_{st,var}$.
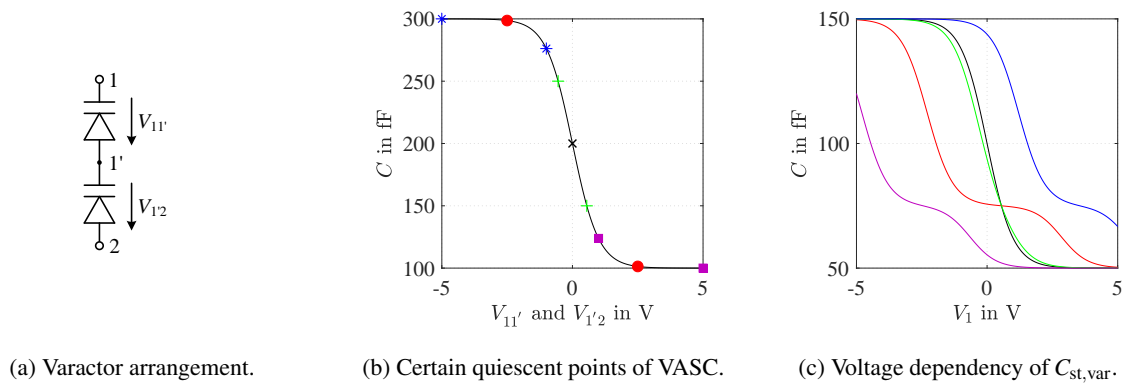
Figure 6.2.22: (a) Principle arrangement, (b) certain quiescent points and (c) the corresponding voltage dependency of two varactor diodes in series (direction: up&up) as VASC.

(a) Certain quiescent points of VASC.   (b) First derivative of $C_{st,var}$.   (c) Second derivative of $C_{st,var}$.
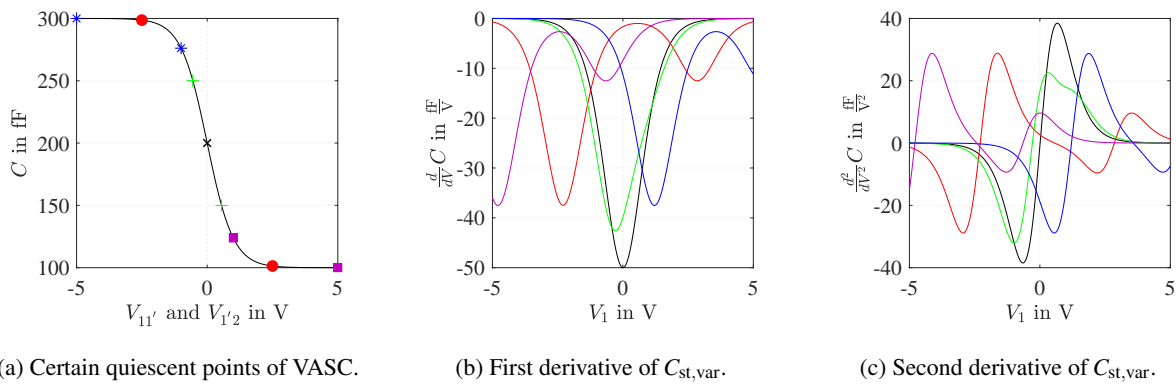
Figure 6.2.23: (a) Certain quiescent points and the corresponding (b) first derivative and (c) second derivative of two varactor diodes in series (direction: up&up) as VASC.

The proposed structures can improve certain parameters in broadband PAs using CCs. Depending on the application the different realizations of the VASC with $C_{st,var}$ have different advantages and disadvantages which will be discussed in the following section.

6.3 Applications

As mentioned in the previous section the new concept can improve certain key-parameters of broadband PAs using CCs. The following section gives an overview and an idea how these parameters can be improved by the new concept and what are the trade-offs between the different realizations of the VASC.

6.3.1 Gain Control

First application of the new concept is to use the VASC with $C_{st,var}$ to control the gain $\underline{S}_{21}$ of broadband PAs using CCs at higher frequencies. The concept is based on [26, 27] which show the RF behavior of a dual-gate GaAs MESFET depending on the gate termination and DC potential of the second gate and propose the dual-gate MESFET to be very suited as automatic gain control in amplifiers. Fig. 6.3.1 shows the *MSG* of a modified CC using the new concept for different $C_{st,var}$. The *MSG* increases for higher $C_{st,var}$.

(a) *MSG* vs. frequency over C_{st} over frequency.   (b) *MSG* vs. C_{st} over frequency.
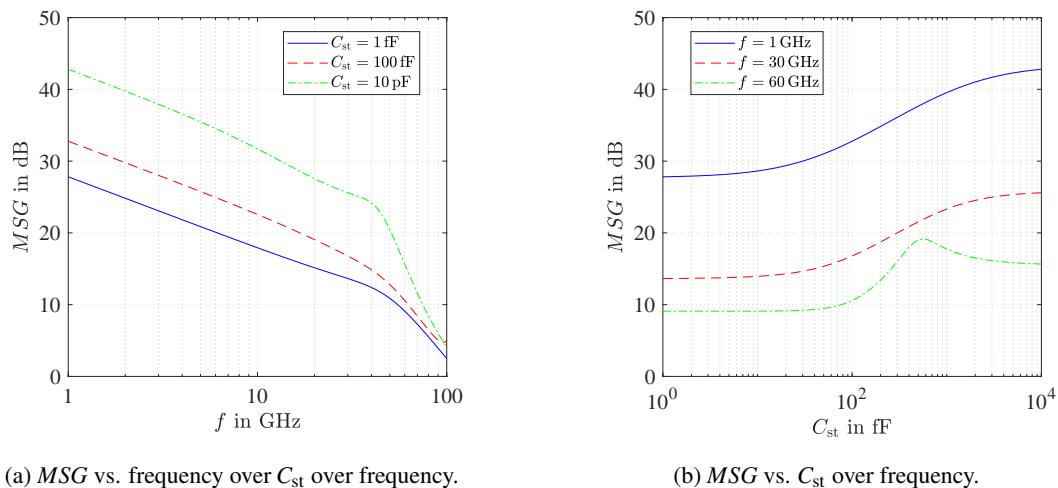
Figure 6.3.1: (a) and (b) *MSG* vs. frequency and vs. C_{st}, respectively, of the modified CC.

Fig. 6.3.2 shows the on-wafer measurement results of the $|\underline{S}_{21}|$ of the CC-FBAs using a CSC and a VASC. The black solid line in Fig. 6.3.2 shows the typical $\underline{S}_{21}$ of the CC-FBA using a CSC. Dashed lines in Fig. 6.3.2 show the $\underline{S}_{21}$ of the new CC-FBA using the new concept for different applied DC voltages at the VASC. For lower values of $C_{\text{st,var}}$ the $\underline{S}_{21}$ will degrade at higher frequencies and for higher values of $C_{\text{st,var}}$ the $\underline{S}_{21}$ will increase at higher frequencies. At low frequencies the $\underline{S}_{21}$ is defined by the parallel feedback resistor with resistance R_{fp}, therefore the VASC with $C_{\text{st,var}}$ has no influence on the $\underline{S}_{21}$ at low frequencies.
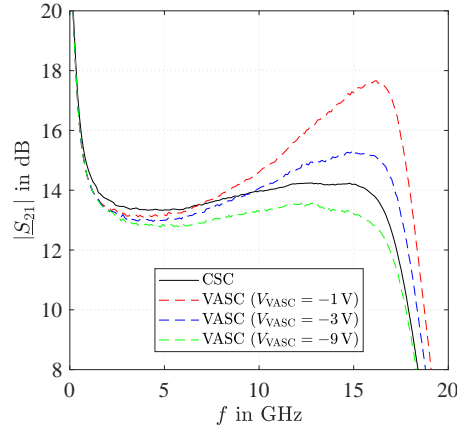
Figure 6.3.2: Measured $|\underline{S}_{21}|$ of the CC-FBAs ($V_{\text{DS}} = 20\,\text{V}$, $I_{\text{DSQ}} = 156\,\text{mA}$) using a CSC (solid line) and a VASC (dashed line) for different control-voltages of the VASC.

If the $\underline{S}_{21}$ is increased at higher frequencies the stability will degrade in this frequency range. Therefore it is a trade-off between stability and gain. As mentioned in the previous section, there are several different possibilities to realize a VASC.

To achieve a large dynamic range of the $\underline{S}_{21}$ of the CC-FBA without changing the large-signal behavior the VASC with $C_{\text{st,var}}$ has to full-fill some key-parameters:

- The $C_{\text{st,var}}$ should be able to be adjusted by an external DC-voltage in a large dynamic range.
- The voltage dependency of the $C_{\text{st,var}}$ should be as small as possible for a fixed applied external DC-voltage to avoid changes in the large-signal performance of the CC-FBA.

Using the structures, shown in Fig. 6.2.4–Fig. 6.2.9, the dynamic range depends on the chosen quiescent point of the two varactor diodes. The dynamic range is fixed using one varactor as VASC and is defined by the process. The only possibility to increase the dynamic range is to use switches in the circuit. Moreover, the different structures differ in the large-signal behavior. Comparing the varactor arrangements Fig. 6.2.10a and Fig. 6.2.11a, Fig. 6.2.14a and Fig. 6.2.16a and Fig. 6.2.20a and Fig. 6.2.22a with each other, the sign of the harmonic distortion of the second order and of the third order differs, which is shown in Fig. 6.2.10c, Fig. 6.2.11c, Fig. 6.2.15, Fig. 6.2.17, Fig. 6.2.21 and Fig. 6.2.23. To minimize any harmonics of the VASC with $C_{\text{st,var}}$ the varactor arrangement shown in Fig. 6.2.12a should be preferred. If the quiescent point of one diode is point-symmetrical to the quiescent point of the other diode, the harmonics of each diode cancel each other, shown in Fig. 6.2.12c. This concept was also used in [153] to cancel the non-linear C_{gs} of the CSS. A similar effect to minimize any harmonics occurs by choosing certain quiescent points for the varactor arrangement shown in Fig. 6.2.18a. Table 6.3.1 shows the advantages and disadvantages regarding the gain control of CC-FBA for different realization concepts.

Table 6.3.1: Advantages and disadvantages of the different structures to realize a VASC to control the gain of CCs.

Number		Complexity	Flexibility	Non-Linearity	Dynamic	Structure
Diodes	Bias Pads				Range	Ref.
1x	1x	low	low	high	high	Fig. 6.2.2
1x	1x	low	low	high	high	Fig. 6.2.3
2x	2x	high	high	low–medium	low–high	Fig. 6.2.4
2x	2x	high	medium	medium–high	medium–high	Fig. 6.2.5
2x	2x	high	medium	medium–high	medium–high	Fig. 6.2.6
2x	2x	high	high	low–medium	low–high	Fig. 6.2.7
2x	2x	high	medium	medium–high	medium–high	Fig. 6.2.8
2x	2x	high	medium	medium–high	medium–high	Fig. 6.2.9

6.3.2 Improved Compression

The second application of the new concept is to use the VASC with $C_{st,var}$ to improve the compression behavior ($P1dB$) at higher frequencies of broadband PAs using CCs. In principle the second application is a modification of the first one. Fig. 6.3.3 shows the on-wafer measurement results of the power compression of the CC-FBAs using a CSC and a VASC. Fig. 6.3.3a shows a typical $P1dB$ improvement of the new CC-FBA versus frequency. Fig. 6.3.3b shows a typical power compression characteristic versus P_{out} of the CC-FBAs using a CSC and a VASC.

(a) $P1dB$ vs. frequency.

(b) Normalized $Gain$ vs. P_{out}.
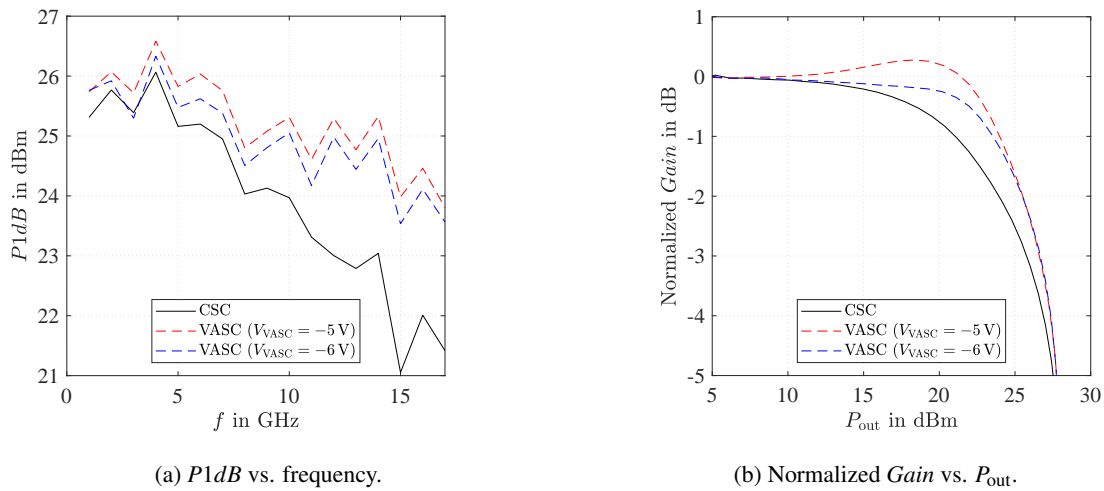
Figure 6.3.3: Measured $P1dB$ vs. frequency and normalized $Gain$ vs. P_{out} ($f = 15\,\text{GHz}$) of the CC-FBAs ($V_{DS} = 10\,\text{V}$, $I_{DSQ} = 104\,\text{mA}$) using a CSC (solid line) and a VASC (dashed line) for different control-voltages of the VASC.

There are two possibilities to use the new concept to improve the compression point:

- If the P_{out} increases, the external DC-voltage of the VASC is adjusted in such a way that the $C_{st,var}$ increases also. As a result the gain increases and therefore the $P1dB$.
- The effective $C_{st,var}$ increases with an increasing voltage drop at the VASC which also leads to a gain increase and as a result a better compression behavior.

Both concepts do not change any small-signal behavior of the CC. Since the first possibility needs a power detector at the output, which is a significant disadvantage, the circuit will no longer be investigated. The second possibility needs a certain voltage dependency of the $C_{st,var}$ to achieve a power compression improvement. As mentioned in the previous section, there are several different possibilities to realize a non-linear stabilization capacitor (NLSC) by a VASC with $C_{st,var}$. However, they can only be used in a certain quiescent point to improve the $P1dB$.

Using the structure shown in Fig. 6.3.4a and biasing the VASC at a low DC-voltage, the effective $C_{st,var}$ increases for a higher positive voltage swing at the source of the CGS illustrated in Fig. 6.3.4b and Fig. 6.3.4c. As a result the positive voltage swing at the CGS increases, shown by the source, gate and source-gate voltage at the CGS ($v_{s,CGS}$, $v_{g,CGS}$ $v_{sg,CGS}$) in Fig. 6.3.5c, due to the capacitance frequency independent voltage divider of the VASC with $C_{st,var}$ and the gate-source capacitor with C_{gs} of the CGS, which has a similar large-signal behavior as shown in Fig. 6.2.11b. If the quiescent point is at a high DC-level, using the structure shown in Fig. 6.3.6a, the negative voltage swing at the source of the CGS increases the effective $C_{st,var}$ which is illustrated in Fig. 6.3.6b and Fig. 6.3.6c.

(a) Schematic of CGS with VASC.

(b) Quiescent point of VASC and voltage dependency of $C_{st,var}$.

(c) Time voltage dependency of $C_{st,var}$ and C_{st}.
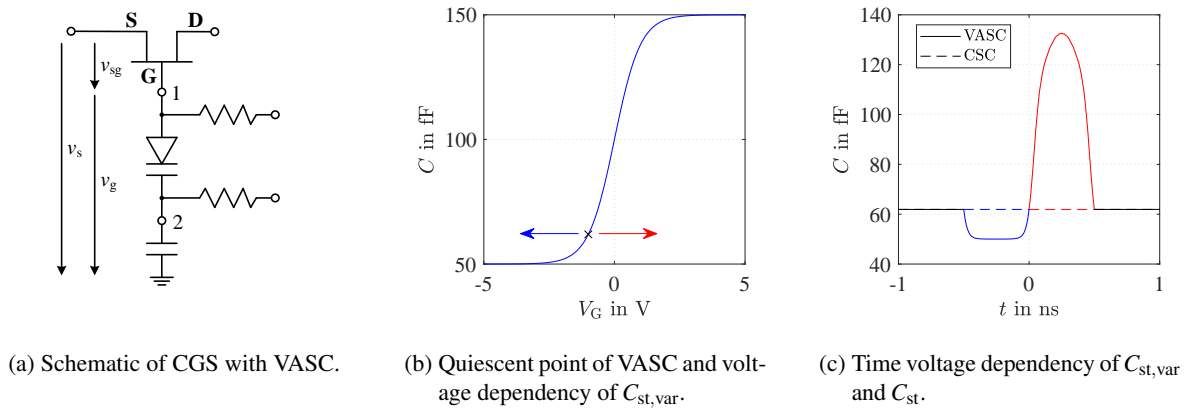
Figure 6.3.4: (a) Schematic of the CGS using a VASC and the corresponding (b) voltage dependency and (c) time voltage dependency of one varactor diode (direction: down) as VASC compared to a CSC.

(a) Time dependency of v_s.

(b) Time dependency of v_g.

(c) Time dependency of v_{sg}.
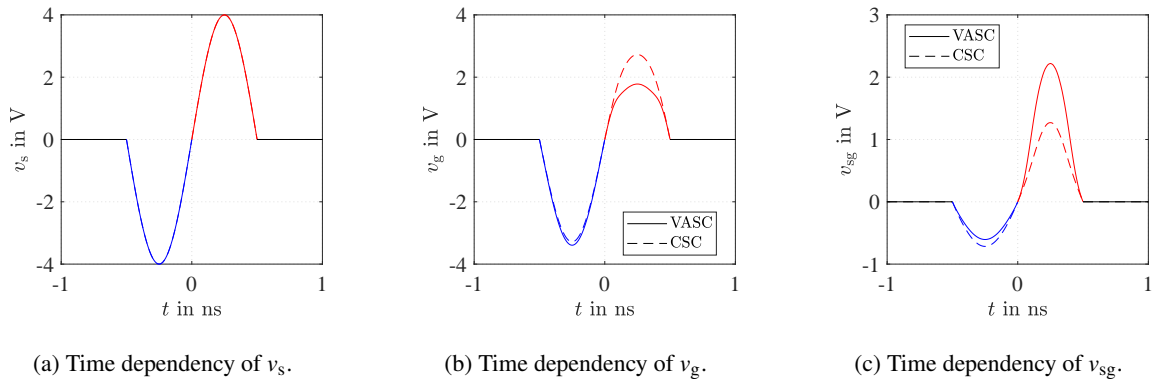
Figure 6.3.5: Time dependency of v_s, v_g and v_{sg} of the CGS using a VASC realized by one varactor diode (direction: down) for a certain quiescent point compared to a CSC.

(a) Schematic of CGS with VASC.

(b) Quiescent point of VASC and voltage dependency of $C_{st,var}$.

(c) Time voltage dependency of $C_{st,var}$ and C_{st}.
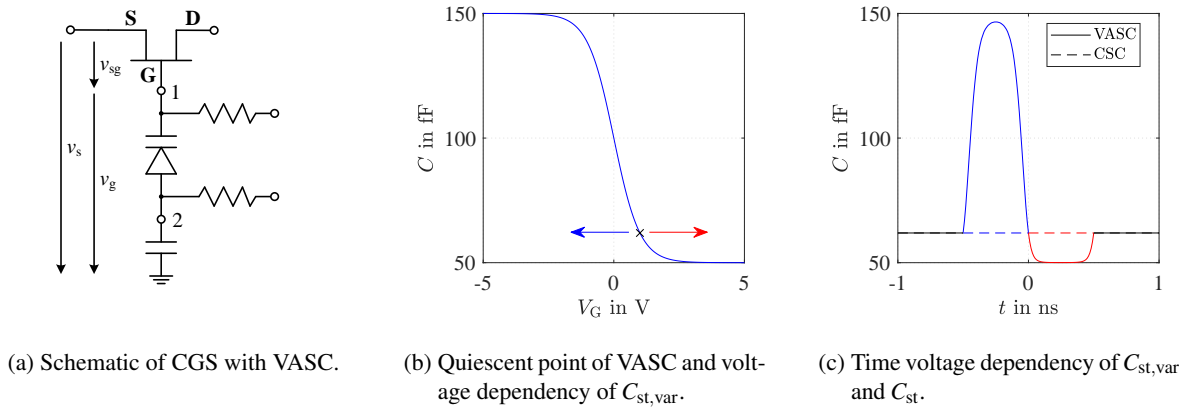
Figure 6.3.6: (a) Schematic of the CGS using a VASC and the corresponding (b) voltage dependency and (c) time voltage dependency of one varactor diode (direction: up) as VASC compared to a CSC.

(a) Time dependency of v_s.

(b) Time dependency of v_g.

(c) Time dependency of v_{sg}.
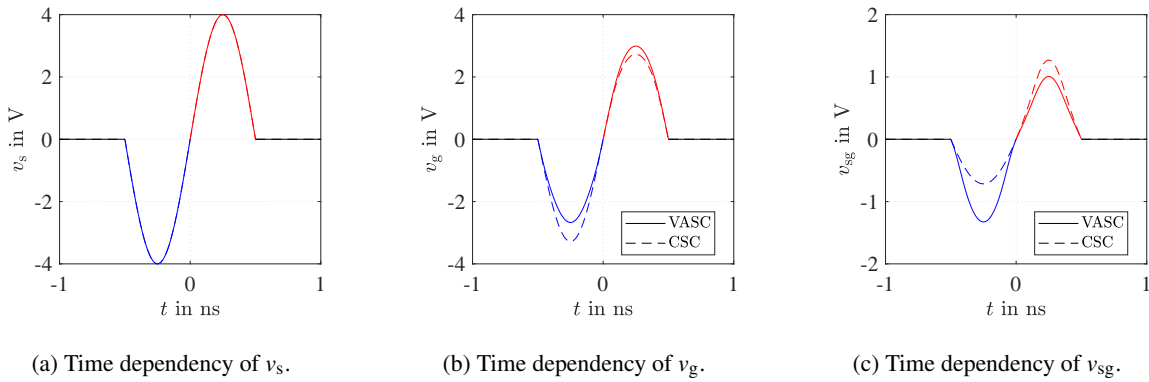
Figure 6.3.7: Time dependency of v_s, v_g and v_{sg} of the CGS using a VASC realized by one varactor diode (direction: up) for a certain quiescent point as VASC compared to a CSC.

Using the structure shown in Fig. 6.3.8a with two certain quiescent points for each varactor diode, the effective $C_{st,var}$ increases for positive and negative voltage swing illustrated in Fig. 6.3.8b and Fig. 6.3.8c. As a result the compression point can be significantly improved.

(a) Schematic of CGS with VASC.

(b) Quiescent point of VASC and voltage dependency of $C_{st,var}$.

(c) Time voltage dependency of $C_{st,var}$ and C_{st}.
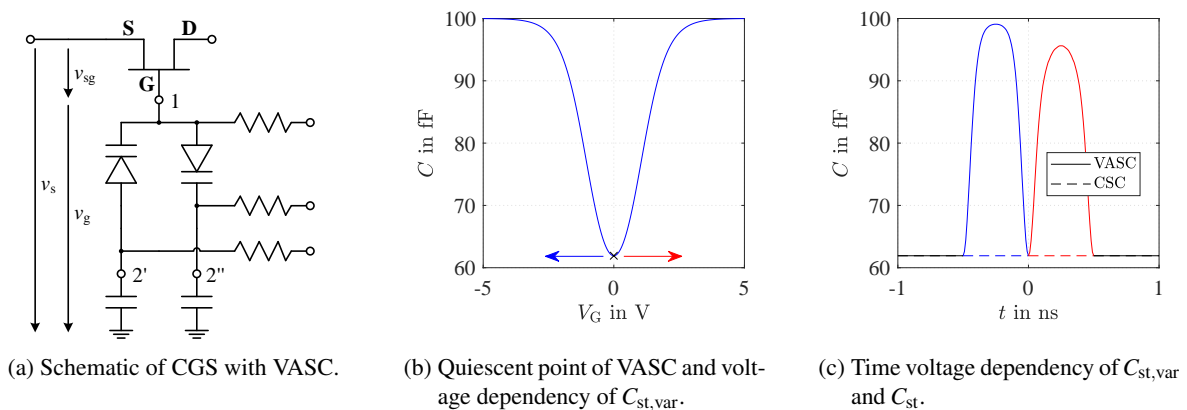
Figure 6.3.8: (a) Schematic of the CGS using a VASC and the corresponding (b) voltage dependency and (c) time voltage dependency of two varactor diodes in parallel (direction: up&down) as VASC compared to a CSC.

(a) Time dependency of v_s.

(b) Time dependency of v_g.

(c) Time dependency of v_{sg}.
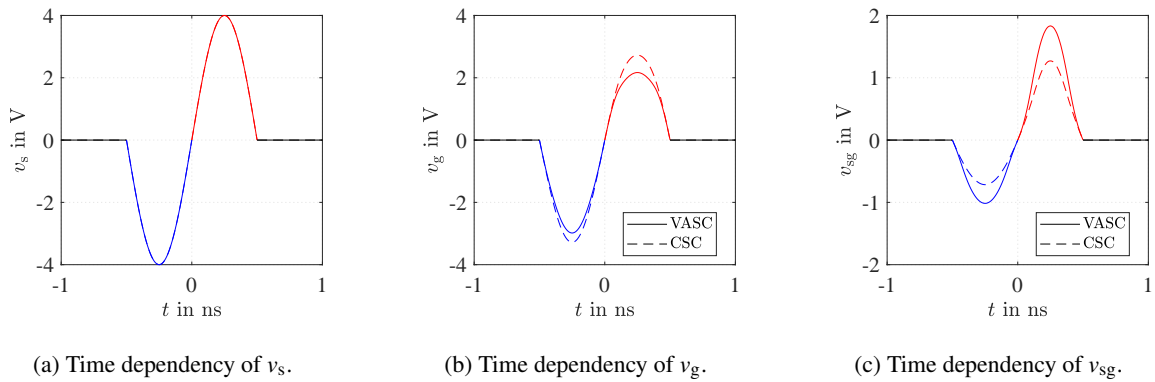
Figure 6.3.9: Time dependency of v_s, v_g and v_{sg} of the CGS using a VASC realized by two varactor diodes in parallel (direction: up&down) for a certain quiescent point as VASC compared to a CSC.

Comparing structures shown in Fig. 6.3.10a and Fig. 6.3.12a with Fig. 6.3.4a and Fig. 6.3.6a respectively, structures have similar large-signal behavior. However using two varactor diodes in parallel allows to adjust the non-linearity in a small range without changing the small-signal behavior, shown in Fig. 6.2.14–Fig. 6.2.17.

(a) Schematic of CGS with VASC.

(b) Quiescent point of VASC and voltage dependency of $C_{st,var}$.

(c) Time voltage dependency of $C_{st,var}$ and C_{st}.
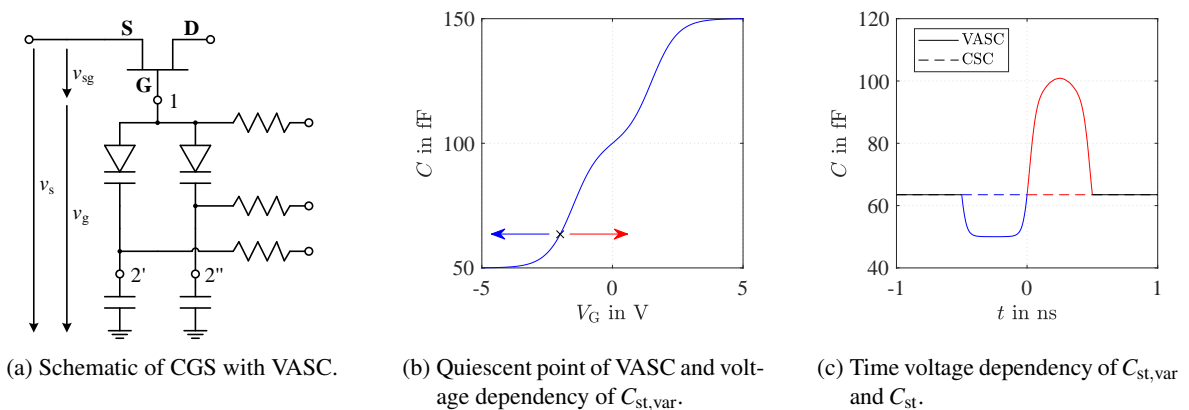
Figure 6.3.10: (a) Schematic of the CGS using a VASC and the corresponding (b) voltage dependency and (c) time voltage dependency of two varactor diodes in parallel (direction: down&down) as VASC compared to a CSC.

(a) Time dependency of v_s.

(b) Time dependency of v_g.

(c) Time dependency of v_{sg}.
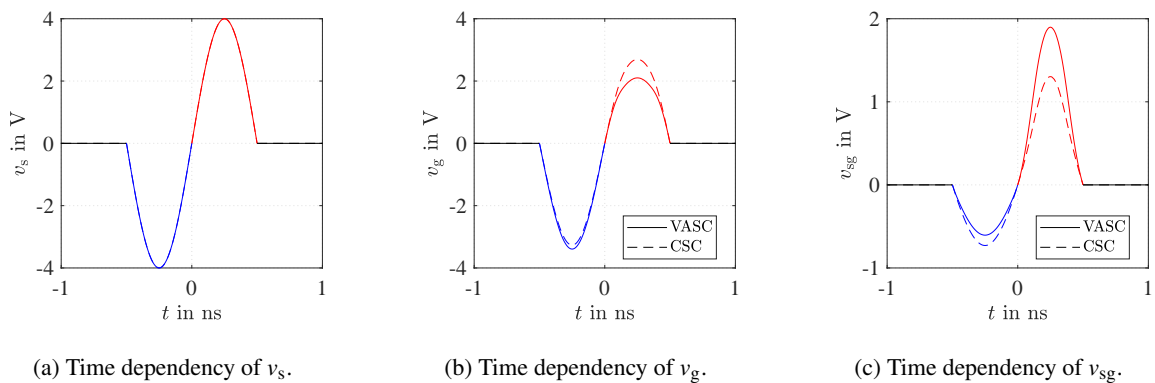
Figure 6.3.11: Time dependency of v_s, v_g and v_{sg} of the CGS using a VASC realized by two varactor diodes in parallel (direction: down&down) for a certain quiescent point as VASC compared to a CSC.

(a) Schematic of CGS with VASC.

(b) Quiescent point of VASC and voltage dependency of $C_{st,var}$.

(c) Time voltage dependency of $C_{st,var}$ and C_{st}.
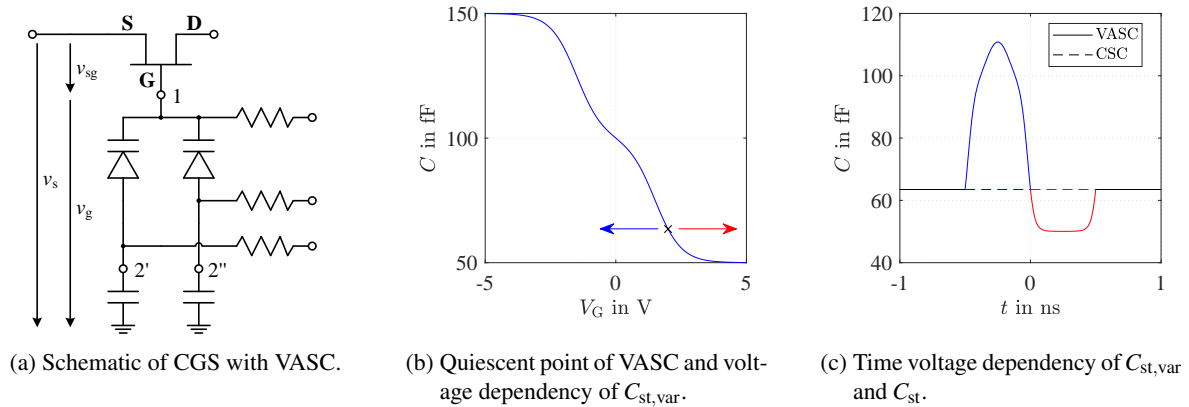
Figure 6.3.12: (a) Schematic of the CGS using a VASC and the corresponding (b) voltage dependency and (c) time voltage dependency of two varactor diodes in parallel (direction: up&up) as VASC compared to a CSC.

(a) Time dependency of v_s.

(b) Time dependency of v_g.

(c) Time dependency of v_{sg}.
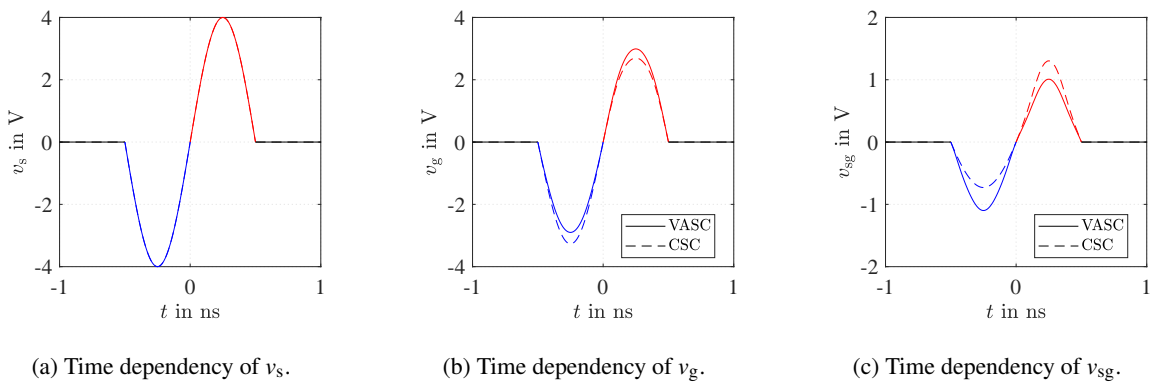
Figure 6.3.13: Time dependency of v_s, v_g and v_{sg} of the CGS using a VASC realized by two varactor diodes in parallel (direction: up&up) for a certain quiescent point as VASC compared to a CSC.

Using two diodes in series can also improve the compression behavior depending on the quiescent point of each diode. Comparing structures shown in Fig. 6.3.16a and Fig. 6.3.18a with Fig. 6.3.4a and Fig. 6.3.6a respectively, structures have similar large-signal behavior. However using two varactor diodes in series allows to adjust the non-linearity in a small range without changing the small-signal behavior, shown in Fig. 6.2.20–Fig. 6.2.23.

Comparing structures using two diodes in series and two diodes in parallel with each other, the large-signal behavior can be very different from each other depending on the quiescent point of the diodes. The dynamic range of $C_{st,var}$ of structure shown in Fig. 6.3.8a —using two anti-parallel diodes— is much higher in contrast of using two anti-series diodes as shown in Fig. 6.3.14a. However, due to the fact that the device size of two diodes in series is much higher —allowing a higher maximum gate current— compared to two anti-parallel diodes to achieve the same $C_{st,var}$, the anti-series diodes withstand a much higher voltage swing which leads to a robust structure.

(a) Schematic of CGS with VASC.

(b) Quiescent point of VASC and voltage dependency of $C_{st,var}$.

(c) Time voltage dependency of $C_{st,var}$ and C_{st}.
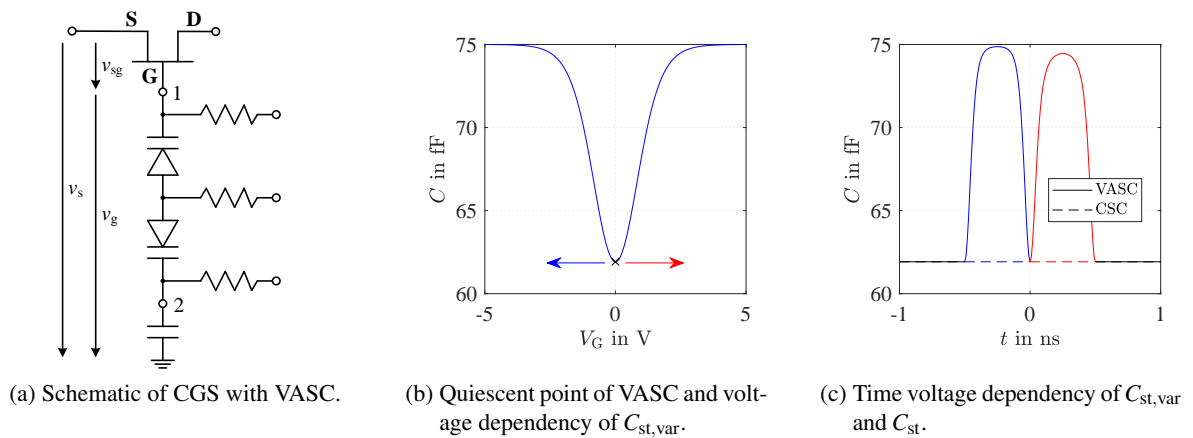
Figure 6.3.14: (a) Schematic of the CGS using a VASC and the corresponding (b) voltage dependency and (c) time voltage dependency of two varactor diodes in series (direction: up&down) as VASC compared to a CSC.

(a) Time dependency of v_s.

(b) Time dependency of v_g.

(c) Time dependency of v_{sg}.
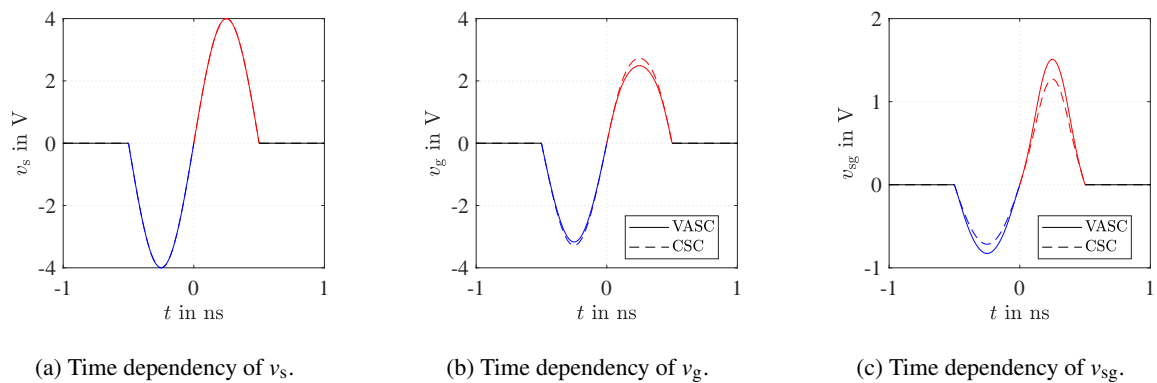
Figure 6.3.15: Time dependency of v_s, v_g and v_{sg} of the CGS using a VASC realized by two varactor diodes in series (direction: up&down) for a certain quiescent point as VASC compared to a CSC.

(a) Schematic of CGS with VASC.

(b) Quiescent point of VASC and voltage dependency of $C_{st,var}$.

(c) Time voltage dependency of $C_{st,var}$ and C_{st}.
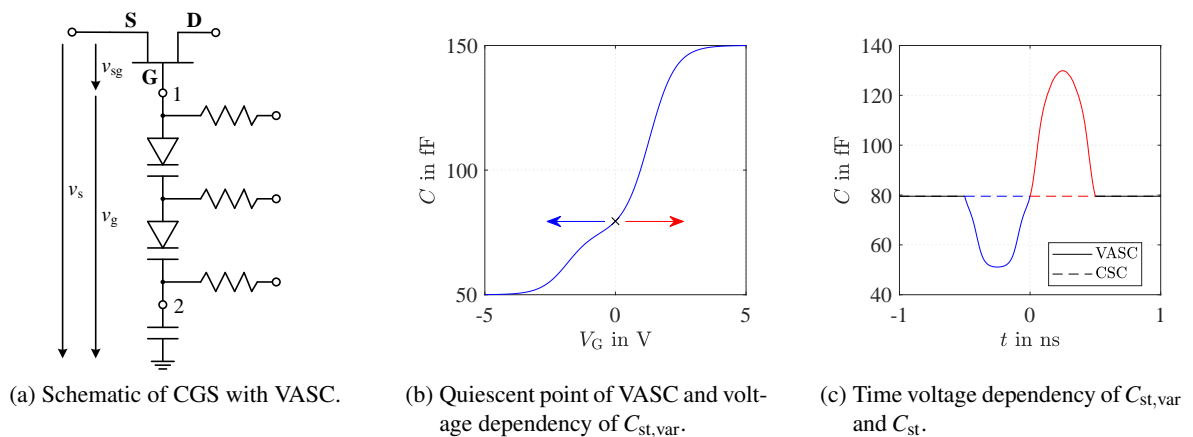
Figure 6.3.16: (a) Schematic of the CGS using a VASC and the corresponding (b) voltage dependency and (c) time voltage dependency of two varactor diodes in series (direction: down&down) as VASC compared to a CSC.

(a) Time dependency of v_s.

(b) Time dependency of v_g.

(c) Time dependency of v_{sg}.
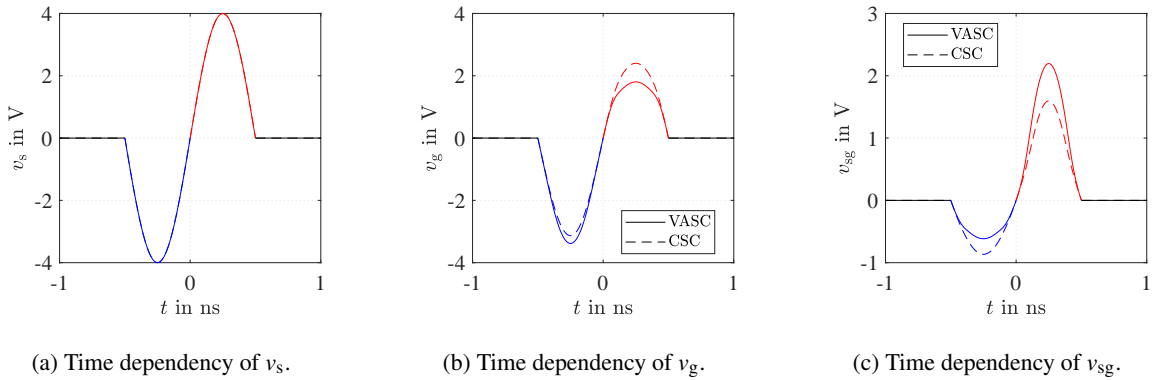
Figure 6.3.17: Time dependency of v_s, v_g and v_{sg} of the CGS using a VASC realized by two varactor diodes in series (direction: down&down) for a certain quiescent point as VASC compared to a CSC.

(a) Schematic of CGS with VASC.

(b) Quiescent point of VASC and voltage dependency of $C_{st,var}$.

(c) Time voltage dependency of $C_{st,var}$ and C_{st}.
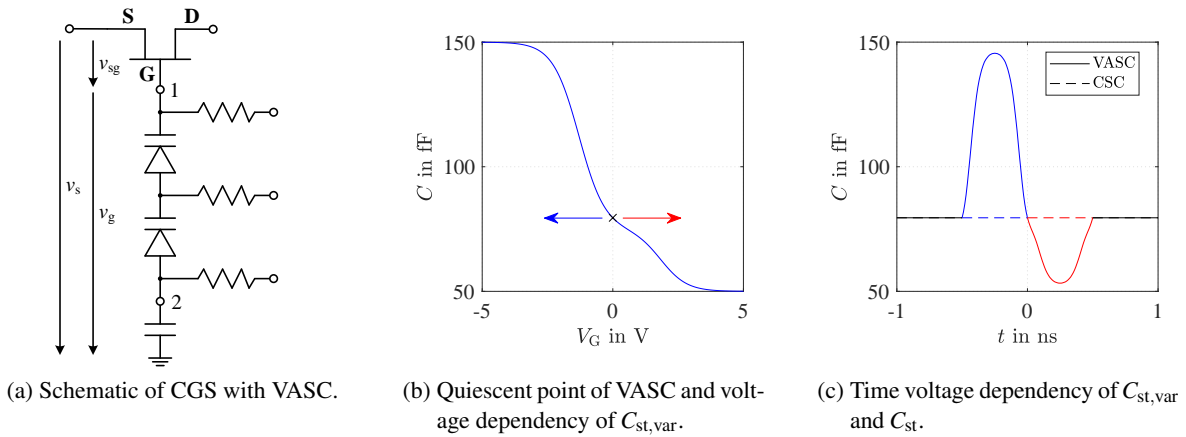
Figure 6.3.18: (a) Schematic of the CGS using a VASC and the corresponding (b) voltage dependency and (c) time voltage dependency of two varactor diodes in series (direction: up&up) as VASC compared to a CSC.

(a) Time dependency of v_s.

(b) Time dependency of v_g.

(c) Time dependency of v_{sg}.
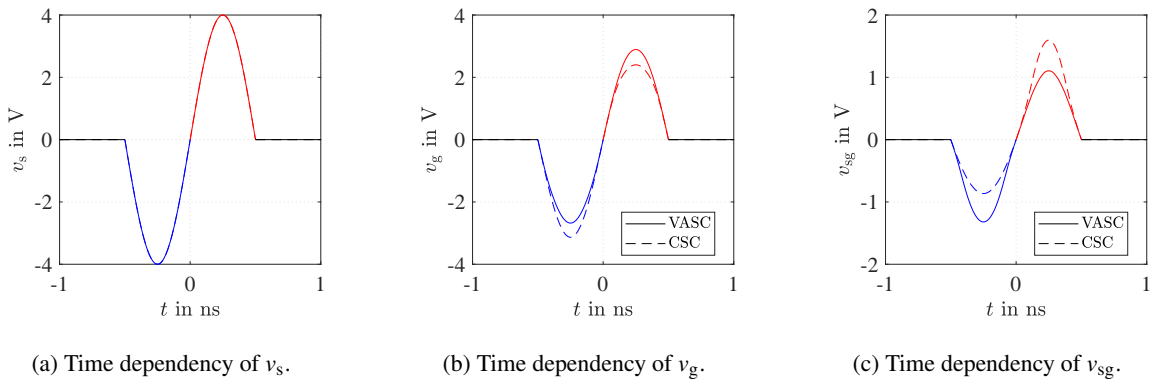
Figure 6.3.19: Time dependency of v_s, v_g and v_{sg} of the CGS using a VASC realized by two varactor diodes in series (direction: up&up) for a certain quiescent point as VASC compared to a CSC.

Table 6.3.2 shows the advantages and disadvantages regarding the power compression improvement of CC-FBA using different realization concepts of the NLSC using a VASC.

Table 6.3.2: Advantages and disadvantages of the different structures to realize a NLSC by a VASC to improve the gain compression of CCs.

| Number | | Complexity | Flexibility | Non-Linearity | Compression | Structure |
Diodes	Bias Pads				Improvement	Ref.
1x	1x	low	low	high	high	Fig. 6.2.2
1x	1x	low	low	high	medium–high	Fig. 6.2.3
2x	2x	high	high	low–medium	medium–high	Fig. 6.2.4
2x	2x	high	medium	medium–high	high	Fig. 6.2.5
2x	2x	high	medium	medium–high	medium–high	Fig. 6.2.6
2x	2x	high	medium–high	low–medium	medium	Fig. 6.2.7
2x	2x	high	medium	medium–high	high	Fig. 6.2.8
2x	2x	high	medium	medium–high	medium–high	Fig. 6.2.9

Since the change of the $\underline{Z}_{\text{load}}$ of the CSS with higher output voltage swing was neglected among other things, the properties of the different realization concepts shown in Table 6.3.2 can change and should be examined in detail for each circuit design.

6.3.3 Improved Linearity

To improve the linearity in PAs, there are several different techniques which can be found in literature. In [53], a short overview about the different linearization methods —i.e. class A amplifier in back-off, feedforward, adaptive predistortion, envelope elimination and recovery and so on— are given. The third application of the new concept is to use the VASC with $C_{\text{st,var}}$ to change the linearity behavior of broadband PAs using CCs. The linearity of the CC can be improved by using a certain non-linearity of the VASC to reduce the non-linearity of the CGS caused by the intrinsic non-linear large-signal elements C_{gs} and G_{m} of the CGS, shown in Fig. 4.3.5. The non-linearity of the intrinsic C_{gs} and G_{m} of the CGS can be approximated by

$$C_{\text{gs}}(V_{\text{GS}}) = C_{\text{gs},0} + \underbrace{C_{\text{gs},1}V_{\text{GS}}}_{\text{Term1}} + \underbrace{C_{\text{gs},2}V_{\text{GS}}^2}_{\text{Term2}} \qquad (6.3.1)$$

and

$$G_{\text{m}}(V_{\text{GS}}) = G_{\text{m},0} + \underbrace{G_{\text{m},1}V_{\text{GS}}}_{\text{Term1}} + \underbrace{G_{\text{m},2}V_{\text{GS}}^2}_{\text{Term2}} \, . \qquad (6.3.2)$$

Term1 and Term2 defines the amount of the second and third order respectively.

Fig. 6.3.20 shows the on-wafer measurement results of the harmonic distortion of the CC-FBAs using a CSC and a VASC. Fig. 6.3.20a and Fig. 6.3.20b show a typical *HD*2 and *HD*3 improvement of the CC-FBAs using a CSC and a VASC versus frequency and versus P_{out} respectively.

(a) $HD2$ and $HD3$ vs. frequency.
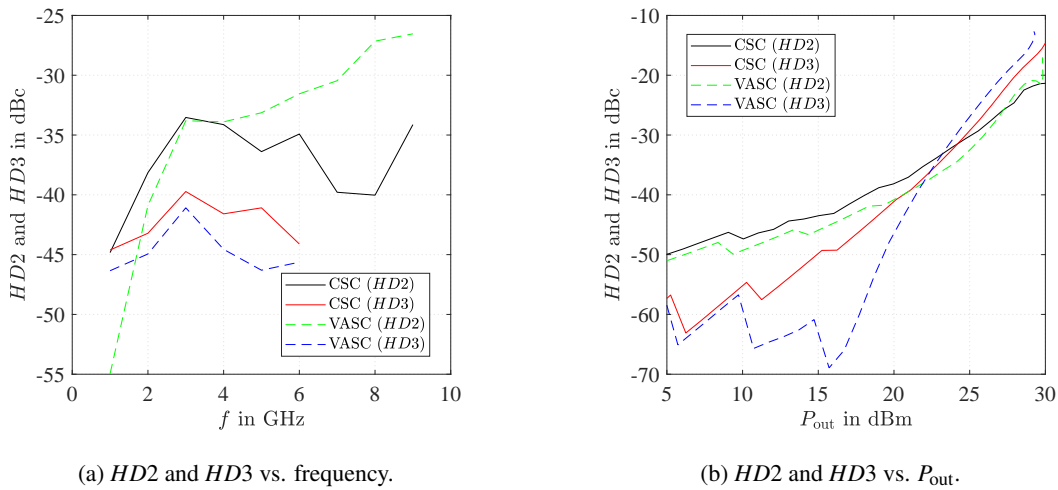
(b) $HD2$ and $HD3$ vs. P_{out}.

Figure 6.3.20: Measured $HD2$ and $HD3$ of the CC-FBAs ($V_{\text{DS}} = 10\,\text{V}$, $I_{\text{DSQ}} = 156\,\text{mA}$) using a CSC (solid line) and a VASC (dashed line) at $V_{\text{VASC}} = -5\,\text{V}$. (a) $HD2$ and $HD3$ vs. frequency at $P_{\text{out}} = 20\,\text{dBm}$. (b) $HD2\,(f = 2\,\text{GHz})$ and $HD3\,(f = 5\,\text{GHz})$ vs. P_{out} at .

There are two possibilities to reduce the non-linearity of the CGS which is caused by the non-linear C_{gs} of the CGS:

1. An external capacitor with capacitance $C_{\text{sg,ext}}$ is connected between the source and the gate of the CGS. If the external capacitor with $C_{\text{sg,ext}}$ in parallel to the intrinsic capacitor with C_{gs} has the reversed non-linearity behavior compared to the C_{gs}, shown in Fig. 6.3.21, the overall non-linearity of the CGS which is caused by non-linear C_{gs} can be significantly reduced. In case of very low parasitic intrinsic resistance in the CGS, the non-linearity behavior of both capacitors almost cancel each other.

2. The CSC with C_{st} at the gate of the CGS is replaced by a VASC with $C_{\text{st,var}}$ which has a certain non-linear behavior. If the VASC with $C_{\text{st,var}}$ in series with the intrinsic capacitor with C_{gs} has the same non-linearity behavior compared to the C_{gs}, shown in Fig. 6.3.21, the overall non-linearity of the CGS which is caused by the second and third order non-linearity of the C_{gs} can be significantly reduced assuming that the input voltage swing v_{s} does not change.
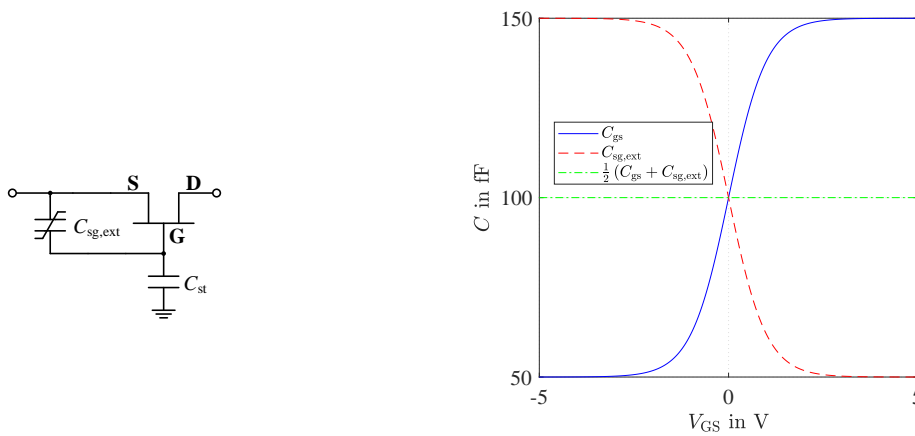
(a) Schematic of CGS with CSC and external capacitor with $C_{\text{sg,ext}}$.

(b) Non-linearity of C_{gs} and $C_{\text{sg,ext}}$.

Figure 6.3.21: (a) Schematic of CGS with CSC and external capacitor with $C_{\text{sg,ext}}$ and (b) the large-signal characteristic of C_{gs} and $C_{\text{sg,ext}}$.

Comparing both possibilities to reduce the non-linearity of the CGS which is caused by the non-linearity of the C_{gs} of the CGS, following advantages and disadvantages can be listed:

- Using the first possibility, the non-linearity behavior of C_{gs} and $C_{sg,ext}$ almost cancel each other. Disadvantage of this concept is the lower bandwidth due to the increased input capacitance which is caused by the parallel capacitances C_{gs} and $C_{sg,ext}$.
- The second possibility does not degrade the bandwidth since the CSC with C_{st} is replaced by a VASC with $C_{st,var}$ which has the same small-signal value as C_{st}. However, choosing a certain non-linearity of $C_{st,var}$ the overall non-linearity caused by C_{gs} can not be canceled completely. Moreover, the cancellation depends also on the P_{in} and effects the input impedance of the CGS.

As mentioned in the previous Sec. 6.3.2 there are several different possibilities to realize a VASC. Fig. 6.3.22, Fig. 6.3.23 and Fig. 6.3.24 compare the different realization concepts with respect to the harmonics assuming that the input voltage swing v_s does not change. Using structures shown in Fig. 6.3.6a, Fig. 6.3.12a and Fig. 6.3.18a and choosing the same quiescent point for the VASC with $C_{st,var}$ as in Sec. 6.3.2, the harmonics of v_{gs} can be reduced, illustrated in Fig. 6.3.22c, Fig. 6.3.23c and Fig. 6.3.24c.

(a) General schematic of CGS with VASC.

(b) $\left|\underline{V}_{gs}\right|$ of one varactor diode (direction: down).

(c) $\left|\underline{V}_{gs}\right|$ of one varactor diode (direction: up).
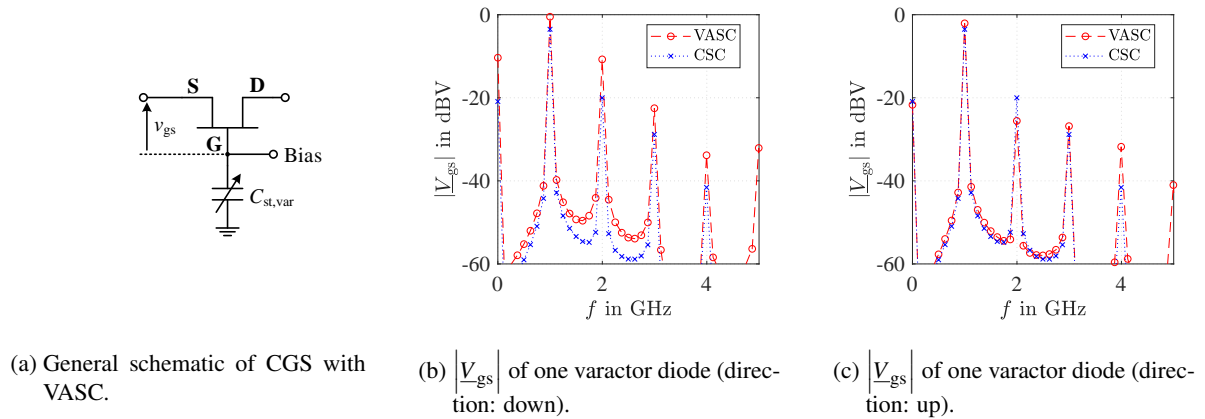
Figure 6.3.22: (a) General schematic of CGS using a VASC and (b, c) the single-sided amplitude spectrum of v_{gs} of one varactor diode for a certain quiescent point as VASC.

(a) $\left|\underline{V}_{gs}\right|$ of two varactor diodes in parallel (direction: up&down).

(b) $\left|\underline{V}_{gs}\right|$ of two varactor diodes in parallel (direction: down&down).

(c) $\left|\underline{V}_{gs}\right|$ of two varactor diodes in parallel (direction: up&up).
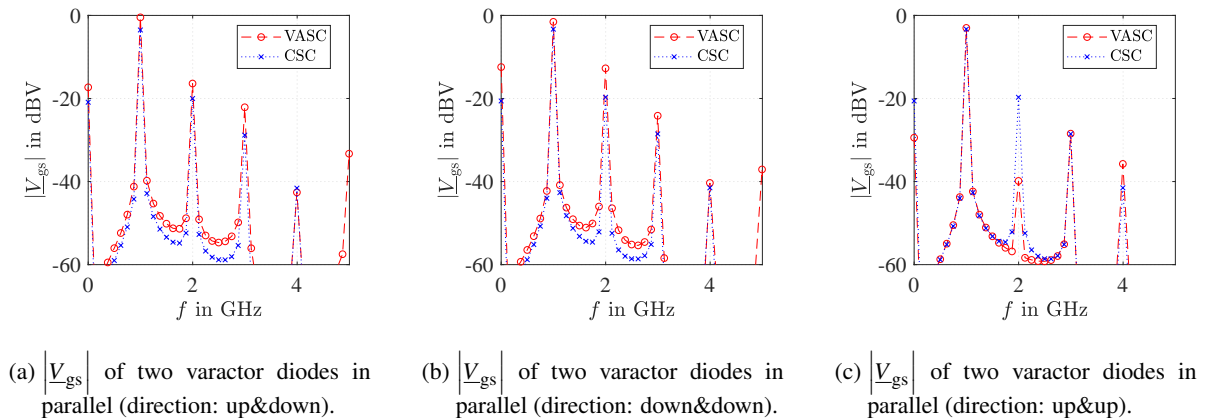
Figure 6.3.23: Single-sided amplitude spectrum of v_{gs} of two varactor diodes in parallel for a certain quiescent point as VASC.

(a) $\left|\underline{V}_{gs}\right|$ of two varactor diodes in series (direction: up&down).

(b) $\left|\underline{V}_{gs}\right|$ of two varactor diodes in series (direction: down&down).

(c) $\left|\underline{V}_{gs}\right|$ of two varactor diodes in series (direction: up&up).
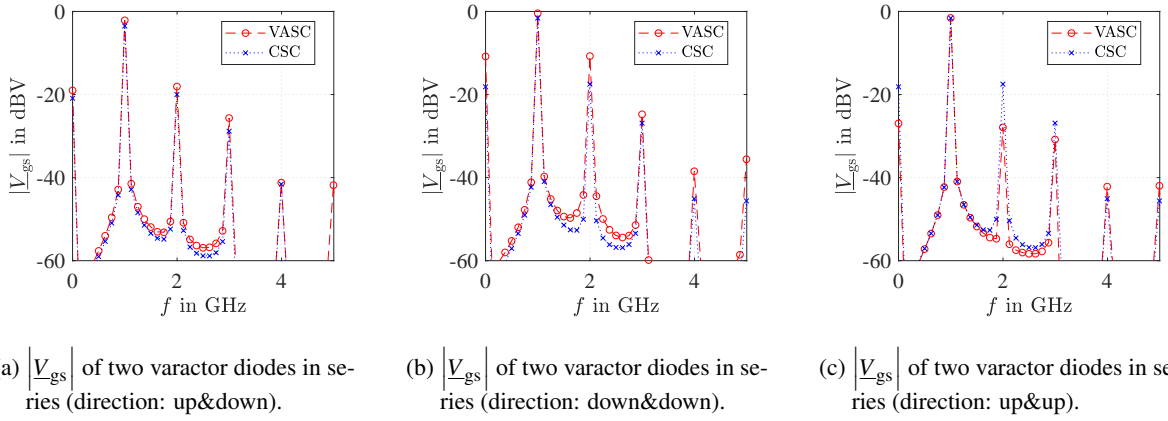
Figure 6.3.24: Single-sided amplitude spectrum of v_{gs} of two varactor diodes in series for a certain quiescent point as VASC.

To reduce the G_m non-linearity of the CGS a predistortion is needed. This can be done by changing the overall voltage swing v_{gs} in the right manner at the gate-source capacitor with C_{gs} of the CGS. Using structures shown in Fig. 6.3.4a, Fig. 6.3.10a and Fig. 6.3.16a and choosing a certain quiescent point for the VASC, the non-linear voltage swing v_{gs} acts like a predistortion to lower the G_m compression of the CGS.

Neglecting the influence of the $\underline{Z}_{load}$ of the CSS with higher output voltage swing, Table 6.3.3 shows in a first approximation the advantages and disadvantages of the different structures to realize a NLSC by a VASC to improve the non-linearity of CCs. Therefore, in each circuit design the different realization concepts should be examined in detail.

Table 6.3.3: Advantages and disadvantages of the different structures to realize a NLSC by a VASC to improve the non-linearity of CCs.

Number		Complexity	Flexibility	Non-Linearity Improvement of v_{gs}		Structure
Diodes	Bias Pads			$HD2$	$HD3$	Ref.
1x	1x	low	low	medium	-	Fig. 6.2.3
2x	2x	high	medium	high	-	Fig. 6.2.6
2x	2x	high	medium	medium–high	medium	Fig. 6.2.9

(a) Non-linearity improvement of v_{gs} using different structures to realize a NLSC.

Number		Complexity	Flexibility	G_m Predistortion	Structure
Diodes	Bias Pads				Ref.
1x	1x	low	low	medium–high	Fig. 6.2.2
2x	2x	high	high	low–medium	Fig. 6.2.4
2x	2x	high	medium	medium–high	Fig. 6.2.5
2x	2x	high	medium–high	low–medium	Fig. 6.2.7
2x	2x	high	medium	medium–high	Fig. 6.2.8

(b) Non-linearity improvement of G_m using different structures to realize a NLSC.

6.4 Summary

In Sec. 6.1 and Sec. 6.2 the general principle and the different realizations of the proposed concept were explained respectively. Afterwards, in Sec. 6.3 three different applications of the new concept were presented and examined in detail to show the advantages and disadvantages of the different realization concepts. The key findings of the new concept are summarized in the following.

Key findings of the proposed concept:

- Electrical behavior of the CGS can be adjusted by a VASC with $C_{st,var}$ in a certain manner.
- Depending on the chosen structure to realize the VASC and as a result a certain voltage dependency of the $C_{st,var}$ certain properties of the CGS can be achieved.

Key findings to improve certain parameters of the CGS:

- By increasing and decreasing $C_{st,var}$ of the CGS the electrical behavior of the CGS can be adjusted in such a way that the gain can be controlled at high frequencies. It is a trade-off between gain and stability. The proposed realizations of the new concept differ in the complexity, flexibility, non-linearity and the dynamic range.
- By changing the $C_{st,var}$ depending on the voltage swing the electrical behavior of the CGS can be changed in such way that the gain of the CGS increases at higher frequencies at higher P_{out}. Due to this fact the power compression behavior can be improved in a certain way. The proposed realizations of the new concept differ in the complexity, flexibility, non-linearity and the compression improvement.
- The non-linearity of the $C_{st,var}$ can be used to partially cancel the non-linearity of the intrinsic large-signal elements C_{gs} and G_m of the CGS. Therefore, the non-linearity of CCs can be improved. Due to the fact that the non-linearity of the $C_{st,var}$ differs to improve the non-linearity of C_{gs} and G_m, it is a trade-off between both elements to improve the overall linearity. The proposed realizations of the new concept differ in their complexity, flexibility and the linearity improvement for C_{gs} and G_m.

7 Broadband Power Amplifiers

To verify the foregoing theoretical investigations in Ch. 5 and Ch. 6 several broadband PAs were designed and fabricated using Northrop Grumman's commercially available $0.2\,\mu$m GaN-HEMT technology with a SiC substrate which has a thickness of $100\,\mu$m. The process achieves a peak f_t and $f_{\max}$ of 60 GHz and 200 GHz, respectively, and a $\frac{g_m}{GP}$ of 325 $\frac{mS}{mm}$. To maintain a safe operating area of the active device

- the maximum applied DC voltage $V_{\mathrm{DS,MAX}}$ is equal to 28 V and
- the maximum current density $\frac{I_{\mathrm{DS,MAX}}}{GP}$ is equal to 250 $\frac{mA}{mm}$.

As a result the maximum dissipation power density $(\frac{P_{\mathrm{DISS,MAX}}}{GP})$ of the active device should no exceed 7 $\frac{W}{mm}$. Further detail of the process can be found in [154].

The performance of the designed broadband FBAs are shown and compared with each other in this chapter to show the trade-off between the CS and the CC topology and to highlight and compare the different realizations of the new concept. Main focus of the designed FBAs was to maximize the small-signal bandwidth with a positive gain slope —to compensate i.e. the later added input and output bond interface or cable losses of the amplifier system— while maintaining a good input and output small-signal match. To gain high P_{out} and low NF was the second priority.

First, the fundamentals of two types of multi-decade PAs are shortly explained. Afterwards, the design and the measurement results of the several designed broadband PAs are illustrated and explained. At the end of this chapter a summary is given to point out the advantages and disadvantages of the CS and CC topology and to highlight the performance using the new concept in broadband PAs.

7.1 Multi-Decade Power Amplifier MMIC Designs

In literature there are different ideas to realize broadband PAs [155, 156]. An good overview is given by [155]. The distributed, push-pull, reactive matching, resistive feedback and the balanced architecture are the widespread basic amplifier topologies to design broadband PAs. Although there are many amplifier architectures to achieve an octave frequency bandwidth, only two types of amplifier topologies are capable of realizing multi-decade bandwidth PAs:

- The distributed architecture which is used in distributed power amplifiers (DPAs), also known as traveling-wave power amplifier.
- The resistive feedback architecture which usually uses a resistive parallel feedback, called feedback power amplifier.

7.1.1 Traveling-Wave Power Amplifier

The distributed architecture was first proposed and patented by Percival in 1936 [157]. It is one of the most widespread and popular architecture to design multi-decade power amplifiers. The fundamental operation principle of the traveling-wave power amplifier is the absorption of the input and output parasitics of the cascaded transistors into the gate and drain transmission line to achieve a very broad bandwidth and maintaining moderate small-signal gain. Fig. 7.1.1 shows the principle schematic of a uniform TWA.
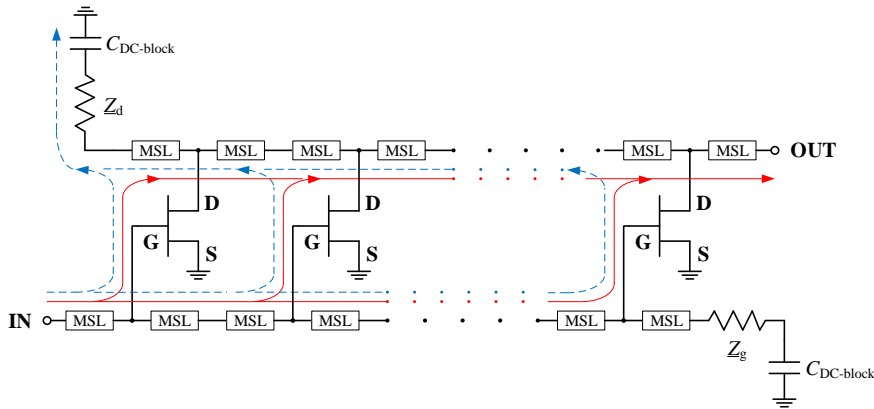
Figure 7.1.1: Principle schematic of a uniform TWA in CS topology.

In [17] the operation principle of the distributed architecture is explained in more detail to get a in-depth understanding. Furthermore, in [17, 158] the evolution of the DPA architecture is summarized and an overview about the different developments to improve certain RF parameters —i.e. gain, power, bandwidth and noise— are given. These developments comprise i.e. capacitive coupled DPA, nonuniform DPA, gate-line and drain-line tapering as well as an active gate termination in the DPA. Table 7.1.1 summaries and compares state-of-the-art TWAs (DPAs) —using the GaN-HEMT technology— with respect to the small-signal bandwidth (SSB), $|\underline{S}_{21}|$, NF, OIP3, P1dB and P_{out}.

Table 7.1.1: State-of-the-art broadband TWAs using the GaN-HEMT technology with SiC as substrate [16, 17, 156, 158]. (a) $l_g \geq 200$ nm.

Technology		SSB	$|\underline{S}_{21}|$	NF	OIP3	P1dB	P_{sat}	Ref.
Foundry	l_g	(GHz)	(dB)	(dB)	(dBm)	(dBm)	(dBm)	
IAF	250 nm	DC–6.5	11–16	2–6	42–84	> 29	> 33.5	[153]
TriQuint[*1]	250 nm	1.5–17	10–14	N/A	N/A	N/A	38–42.5 @ 2–18 GHz	[159, 160]
TriQuint[*1]	250 nm	6–18	9–11	N/A	N/A	N/A	38–38.7[*2]	[161]
			8–10	N/A	N/A	N/A	41.1–41.3[*2]	
UCSB	200 nm	2–18	19–21	N/A	N/A	N/A	26–33	[162]
BAE	200 nm	2–20	9–15	N/A	N/A	N/A	40–43	[163]
			N/A	N/A	N/A	N/A	38–44	
CNR-IFN	250 nm	2–20	22–24	3.5–5.5 @ 2–18 GHz	29 @ 4.5 GHz	22 @ 4.5 GHz	25 @ 4.5 GHz	[164]
NGC	200 nm	DC–20	10–16	5–12.5 @ 1.5–18 GHz	36–45	26–33	29–37.5	[11]
		DC–24	10–12.5	2.5–7.5 @ 0.5–18 GHz	36–44 @ DC–20 GHz	24.5–32 @ DC–20 GHz	30–37.5 @ DC–20 GHz	

[*1] TriQuint Semiconductor and RF Micro Devices merged later to Qorvo

[*2] pulsed power

Table 7.1.1: (Continued..) State-of-the-art broadband TWAs using the GaN-HEMT technology with SiC as substrate [16, 17, 156, 158]. (b) $l_g \leq 150\,\text{nm}$.

Technology		SSB	$|\underline{S}_{21}|$	NF	$OIP3$	$P1dB$	P_{sat}	Ref.
Foundry	l_g	(GHz)	(dB)	(dB)	(dBm)	(dBm)	(dBm)	
Qorvo	150 nm	1–8.5	28–32	N/A	N/A	N/A	39–41.5	[165]
IAF	100 nm	6–37	15–17	N/A	N/A	N/A	29–32	[14]
Qorvo	150 nm	16–40	23–25	N/A	N/A	N/A	36.2–39.4[*]	[166]
			22–24	N/A	N/A	N/A	38.5–42[*]	
IAF	100 nm	6–42	5–7	N/A	N/A	N/A	23–26	[12]
			12–16	N/A	N/A	N/A	24–26	
Qorvo	150 nm	0.1–44	10–19	N/A	30–41 @ 1–44 GHz	N/A	N/A	[167]
				N/A	33.5–45.2 @ 1–44 GHz	N/A	N/A	
Qorvo	150 nm	0.1–45	9–20	2–8 @ 0.1–39 GHz	27.3–40.5 @ 1–40 GHz	N/A	28–33.3 @ 1–35 GHz	[15, 168]
				1.5–7.5 @ 0.1–40 GHz	28.1–40.5 @ 1–40 GHz	N/A	27.6–33 @ 1–35 GHz	
HRL	140 nm	75–100	15–16	N/A	N/A	29–32	33–35	[169]

[*] pulsed power

(b)

7.1.2 Feedback Power Amplifier

The resistive feedback architecture is the second popular amplifier topology to design multi-decade PAs. The feedback principle in PAs, explained in [170], is even as old as the distributed architecture. FBAs are well known due to the many advantages (i.e. increased bandwidth, improved linearity, enhanced stability, adjustment of the input and output impedance and much more). Fig. 7.1.2 and Fig. 7.1.3 shows the general amplifier system with a feedback loop and the general structure of a FBA using a series feedback impedance ($\underline{Z}_\text{fs}$) and a parallel feedback impedance ($\underline{Z}_\text{fp}$) to realize the feedback loop between input and output of the PA, respectively. In return of the RF improvement of the FBA, both feedbacks reduce the *MAG* of the active device . Due to the many benefits of the FBA, the feedback architecture is very suited to achieve multi-decade PAs.
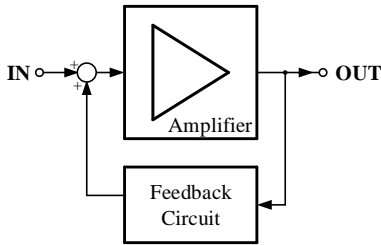
Figure 7.1.2: Amplifier system with feedback [170].
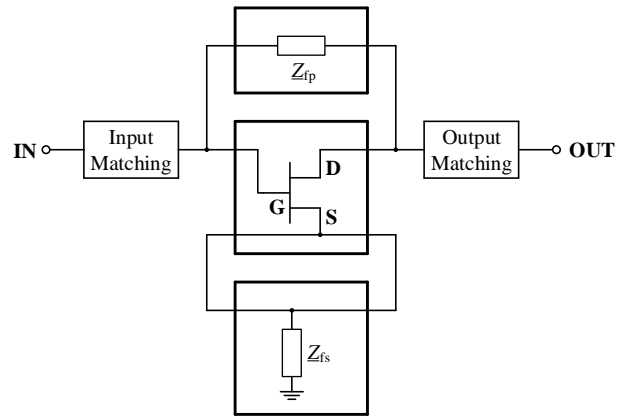
Figure 7.1.3: Schematic of a general FBA in CS topology [171].

Table 7.1.2 summaries and compares state-of-the-art FBAs using the GaN-HEMT technology.

Table 7.1.2: State-of-the-art broadband FBAs using the GaN-HEMT technology with SiC as substrate [13, 16]. (a) $l_\text{g} = 250\,\text{nm}$.

| Technology | | *SSB* | $|\underline{S}_{21}|$ | *NF* | *OIP3* | *P1dB* | P_sat | Ref. |
Foundry	l_g	(GHz)	(dB)	(dB)	(dBm)	(dBm)	(dBm)	
NGC	250 nm	0.25–3	18–21	2.2–3 @ 0.5–3 GHz	48–51 @ 0.5–3 GHz	35.5–39 @ 0.5–3 GHz	36–39.5 @ 0.5–3 GHz	[13, 172]
NGC	250 nm	0.25–3	18–21	2.6–3.8 @ 0.5–3 GHz	51.4–54.3 @ 0.5–3 GHz	37–41.4 @ 0.5–3 GHz	37.3–41.4 @ 0.5–2.5 GHz	[13, 172]
NGC	250 nm	0.25–3.5	17–20	0.88–1.32 @ 0.5–3.5 GHz	35–44 @ 0.5–3.5 GHz	29–31 @ 0.5–3.5 GHz	29.6–31.1 @ 0.5–3.5 GHz	[173]
N/A	N/A	0.2–4	8–11	N/A	N/A	27–30 @ 1–3 GHz	N/A	[174]
N/A	N/A	0.2–4	9–12	N/A	N/A	29–30 @ 1–3 GHz	N/A	[174]

(a)

Table 7.1.2: (Continued..) State-of-the-art broadband FBAs using the GaN-HEMT technology with SiC as substrate [13, 16]. (b) $l_g = 200\,\text{nm}$.

| Technology | | SSB | $|\underline{S}_{21}|$ | NF | $OIP3$ | $P1dB$ | P_{sat} | Ref. |
Foundry	l_g	(GHz)	(dB)	(dB)	(dBm)	(dBm)	(dBm)	
NGC	200 nm	0.3–4	17–18	1.5–4	N/A	17 @ 2 GHz	20 @ 2 GHz	[175]
NGC	200 nm	0.2–8	7–20	0.7–1.1 @ 1–8 GHz	43.2–46.5 @ 2–6 GHz	33.2–32.8 @ 1–4 GHz	34.2–34.7 @ 1–4 GHz	[176]
NGC	200 nm	0.05–12.3	12–14.5	N/A	41.3–44.2 @ 1–4 GHz	30.5–31.3 @ 1–4 GHz	31.5–32.4 @ 1–4 GHz	[29]
NGC	200 nm	1–12	12–18	4–9	27.5–31.5	N/A	20–25	[177]
NGC	200 nm	0.1–12	13–15	4.5–8 @ 1–12 GHz	37.5–40 @ 1–12 GHz	27.5–28 @ 6–12 GHz	30.5–32 @ 6–12 GHz	[16][*]
NGC	200 nm	1–17	13–14	5.5–10	36–41	24–29 @ 6–17 GHz	29–32 @ 6–17 GHz	[16][*]
NGC	200 nm	1–17	13–14	3.5–8	31–39	25.5–28	28–31	[178][*]
NGC	200 nm	1–17	13–17	3.5–8	31–39	22–26	28–31	[179][*]
NGC	200 nm	1.2–18	12.1–13.6	1.8–3.5	N/A	N/A	N/A	[180]
NGC	200 nm	0.05–18.7	9–11	N/A	41.7–42.5 @ 1–4 GHz	29.6–30.3 @ 1–4 GHz	31.5–31.9 @ 1–4 GHz	[29]
NGC	200 nm	1–25	10–13	3.4–4.6 @ 1–21 GHz	28.6–33.3 @ 2–25 GHz	17.5–20 @ 2–25 GHz	N/A	[181]

[*] this work

(b)

7.2 Feedback Power Amplifiers in Common-Source and Cascode Topology

In this section some information (i.e. small-signal and large-signal measurements) are partially already published in [16] © 2016 IEEE.

7.2.1 Schematic and Layout

Using Northrop Grumman's advanced $0.2\,\mu$m GaN-HEMT technology, Fig. 7.2.2 and Fig. 7.2.3 show the chip photo of the fabricated CS-FBA and the CC-FBAs. The corresponding schematic of the CS-FBA and the CC-FBAs can be seen in Fig. 7.2.1a and Fig. 7.2.1b.

(a) CS-FBA with external feedback capacitor.   (b) CC-FBA without external feedback capacitor.
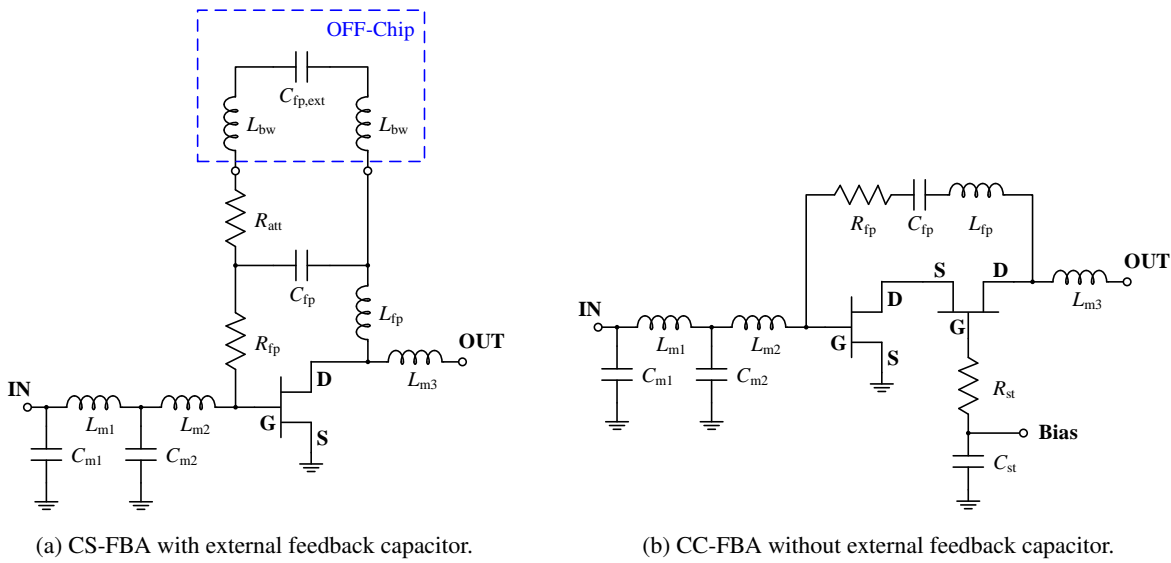
Figure 7.2.1: (a) and (b) Schematic of the CS-FBA and the CC-FBA, respectively [171].
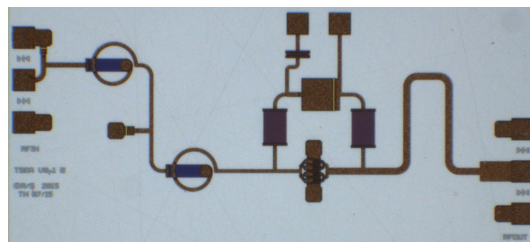
Figure 7.2.2: Layout of the CS-FBA.
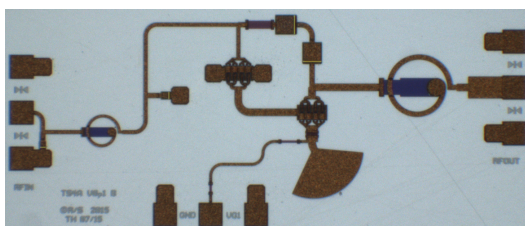
(a) Layout of the CC-FBA-IB [179].   (b) Layout of the CC-FBA-IG.
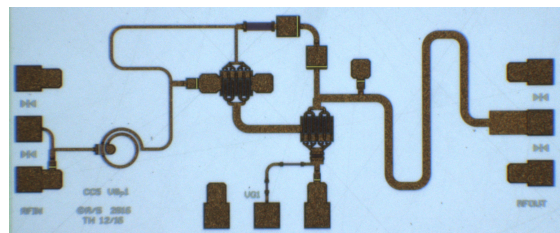
Figure 7.2.3: Layout of the CC-FBA. (a) CC-FBA-IB. (b) CC-FBA-IG.

Fig. 7.2.2 and Fig. 7.2.1a show the layout and the schematic of the CS-FBA with the possibility to use an off-chip external feedback capacitor with high capacitance. As a result the CS-FBA can offer a multi-decade bandwidth performance. This technique was not adapted to the CC-FBAs to due lack of space. Maintaining the same $|\underline{S}_{21}|$ of the CS-FBA the CC-FBA, shown in Fig. 7.2.3a, was designed to improve the bandwidth at higher frequencies (CC-FBA-IB). In contrast to the designed CC-FBA, shown in Fig. 7.2.3b, the $|\underline{S}_{21}|$ and the P_{out} was improved (CC-FBA-IG) for a similar f_{c} of the CS-FBA. The *GP* of the CSS is 0.52 mm (8 × 65 μm) for the CS-FBA and CC-FBA-IB shown in Fig. 7.2.2 and Fig. 7.2.3a. The *GP* of the single CSS is equal to the *GP* of the CSS and the CGS of the CC. The CC-FBA-IG, shown in Fig. 7.2.3b, comprises a CSS and CGS with a *GP* of 0.8 mm (8 × 100 μm) for each stage. To offer a $|\underline{S}_{21}|$ of about 13 dB at lower frequencies for the CS-FBA and CC-FBA-IB and maintain simultaneously a matching at the input and output of the FBA of better than −10 dB, R_{fp} of the parallel feedback resistor was chosen to 280 Ω and 285 Ω respectively. R_{fp} of 300 Ω was chosen for the CC-FBA-IG to achieve the same f_{c} as the CS-FBA. Although the series feedback resistor with resistance R_{fs} —series resistor in the source path of the CSS— can be used to improve the input and output matching of the FBA, it was omitted ($R_{\text{fs}} = 0\,\Omega$) due to the fact that the additional series feedback resistor lead to an additional power degradation and an increased *NF* of the FBA. The width of the transmission line in the feedback path was chosen to 20 μm to realize a moderate parallel feedback inductance (L_{fp}) which leads to an increase in $|\underline{S}_{21}|$ of 1–2 dB at higher frequencies. To get rid off the DC current in the feedback path, the parallel feedback capacitor with capacitance C_{fp} was added in series with the parallel feedback resistor with R_{fp}. However, to achieve multi-decade bandwidth performance of the CS-FBA, shown in Fig. 7.2.2 and Fig. 7.2.1a, an external surface mounted device (SMD) capacitor with capacitance $C_{\text{fp,ext}}$ of about 2 μF is required in parallel to the parallel feedback capacitor with C_{fp} to enable low frequency operation down to 10 kHz. To avoid oscillations in the feedback path due to the bondwire connection between the on-chip parallel feedback capacitor with $C_{\text{fp}} \approx 6.75$ pF and the off-chip capacitor with $C_{\text{fp,ext}}$, an additional series resistor with the attenuation resistance (R_{att}) of about 10 Ω was added. Due to the fact that the output impedance of the CGS can become negative which could lead to unstable behavior of the CGS, a stabilization resistor with R_{st} and a stabilization capacitor with C_{st} was added in the gate path of the CGS. Input matching network consists of a two stage network with two capacitors and two inductors. The output matching network comprises only one inductor realized by a coupled transmission line for the CS-FBA design. Iterative design steps for the input and output matching networks were needed to achieve the desired matching network of better than −10 dB. Due to the fact that the networks cannot be designed independently of each other ($\underline{S}_{12}$ of the CSS and $\underline{S}_{12}$ of the CGS are not equal zero). The on-chip capacitors are fabricated by metal-insulator-metal (MIM) capacitors and the on-chip resistors are fabricated by thin-film resistors (TFRs).

7.2.2 On-Wafer Measurement Results

7.2.2.1 S-Parameter Results

Fig. 7.2.4 and Fig. 7.2.5 show the measured S-parameters of the CS-FBA. A bandwidth between 10 GHz and 12 GHz is achieved depending on the chosen quiescent point, shown in Fig. 7.2.4a. The $|\underline{S}_{21}|$ of 13 dB at lower frequencies increases 1–2 dB up to 9 GHz. Reducing I_{DSQ} of the active device has only a minor influence on the S-parameters. However, to achieve maximum bandwidth it is necessary to use a higher V_{DS}. Input and output matching, shown in Fig. 7.2.5, is better than −10 dB over the complete frequency range. Fig. 7.2.6 and Fig. 7.2.7 show the measured S-parameters of the CC-FBA-IB. A bandwidth between 15 GHz and 17 GHz is achieved depending on the chosen quiescent point, shown in Fig. 7.2.6a. Choosing $V_{\text{DS}} = 20$ V, the $|\underline{S}_{21}|$ of 13 dB at lower frequencies increases 1–2 dB up to 15 GHz while maintaining the input and output matching of better than −10 dB over the complete frequency range. Reducing V_{DS} results in lower bandwidth as well as in a degradation of the input matching, shown in Fig. 7.2.6a and Fig. 7.2.7a respectively. A lower I_{DSQ} has only a minor influence on the small-signal parameters.
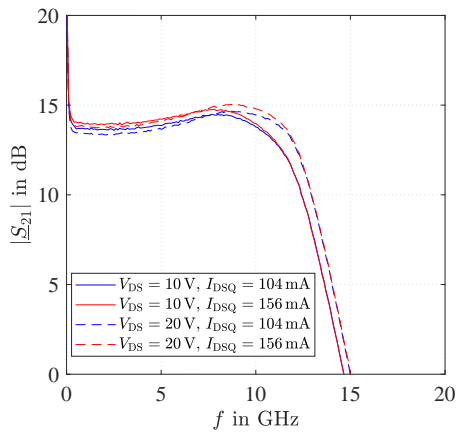
(a) $|\underline{S}_{21}|$ of the CS-FBA.
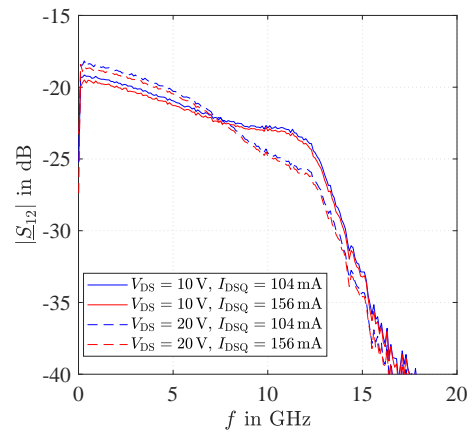
(b) $|\underline{S}_{12}|$ of the CS-FBA.

Figure 7.2.4: (a) Measured $|\underline{S}_{21}|$ and (b) measured $|\underline{S}_{12}|$ of the CS-FBA at different quiescent points.
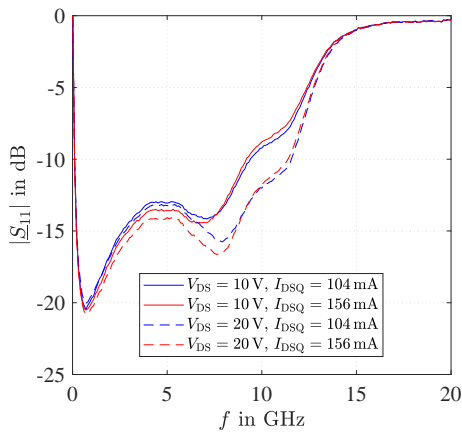
(a) $|\underline{S}_{11}|$ of the CS-FBA.
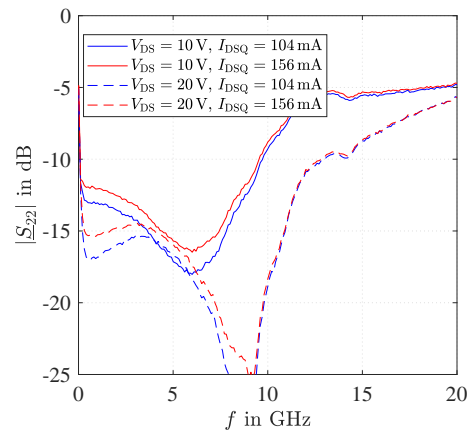
(b) $|\underline{S}_{22}|$ of the CS-FBA.

Figure 7.2.5: (a) Measured $|\underline{S}_{11}|$ and (b) measured $|\underline{S}_{22}|$ of the CS-FBA at different quiescent points.
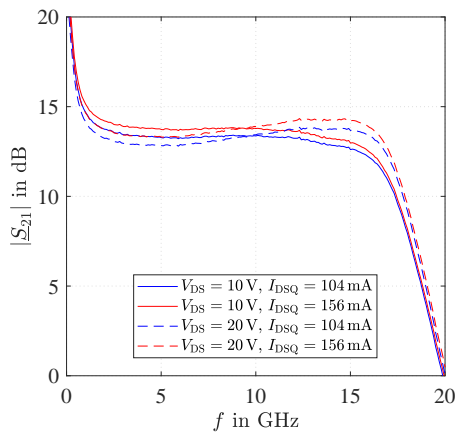
(a) $|\underline{S}_{21}|$ of the CC-FBA-IB.
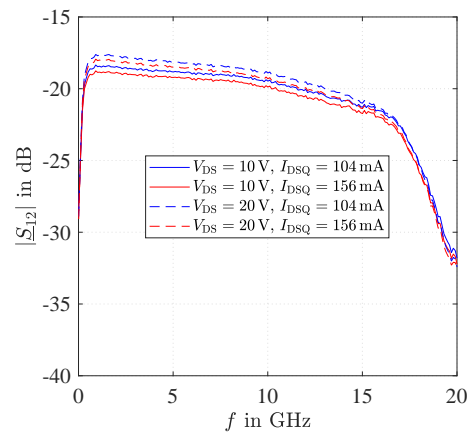
(b) $|\underline{S}_{12}|$ of the CC-FBA-IB.

Figure 7.2.6: (a) Measured $|\underline{S}_{21}|$ and (b) measured $|\underline{S}_{12}|$ of the CC-FBA-IB at different quiescent points.

(a) $|\underline{S}_{11}|$ of the CC-FBA-IB.
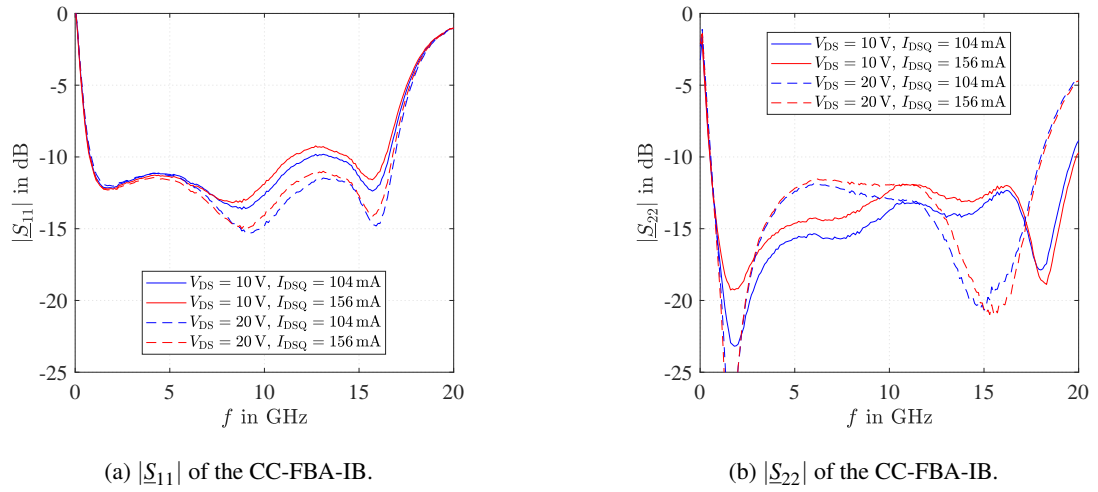
(b) $|\underline{S}_{22}|$ of the CC-FBA-IB.

Figure 7.2.7: (a) Measured $|\underline{S}_{11}|$ and (b) measured $|\underline{S}_{22}|$ of the CC-FBA-IB at different quiescent points.

(a) $|\underline{S}_{21}|$ of the CC-FBA-IG.
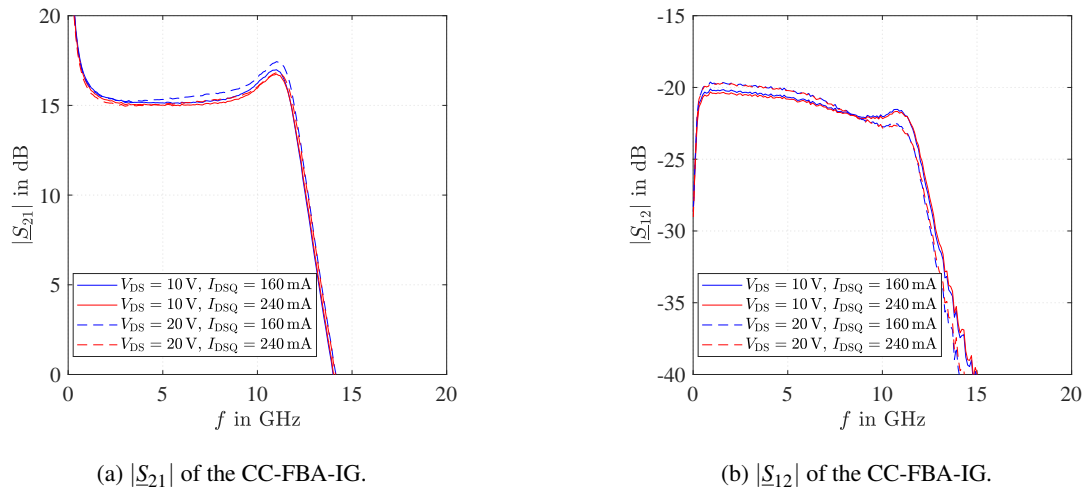
(b) $|\underline{S}_{12}|$ of the CC-FBA-IG.

Figure 7.2.8: (a) Measured $|\underline{S}_{21}|$ and (b) measured $|\underline{S}_{12}|$ of the CC-FBA-IG at different quiescent points.

(a) $|\underline{S}_{11}|$ of the CC-FBA-IG.
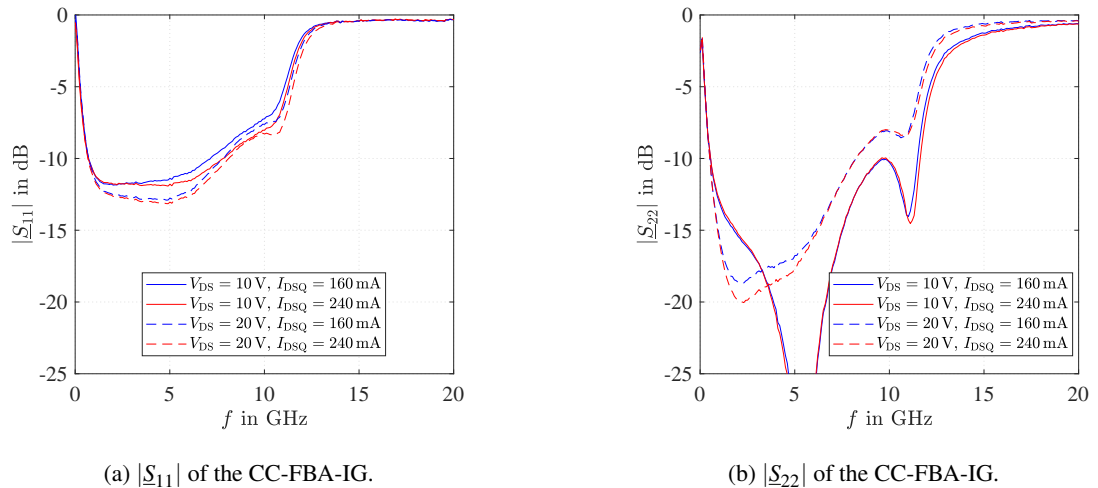
(b) $|\underline{S}_{22}|$ of the CC-FBA-IG.

Figure 7.2.9: (a) Measured $|\underline{S}_{11}|$ and (b) measured $|\underline{S}_{22}|$ of the CC-FBA-IG at different quiescent points.

Fig. 7.2.8 and Fig. 7.2.9 show the measured S-parameters of the CC-FBA–IG. A bandwidth of 12 GHz is achieved while maintaining a $|\underline{S}_{21}|$ of 15 dB at lower frequencies, shown in Fig. 7.2.8a. At higher frequencies the $|\underline{S}_{21}|$ increases up to 17 dB at 11 GHz. Reducing the quiescent point by reducing V_{DS} or I_{DSQ} has only a minor influence on the $|\underline{S}_{21}|$ and the input matching. The output matching can be significantly improved by choosing $V_{DS} = 20$ V, shown in Fig. 7.2.9b. An input matching and output matching of better than -7 dB and -10 dB are achieved respectively over the complete frequency range.

7.2.2.2 Noise Figure Results

Fig. 7.2.10 and Fig. 7.2.11 show the measured NF of the CS-FBA, CC-FBA-IB and CC-FBA-IG. A NF of about 4 dB is obtained in a wide frequency range for the CS-FBA and the CC-FBA-IB, shown in Fig. 7.2.10 and Fig. 7.2.11a, choosing the quiescent point $V_{DS} = 10$ V. The CC-FBA-IG even achieves a $NF = 3$ dB at moderate frequencies. Increasing V_{DS} degrades the NF of all three designs by 1–2 dB. I_{DSQ} has only a minor influence on the noise performance.
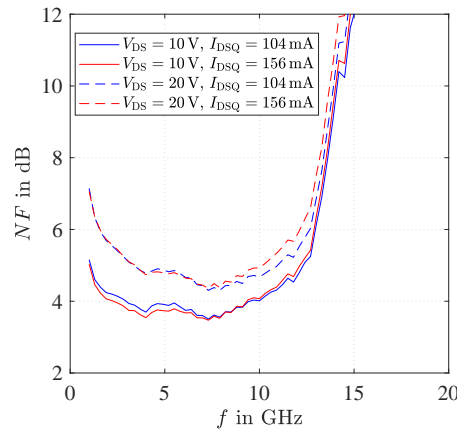
Figure 7.2.10: Measured NF of the CS-FBA at different quiescent points.
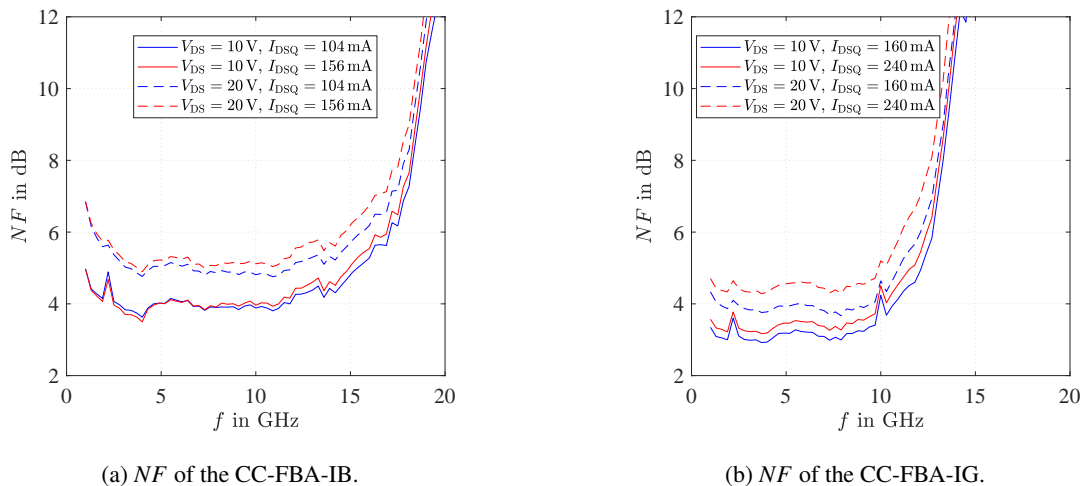
(a) NF of the CC-FBA-IB.

(b) NF of the CC-FBA-IG.

Figure 7.2.11: (a) and (b) Measured NF of the CC-FBA-IB and the CC-FBA-IG, respectively, at different bias points.

7.2.2.3 1-Tone Results of the CS-FBA

Fig. 7.2.12–Fig. 7.2.16 show the measured 1-Tone results of the CS-FBA. Fig. 7.2.12a shows the P_{out}, the *Gain* and the *PAE* versus P_{in} over frequency at a certain quiescent point ($V_{DS} = 20\,V$, $I_{DSQ} = 156\,mA$). The blue solid lines in Fig. 7.2.12a highlight the large-signal performance in the frequency range of 1–11 GHz. The red dashed line highlights the f_c of 12 GHz. The CS-FBA design achieves a $P_{out,max}$ of about 1 W over the complete frequency range for a $P_{DISS,MAX}$ of 3.64 W ($\frac{P_{DISS,MAX}}{GP} = 7\,\frac{W}{mm}$) at a certain quiescent point ($V_{DS} = 20\,V$, $I_{DSQ} = 156\,mA$). At lower frequencies the P_{out} is even slightly higher, shown in Fig. 7.2.12b.

Fig. 7.2.13 shows the *Gain* and the *PAE* versus frequency and versus P_{out} at a certain quiescent point ($V_{DS} = 20\,V$, $I_{DSQ} = 156\,mA$). At a $P_{out} = 30\,dBm$ the CS-FBA offers a *Gain* of about 11 dB, shown in Fig. 7.2.13a. Furthermore, the f_c can be recognized due to the degradation of the *Gain* at 12 GHz. A maximum *PAE* of 27 % is achieved at lower frequencies and the *PAE* is better than 20 % at a $P_{out} = 30\,dBm$ over the complete frequency range, shown in Fig. 7.2.13b.

(a) P_{out}, *Gain* and *PAE* vs. P_{in} over frequency.

(b) P_{out} vs. frequency vs. P_{in}.
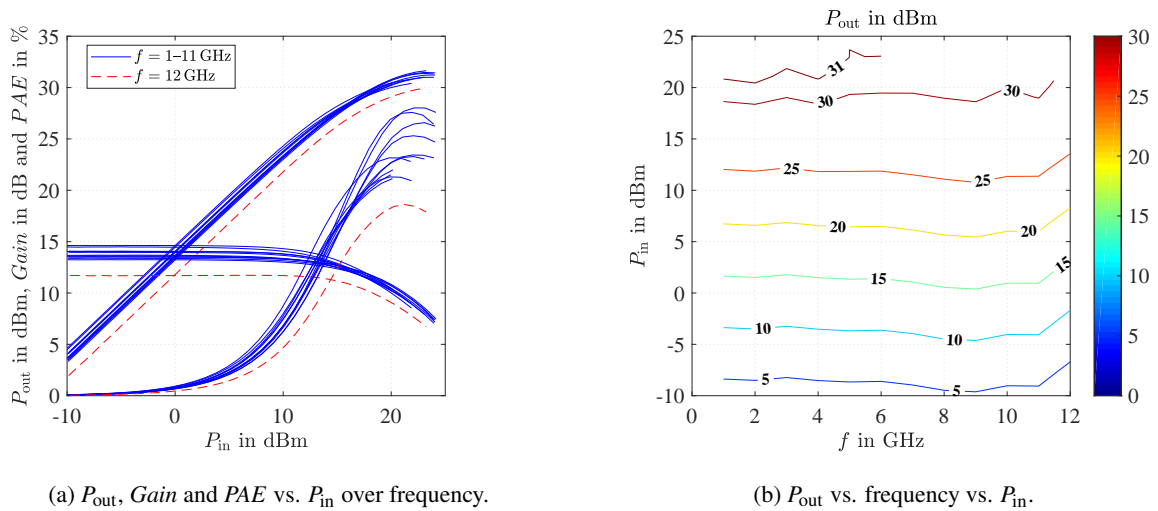
Figure 7.2.12: (a) Measured P_{out}, *Gain* and *PAE* vs. P_{in} over frequency and (b) measured P_{out} vs. frequency vs. P_{in} of the CS-FBA at $V_{DS} = 20\,V$ and $I_{DSQ} = 156\,mA$.

(a) *Gain* vs. frequency vs. P_{out}.

(b) P_{out} vs. P_{in} vs. frequency.

Figure 7.2.13: (a) Measured *Gain* vs. frequency vs. P_{out} and (b) measured *PAE* vs. frequency vs. P_{out} of the CS-FBA at $V_{DS} = 20\,V$ and $I_{DSQ} = 156\,mA$.

Fig. 7.2.14 shows the $P1dB$ versus frequency over different quiescent points and the normalized *Gain* versus frequency and versus P_{out} at a certain quiescent point ($V_{DS} = 20\,V$, $I_{DSQ} = 156\,mA$). Increasing $V_{DS} = 10\,V$ to $V_{DS} = 20\,V$ or $I_{DSQ} = 104\,mA$ to $I_{DSQ} = 156\,mA$ improves the $P1dB$ by 1 dB. A maximum $P1dB$ of 27–28 dBm is achieved over the complete frequency range, shown in Fig. 7.2.14a. Using Fig. 7.2.14b, the $P0.5dB$ and $P3dB$ can be determined to 26 dBm and 30 dBm respectively at a certain quiescent point ($V_{DS} = 20\,V$, $I_{DSQ} = 156\,mA$).
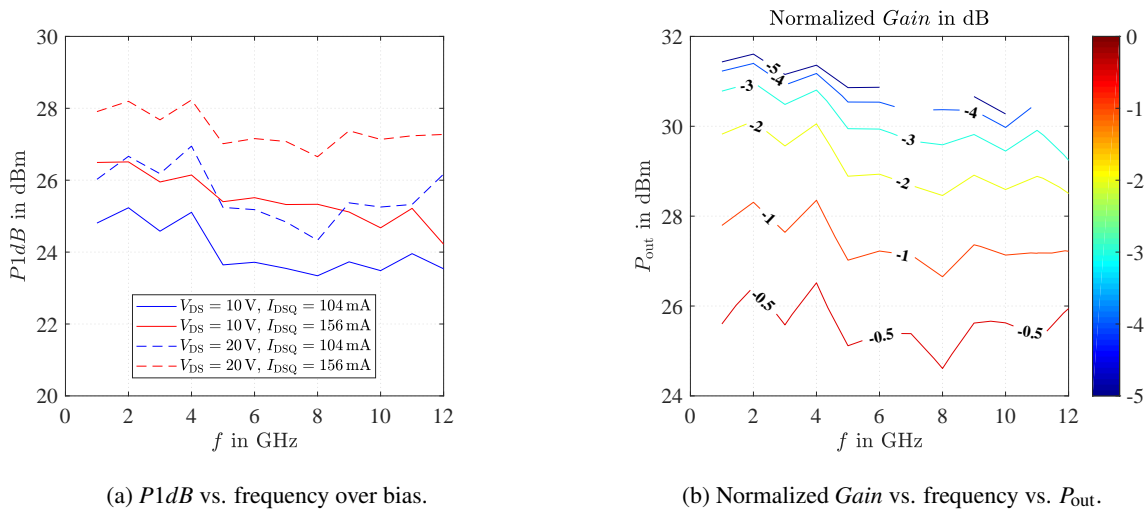
(a) *P1dB* vs. frequency over bias.

(b) Normalized *Gain* vs. frequency vs. P_{out}.

Figure 7.2.14: (a) Measured *P1dB* vs. frequency over different quiescent points and (b) measured normalized *Gain* vs. frequency vs. P_{out} at $V_{DS} = 20\,V$ and $I_{DSQ} = 156\,mA$ of the CS-FBA.

Fig. 7.2.15 shows the $HD2$ and $HD3$ versus frequency and versus P_{out} at a certain quiescent point ($V_{DS} = 20\,V$, $I_{DSQ} = 156\,mA$). A $HD2$ and $HD3$ of about $-20\,dBc$ are achieved at a $P_{out} = 30\,dBm$ over a wide frequency range, shown in Fig. 7.2.15a and Fig. 7.2.15b. $HD2$ and $HD3$ are only plotted up to 6 GHz and 4 GHz, respectively due to the fact that the harmonics at higher frequencies are above the f_c of the CS-FBA and therefore can be filtered by a low-pass filter. At a P_{out} which is $\approx 10\,dB$ lower than the $P1dB$, a $HD2$ between $-30\,dBc$ and $-35\,dBc$ and a $HD3$ of better than $-40\,dBc$ are achieved.
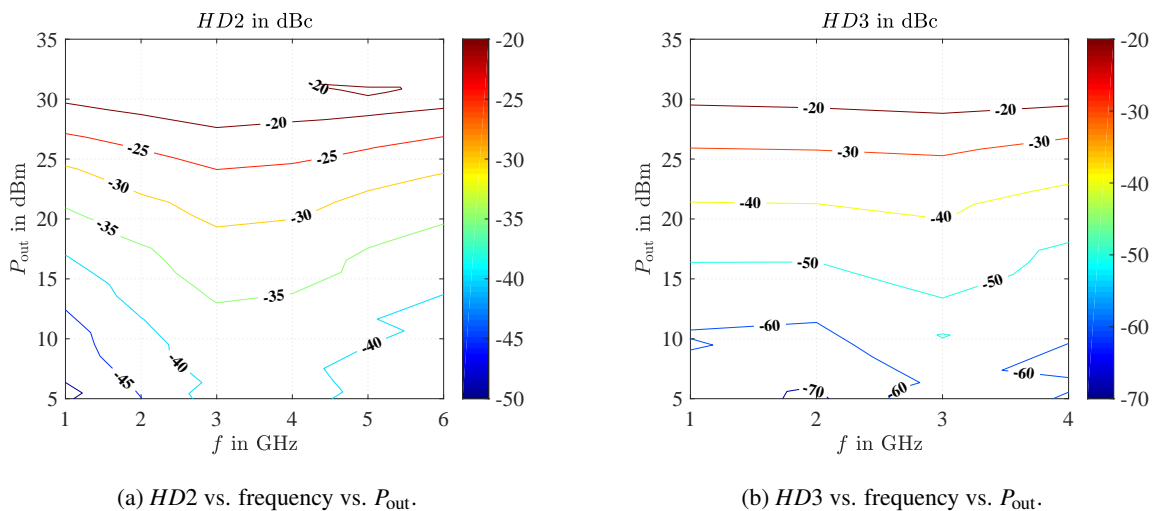
(a) *HD2* vs. frequency vs. P_{out}.

(b) *HD3* vs. frequency vs. P_{out}.

Figure 7.2.15: (a) Measured *HD2* and (b) measured *HD3* vs. frequency vs. P_{out} of the CS-FBA at $V_{DS} = 20\,V$ and $I_{DSQ} = 156\,mA$.

Fig. 7.2.16 shows the total P_{DISS} and the I_{DS} versus frequency and versus P_{out} at a certain quiescent point ($V_{\text{DS}} = 20\,\text{V}$, $I_{\text{DSQ}} = 156\,\text{mA}$). A minimum P_{DISS} of $\approx 2.7\,\text{W}$ is achieved at a $P_{\text{out}} \approx 26\,\text{dBm}$, shown in Fig. 7.2.16a, which is relatively close to the $P1dB$. At lower P_{out} the $P_{\text{DISS}} \approx 3.1\,\text{W}$ and at $P_{\text{out,max}}$ the $P_{\text{DISS,MAX}} \approx 3.6\,\text{W}$. The P_{DISS} only slightly depends on frequency and is therefore relatively flat over the complete frequency range. Fig. 7.2.16b shows the self-biasing effect of the CSS. The I_{DS} increases from $I_{\text{DSQ}} = 156\,\text{mA}$ up to $I_{\text{DS}} = 230\,\text{mA}$.

(a) P_{DISS} vs. frequency vs. P_{out}.

(b) I_{DS} vs. frequency vs. P_{out}.
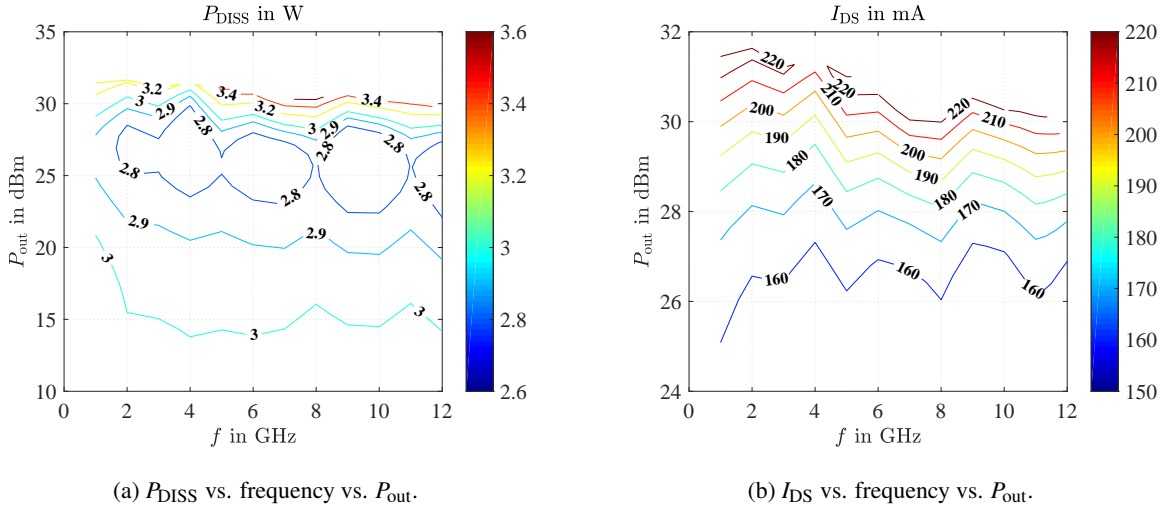
Figure 7.2.16: (a) Measured P_{DISS} and (b) measured I_{DS} vs. frequency vs. P_{out} of the CS-FBA at $V_{\text{DS}} = 20\,\text{V}$ and $I_{\text{DSQ}} = 156\,\text{mA}$.

7.2.2.4 1-Tone Results of the CC-FBA-IB

Fig. 7.2.17–Fig. 7.2.21 show the measured 1-Tone results of the CC-FBA-IB. Fig. 7.2.17a shows the P_{out}, the *Gain* and the *PAE* versus P_{in} over frequency at a certain quiescent point ($V_{\text{DS}} = 20\,\text{V}$, $I_{\text{DSQ}} = 156\,\text{mA}$). The blue solid lines in Fig. 7.2.17a highlight the large-signal performance in the frequency range of 1–16 GHz. The red dashed line highlights the f_{c} of 17 GHz. The CC-FBA-IB design achieves a $P_{\text{out,max}}$ of about 27–30 dBm over the complete frequency range for a $P_{\text{DISS,MAX}}$ of 7.28 W ($\frac{P_{\text{DISS,MAX}}}{GP} = 7\,\frac{\text{W}}{\text{mm}}$) at a certain quiescent point ($V_{\text{DS}} = 20\,\text{V}$, $I_{\text{DSQ}} = 156\,\text{mA}$). The P_{out} decreases at higher frequencies, shown in Fig. 7.2.17b.

(a) P_{out}, *Gain* and *PAE* vs. P_{in} over frequency.

(b) P_{out} vs. frequency vs. P_{in}.
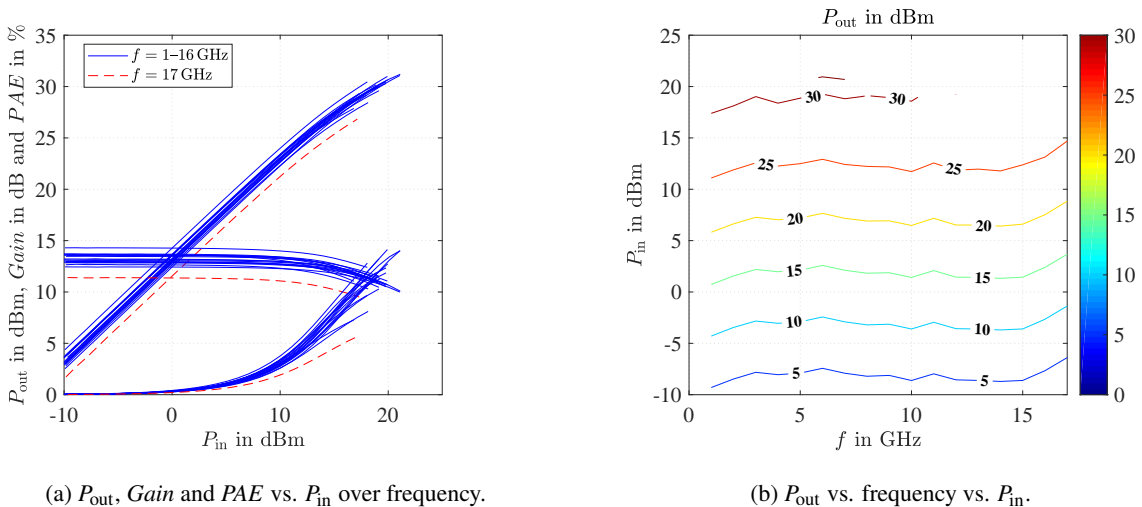
Figure 7.2.17: (a) Measured P_{out}, *Gain* and *PAE* vs. P_{in} over frequency and (b) measured P_{out} vs. frequency vs. P_{in} of the CC-FBA-IB at $V_{\text{DS}} = 20\,\text{V}$ and $I_{\text{DSQ}} = 156\,\text{mA}$.

Fig. 7.2.18 shows the *Gain* and the *PAE* versus frequency and versus P_{out} at a certain quiescent point ($V_{DS} = 20\,V$, $I_{DSQ} = 156\,mA$). At a $P_{out} = 28\,dBm$ the CC-FBA-IB offers a *Gain* of 13–10 dB, shown in Fig. 7.2.18a. Furthermore, the f_c can be recognized due to the degradation of the *Gain* at 17 GHz. However, the power degradation seems to take place much earlier at higher frequencies. At lower frequencies the *PAE* is about 12 % at a $P_{out} = 30\,dBm$ and the *PAE* is better than 6 % over the complete frequency range at a $P_{out} = 26\,dBm$, shown in Fig. 7.2.18b.

(a) *Gain* vs. frequency vs. P_{out}.

(b) P_{out} vs. P_{in} vs. frequency.
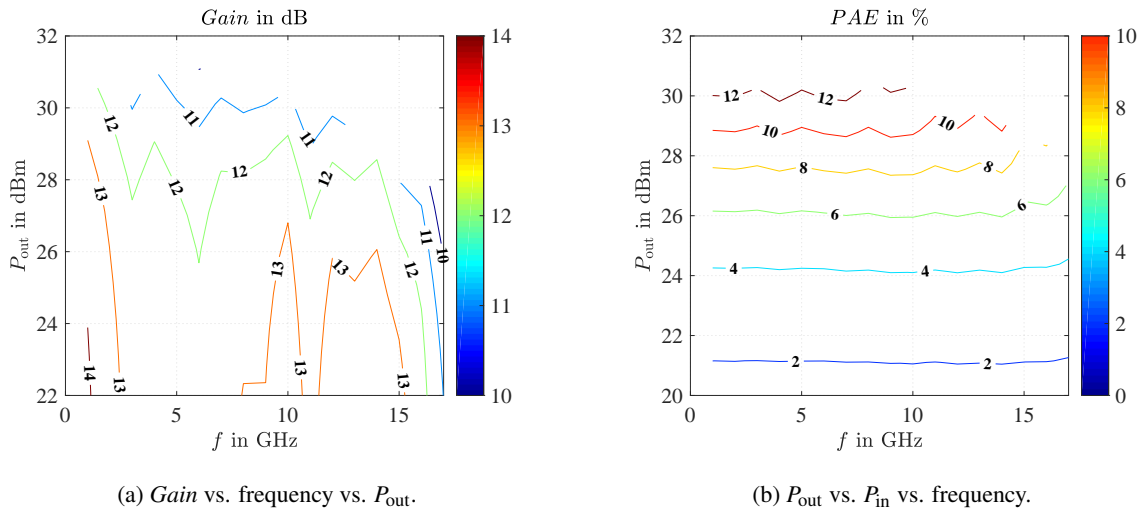
Figure 7.2.18: (a) Measured *Gain* vs. frequency vs. P_{out} and (b) measured *PAE* vs. frequency vs. P_{out} of the CC-FBA-IB at $V_{DS} = 20\,V$ and $I_{DSQ} = 156\,mA$.

Fig. 7.2.19 shows the *P1dB* versus frequency over different quiescent points and the normalized *Gain* versus frequency and versus P_{out} at a certain quiescent point ($V_{DS} = 20\,V$, $I_{DSQ} = 156\,mA$). Increasing $V_{DS} = 10\,V$ to $V_{DS} = 20\,V$ improves the *P1dB* by $\approx 1\,dB$ and increasing $I_{DSQ} = 104\,mA$ to $I_{DSQ} = 156\,mA$ improves the *P1dB* by $\approx 2\,dB$. A maximum *P1dB* of 25–29 dBm is achieved over the complete frequency range, shown in Fig. 7.2.19a. Using Fig. 7.2.19b, the *P0.5dB* and *P2dB* can be determined to 22–26 dBm and 27–30 dBm respectively at a certain quiescent point ($V_{DS} = 20\,V$, $I_{DSQ} = 156\,mA$).

(a) *P1dB* vs. frequency over bias.

(b) Normalized *Gain* vs. frequency vs. P_{out}.
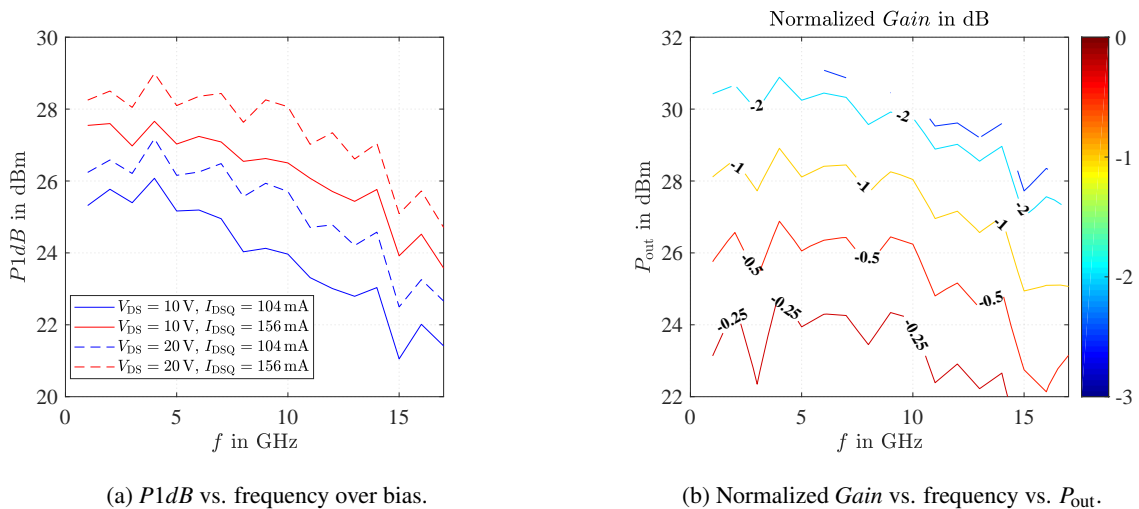
Figure 7.2.19: (a) Measured *P1dB* vs. frequency over different quiescent points and (b) measured normalized *Gain* vs. frequency vs. P_{out} at $V_{DS} = 20\,V$ and $I_{DSQ} = 156\,mA$ of the CC-FBA-IB.

Fig. 7.2.20 shows the $HD2$ and $HD3$ versus frequency and versus P_{out} at a certain quiescent point ($V_{\text{DS}} =$ 20 V, $I_{\text{DSQ}} = 156$ mA). A $HD2$ and $HD3$ of about -20 dBc are achieved at a $P_{\text{out}} = 30$ dBm over a wide frequency range, shown in Fig. 7.2.20a and Fig. 7.2.20b. $HD2$ and $HD3$ are only plotted up to 8.5 GHz and 5.7 GHz, respectively as the harmonics at higher frequencies are above the f_{c} of the CC-FBA-IB and therefore can be filtered by a low-pass filter. At a P_{out} which is ≈ 10 dB lower than the $P1dB$, a $HD2$ between -30 dBc and -35 dBc and a $HD3$ between -40 dBc and -50 dBc are achieved.

(a) $HD2$ vs. frequency vs. P_{out}.

(b) $HD3$ vs. frequency vs. P_{out}.
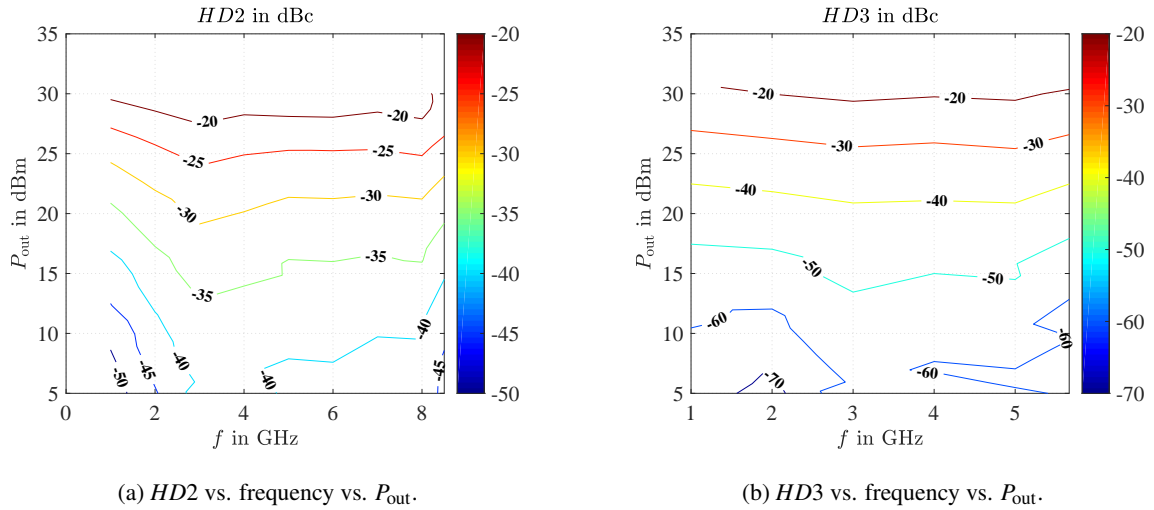
Figure 7.2.20: (a) Measured $HD2$ and (b) measured $HD3$ vs. frequency vs. P_{out} of the CC-FBA-IB at $V_{\text{DS}} = 20$ V and $I_{\text{DSQ}} = 156$ mA.

Fig. 7.2.21 shows the total P_{DISS} and the I_{DS} versus frequency and versus P_{out} at a certain quiescent point ($V_{\text{DS}} = 20$ V, $I_{\text{DSQ}} = 156$ mA). A minimum P_{DISS} of ≈ 5.8 W is achieved at a $P_{\text{out}} \approx 25$ dBm, shown in Fig. 7.2.21a. At lower P_{out} the $P_{\text{DISS}} \approx 6.1$ W and at $P_{\text{out,max}}$ the $P_{\text{DISS,MAX}} \approx 7.2$ W. Fig. 7.2.21b shows the self-biasing effect of the CC. The I_{DS} increases from $I_{\text{DSQ}} = 156$ mA up to $I_{\text{DS}} = 210$ mA.

(a) P_{DISS} vs. frequency vs. P_{out}.

(b) I_{DS} vs. frequency vs. P_{out}.
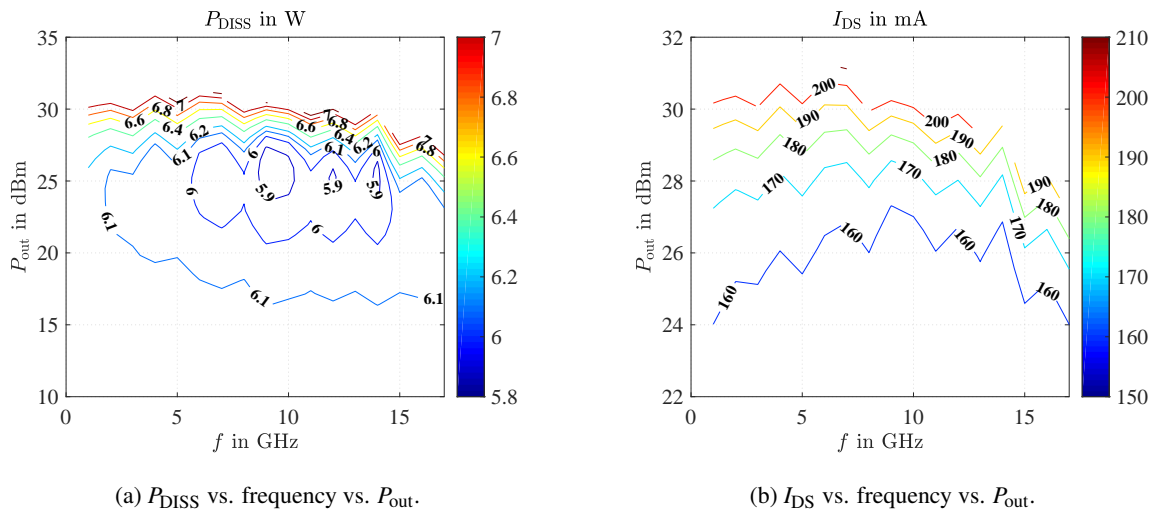
Figure 7.2.21: (a) Measured P_{DISS} and (b) measured I_{DS} vs. frequency vs. P_{out} of the CC-FBA-IB at $V_{\text{DS}} = 20$ V and $I_{\text{DSQ}} = 156$ mA.

7.2.2.5 1-Tone Results of the CC-FBA-IG

Fig. 7.2.22–Fig. 7.2.26 show the measured 1-Tone results of the CC-FBA-IG. Fig. 7.2.22a shows the P_{out}, the *Gain* and the *PAE* versus P_{in} over frequency at a certain quiescent point ($V_{DS} = 20$ V, $I_{DSQ} = 240$ mA). The blue solid lines in Fig. 7.2.22a highlight the large-signal performance in the frequency range of 1–11 GHz. The red dashed line highlights the f_c of 12 GHz. The CC-FBA-IG design achieves a $P_{out,max}$ of about 27–35 dBm over the complete frequency range for a $P_{DISS,MAX}$ of 11.2 W ($\frac{P_{DISS,MAX}}{GP} = 7 \frac{W}{mm}$) at a certain quiescent point ($V_{DS} = 20$ V, $I_{DSQ} = 240$ mA). The P_{out} decreases significantly at higher frequencies, shown in Fig. 7.2.22b.

(a) P_{out}, *Gain* and *PAE* vs. P_{in} over frequency.   (b) P_{out} vs. frequency vs. P_{in}.
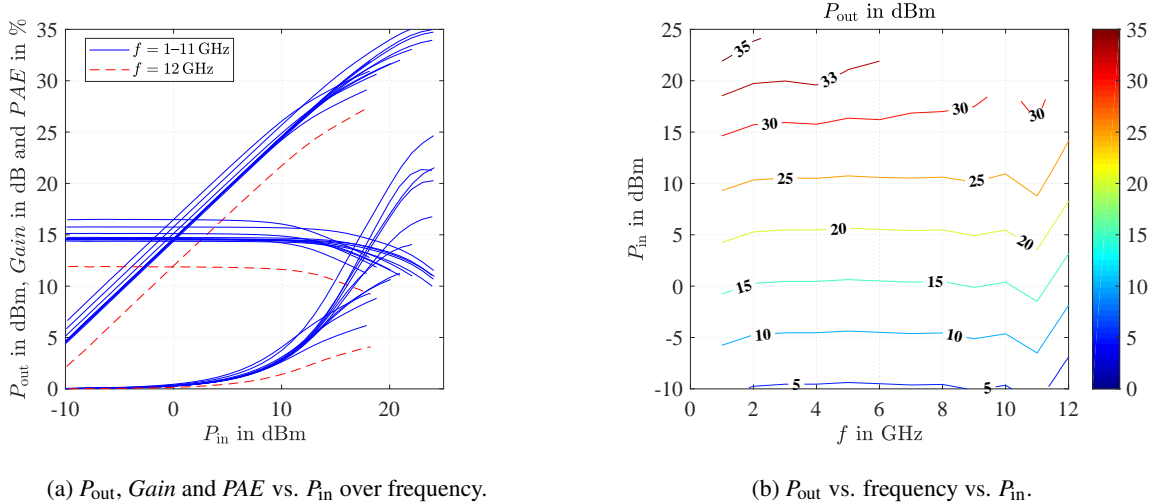
Figure 7.2.22: (a) Measured P_{out}, *Gain* and *PAE* vs. P_{in} over frequency and (b) measured P_{out} vs. frequency vs. P_{in} of the CC-FBA-IG at $V_{DS} = 20$ V and $I_{DSQ} = 240$ mA.

Fig. 7.2.23 shows the *Gain* and the *PAE* versus frequency and versus P_{out} at a certain quiescent point ($V_{DS} = 20$ V, $I_{DSQ} = 240$ mA). At a $P_{out} = 28$ dBm the CC-FBA-IG offers a *Gain* of 15–10 dB, shown in Fig. 7.2.23a. Furthermore, the f_c can be recognized due to the degradation of the *Gain* at 12 GHz. However, the power degradation seems to take place much earlier at higher frequencies. At lower frequencies the *PAE* is about 21 % at a $P_{out} = 35$ dBm and the *PAE* is better than 5 % over the complete frequency range at a $P_{out} = 27$ dBm, shown in Fig. 7.2.23b.

(a) *Gain* vs. frequency vs. P_{out}.   (b) P_{out} vs. P_{in} vs. frequency.
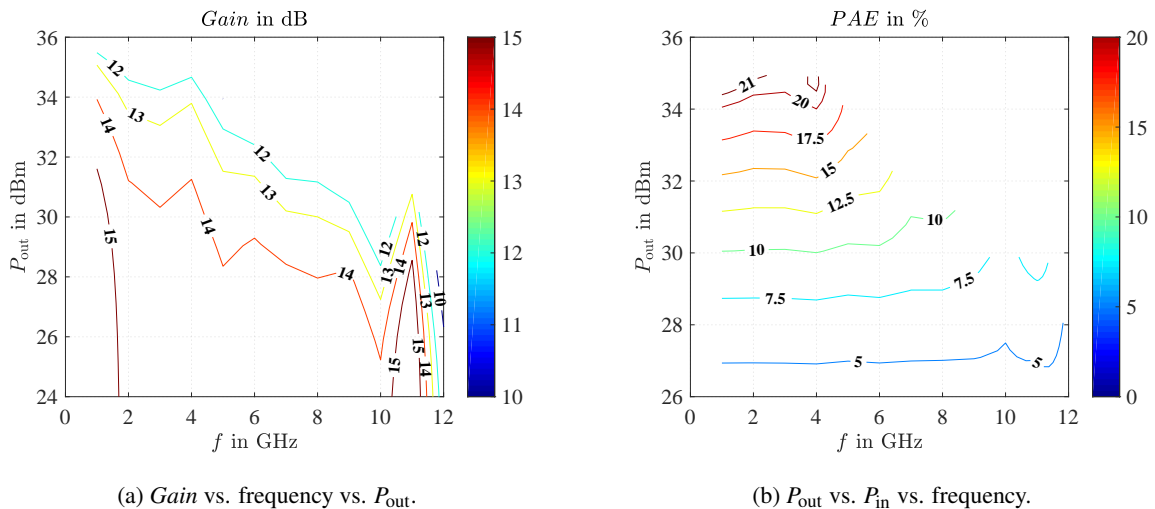
Figure 7.2.23: (a) Measured *Gain* vs. frequency vs. P_{out} and (b) measured *PAE* vs. frequency vs. P_{out} of the CC-FBA-IG at $V_{DS} = 20$ V and $I_{DSQ} = 240$ mA.

Fig. 7.2.24 shows the $P1dB$ versus frequency over different quiescent points and the normalized *Gain* versus frequency and versus P_{out} at a certain quiescent point ($V_{DS} = 20\,$V, $I_{DSQ} = 240\,$mA). Increasing $V_{DS} = 10\,$V to $V_{DS} = 20\,$V improves the $P1dB$ by ≈ 1–$2\,$dB 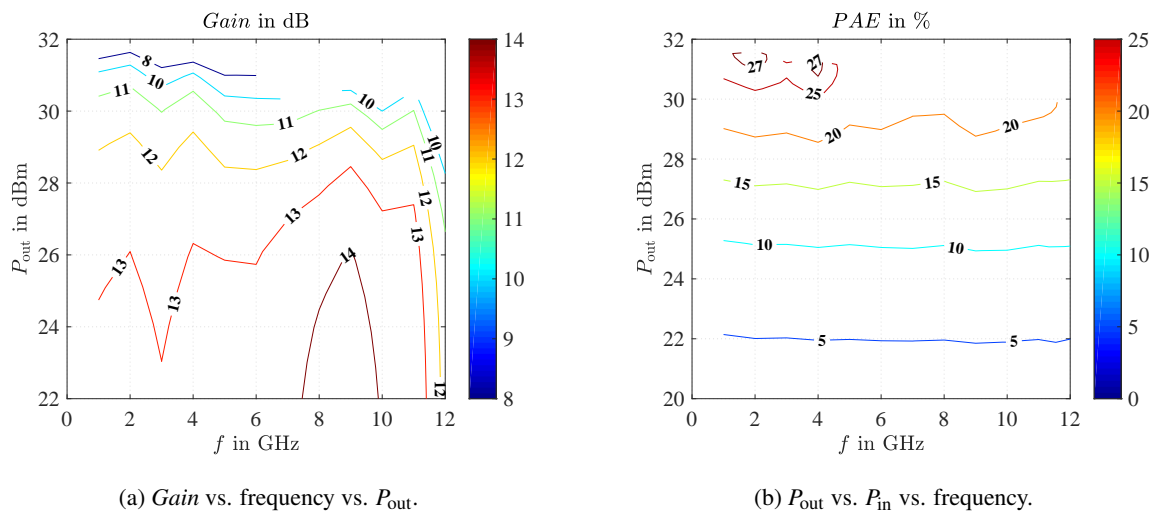and increasing $I_{DSQ} = 160\,$mA to $I_{DSQ} = 240\,$mA improves the $P1dB$ by ≈ 2–$3\,$dB. A maximum $P1dB$ of 25–$33\,$dBm is achieved over the complete frequency range, shown in Fig. 7.2.24a. Using Fig. 7.2.24b, the $P2dB$ and $P3dB$ can be determined to 26–$34\,$dBm and 28–$35\,$dBm respectively at a certain quiescent point ($V_{DS} = 20\,$V, $I_{DSQ} = 240\,$mA).


(a) *P1dB* vs. frequency over bias.

(b) Normalized *Gain* vs. frequency vs. P_{out}.
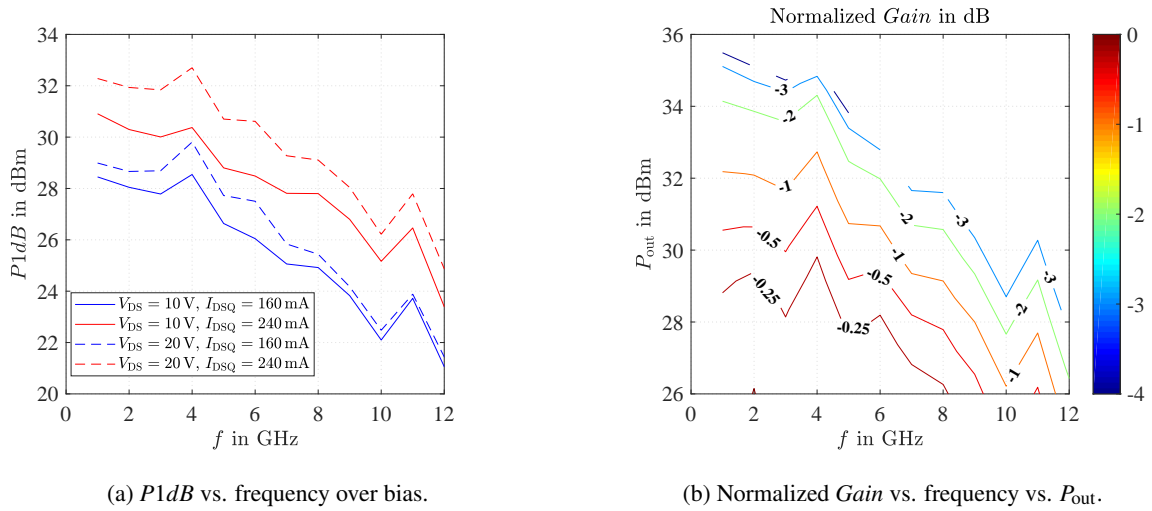
Figure 7.2.24: (a) Measured *P1dB* vs. frequency over different quiescent points and (b) measured normalized *Gain* vs. frequency vs. P_{out} at $V_{DS} = 20\,$V and $I_{DSQ} = 240\,$mA of the CC-FBA-IG.

Fig. 7.2.25 shows the *HD2* and *HD3* versus frequency and versus P_{out} at a certain quiescent point ($V_{DS} = 20\,$V, $I_{DSQ} = 240\,$mA). *HD2* and *HD3* of about $-20\,$dBc are achieved at a $P_{out} = 34\,$dBm over a wide frequency range, shown in Fig. 7.2.25a and Fig. 7.2.25b. *HD2* and *HD3* are only plotted up to $6\,$GHz and $4\,$GHz, respectively due to the fact that the harmonics at higher frequencies are above the f_c of the CC-FBA-IG and can therefore be filtered by a low-pass filter. At a P_{out} which is $\approx 10\,$dB lower than the *P1dB*, a *HD2* between $-40\,$dBc and $-45\,$dBc and a *HD3* of about $-50\,$dBc are achieved.

(a) *HD2* vs. frequency vs. P_{out}.

(b) *HD3* vs. frequency vs. P_{out}.
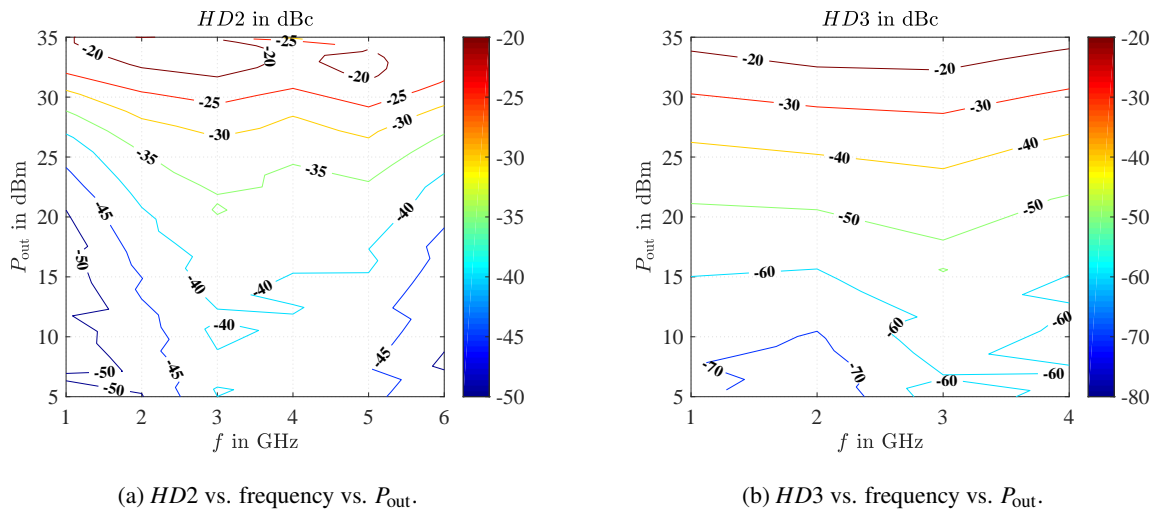
Figure 7.2.25: (a) Measured *HD2* and (b) measured *HD3* vs. frequency vs. P_{out} of the CC-FBA-IG at $V_{DS} = 20\,$V and $I_{DSQ} = 240\,$mA.

Fig. 7.2.26 shows the total P_{DISS} and the I_{DS} versus frequency and versus P_{out} at a certain quiescent point ($V_{DS} = 20\,\text{V}$, $I_{DSQ} = 240\,\text{mA}$). A minimum P_{DISS} of $\approx 8.7\,\text{W}$ is achieved at a $P_{out} \approx 30\,\text{dBm}$, shown in Fig. 7.2.26a. At lower P_{out} the $P_{DISS} \approx 9.5\,\text{W}$ and at $P_{out,max}$ the $P_{DISS,MAX} \approx 11.2\,\text{W}$. Fig. 7.2.26b shows the self-biasing effect of the CC. The I_{DS} increases from $I_{DSQ} = 240\,\text{mA}$ up to $I_{DS} = 340\,\text{mA}$.

(a) P_{DISS} vs. frequency vs. P_{out}.

(b) I_{DS} vs. frequency vs. P_{out}.
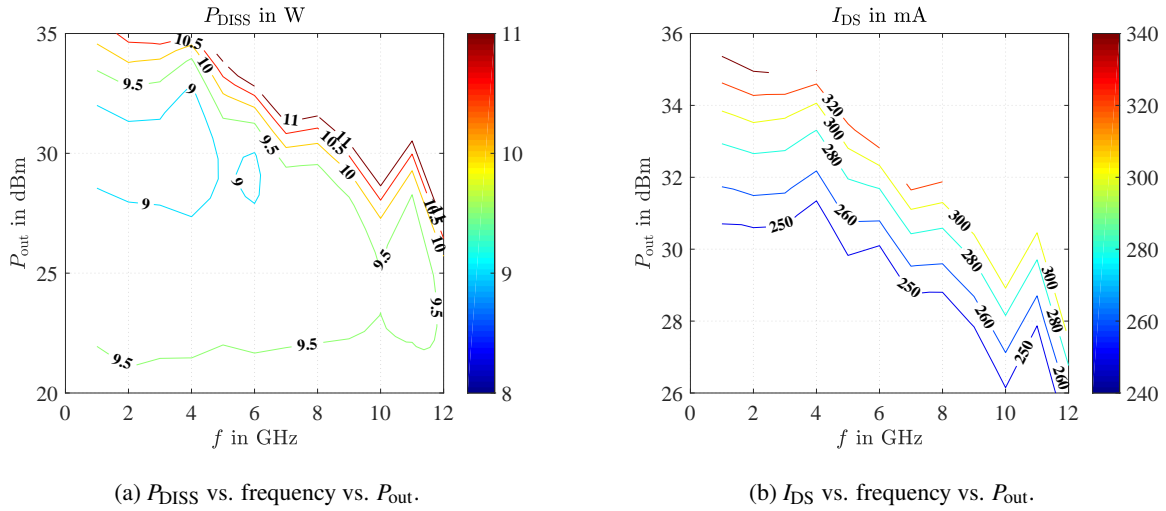
Figure 7.2.26: (a) Measured P_{DISS} and (b) measured I_{DS} vs. frequency vs. P_{out} of the CC-FBA-IG at $V_{DS} = 20\,\text{V}$ and $I_{DSQ} = 240\,\text{mA}$.

7.2.3 Comparison of Common-Source and Cascode Topology

7.2.3.1 Comparison of S-Parameter Results

Fig. 7.2.27 compares the measured $|\underline{S}_{21}|$ of the CS-FBA with the CC-FBAs at different bias conditions.

(a) $|\underline{S}_{21}|$ of the CS-FBA and the CC-FBAs (same P_{DISS} as the CS-FBA).

(b) $|\underline{S}_{21}|$ of the CS-FBA and the CC-FBAs (same quiescent point as the CS-FBA for each active cell).
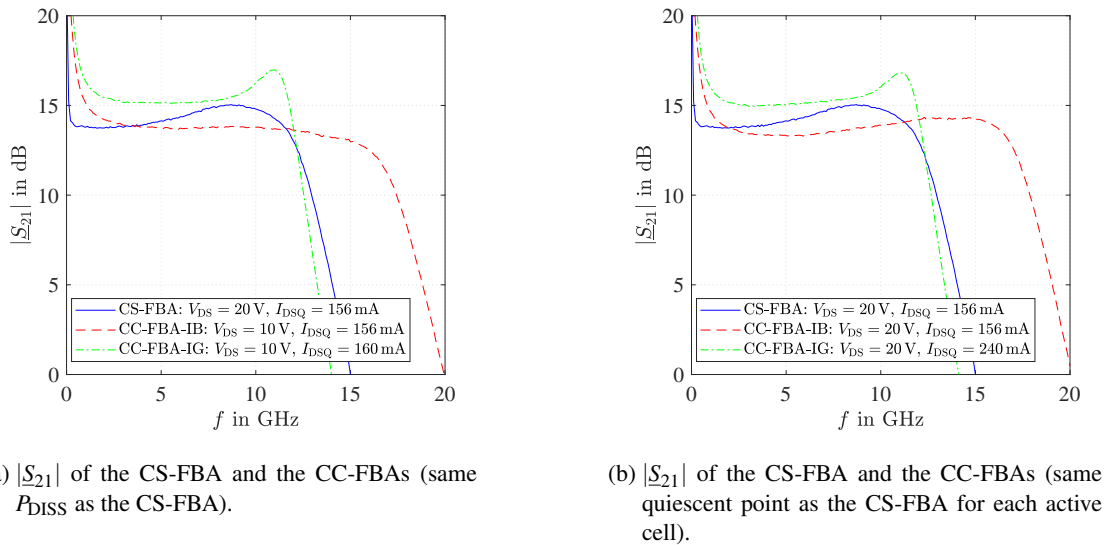
Figure 7.2.27: Comparison of measured $|\underline{S}_{21}|$ of the CS-FBA, the CC-FBA-IB and the CC-FBA-IG at different quiescent points.

Fig. 7.2.27a shows the performance of the CS-FBA and the CC-FBAs, biasing the FBAs in such a way that they dissipate similar DC power. The bandwidth of the CC-FBA-IB is increased by 4 GHz from

12 GHz to 16 GHz, which is an improvement of about 30 %. The CC-FBA-IG has a similar f_c as the CS-FBA but an increased $|\underline{S}_{21}|$ of $\approx$ 1–2 dB. Fig. 7.2.27b highlights the maximum improvement of the CC-FBAs compared to the CS-FBA using the same quiescent point for each active device. The bandwidth improvement of the CC-FBA-IB increases up to 40 % compared to the CS-FBA. However, the $|\underline{S}_{21}|$ of the CC-FBA-IG is very similar increasing the quiescent point by using a higher quiescent point.

7.2.3.2 Comparison of Noise Figure Results

Fig. 7.2.28 compares the measured NF of the CS-FBA with the CC-FBAs at different bias conditions. Fig. 7.2.28a shows the noise performance of the CS-FBA and the CC-FBAs, biasing the FBAs in such a way that they dissipate similar DC power. The NF of the CC-FBAs are 1–3 dB lower than the CS-FBA. The higher NF of the CS-FBA is mainly caused by the higher V_{DS} of the CS-FBA. The best noise performance of the active device cell can be achieved by using a $V_{DS} = 10$ V. The NF of the CS-FBA and the CC-FBAs can be compared in a better way in Fig. 7.2.28b using the same quiescent point for each active cell in both FBA topologies. However, the dissipated DC power of the CC-FBAs is much higher compared to the CS-FBA. The NF of the CS-FBA and the CC-FBA-IG is very similar at moderate and high frequencies. At lower frequencies the NF of the CC-FBA-IG is lower than NF of the CS-FBA due to the higher $|\underline{S}_{21}|$ in this frequency range. The NF of the CC-FBA-IB is slightly higher than the CS-FBA at moderate frequencies. At higher frequencies the NF of the CC-FBA-IB is better compared to the CS-FBA due to the higher f_c.
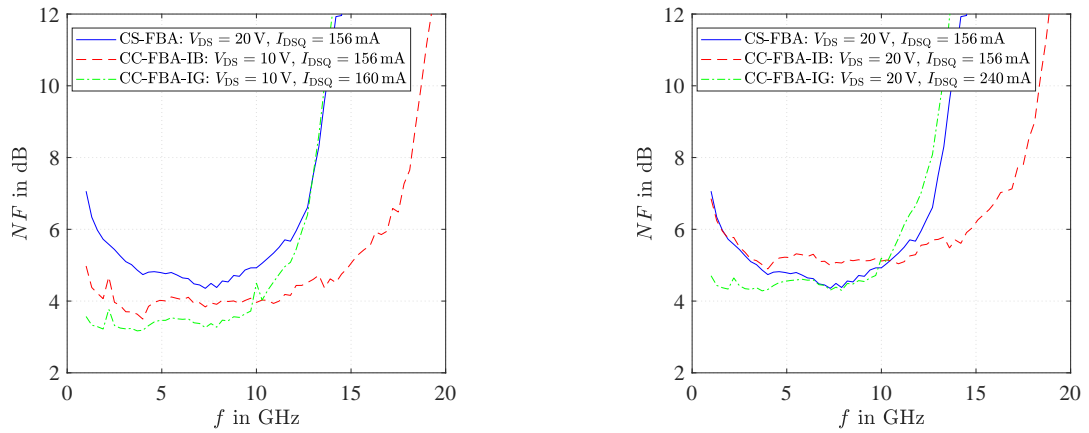
(a) NF of the CS-FBA and the CC-FBAs (same P_{DISS} as CS-FBA).

(b) NF of the CS-FBA and the CC-FBAs (same quiescent point as the CS-FBA for each active cell).

Figure 7.2.28: Comparison of measured NF of the CS-FBA, CC-FBA-IB and CC-FBA-IG at different quiescent points.

7.2.3.3 Comparison of 1-Tone Results

Fig. 7.2.29 compares the $P_{out,max}$ of the CS-FBA with the CC-FBAs for a $\frac{P_{DISS,MAX}}{GP}$ of 7 $\frac{W}{mm}$ at different bias conditions. Fig. 7.2.29a shows the $P_{out,max}$ of the CS-FBA and the CC-FBAs, biasing the FBAs in such a way that they dissipate similar DC power. The $P_{out,max}$ of the CS-FBA is $\approx$ 1 dB higher than the CC-FBA-IB and $\approx$ 1 dB lower at lower frequencies than the CC-FBA-IG. Another very important characteristic is the degradation of the $P_{out,max}$ over frequency. The $P_{out,max}$ of the CS-FBA degrades only by 1 dB over the useful bandwidth. In comparison to the CC-FBA-IB the $P_{out,max}$ degrades by 3 dB and the CC-FBA-IG even degrades by 6 dB, which is much higher than power degradation of the CS-FBA. Increasing the quiescent point of the CC-FBAs the power degradation of the CC-FBAs does not change significantly, shown in Fig. 7.2.29b. However, the $P_{out,max}$ of the CC-FBA-IG is $\approx$ 3 dB higher than the CS-FBA. Furthermore the $P_{out,max}$ of the CC-FBA-IB is similar to the $P_{out,max}$ of the CS-FBA in the same frequency range and only differs slightly at lower frequencies.
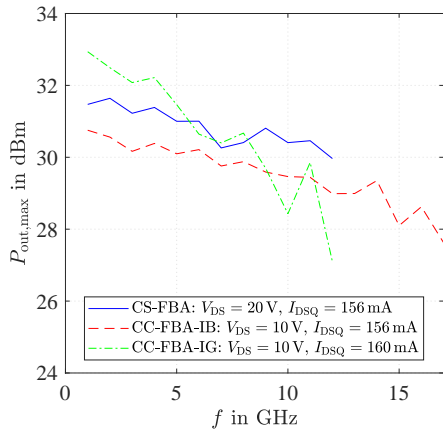
(a) $P_{out,max}$ vs. frequency of the CS-FBA and the CC-FBAs (same P_{DISS} as CS-FBA).
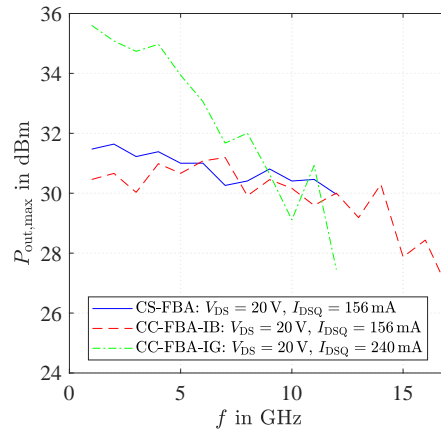
(b) $P_{out,max}$ vs. frequency of the CS-FBA and the CC-FBAs (same quiescent point as the CS-FBA for each active cell).

Figure 7.2.29: Comparison of measured $P_{out,max}$ vs. frequency of the CS-FBA, the CC-FBA-IB and the CC-FBA-IG at different quiescent points.

Fig. 7.2.30 compares the $P1dB$ of the CS-FBA with the CC-FBAs at different bias conditions. Fig. 7.2.30a shows the $P1dB$ of the CS-FBA and the CC-FBAs, biasing the FBAs in such a way that they dissipate similar DC power. The $P1dB$ is very similar of the CS-FBA in comparison to the CC-FBA-IG and the CC-FBA-IB at lower frequencies up to 5 GHz and 10 GHz respectively. At higher frequencies the $P1dB$ of the CC-FBAs degrades significantly. The $P1dB$ of the CC-FBA-IB decreases by ≈ 3 dB over the entire useful bandwidth and the CC-FBA-IG even decreases by ≈ 6 dB. Increasing the quiescent point of the CC-FBAs, the $P1dB$ of the CC-FBA-IG is improved by 4 dB over the whole bandwidth, shown in Fig. 7.2.30b and the $P1dB$ is slightly increased at moderate frequencies for the CC-FBA-IB. However, the $P1dB$ degradation of the CC-FBA-IG remains unaffected over the entire bandwidth. The $P1dB$ degradation of the CC-FBA-IB is slightly improved at moderate frequencies but is similar at higher frequencies.
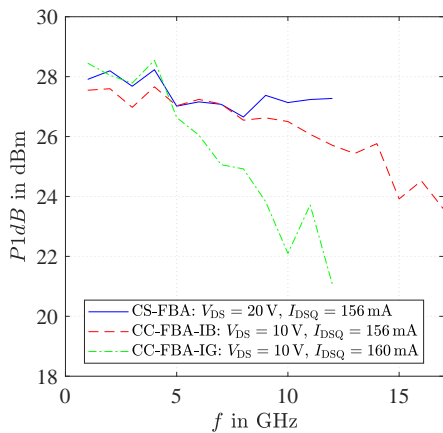
(a) $P1dB$ vs. frequency of the CS-FBA and the CC-FBAs (same P_{DISS} as CS-FBA).
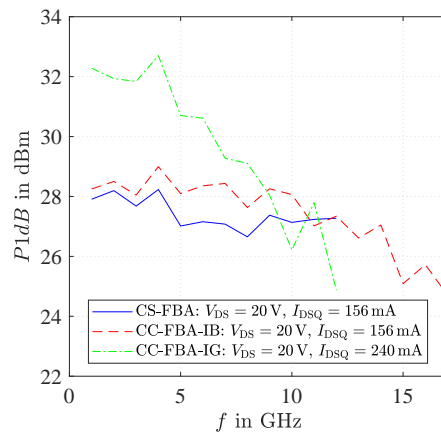
(b) $P1dB$ vs. frequency of the CS-FBA and the CC-FBAs (same quiescent point as the CS-FBA for each active cell).

Figure 7.2.30: Comparison of measured $P1dB$ vs. frequency of the CS-FBA, the CC-FBA-IB and the CC-FBA-IG at different quiescent points.

Fig. 7.2.31 compares the $HD2$ of the CS-FBA with the CC-FBAs at a P_{out} of 25 dBm at different bias conditions. Fig. 7.2.31a shows the $HD2$ of the CS-FBA and the CC-FBAs, biasing the FBAs in such a way that they dissipate similar DC power. The $HD2$ frequency response of the CS-FBA and the CC-FBAs is similar but the absolute level of the $HD2$ is different for the FBAs. The $HD2$ of the CC-FBA-IG is ≈ 1 dB less and the CC-FBA-IB is ≈ 2 dB less than the $HD2$ of the CS-FBA. Increasing the quiescent point of the CC-FBAs changes the $HD2$ performance significantly, shown in Fig. 7.2.31b. The $HD2$ of the CC-FBA-IG is improved by ≈ 5 dB over the whole bandwidth and even up to 10 dB at lower frequencies. The $HD2$ of the CC-FBA-IB is almost equal at lower and moderate frequencies to the CS-FBA. Due to the large rise of the $HD2$ of the CC-FBA-IB at higher frequencies the $HD2$ is even higher compared to the CS-FBA in this frequency range.
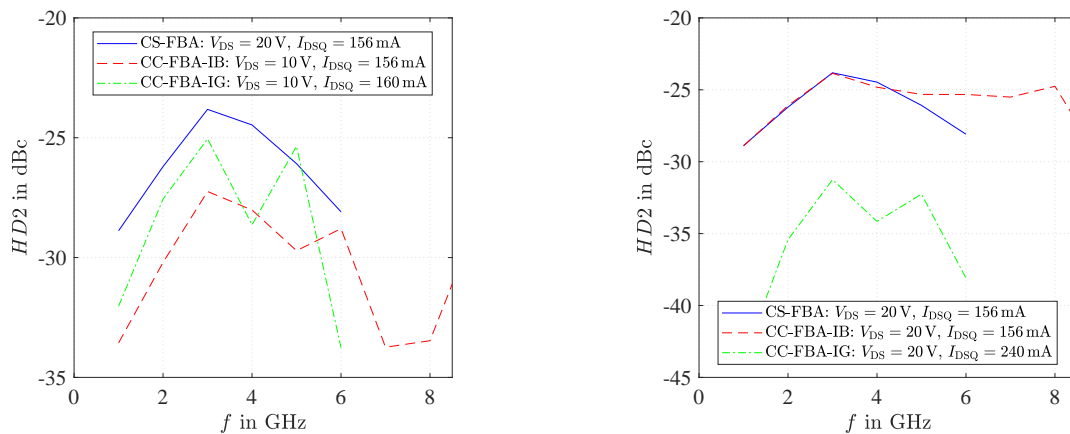
(a) $HD2$ vs. frequency of the CS-FBA and the CC-FBAs (same P_{DISS} as CS-FBA).

(b) $HD2$ vs. frequency of the CS-FBA and the CC-FBAs (same quiescent point as the CS-FBA for each active cell).

Figure 7.2.31: Comparison of measured $HD2$ vs. frequency of the CS-FBA, the CC-FBA-IB and the CC-FBA-IG at a $P_{\text{out}} = 25$ dBm at different quiescent points.

Fig. 7.2.32 compares the $HD3$ of the CS-FBA with the CC-FBAs at a P_{out} of 25 dBm at different bias conditions. Fig. 7.2.32a shows the $HD3$ of the CS-FBA and the CC-FBAs, biasing the FBAs in such a way that they dissipate similar DC power. The $HD3$ of the CS-FBA is 1–2 dB higher in the low frequency range compared to the CC-FBAs. At higher frequencies the $HD3$ of the CC-FBAs is 2–4 dB worse than the CS-FBA. Increasing the quiescent point of the CC-FBA-IG the $HD3$ is improved by ≈ 8–11 dB, shown in Fig. 7.2.32b. Therefore the $HD3$ of the CC-FBA-IG is much better than the CS-FBA. The $HD3$ of the CC-FBA-IB is also improved using a higher V_{DS} which leads to a slightly better behavior of the $HD3$ at lower and moderate frequencies compared to the CS-FBA. However, the improvement of the CC-FBA-IB amounts only 1–2 dB.
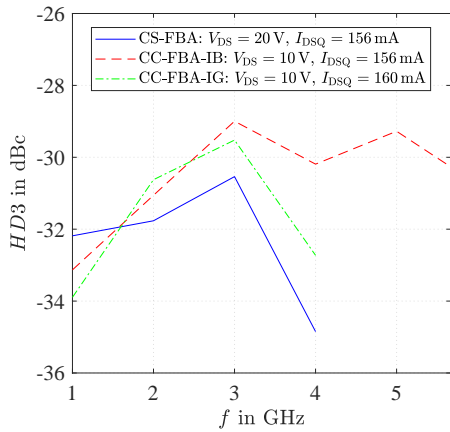
(a) *HD*3 vs. frequency of the CS-FBA and the CC-FBAs (same P_{DISS} as CS-FBA).
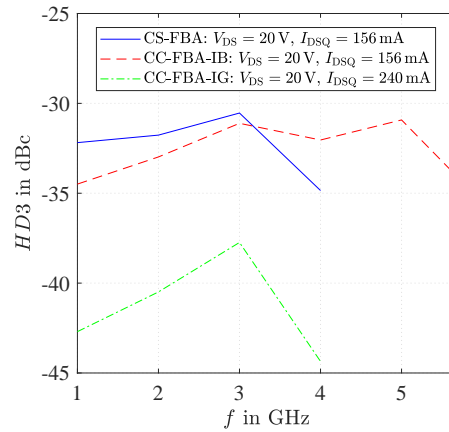
(b) *HD*3 vs. frequency of the CS-FBA and the CC-FBAs (same quiescent point as the CS-FBA for each active cell).

Figure 7.2.32: Comparison of measured *HD*3 vs. frequency of the CS-FBA, the CC-FBA-IB and the CC-FBA-IG at a $P_{out} = 25$ dBm at different quiescent points.

Fig. 7.2.33 compares the *PAE* of the CS-FBA with the CC-FBAs at a P_{out} of 25 dBm at different bias conditions. Fig. 7.2.33a shows the *PAE* of the CS-FBA and the CC-FBAs, biasing the FBAs in such a way that they dissipate similar DC power. The *PAE* of the CS-FBA and the CC-FBA-IB are similar and very flat over a wide frequency range. The *PAE* of the CC-FBA-IG degrades significantly with frequency and is much lower at higher frequencies than the CS-FBA. Increasing the quiescent point to gain maximum RF performance of the CC-FBAs lowers the *PAE* of the CC-FBAs significantly, shown in Fig. 7.2.33b. As a result the *PAE* of the CC-FBAs is much lower compared to the CS-FBA.
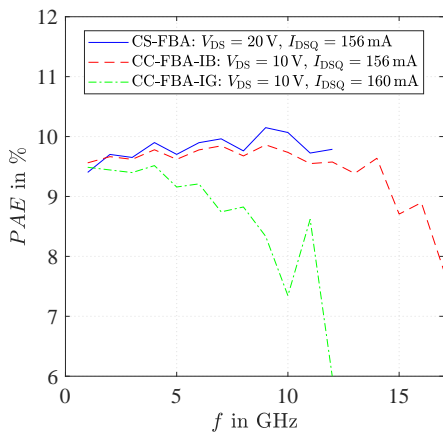
(a) *PAE* vs. frequency of the CS-FBA and the CC-FBAs (same P_{DISS} as CS-FBA).
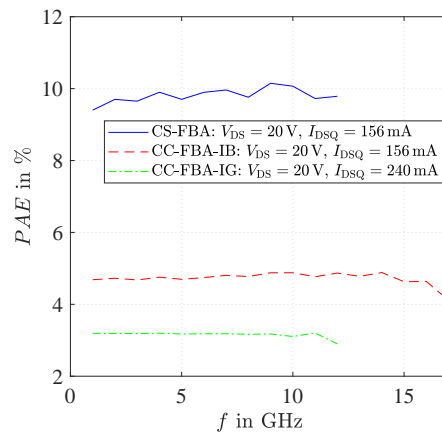
(b) *PAE* vs. frequency of the CS-FBA and the CC-FBAs (same quiescent point as the CS-FBA for each active cell).

Figure 7.2.33: Comparison of measured *PAE* vs. frequency of the CS-FBA, the CC-FBA-IB and the CC-FBA-IG at a $P_{out} = 25$ dBm at different quiescent points.

7.2.4 Conclusion

In Sec. 7.2 three different designed FBAs using the CS and the CC topology were presented to verify the theory described in Ch. 5. The small-signal measurements and large-signal measurements of the CS-FBA and the CC-FBAs were compared with each other to point out the advantages and disadvantages using CCs in broadband PAs.

Key advantages of the CC compared to the CSS in the FBA:

- The $|\underline{S}_{21}|$ of the CS-FBA was improved by two different ways using the CC topology:
  1. The bandwidth of the $|\underline{S}_{21}|$ was extended by 30 % up to 16 GHz (same P_{DISS} of CS-FBA and CC-FBA) and by 40 % up to 17 GHz (same quiescent point as the CS-FBA for each active cell) using the CC-FBA-IB.
  2. The $|\underline{S}_{21}|$ was increased by 1–2 dB using the CC-FBA-IG.
- Due to the higher $|\underline{S}_{21}|$ of the CC-FBA-IG compared to the CS-FBA, the *NF* of the CS-FBA was reduced by ≈ 2 dB at lower frequencies using the CC-FBA-IG (same quiescent point as the CS-FBA for each active cell).
- Furthermore, the $P_{\text{out,max}}$ of the CS-FBA was also improved by two different ways using the CC topology:
  1. Due to the extension of the bandwidth of the $|\underline{S}_{21}|$, the $P_{\text{out,max}}$ was also increased in this frequency range using the CC-FBA-IB.
  2. The $P_{\text{out,max}}$ was enhanced by ≈ 3 dB at lower and moderate frequencies using the CC-FBA-IG (same quiescent point as the CS-FBA for each active cell).
- The *P1dB* of the CS-FBA was increased by ≈ 4 dB at lower frequencies and by ≈ 2 dB at moderate frequencies using the CC-FBA-IG (same quiescent point as the CS-FBA for each active cell).
- Moreover, using the CC topology, the *HD*2 and the *HD*3 of the CS-FBA was improved, too. On the one hand the *HD*2 was enhanced by ≈ 1 dB and ≈ 2 dB (same P_{DISS} of CS-FBA and CC-FBA) using the CC-FBA-IG and CC-FBA-IB, respectively. On the other hand, using the CC-FBA-IG (same quiescent point as the CS-FBA for each active cell), the *HD*2 was even lowered by ≈ 5 dB. Additionally, the *HD*3 was also significantly enhanced by ≈ 8–11 dB using the CC-FBA-IG (same quiescent point as the CS-FBA for each active cell).

Key disadvantages of the CC compared to the CSS in the FBA:

- Using the same quiescent point of the CS-FBA and CC-FBA-IB for each active cell, the *NF* of the CC-FBA-IB degraded a little bit at moderate frequencies.
- Although the $P_{\text{out,max}}$ and the *P1dB* of the CS-FBA was increased at lower and moderate frequencies, using the CC-FBA-IG, the $P_{\text{out,max}}$ as well as the *P1dB* degraded by 6 dB over the useful bandwidth.
- One of the key disadvantages of the CC topology was the additional P_{DISS} of the CGS and as a result a lower *PAE* compared to the CS topology. Using the same P_{DISS} of CS-FBA and CC-FBA-IB by lowering the quiescent point of the CC-FBA-IB, the *PAE* of both topologies were in the same range. However, the RF performance of the CC-FBA-IB suffered using a lower quiescent point.

7.3 Modified Cascode with New Concept in Broadband Power Amplifiers

Some of the following information and key findings in this section are partially already published and can be found in [178] © 2017 IEEE and [179] © 2017 IEEE. In this section the functionality and the theory of the new concept in broadband PAs is underlined by many small-signal and large-signal measurements of the different realization structures of the VASC.

7.3.1 Schematic and Layout

Using Northrop Grumman's advanced $0.2\,\mu$m GaN-HEMT technology, Fig. 7.3.2 and Fig. 7.3.3 show the chip photo of the fabricated CC-FBAs using the new concept which replaces the CSC at the gate of the CGS by a VASC (CC-FBA-IB-D1D, CC-FBA-IB-D1U, CC-FBA-IB-D2 and CC-FBA-IG-D2). Due to the fact that the used monolithic microwave integrated circuit (MMIC) technology does not offer single diodes, at time of fabrication, the diode was realized by a transistor. The schematic of the different realizations of the VASC with $C_{\text{st,var}}$ is shown in Fig. 7.3.1. The remaining schematic structure including the active device cells, input and output matching as well as the feedback path is equal to the CC-FBAs using a CSC with C_{st} shown in Fig. 7.2.1. A detailed explanation of the schematic of the CC-FBA is given in Sec. 7.2.1.

To achieve the same small-signal performance of the CC-FBAs using a CSC and VASC, the VASC is designed in such a way that the $C_{\text{st,var}}$ of the VASC is equal to C_{st} of the CSC. However, the large-signal behavior is completely different. Three different realizations of the VASC with $C_{\text{st,var}}$ of the CC-FBA-IB were fabricated, shown in Fig. 7.3.2

and Fig. 7.3.3a, and are explained in the following:

- The CC-FBA-IB-D1D, shown in Fig. 7.3.2a, uses the input capacitance of a transistor in CS configuration to realize the VASC with $C_{\text{st,var}}$. There are three DC pads to achieve a certain quiescent point of VASC. As the DC gate voltage of the transistor is fixed due to the quiescent point of the CGS, a DC blocking capacitor at the source of the transistor is needed to be able to adjust the source potential and as a result the gate-source voltage of the VASC, shown in Fig. 7.3.1a. To avoid oscillations of the VASC (output drain-source of the CSS) and to minimize any additional DC power a resistor with resistance R_1 and a capacitor with capacitance C_1 is inserted between the drain and the source of the VASC (drain-source of the CSS). However, to enable a better comparison of the different realizations of the VASC, the drain and the source of the VASC were connected together via a bond wire to have the same DC voltage. The *GP* of the CSS of the VASC was chosen to $220\,\mu$m ($4 \times 55\,\mu$m) to offer similar small-signal performance as the CC-FBA with a CSC for a quiescent point V_{VASC} between $-9\,$V and $-6\,$V.

- The CC-FBA-IB-D1U, shown in Fig. 7.3.2b, uses a transistor (drain and source are connected together) as varactor diode to realize the VASC with $C_{\text{st,var}}$. Therefore only two DC pads are required to bias the varactor diode. Another very important difference of the VASC of the CC-FBA-IB-D1U compared to the VASC of the CC-FBA-IB-D1D is the direction of the varactor diode (transistor). In contrast to the CC-FBA-IB-D1D, the drain and source of the varactor diode is connected to the CGS of the CC-FBA-IB-D1U. Therefore, the voltage dependency of $C_{\text{st,var}}$ of the CC-FBA-IB-D1U is reversed in comparison to the $C_{\text{st,var}}$ of the CC-FBA-IB-D1D. Furthermore, an additional series resistor with R_{st} was added in the gate path of the CGS to avoid stability problems at higher frequencies, shown in Fig. 7.3.1b. To offer similar small-signal performance as the CC-FBA with a CSC, a *GP* of $180\,\mu$m ($4 \times 45\,\mu$m) was chosen for the varactor diode of the VASC for a quiescent point V_{VASC} between $-9\,$V and $-6\,$V.

- The CC-FBA-IB-D2, shown in Fig. 7.3.3a, uses two varactor diodes in parallel to realize the VASC with $C_{\text{st,var}}$. The voltage dependency of $C_{\text{st,var}}$ of both varactor diodes is opposed. Both varactor diodes can have different quiescent points. Therefore each varactor diode has its own DC blocking

capacitance. Three DC pads are necessary to bias the two varactor diodes individually. As well as the CC-FBA-IB-D1U, an additional series resistor with R_{st} was added in the gate path of the CGS to avoid stability problems at higher frequencies. The *GP* of each varactor diode of the VASC was chosen to $96\,\mu m$ $(4 \times 24\,\mu m)$ to offer similar small-signal performance as the CC-FBA with a CSC for a quiescent point $V_{VASC1} = V_{VASC2} = V_{VASC}$ between $-9\,V$ and $-6\,V$.

CC-FBA-IG-D2, shown in Fig. 7.3.3b, uses two varactor diodes in parallel as well as the CC-FBA-IB-D2. Due to the fact that the C_{st} of the CC-FBA-IG is about two times the C_{st} of the CC-FBA-IB, the *GP* of each varactor diode of the VASC is much higher and was chosen to $220\,\mu m$ $(4 \times 55\,\mu m)$. For a quiescent point $V_{VASC1} = V_{VASC2} = V_{VASC}$ between $-9\,V$ and $-6\,V$ the CC-FBA-IG-D2 offers similar small-signal performance as the CC-FBA-IG with a CSC.

$V_{VASC1} = V_{VASC2} = V_{VASC}$ is valid in the following sections for simplifications.

(a) VASC of the CC-FBA-IB-D1D [171].

(b) VASC of the CC-FBA-IG-D1U.

(c) VASC of the CC-FBA-IB-D2 and the CC-FBA-IG-D2.
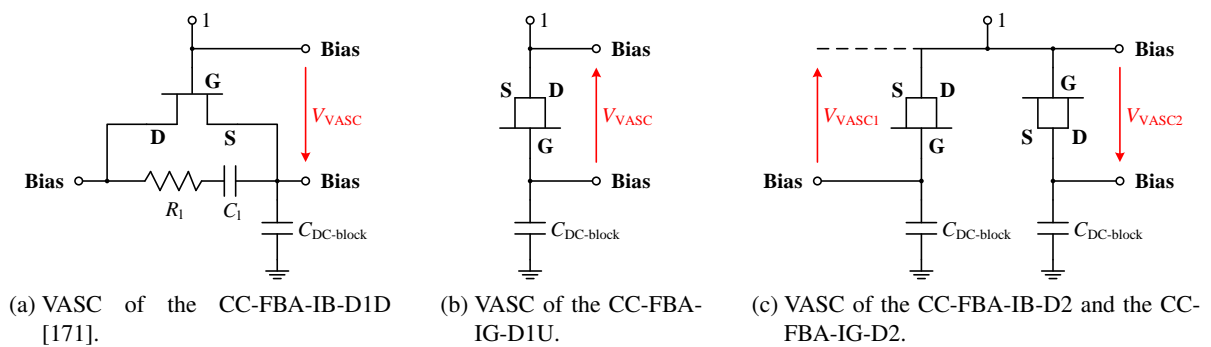
Figure 7.3.1: Schematic of VASC of the CC-FBA. (a) CC-FBA-IB-D1D. (b) CC-FBA-IB-D1U. (c) CC-FBA-IB-D2 and CC-FBA-IG-D2.
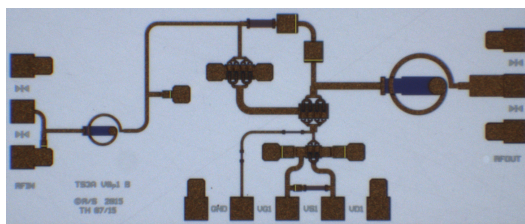
(a) Layout of CC-FBA-IB-D1D [179].
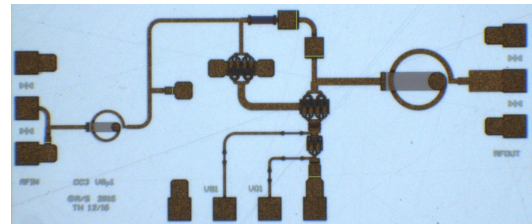
(b) Layout of the CC-FBA-IB-D1U.

Figure 7.3.2: Layout of the CC-FBA. (a) CC-FBA-IB-D1D. (b) CC-FBA-IB-D1U.
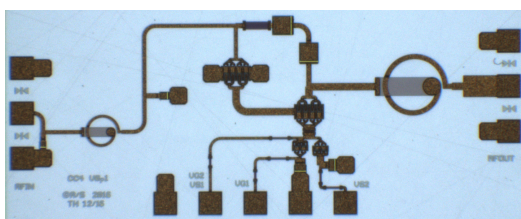
(a) Layout of CC-FBA-IB-D2.
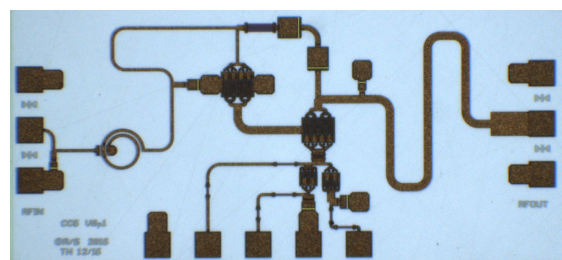
(b) Layout of the CC-FBA-IG-D2.

Figure 7.3.3: Layout of the CC-FBA. (a) CC-FBA-IB-D2. (b) CC-FBA-IG-D2.

7.3.2 On-Wafer Measurement Results

In this subsection the on-wafer measurement results of the CC-FBAs using a CSC with C_{st} and using a VASC with $C_{st,var}$ are compared with each other to point out the advantages and disadvantages of the different realizations of the VASC and to underline the functionality of the proposed concept. The comparisons of the on-wafer measurement results of the CC-FBAs using a CSC and a VASC are split into the different applications:

- Controlling the $\underline{S}_{21}$ at high frequencies.
- Improving the compression behavior ($P1dB$).
- Improving the linearity ($HD2$, $HD3$).

7.3.2.1 Gain-Control

S-Parameter Results

Fig. 7.3.4–Fig. 7.3.7 show the measured S-parameters of the CC-FBAs using a CSC with C_{st} and a VASC with $C_{st,var}$ at a certain quiescent point of the CSS and the CGS (CC-FBAs-IB: $V_{DS} = 10\,\text{V}$, $I_{DSQ} = 156\,\text{mA}$, CC-FBAs-IG: $V_{DS} = 10\,\text{V}$, $I_{DSQ} = 240\,\text{mA}$) for different V_{VASC}.

Fig. 7.3.4 compares the $|\underline{S}_{21}|$ of the CC-FBAs using a CSC and a VASC. Choosing $V_{VASC} = -9\,\text{V}$ (dashed lines) the $|\underline{S}_{21}|$ of the CC-FBA-IB-(D1D/D1U/D2) and CC-FBA-IG-D2 are similar to the $|\underline{S}_{21}|$ of the CC-FBA-IB ($|\underline{S}_{21}| \approx 13\,\text{dB}$) and CC-FBA-IG ($|\underline{S}_{21}| \approx 15\,\text{dB}$) using a CSC respectively, shown in Fig. 7.3.4a and Fig. 7.3.4b. Increasing the V_{VASC} up to $-1\,\text{V}$, the $|\underline{S}_{21}|$ can be increased by 4–5 dB at higher frequencies (solid lines). As a result of the increased $|\underline{S}_{21}|$, the bandwidth of the CC-FBAs-IB using the VASC increases as well from 15 GHz up to 17 GHz, shown in Fig. 7.3.4a. The bandwidth of the CC-FBA-IG-D2, shown in Fig. 7.3.4b, increases only slightly using a higher V_{VASC}.
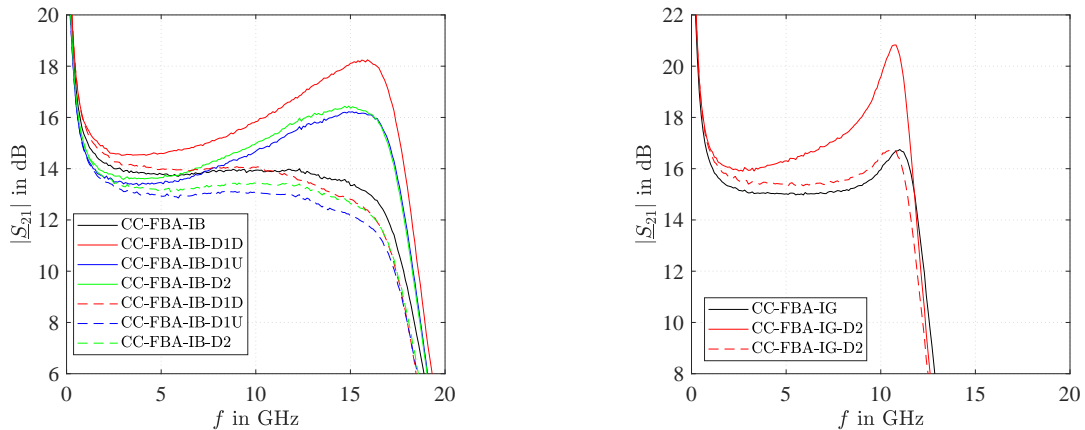
(a) $|\underline{S}_{21}|$ of CC-FBA-IB and CC-FBA-IB-(D1D/D1U/D2).

(b) $|\underline{S}_{21}|$ of CC-FBA-IG and CC-FBA-IG-D2.

Figure 7.3.4: Comparison of measured $|\underline{S}_{21}|$ of the CC-FBAs-IB ($V_{DS} = 10\,\text{V}$, $I_{DSQ} = 156\,\text{mA}$) and CC-FBAs-IG ($V_{DS} = 10\,\text{V}$, $I_{DSQ} = 240\,\text{mA}$) using a CSC and a VASC at $V_{VASC} = -1\,\text{V}$ (solid line) and $V_{VASC} = -9\,\text{V}$ (dashed line).

The $|\underline{S}_{12}|$ (CC-FBAs-IB:$|\underline{S}_{12}| < -17\,\text{dB}$, CC-FBAs-IG:$|\underline{S}_{12}| < -20\,\text{dB}$), shown in Fig. 7.3.5, of the CC-FBAs using a CSC and a VASC, is relatively unaffected of the V_{VASC}.

(a) $|\underline{S}_{12}|$ of CC-FBA-IB and CC-FBA-IB-(D1D/D1U/D2).

(b) $|\underline{S}_{12}|$ of CC-FBA-IG and CC-FBA-IG-D2.
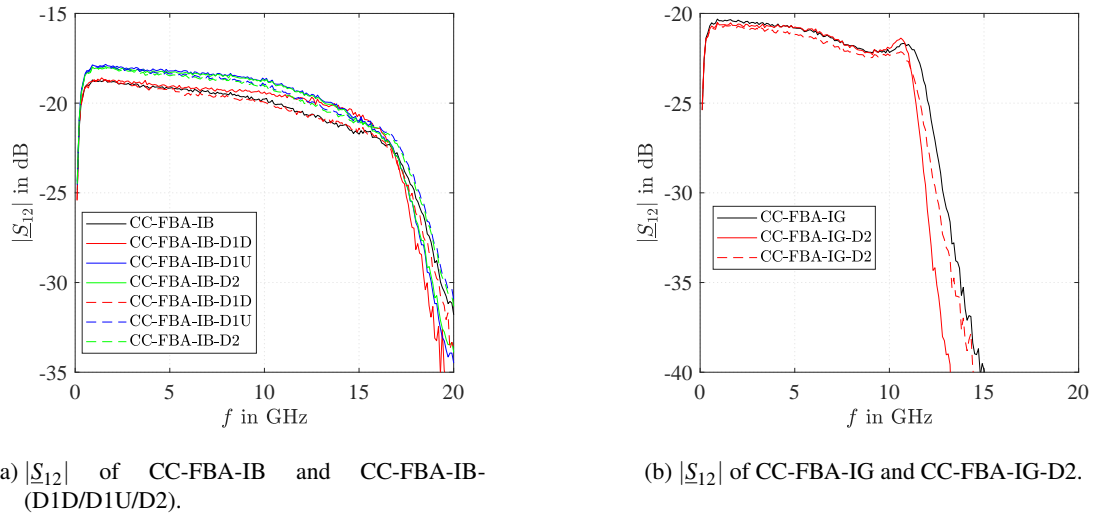
Figure 7.3.5: Comparison of measured $|\underline{S}_{12}|$ of the CC-FBAs-IB ($V_{DS} = 10$ V, $I_{DSQ} = 156$ mA) and CC-FBAs-IG ($V_{DS} = 10$ V, $I_{DSQ} = 240$ mA) using a CSC and a VASC at $V_{VASC} = -1$ V (solid line) and $V_{VASC} = -9$ V (dashed line).

Adjusting the VASC by V_{VASC} has only a small influence on the $|\underline{S}_{11}|$ which is between -10 dB and -8 dB of the CC-FBAs-IB, shown in Fig. 7.3.6a. However, $|\underline{S}_{11}|$ of the CC-FBA-IG-D2 gets almost > 0 dB at 11 GHz for $V_{VASC} = -1$ V. As a result the CC-FBA-IG-D2 has the potential to oscillate at the input for higher V_{VASC}.

(a) $|\underline{S}_{11}|$ of CC-FBA-IB and CC-FBA-IB-(D1D/D1U/D2).

(b) $|\underline{S}_{11}|$ of CC-FBA-IG and CC-FBA-IG-D2.

Figure 7.3.6: Comparison of measured $|\underline{S}_{11}|$ of the CC-FBAs-IB ($V_{DS} = 10$ V, $I_{DSQ} = 156$ mA) and CC-FBAs-IG ($V_{DS} = 10$ V, $I_{DSQ} = 240$ mA) using a CSC and a VASC at $V_{VASC} = -1$ V (solid line) and $V_{VASC} = -9$ V (dashed line).

The $|\underline{S}_{22}|$ of the CC-FBAs using a VASC can be adjusted in a wide range at higher frequencies by V_{VASC}. The $|\underline{S}_{22}|$ of the CC-FBAs using a CSC and a VASC is shown in Fig. 7.3.7. The $|\underline{S}_{22}|$ is better than -10 dB over the useful bandwidth for $V_{VASC} = -9$ V. However, increasing V_{VASC} to achieve a higher $|\underline{S}_{21}|$ results in a degradation of $|\underline{S}_{22}|$.

(a) $|\underline{S}_{22}|$ of CC-FBA-IB and CC-FBA-IB-(D1D/D1U/D2).

(b) $|\underline{S}_{22}|$ of CC-FBA-IG and CC-FBA-IG-D2.

Figure 7.3.7: Comparison of measured $|\underline{S}_{22}|$ of the CC-FBAss-IB ($V_{DS} = 10\,V$, $I_{DSQ} = 156\,mA$) and CC-FBAs-IG ($V_{DS} = 10\,V$, $I_{DSQ} = 240\,mA$) using a CSC and a VASC at $V_{VASC} = -1\,V$ (solid line) and $V_{VASC} = -9\,V$ (dashed line).

Noise Figure Results

Fig. 7.3.8 shows the measured NF of the CC-FBAs using a CSC and a VASC at a certain quiescent point of the CSS and the CGS (CC-FBAs-IB: $V_{DS} = 10\,V$, $I_{DSQ} = 156\,mA$, CC-FBAs-IG: $V_{DS} = 10\,V$, $I_{DSQ} = 240\,mA$) for different V_{VASC}. The NF is about 4 dB at lower and moderate frequencies and increases up to 6 dB at the f_c. The CC-FBAs-IG using a CSC and a VASC even achieve a minimum NF of 3 dB, shown in Fig. 7.3.8b. Despite the VASC which includes an additional active element, the corresponding NF is very similar to the CC-FBAs using a CSC.

(a) NF of CC-FBA-IB and CC-FBA-IB-(D1D/D1U/D2).

(b) NF of CC-FBA-IG and CC-FBA-IG-D2.
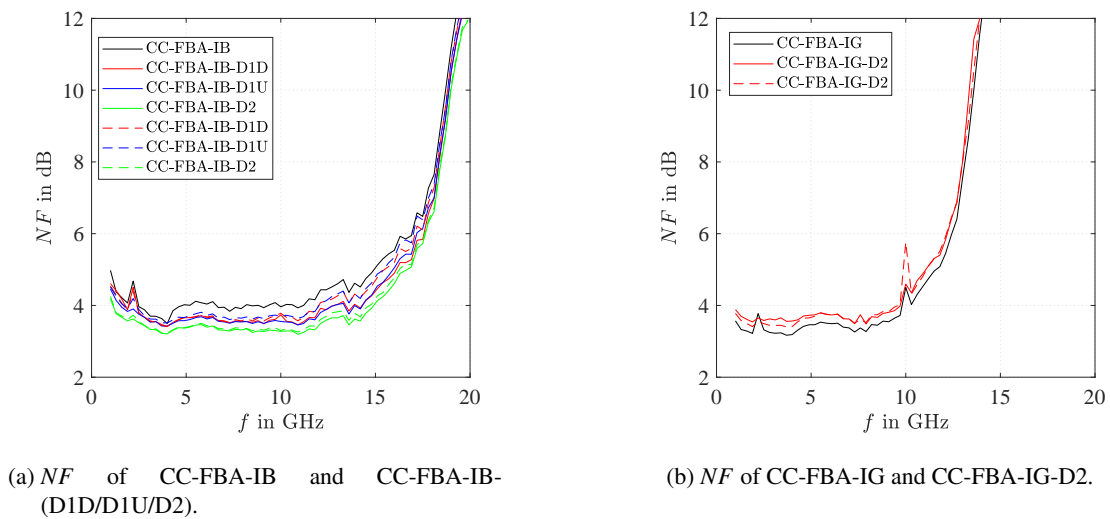
Figure 7.3.8: Comparison of measured NF of the CC-FBA-IB ($V_{DS} = 10\,V$, $I_{DSQ} = 156\,mA$) and CC-FBA-IG ($V_{DS} = 10\,V$, $I_{DSQ} = 240\,mA$) using a CSC and a VASC at $V_{VASC} = -4\,V$ (solid line) and $V_{VASC} = -9\,V$ (dashed line).

1-Tone Results

Fig. 7.3.9–Fig. 7.3.11 compares the measured 1-Tone results of the CC-FBAs using a CSC and a VASC at a certain quiescent point of the CSS and the CGS (CC-FBA-IBs: $V_{DS} = 10\,V$, $I_{DSQ} = 156\,mA$, CC-FBA-IGs: $V_{DS} = 10\,V$, $I_{DSQ} = 240\,mA$) for different V_{VASC}.

Fig. 7.3.9 depicts the $P_{out,max}$ of the CC-FBAs using a CSC and a VASC. The CC-FBAs-IB using a CSC and a VASC achieve a $P_{out,max}$ of about 30–31 dBm at 1 GHz and about 27–28 dBm at 17 GHz for a $P_{DISS,MAX}$ of 7.28 W ($\frac{P_{DISS,MAX}}{GP} = 7\,\frac{W}{mm}$), shown in Fig. 7.3.9a. Increasing V_{VASC} from $-9\,V$ to $-4\,V$, the $P_{out,max}$ can be slightly increased by $\approx 0.5\,dB$. The $P_{out,max}$ of the CC-FBA-IB-D1D and the CC-FBA-IB using a CSC is similar. The $P_{out,max}$ of the CC-FBA-IB-(D1U/D2) is about $\approx 1\,dB$ lower than the CC-FBA-IB-D1D and as a result lower than the CC-FBA-IB using a CSC. In contrast to the CC-FBAs-IB using a CSC and a VASC, a $P_{out,max}$ of even $\approx 33\,dBm$ at 1 GHz is achieved for a $P_{DISS,MAX}$ of 11.2 W ($\frac{P_{DISS,MAX}}{GP} = 7\,\frac{W}{mm}$) of the CC-FBAs-IG using a CSC and a VASC. However, at higher frequencies the $P_{out,max}$ decreases significantly, shown in Fig. 7.3.9b.
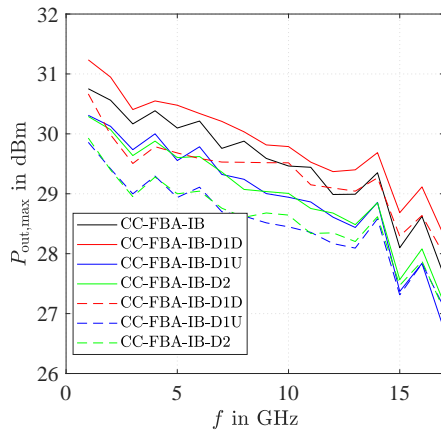
(a) $P_{out,max}$ vs. frequency of CC-FBA-IB and CC-FBA-IB-(D1D/D1U/D2).
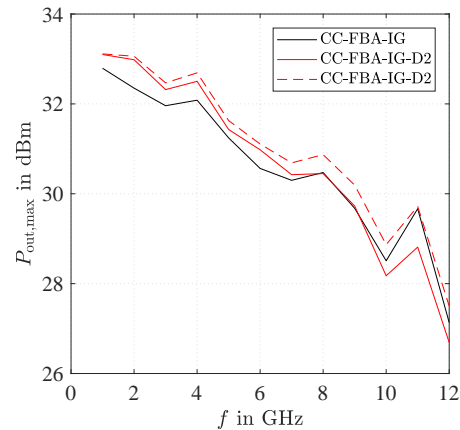
(b) $P_{out,max}$ vs. frequency of CC-FBA-IG and CC-FBA-IG-D2.

Figure 7.3.9: Comparison of measured $P_{out,max}$ vs. frequency of the CC-FBA-IB ($V_{DS} = 10\,V$, $I_{DSQ} = 156\,mA$) and CC-FBA-IG ($V_{DS} = 10\,V$, $I_{DSQ} = 240\,mA$) using a CSC and a VASC at $V_{VASC} = -4\,V$ (solid line) and $V_{VASC} = -9\,V$ (dashed line).

Fig. 7.3.10 shows the $HD2$ of the CC-FBAs using a CSC and a VASC. The $HD2$ of the CC-FBAs are only depicted up to 6 GHz and 8.5 GHz respectively, as higher frequencies can be filtered using a low-pass filter after the PA. The $HD2$ of the CC-FBAs-IG using a CSC and a VASC is very similar and is better than $-37\,dBc$ up to 6 GHz, shown in Fig. 7.3.10b. Although, the $HD2$ of the CC-FBAs-IB using a CSC and a VASC is also very similar at lower frequencies, at higher frequencies the $HD2$ depends on the chosen realization of the VASC and the V_{VASC}. As shown in Fig. 7.3.10a, the $HD2$ is about 5–15 dB higher than the CC-FBA-IB using the CSC at 8.5 GHz for $V_{VASC} = -4\,V$. However, the degradation can be improved for $V_{VASC} = -9\,V$.
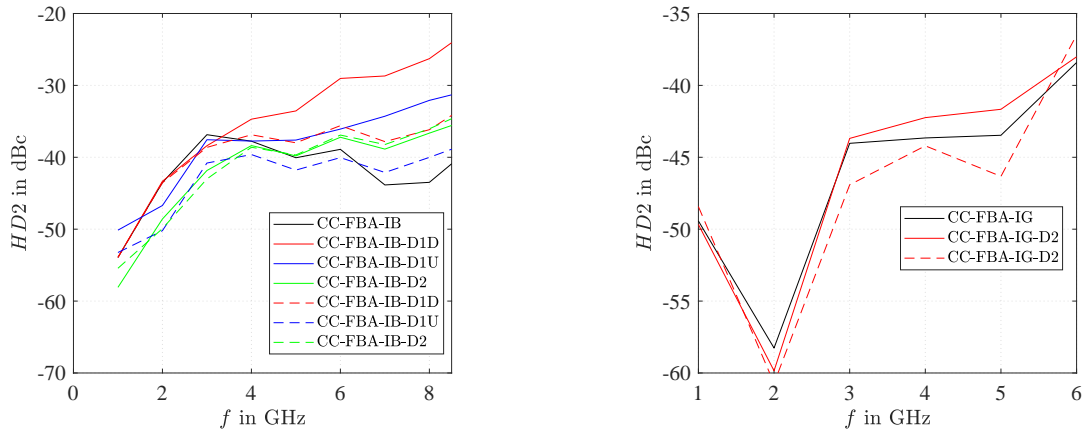
(a) *HD*2 vs. frequency of CC-FBA-IB and CC-FBA-IB-(D1D/D1U/D2).

(b) *HD*2 vs. frequency of CC-FBA-IG and CC-FBA-IG-D2.

Figure 7.3.10: Comparison of measured *HD*2 vs. frequency of the CC-FBA-IB ($V_{DS} = 10\,V$, $I_{DSQ} = 156\,mA$) and CC-FBA-IG ($V_{DS} = 10\,V$, $I_{DSQ} = 240\,mA$) using a CSC and a VASC at a $P_{out} = 15\,dBm$ at $V_{VASC} = -4\,V$ (solid line) and $V_{VASC} = -9\,V$ (dashed line).

Fig. 7.3.11 compares the *HD*3 of the CC-FBAs using a CSC and a VASC. Due to the fact that higher frequencies can be filtered using a low-pass filter after the PA, the *HD*3 of the CC-FBAs are only depicted up to 4 GHz and ≈ 5.7 GHz, respectively. The *HD*3 of the CC-FBAs-IB using a CSC and a VASC is very similar and is better than -45 dBc up to 5.7 GHz for $V_{VASC} = -9\,V$, shown in Fig. 7.3.11a. Fig. 7.3.11b depicts the *HD*3 of the CC-FBAs-IG using a CSC and a VASC ($V_{VASC} = -9\,V$) which is even better than -50 dBc up to 4 GHz. However, increasing V_{VASC} to $V_{VASC} = -4\,V$, the performance of *HD*3 strongly depends on the realization structure of the VASC:

- The *HD*3 of the CC-FBA-IB-D1D is 15 dB higher than the CC-FBA-IB using a CSC at 5.7 GHz.
- The CC-FBA-IB-D2 and the CC-FBA-IG-D2 raise the *HD*3 only by 1–3 dB compared to the CC-FBA-(IB/IG) using a CSC.
- Using the CC-FBA-IB-D1U the *HD*3 can be improved by 10 dB at 5 GHz.

(a) *HD*3 vs. frequency of CC-FBA-IB and CC-FBA-IB-(D1D/D1U/D2).

(b) *HD*3 vs. frequency of CC-FBA-IG and CC-FBA-IG-D2.

Figure 7.3.11: Comparison of measured *HD*3 vs. frequency of the CC-FBA-IB ($V_{DS} = 10\,V$, $I_{DSQ} = 156\,mA$) and CC-FBA-IG ($V_{DS} = 10\,V$, $I_{DSQ} = 240\,mA$) using a CSC and a VASC at a $P_{out} = 15\,dBm$ at $V_{VASC} = -4\,V$ (solid line) and $V_{VASC} = -9\,V$ (dashed line).

7.3.2.2 Improved Compression

S-Parameter Results

The measured S-parameters of the CC-FBAs using a CSC with C_{st} and a VASC with $C_{st,var}$ at a certain quiescent point of the CSS and the CGS (CC-FBAs-IB: $V_{DS} = 10\,V$, $I_{DSQ} = 104\,mA$, CC-FBAs-IG: $V_{DS} = 20\,V$, $I_{DSQ} = 240\,mA$) and a certain V_{VASC} are shown in Fig. 7.3.12–Fig. 7.3.15. The V_{VASC} of the CC-FBA-IB-(D1D/D1U/D2) is equal to $-6\,V$ and is chosen to $-5\,V$ and $-9\,V$ for the CC-FBA-IG-D2. Fig. 7.3.12 shows the $|\underline{S}_{21}|$ of the CC-FBAs using a CSC and a VASC. The $|\underline{S}_{21}|$ of the CC-FBA-IB-(D1D/D1U/D2) (dashed lines, $V_{VASC} = -6\,V$) and of the CC-FBA-IG-D2 (dashed lines, $V_{VASC} = -9\,V$) are almost equal to the $|\underline{S}_{21}|$ of the CC-FBA-IB ($|\underline{S}_{21}| \approx 13\,dB$) and CC-FBA-IG ($|\underline{S}_{21}| \approx 15$–$17\,dB$) using a CSC, shown in Fig. 7.3.12a and Fig. 7.3.12b respectively. A bandwidth of about $17\,GHz$ and $12\,GHz$ is achieved for the CC-FBAs-IB and the CC-FBAs-IG. Increasing the V_{VASC} up to $-5\,V$ of the CC-FBA-IG-D2, the $\underline{S}_{21}$ can be increased by $2\,dB$ at higher frequencies (solid lines). The f_c remains at $\approx 12\,GHz$, shown in Fig. 7.3.12b.

(a) $|\underline{S}_{21}|$ of CC-FBA-IB and CC-FBA-IB-(D1D/D1U/D2) at $V_{VASC} = -6\,V$.

(b) $|\underline{S}_{21}|$ of CC-FBA-IG and CC-FBA-IG-D2 at $V_{VASC} = -5\,V$ (solid line) and $V_{VASC} = -9\,V$ (dashed line).
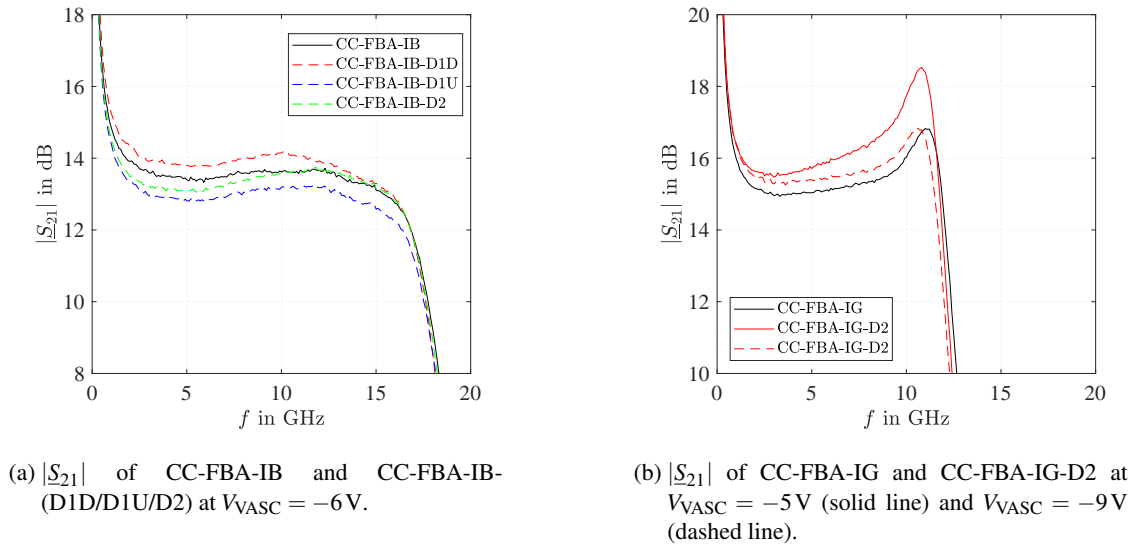
Figure 7.3.12: Comparison of measured $|\underline{S}_{21}|$ of the CC-FBA-IB ($V_{DS} = 10\,V$, $I_{DSQ} = 104\,mA$) and CC-FBA-IG ($V_{DS} = 20\,V$, $I_{DSQ} = 240\,mA$) using a CSC and a VASC at different V_{VASC}.

(a) $|\underline{S}_{12}|$ of CC-FBA-IB and CC-FBA-IB-(D1D/D1U/D2) at $V_{VASC} = -6\,V$.

(b) $|\underline{S}_{12}|$ of CC-FBA-IG and CC-FBA-IG-D2 at $V_{VASC} = -5\,V$ (solid line) and $V_{VASC} = -9\,V$ (dashed line).
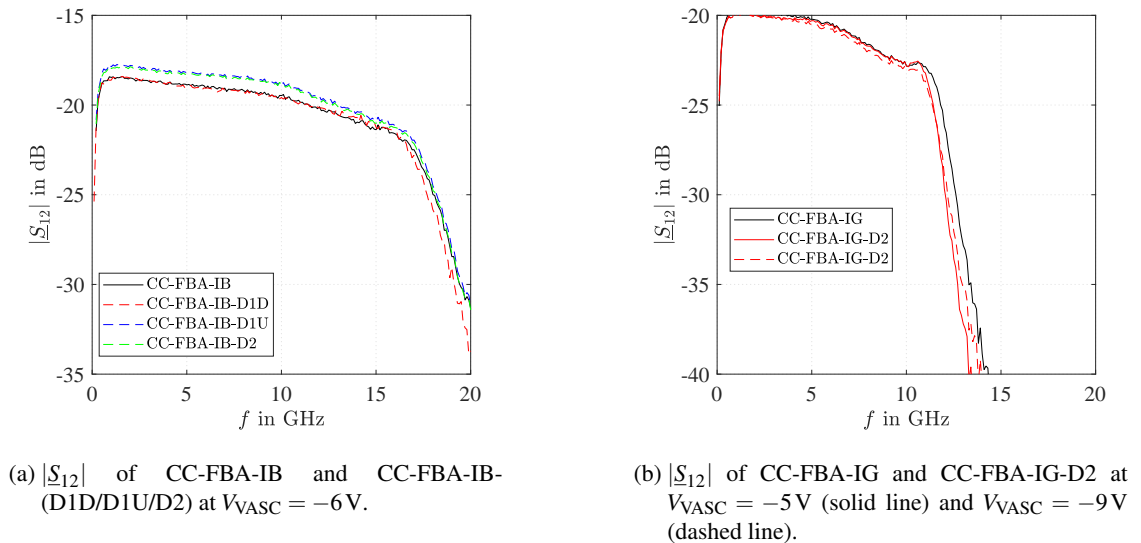
Figure 7.3.13: Comparison of measured $|\underline{S}_{12}|$ of the CC-FBA-IB ($V_{DS} = 10\,V$, $I_{DSQ} = 104\,mA$) and CC-FBA-IG ($V_{DS} = 20\,V$, $I_{DSQ} = 240\,mA$) using a CSC and a VASC at different V_{VASC}.

Fig. 7.3.13 compares the $|\underline{S}_{12}|$ of the CC-FBAs using a CSC and a VASC (CC-FBAs-IB: $|\underline{S}_{12}| < -17\,\text{dB}$, CC-FBAs-IG: $|\underline{S}_{12}| < -20\,\text{dB}$) which is almost equal. The $|\underline{S}_{11}|$ of the CC-FBAs using a CSC and a VASC is shown in Fig. 7.3.14 which is in range of $-10\,\text{dB}$ and $-8\,\text{dB}$ over the complete bandwidth. The $|\underline{S}_{11}|$ of the CC-FBAs-IB using a VASC is $2\,\text{dB}$ worse than the CC-FBA-IB using a CSC, depicted in Fig. 7.3.14a. This effect can be traced back to the additional series inductance between the gate of the CGS and the shunt capacitance of the VASC. V_{VASC} has only a small influence on the $|\underline{S}_{11}|$ of the CC-FBA-IG-D2 which is very similar to the CC-FBA-IG using a CSC, shown in Fig. 7.3.14b. Fig. 7.3.15 shows the $|\underline{S}_{22}|$ of the CC-FBAs using a CSC and a VASC. The $|\underline{S}_{22}|$ is better $-10\,\text{dB}$ of the CC-FBAs-IB and in the range of $-10\,\text{dB}$ and $-8\,\text{dB}$ of the CC-FBAs-IG using a CSC and a VASC over the complete frequency range. The $|\underline{S}_{22}|$ of the CC-FBAs-IB using a CSC and a VASC is very similar as well as the CC-FBAs-IG using a CSC and a VASC.
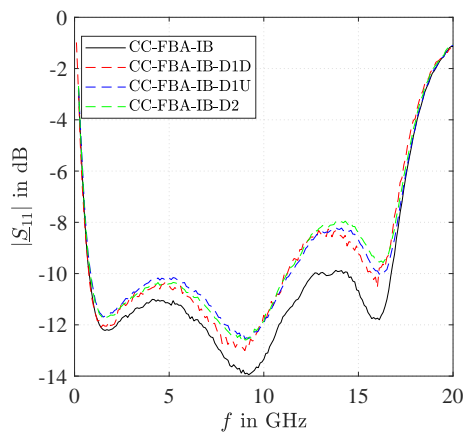
(a) $|\underline{S}_{11}|$ of CC-FBA-IB and CC-FBA-IB-(D1D/D1U/D2) at $V_{\text{VASC}} = -6\,\text{V}$.
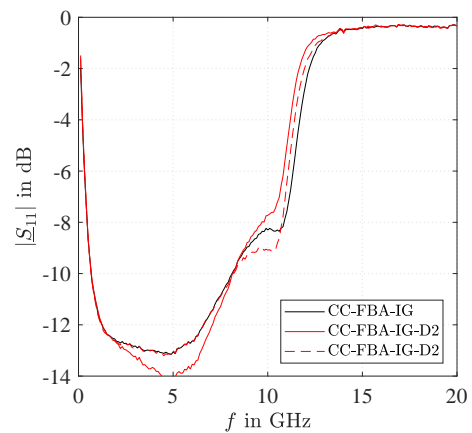
(b) $|\underline{S}_{11}|$ of CC-FBA-IG and CC-FBA-IG-D2 at $V_{\text{VASC}} = -5\,\text{V}$ (solid line) and $V_{\text{VASC}} = -9\,\text{V}$ (dashed line).

Figure 7.3.14: Comparison of measured $|\underline{S}_{11}|$ of the CC-FBA-IB ($V_{\text{DS}} = 10\,\text{V}$, $I_{\text{DSQ}} = 104\,\text{mA}$) and CC-FBA-IG ($V_{\text{DS}} = 20\,\text{V}$, $I_{\text{DSQ}} = 240\,\text{mA}$) using CSC and a VASC at different V_{VASC}.
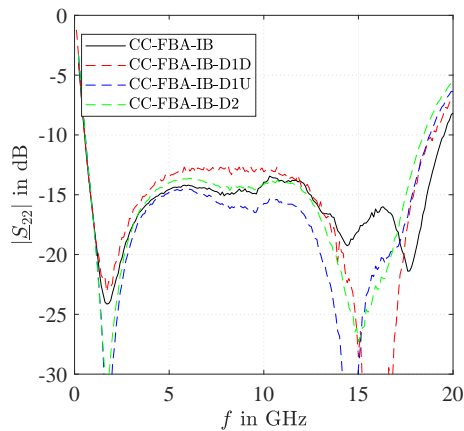
(a) $|\underline{S}_{22}|$ of CC-FBA-IB and CC-FBA-IB-(D1D/D1U/D2) at $V_{\text{VASC}} = -6\,\text{V}$.
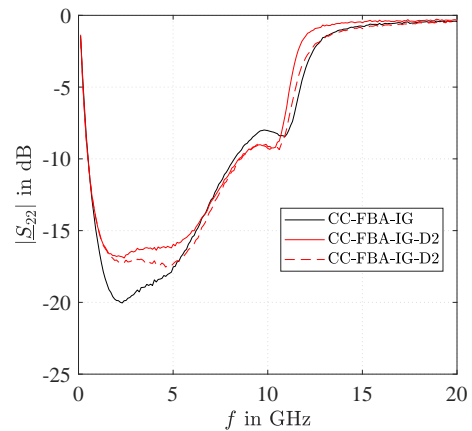
(b) $|\underline{S}_{22}|$ of CC-FBA-IG and CC-FBA-IG-D2 at $V_{\text{VASC}} = -5\,\text{V}$ (solid line) and $V_{\text{VASC}} = -9\,\text{V}$ (dashed line).

Figure 7.3.15: Comparison of measured $|\underline{S}_{22}|$ of the CC-FBA-IB ($V_{\text{DS}} = 10\,\text{V}$, $I_{\text{DSQ}} = 104\,\text{mA}$) and CC-FBA-IG ($V_{\text{DS}} = 20\,\text{V}$, $I_{\text{DSQ}} = 240\,\text{mA}$) using CSC and a VASC at different V_{VASC}.

Noise Figure Results

The measured *NF* of the CC-FBAs using a CSC and a VASC at a certain quiescent point of the CSS and the CGS (CC-FBAs-IB: $V_{DS} = 10\,V$, $I_{DSQ} = 104\,mA$, CC-FBAs-IG: $V_{DS} = 20\,V$, $I_{DSQ} = 240\,mA$) and a certain V_{VASC} is compared in Fig. 7.3.16. The V_{VASC} of the CC-FBA-IB-(D1D/D1U/D2) is equal to $-6\,V$ and is chosen to $-5\,V$ and $-9\,V$ for the CC-FBA-IG-D2. At lower and moderate frequencies the *NF* of the CC-FBAs-IB using a CSC and a VASC is about 3–4 dB and increases up to 6 dB at the f_c, depicted in Fig. 7.3.16a. Despite the VASC which includes an additional active element, the corresponding *NF* of the CC-FBAs-IB using a VASC is even $\approx 1\,dB$ lower than the CC-FBA-IB using a CSC. The *NF* of the CC-FBA-IG-D2 is about 5 dB in the lower and moderate frequency range in increases up to 7 dB at 12 GHz, shown in Fig. 7.3.16b. The *NF* of the CC-FBA-IG-D2 is slightly higher than the CC-FBA-IG using a CSC.

(a) *NF* of CC-FBA-IB and CC-FBA-IB-(D1D/D1U/D2) at $V_{VASC} = -6\,V$.

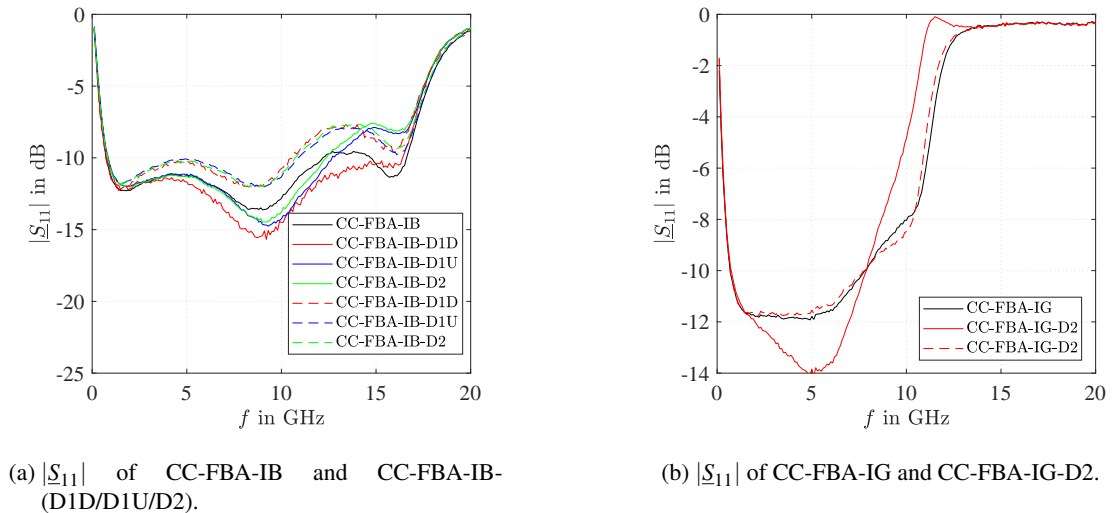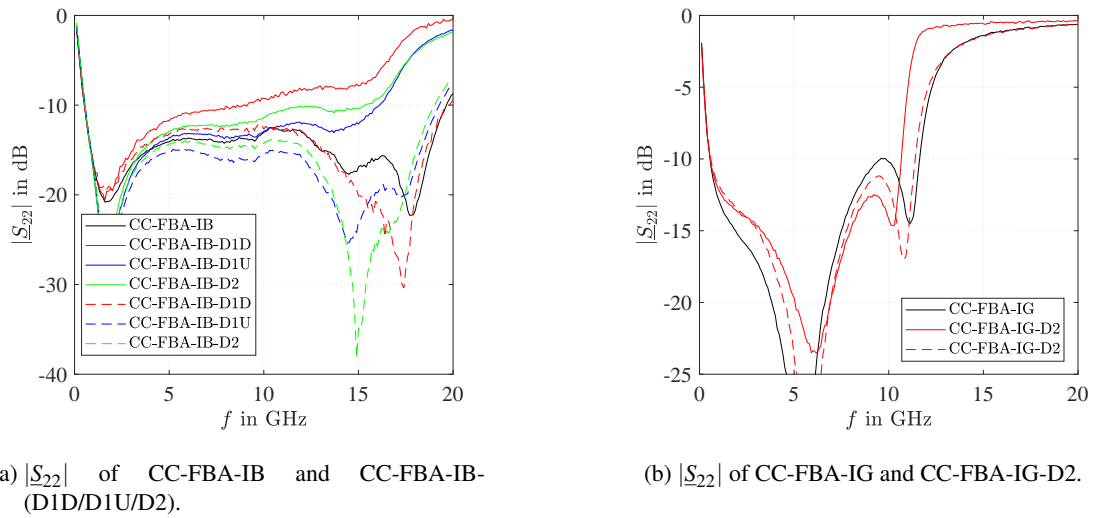(b) *NF* of CC-FBA-IG and CC-FBA-IG-D2 at $V_{VASC} = -5\,V$ (solid line) and $V_{VASC} = -9\,V$ (dashed line).
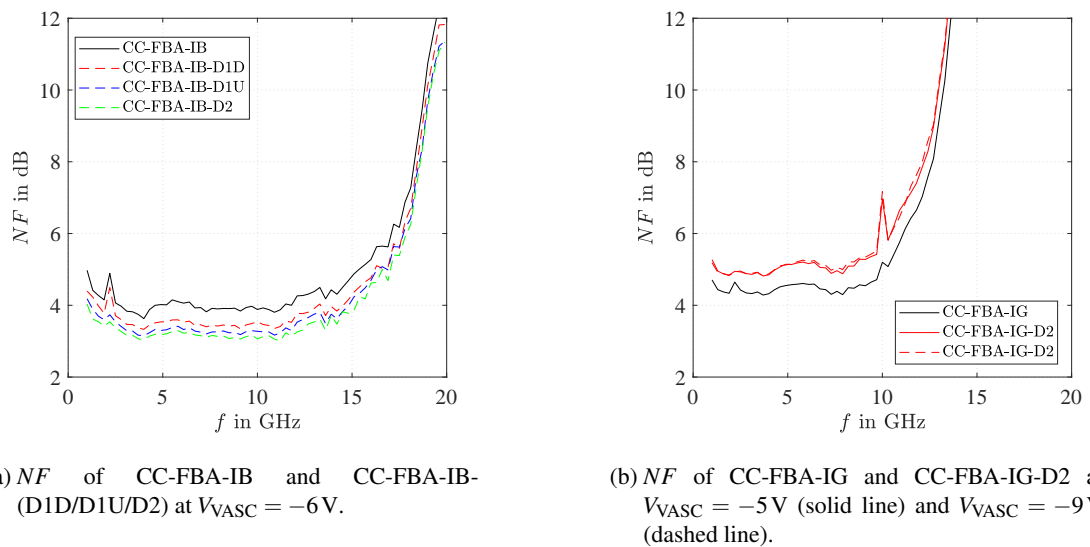
Figure 7.3.16: Comparison of measured *NF* of the CC-FBA-IB ($V_{DS} = 10\,V$, $I_{DSQ} = 104\,mA$) and CC-FBA-IG ($V_{DS} = 20\,V$, $I_{DSQ} = 240\,mA$) using a CSC and a VASC at different V_{VASC}.

1-Tone Results

The measured 1-Tone results of the CC-FBAs using a CSC and a VASC at a certain quiescent point of the CSS and the CGS (CC-FBA-IBs: $V_{DS} = 10\,V$, $I_{DSQ} = 104\,mA$, CC-FBA-IGs: $V_{DS} = 20\,V$, $I_{DSQ} = 240\,mA$) and a certain V_{VASC} are shown in Fig. 7.3.17–Fig. 7.3.27. The V_{VASC} of the CC-FBA-(D1D/D1U/D2) is equal to $-6\,V$ and is chosen to $-5\,V$ and $-9\,V$ for the CC-FBA-IG-D2.

The $P_{out,max}$ of the CC-FBAs using a CSC and a VASC is depicted in Fig. 7.3.17. A $P_{out,max}$ of about 30–30.5 dBm at 1 GHz and about 26.5–27.5 dBm at 17 GHz for a $P_{DISS,MAX}$ of 7.28 W ($\frac{P_{DISS,MAX}}{GP} = 7\,\frac{W}{mm}$), shown in Fig. 7.3.17a, is achieved of the CC-FBAs-IB using a CSC and a VASC. The $P_{out,max}$ of the CC-FBAs-IB using a VASC is up to 0.5 dB lower than the CC-FBA-IB using a CSC. In contrast to the CC-FBAs-IB using a CSC and a VASC, a $P_{out,max}$ of even $\approx 35.5\,dBm$ at 1 GHz is achieved for a $P_{DISS,MAX}$ of 11.2 W ($\frac{P_{DISS,MAX}}{GP} = 7\,\frac{W}{mm}$) of the CC-FBAs-IG using a CSC and a VASC. However, shown in Fig. 7.3.17b, at higher frequencies the $P_{out,max}$ decreases significantly. There is almost no change in $P_{out,max}$ of the CC-FBA-IG-D2 increasing V_{VASC} from $-9\,V$ to $-5\,V$.
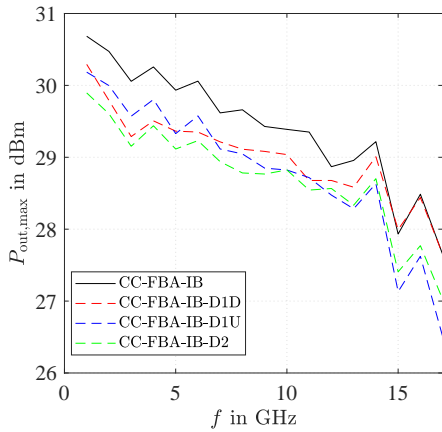
(a) $P_{\text{out,max}}$ vs. frequency of CC-FBA-IB and CC-FBA-IB-(D1D/D1U/D2) at $V_{\text{VASC}} = -6\,\text{V}$.
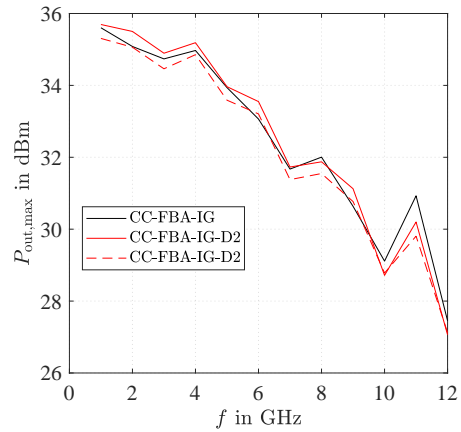
(b) $P_{\text{out,max}}$ vs. frequency of CC-FBA-IG and CC-FBA-IG-D2 at $V_{\text{VASC}} = -5\,\text{V}$ (solid line) and $V_{\text{VASC}} = -9\,\text{V}$ (dashed line).

Figure 7.3.17: Comparison of measured $P_{\text{out,max}}$ vs. frequency of the CC-FBA-IB ($V_{\text{DS}} = 10\,\text{V}$, $I_{\text{DSQ}} = 104\,\text{mA}$) and CC-FBA-IG ($V_{\text{DS}} = 20\,\text{V}$, $I_{\text{DSQ}} = 240\,\text{mA}$) using a CSC and a VASC at different V_{VASC}.

Fig. 7.3.18 and Fig. 7.3.19 show the normalized *Gain* versus frequency and versus P_{out} of the CC-FBA-IB-(D1D/D1U/D2) and of the CC-FBA-IG-D2 at $V_{\text{VASC}} = -5\,\text{V}$ and $V_{\text{VASC}} = -9\,\text{V}$. Increasing V_{VASC} from $-9\,\text{V}$ to $-5\,\text{V}$ improves the compression behavior especially at higher frequencies at moderate P_{out} of the CC-FBAs using a VASC.
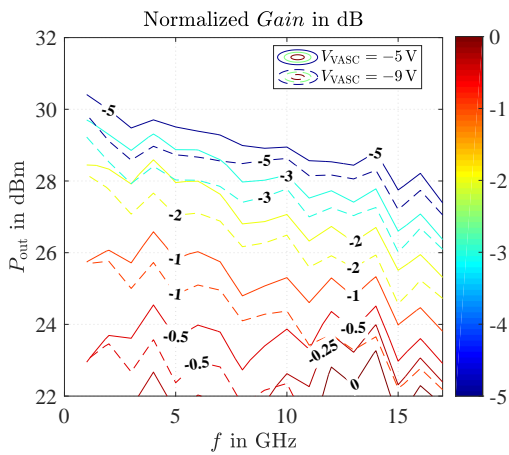
(a) Normalized *Gain* vs. frequency vs. P_{out} of CC-FBA-IB-D1D.
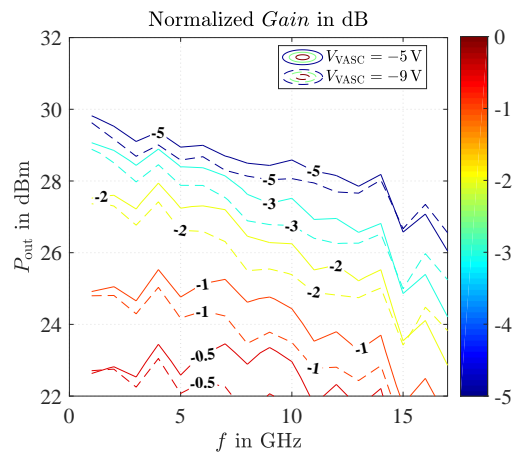
(b) Normalized *Gain* vs. frequency vs. P_{out} of CC-FBA-IB-D1U.

Figure 7.3.18: Measured normalized *Gain* vs. frequency vs. P_{out} of the CC-FBA-IB-D1D and CC-FBA-IB-D1U ($V_{\text{DS}} = 10\,\text{V}$, $I_{\text{DSQ}} = 104\,\text{mA}$) at $V_{\text{VASC}} = -5\,\text{V}$ and $V_{\text{VASC}} = -9\,\text{V}$.

(a) Normalized *Gain* vs. frequency vs. P_{out} of CC-FBA-IB-D2.

(b) Normalized *Gain* vs. frequency vs. P_{out} of CC-FBA-IG-D2.
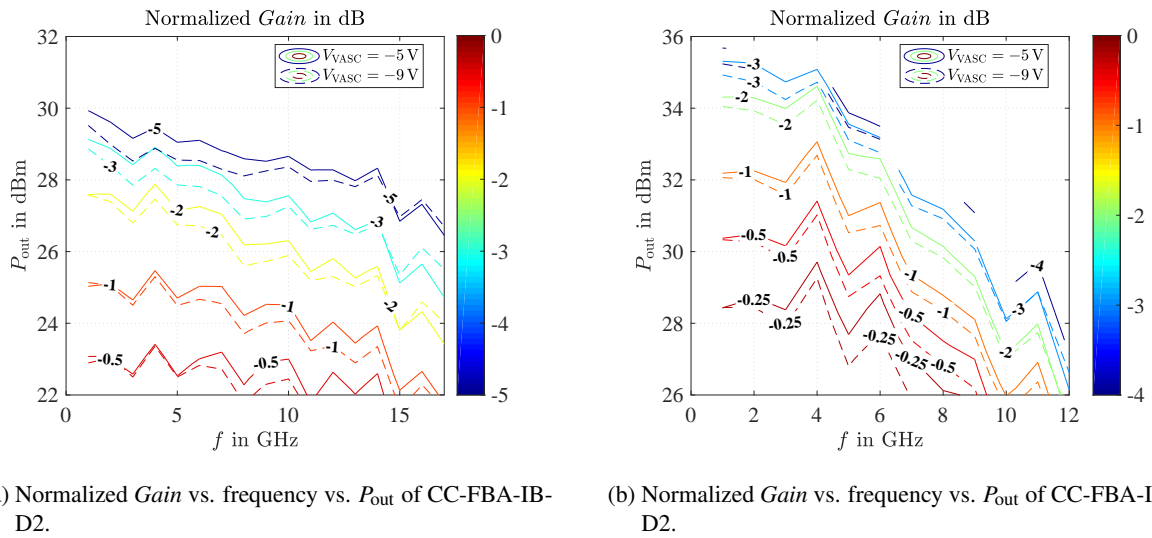
Figure 7.3.19: Measured normalized *Gain* vs. frequency vs. P_{out} of the CC-FBA-IB-D2 ($V_{DS} = 10\,V$, $I_{DSQ} = 104\,mA$) and CC-FBA-IG-D2 ($V_{DS} = 20\,V$, $I_{DSQ} = 240\,mA$) at $V_{VASC} = -5\,V$ and $V_{VASC} = -9\,V$.

The $P1dB$, $P0.5dB$ and $P0.1dB$ of the CC-FBAs-IB using a CSC and a VASC are compared in Fig. 7.3.20, Fig. 7.3.21 and Fig. 7.3.22 respectively. A $P1dB$ of the CC-FBA-IB using a CSC, shown in Fig. 7.3.20, of 21–26 dBm is achieved over the complete bandwidth. The $P1dB$ is increased by 2.5 dB at higher frequencies using a VASC instead of a CSC.

(a) $P1dB$ vs. frequency of CC-FBA-IB and CC-FBA-IB-(D1D/D1U/D2) at $V_{VASC} = -5\,V$.

(b) $P1dB$ vs. frequency of CC-FBA-IB and CC-FBA-IB-(D1D/D1U/D2) at $V_{VASC} = -6\,V$.
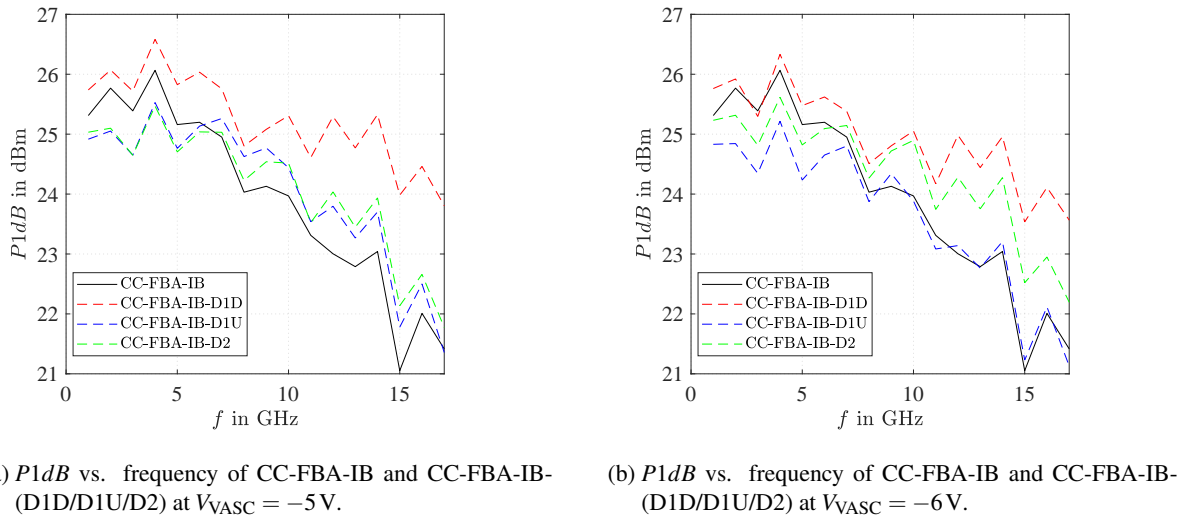
Figure 7.3.20: Comparison of measured $P1dB$ vs. frequency of the CC-FBA-IB ($V_{DS} = 10\,V$, $I_{DSQ} = 104\,mA$) using a CSC and a VASC at different V_{VASC}.

A $P0.5dB$ of the CC-FBA-IB using a CSC of 18.5–23.5 dBm is achieved over the complete bandwidth, shown in Fig. 7.3.21. At higher frequencies the $P0.5dB$ is increased by 4 dB using a VASC instead of a CSC, depicted in Fig. 7.3.20. The $P0.5dB$ of the CC-FBA-IB-D1D is significantly higher compared to the $P0.5dB$ of the CC-FBA-IB-(D1U/D2).
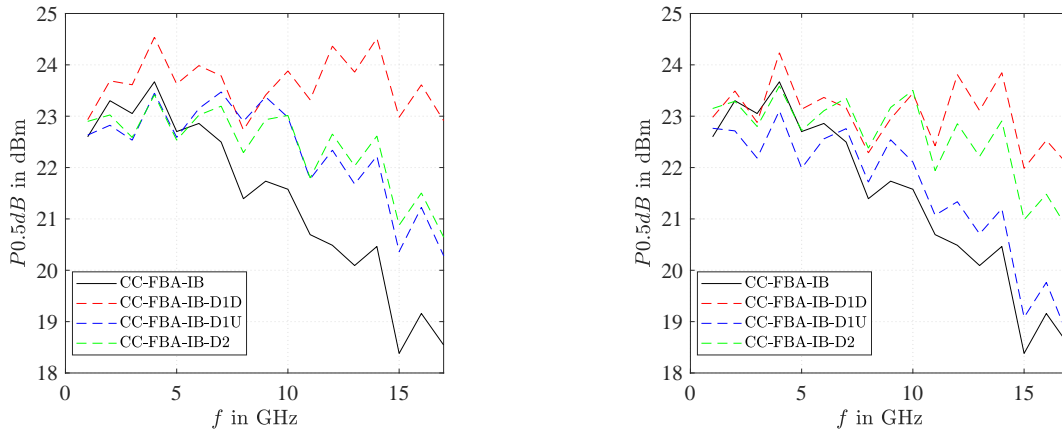
(a) $P0.5dB$ vs. frequency of CC-FBA-IB and CC-FBA-IB-(D1D/D1U/D2) at $V_{\mathrm{VASC}} = -5\,\mathrm{V}$.

(b) $P0.5dB$ vs. frequency of CC-FBA-IB and CC-FBA-IB-(D1D/D1U/D2) at $V_{\mathrm{VASC}} = -6\,\mathrm{V}$.

Figure 7.3.21: Comparison of measured $P0.5dB$ vs. frequency of the CC-FBA-IB ($V_{\mathrm{DS}} = 10\,\mathrm{V}$, $I_{\mathrm{DSQ}} = 104\,\mathrm{mA}$) using a CSC and a VASC at different V_{VASC}.

The CC-FBA-IB using a CSC, shown in Fig. 7.3.22, achieves a $P0.1dB$ of 11–19 dBm over the complete bandwidth. Compared to the CC-FBA-IB using a CSC, the CC-FBA-IB-(D1U/D2) improves the $P0.1dB$ by 7 dB at higher frequencies. The CC-FBA-IB-D1D even increases the $P0.1dB$ more than 10 dB using a VASC instead of a CSC, depicted in Fig. 7.3.22, at higher frequencies. At 17 GHz the $P0.1dB$ of the CC-FBA-D1D is about 3 dB higher compared to the $P0.1dB$ of the CC-FBA-(D1U/D2) at $V_{\mathrm{VASC}} = -5\,\mathrm{V}$.
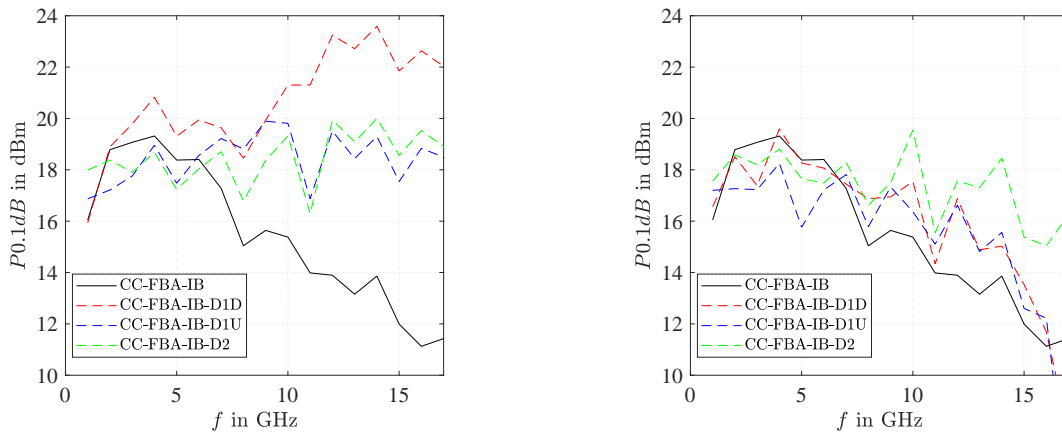
(a) $P0.1dB$ vs. frequency of CC-FBA-IB and CC-FBA-IB-(D1D/D1U/D2) at $V_{\mathrm{VASC}} = -5\,\mathrm{V}$.

(b) $P0.1dB$ vs. frequency of CC-FBA-IB and CC-FBA-IB-(D1D/D1U/D2) at $V_{\mathrm{VASC}} = -6\,\mathrm{V}$.

Figure 7.3.22: Comparison of measured $P0.1dB$ vs. frequency of the CC-FBA-IB ($V_{\mathrm{DS}} = 10\,\mathrm{V}$, $I_{\mathrm{DSQ}} = 104\,\mathrm{mA}$) using a CSC and a VASC at different V_{VASC}.

Fig. 7.3.23 compares the $P1dB$ and $P0.1dB$ of the CC-FBAs-IG using a CSC and a VASC. A $P1dB$ of 24–33 dBm is achieved over the complete bandwidth. The $P1dB$ of the CC-FBAs-IG using a CSC and a VASC is very similar, depicted in Fig. 7.3.23a. Fig. 7.3.23b shows the $P0.1dB$ of 18–28 dBm of the CC-FBAs-IG using a CSC and a VASC. At higher frequencies the $P0.1dB$ of the CC-FBA-IG using a CSC can be increased by 0.5–1 dB using a VASC with $V_{\mathrm{VASC}} = -5\,\mathrm{V}$.
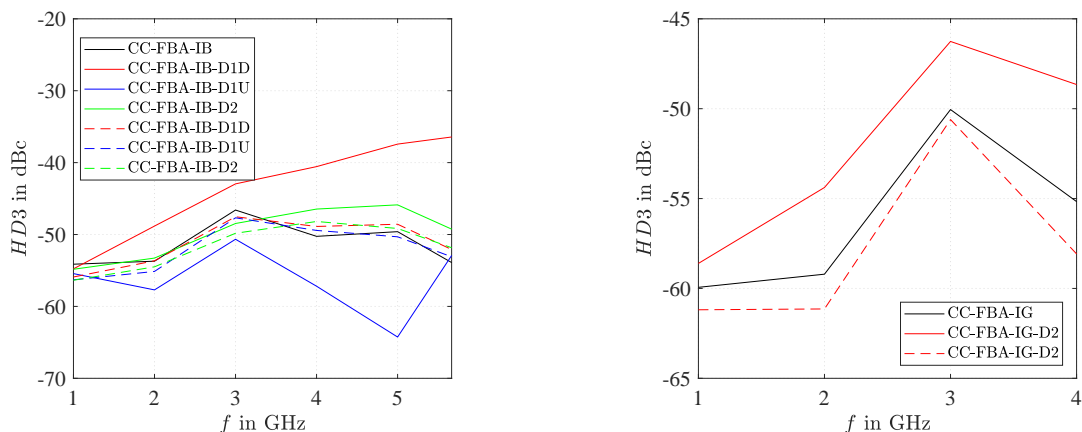
(a) $P1dB$ vs. frequency of CC-FBA-IG and CC-FBA-IG-D2.

(b) $P0.1dB$ vs. frequency of CC-FBA-IG and CC-FBA-IG-D2.
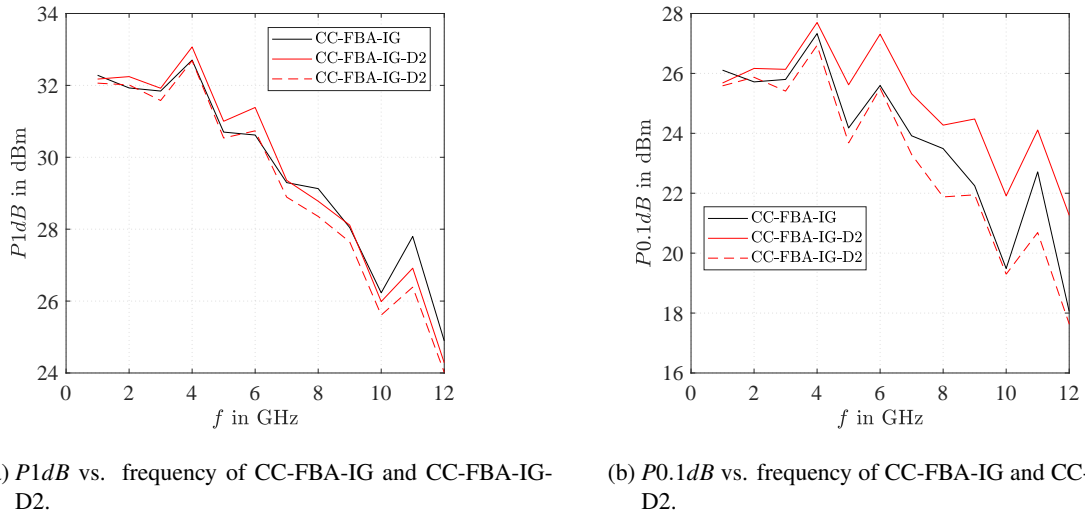
Figure 7.3.23: Comparison of measured $P1dB$ and $P0.1dB$ vs. frequency of the CC-FBA-IG ($V_{DS} = 20\,V$, $I_{DSQ} = 240\,mA$) using a CSC and a VASC at $V_{VASC} = -5\,V$ (solid line) and $V_{VASC} = -9\,V$ (dashed line).

The gain compression at 15 GHz of the CC-FBAs-IB using a CSC and a VASC ($V_{VASC} = -5\,V$ and $V_{VASC} = -6\,V$) are shown in Fig. 7.3.24. At $V_{VASC} = -6\,V$ the CC-FBA-IB-D2 achieves the best gain compression improvement compared to the other realizations of the VASC, illustrated in Fig. 7.3.24b. The normalized *Gain* of the CC-FBA-IB-D1U and the CC-FBA-IB using a CSC are even very similar. However, using a higher V_{VASC}, shown in Fig. 7.3.24a, the gain compression of the CC-FBAs-IB-(D1D/D1U/D2) can be further increased in the 0–1 dB gain compression range. The normalized *Gain* of the CC-FBA-IB-D1U and the CC-FBA-IB-D2 are almost equal. Furthermore, the CC-FBA-IB-D1D even offers a gain expansion up to 0.25 dB at a $P_{out} = 10\text{--}22\,dBm$.

(a) Normalized *Gain* vs. P_{out} of CC-FBA-IB and CC-FBA-IB-(D1D/D1U/D2) at $V_{VASC} = -5\,V$.

(b) Normalized *Gain* vs. P_{out} of CC-FBA-IB and CC-FBA-IB-(D1D/D1U/D2) at $V_{VASC} = -6\,V$.
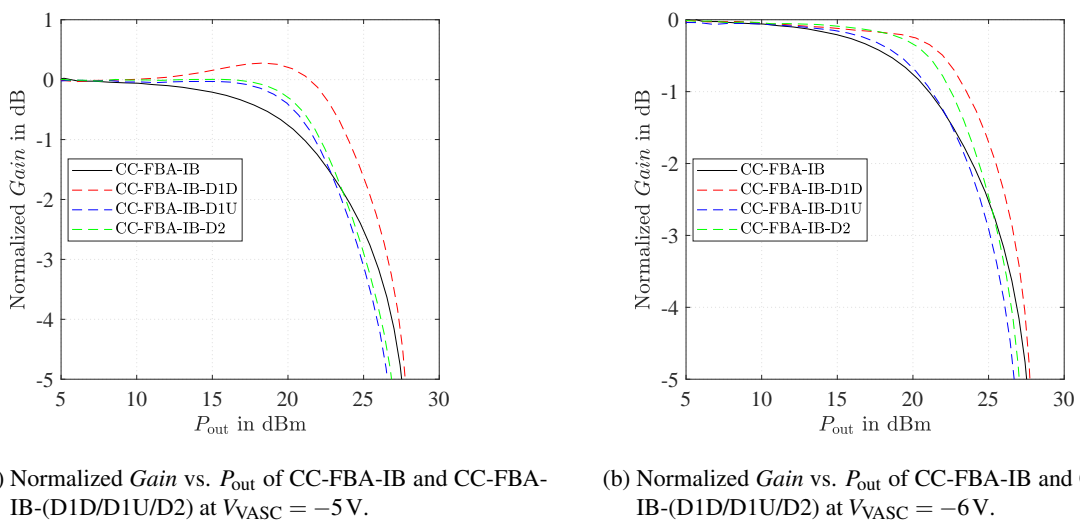
Figure 7.3.24: Comparison of measured normalized *Gain* vs. P_{out} of the CC-FBA-IB ($V_{DS} = 10\,V$, $I_{DSQ} = 104\,mA$) using a CSC and a VASC at $f = 15\,GHz$ at different V_{VASC}.

Fig. 7.3.25 shows the gain compression of the CC-FBAs-IG using a CSC and a VASC ($V_{VASC} = -5\,V$ and $V_{VASC} = -9\,V$) at 10 GHz and 12 GHz. The normalized *Gain* of the CC-FBA-IG using a CSC can only

slightly be increased by using a VASC ($V_{VASC} = -5\,V$) in the 0–0.5 dB gain compression range, shown in Fig. 7.3.25a and Fig. 7.3.25b. At higher compression levels at 12 GHz, the CC-FBA-IG-D2 behaves even worse than the CC-FBA-IG using a CSC, illustrated in Fig. 7.3.25b. Furthermore, at $V_{VASC} = -9\,V$ the normalized *Gain* of the CC-FBA-IG using a CSC is even better than the CC-FBA-IG-D2 over the hole P_{out} range.
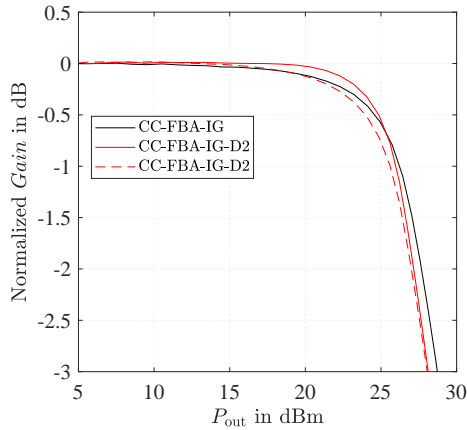
(a) Normalized *Gain* vs. P_{out} of CC-FBA-IG and CC-FBA-IG-D2 at $f = 10\,GHz$.
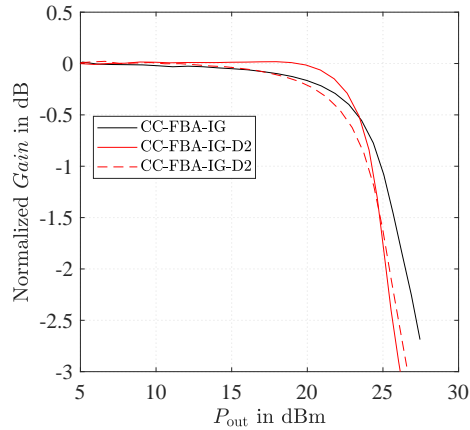
(b) Normalized *Gain* vs. P_{out} of CC-FBA-IG and CC-FBA-IG-D2 at $f = 12\,GHz$.

Figure 7.3.25: Comparison of measured normalized *Gain* vs. P_{out} of the CC-FBA-IG ($V_{DS} = 20\,V$, $I_{DSQ} = 240\,mA$) using a CSC and a VASC at different frequencies at $V_{VASC} = -5\,V$ (solid line) and $V_{VASC} = -9\,V$ (dashed line).

The $HD2$ of the CC-FBAs using a CSC and a VASC are depicted in Fig. 7.3.26a and Fig. 7.3.10b. Due to the fact that at higher frequencies the $HD2$ is outside of the usable band of the FBAs and can be filtered by a low-pass filter at the output the FBA, the $HD2$ of the CC-FBAs are only illustrated up to 6 GHz and 8.5 GHz respectively. The $HD2$ of the CC-FBA-IB using a CSC is better than $-27\,dBc$ up to 8.5 GHz and can be significantly improved using a VASC. The improvement depends on the chosen realization structure of the VASC, shown in Fig. 7.3.26a:

- The CC-FBA-IB-D2 achieves a $HD2$ of better than $-33\,dBc$, which results in an improvement of about 6 dB.
- The $HD2$ is improved by the CC-FBA-IB-D1D up to 5 dB at lower frequencies, but is similar in the region of about 8.5 GHz.
- The CC-FBA-IB-D1U behaves vice versa than the CC-FBA-IB-D1D. The $HD2$ is only slightly improved at low frequencies, using the CC-FBA-IB-D1U. However, at higher frequencies, an improvement of more than 5 dB can be achieved. A $HD2$ of $-40\,dBc$ is achieved at 8 GHz.

The CC-FBA-IG using a CSC achieves a $HD2$ from $-36\,\text{dBc}$ to $-52\,\text{dBc}$ in the frequency range of 1–6 GHz, shown in Fig. 7.3.26b. However, using a VASC instead of a CSC, the $HD2$ increases by about 1 dB at low frequencies and up to 5 dB at 6 GHz.
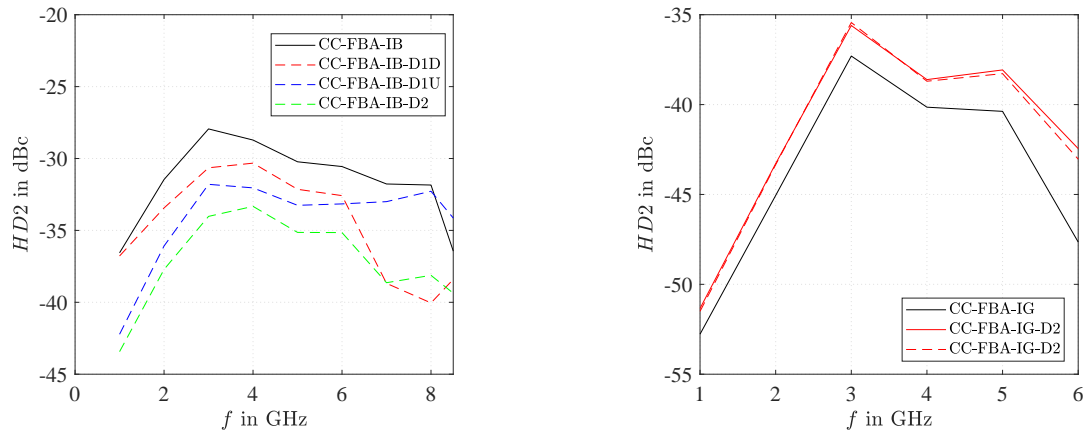
(a) $HD2$ vs. frequency of CC-FBA-IB and CC-FBA-IB-(D1D/D1U/D2) at $V_{\text{VASC}} = -6\,\text{V}$.

(b) $HD2$ vs. frequency of CC-FBA-IG and CC-FBA-IG-D2 at $V_{\text{VASC}} = -5\,\text{V}$ (solid line) and $V_{\text{VASC}} = -9\,\text{V}$ (dashed line).

Figure 7.3.26: Comparison of measured $HD2$ vs. frequency of the CC-FBA-IB ($V_{\text{DS}} = 10\,\text{V}$, $I_{\text{DSQ}} = 104\,\text{mA}$) and CC-FBA-IG ($V_{\text{DS}} = 20\,\text{V}$, $I_{\text{DSQ}} = 240\,\text{mA}$) using a CSC and a VASC at a $P_{\text{out}} = 15\,\text{dBm}$ at different V_{VASC}.

Fig. 7.3.27 compares the $HD3$ of the CC-FBAs using a CSC and a VASC. The $HD3$ of the CC-FBAs are only illustrated up to 4 GHz and $\approx 5.7\,\text{GHz}$, respectively, as the harmonics can be filtered out using a low-pass filter after the PA at higher frequencies. The CC-FBA-IB using a CSC illustrates a $HD3$ of better than $-43\,\text{dBc}$ up to 5.7 GHz, which can be significantly improved by using a VASC instead of a CSC. Fig. 7.3.27a shows the improvement depending on the chosen realization structure of the VASC:

- The CC-FBA-IB-D2 achieves a $HD3$ of better than $-46\,\text{dBc}$ in the frequency range of 1–5.7 GHz. The improvement amounts to 1–4 dB depending on frequency.
- The $HD3$ of the CC-FBA-IB-D1D, which is better than $-43\,\text{dBc}$ up to 5.7 GHz, is slightly improved up to 1.5 dB at lower frequencies (1–3.5 GHz) and is degraded in the frequency range of 3.5–5.7 GHz up to 1 dB.
- In the frequency range of 1–5.7 GHz a $HD3$ of better than $-45\,\text{dBc}$ is achieved of the CC-FBA-IB-D1U. The improvement of the CC-FBA-IB-D1U is slightly smaller (0.5–1 dB) than the CC-FBA-IB-D2 at lower frequencies (1–3.5 GHz) and is negligible better in the frequency range of 3.5–5.7 GHz.

Fig. 7.3.27b shows the $HD3$ of the CC-FBA-IG using a CSC which is the range of $-50\,\text{dBc}$ to $-61\,\text{dBc}$ in the frequency range of 1–4 GHz. The $HD3$ of the CC-FBA-IG using a CSC and a VASC at $V_{\text{VASC}} = -9\,\text{V}$ is very similar. The $HD3$ can be slightly improved in a certain frequency range by increasing V_{VASC} from $-9\,\text{V}$ to $-5\,\text{V}$.

(a) $HD3$ vs. frequency of CC-FBA-IB and CC-FBA-IB-(D1D/D1U/D2) at $V_{\text{VASC}} = -6\,\text{V}$.

(b) $HD3$ vs. frequency of CC-FBA-IG and CC-FBA-IG-D2 at $V_{\text{VASC}} = -5\,\text{V}$ (solid line) and $V_{\text{VASC}} = -9\,\text{V}$ (dashed line).
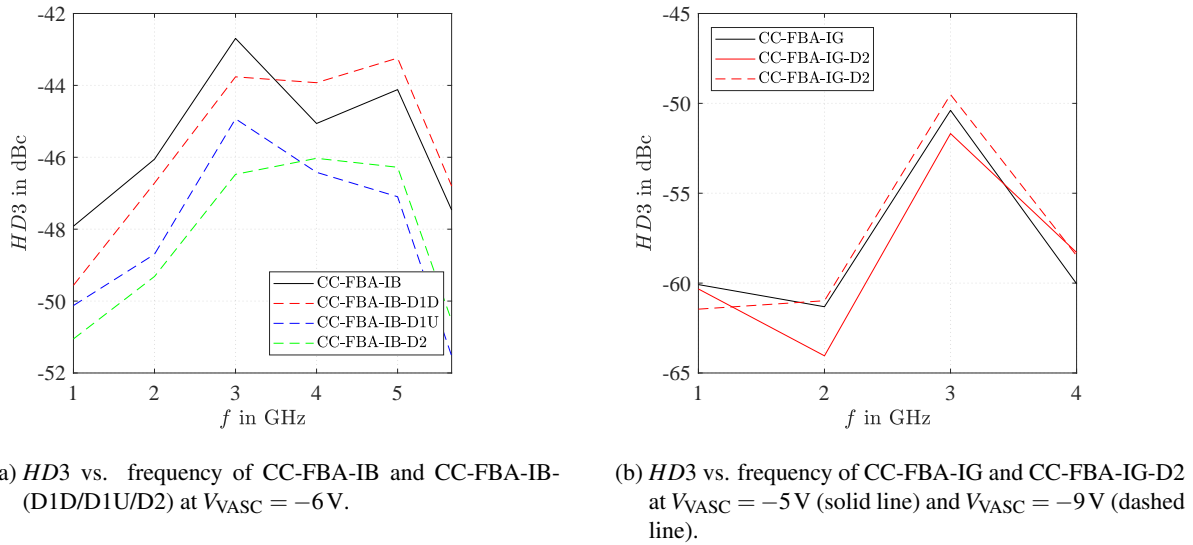
Figure 7.3.27: Comparison of measured $HD3$ vs. frequency of the CC-FBA-IB ($V_{\text{DS}} = 10\,\text{V}$, $I_{\text{DSQ}} = 104\,\text{mA}$) and CC-FBA-IG ($V_{\text{DS}} = 20\,\text{V}$, $I_{\text{DSQ}} = 240\,\text{mA}$) using a CSC and a VASC at a $P_{\text{out}} = 15\,\text{dBm}$ at different V_{VASC}.

7.3.2.3 Improved Linearity

S-Parameter Results

Fig. 7.3.28–Fig. 7.3.31 compares the measured S-parameters of the CC-FBAs using a CSC with C_{st} and a VASC with $C_{\text{st,var}}$ at a certain quiescent point of the CSS and the CGS (CC-FBAs-IB: $V_{\text{DS}} = 10\,\text{V}$, $I_{\text{DSQ}} = 156\,\text{mA}$, CC-FBAs-IG: $V_{\text{DS}} = 10\,\text{V}$, $I_{\text{DSQ}} = 240\,\text{mA}$) at $V_{\text{VASC}} = -6\,\text{V}$. The $|\underline{S}_{21}|$ of the CC-FBAs using a CSC and a VASC is shown in Fig. 7.3.28. The $|\underline{S}_{21}|$ of the CC-FBA-IB ($|\underline{S}_{21}| \approx 13\text{--}14\,\text{dB}$) and of the CC-FBA-IG ($|\underline{S}_{21}| \approx 15\text{--}17\,\text{dB}$) using a CSC are very similar to the $|\underline{S}_{21}|$ of the CC-FBA-IB-(D1D/D1U/D2) and of the CC-FBA-IG-D2 at $V_{\text{VASC}} = -6\,\text{V}$ (dashed lines), shown in Fig. 7.3.28a and Fig. 7.3.28b respectively. The f_{c} is about $17\,\text{GHz}$ of the CC-FBAs-IB and is about $12\,\text{GHz}$ of the CC-FBAs-IG.

(a) $|\underline{S}_{21}|$ of CC-FBA-IB and CC-FBA-IB-(D1D/D1U/D2).

(b) $|\underline{S}_{21}|$ of CC-FBA-IG and CC-FBA-IG-D2.
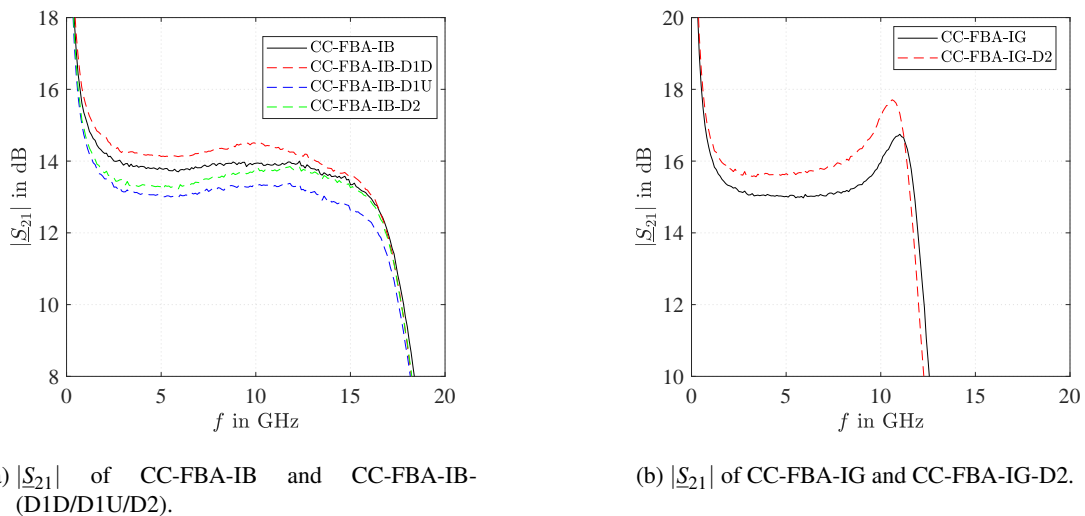
Figure 7.3.28: Comparison of measured $|\underline{S}_{21}|$ of the CC-FBA-IB ($V_{\text{DS}} = 10\,\text{V}$, $I_{\text{DSQ}} = 156\,\text{mA}$) and CC-FBA-IG ($V_{\text{DS}} = 10\,\text{V}$, $I_{\text{DSQ}} = 240\,\text{mA}$) using a CSC and a VASC at $V_{\text{VASC}} = -6\,\text{V}$.

The difference between the $|\underline{S}_{12}|$ of the CC-FBAs using a CSC and a VASC (CC-FBAs-IB: $|\underline{S}_{12}| < -17\,\mathrm{dB}$, CC-FBAs-IG: $|\underline{S}_{12}| < -20\,\mathrm{dB}$) is negligible shown in Fig. 7.3.29.

(a) $|\underline{S}_{12}|$ of CC-FBA-IB and CC-FBA-IB-(D1D/D1U/D2).

(b) $|\underline{S}_{12}|$ of CC-FBA-IG and CC-FBA-IG-D2.
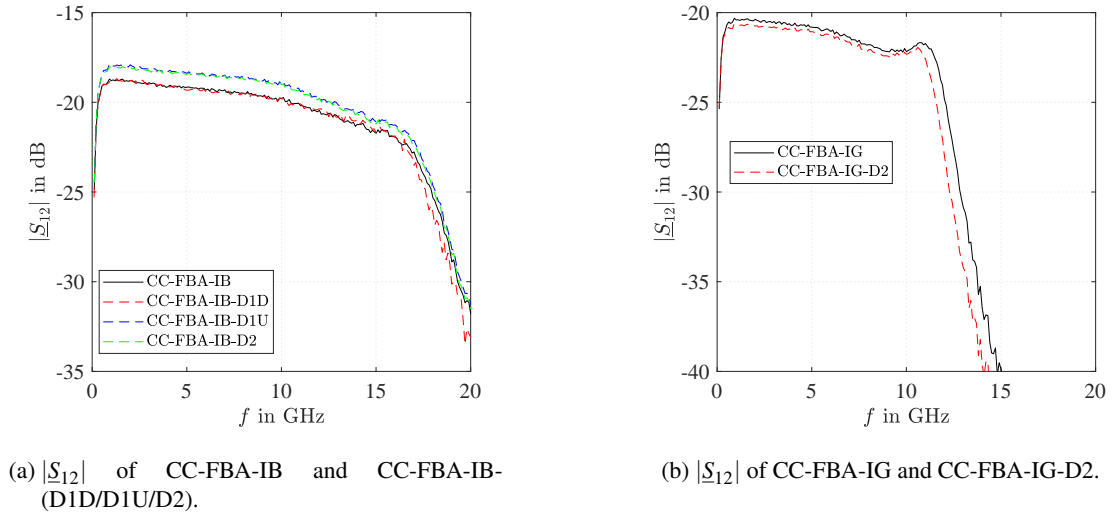
Figure 7.3.29: Comparison of measured $|\underline{S}_{12}|$ of the CC-FBA-IB ($V_{\mathrm{DS}} = 10\,\mathrm{V}$, $I_{\mathrm{DSQ}} = 156\,\mathrm{mA}$) and CC-FBA-IG ($V_{\mathrm{DS}} = 10\,\mathrm{V}$, $I_{\mathrm{DSQ}} = 240\,\mathrm{mA}$) using a CSC and a VASC at $V_{\mathrm{VASC}} = -6\,\mathrm{V}$.

Fig. 7.3.30 compares the $|\underline{S}_{11}|$ of the CC-FBAs using a CSC and a VASC. The $|\underline{S}_{11}|$ of the CC-FBAs-IB using a VASC is in the range of $-10\,\mathrm{dB}$ and $-8\,\mathrm{dB}$ over the complete bandwidth which results in a degradation of up to $2\,\mathrm{dB}$ compared to the CC-FBA-IB using a CSC, illustrated in Fig. 7.3.30a. The $|\underline{S}_{11}|$ of the CC-FBA-IG-D2 is very similar to the CC-FBA-IG using a CSC, shown in Fig. 7.3.30b.

(a) $|\underline{S}_{11}|$ of CC-FBA-IB and CC-FBA-IB-(D1D/D1U/D2).

(b) $|\underline{S}_{11}|$ of CC-FBA-IG and CC-FBA-IG-D2.
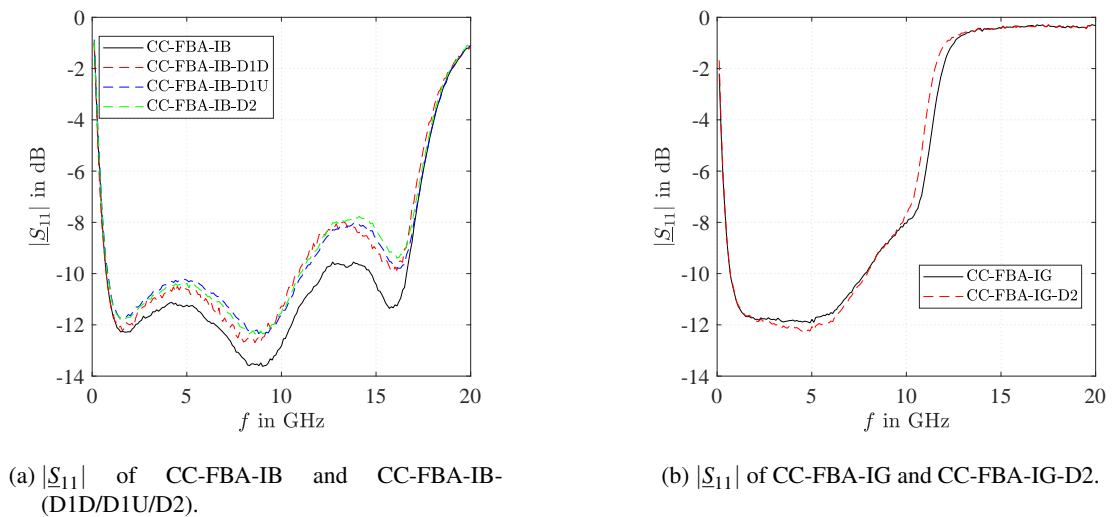
Figure 7.3.30: Comparison of measured $|\underline{S}_{11}|$ of the CC-FBA-IB ($V_{\mathrm{DS}} = 10\,\mathrm{V}$, $I_{\mathrm{DSQ}} = 156\,\mathrm{mA}$) and CC-FBA-IG ($V_{\mathrm{DS}} = 10\,\mathrm{V}$, $I_{\mathrm{DSQ}} = 240\,\mathrm{mA}$) using a CSC and a VASC at $V_{\mathrm{VASC}} = -6\,\mathrm{V}$.

The $|\underline{S}_{22}|$ of the CC-FBAs using a CSC and a VASC, which is in the range of $-10\,\mathrm{dB}$ and $-8\,\mathrm{dB}$ over the complete bandwidth, is shown in Fig. 7.3.31. Although, the $|\underline{S}_{22}|$ of the CC-FBAs-IB using a CSC and a VASC is very similar as well as the CC-FBAs-IG using a CSC and a VASC, the f_{c} of $|\underline{S}_{22}|$ is slightly shifted to lower frequencies using a VASC.

(a) $|\underline{S}_{22}|$ of CC-FBA-IB and CC-FBA-IB-(D1D/D1U/D2).

(b) $|\underline{S}_{22}|$ of CC-FBA-IG and CC-FBA-IG-D2.
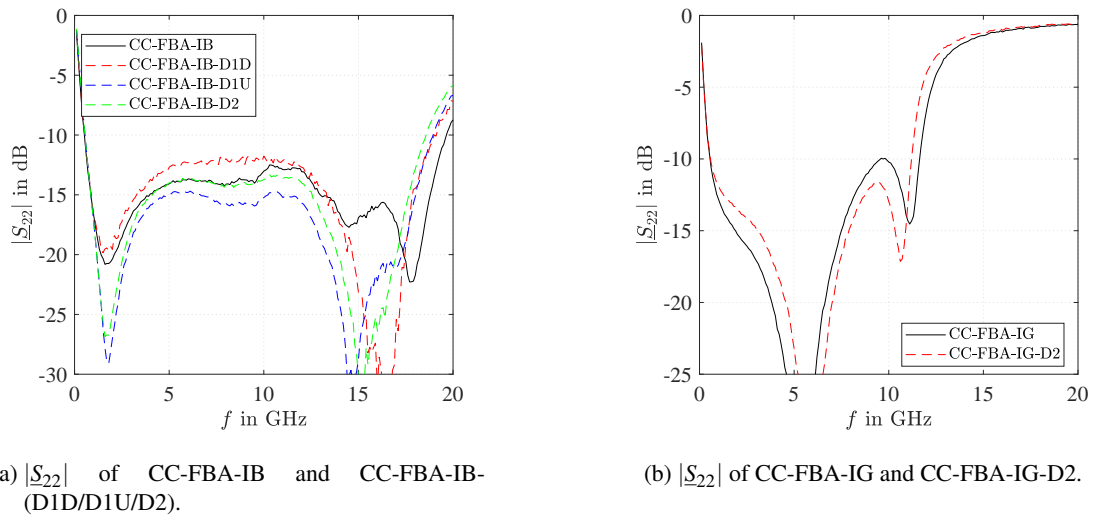
Figure 7.3.31: Comparison of measured $|\underline{S}_{22}|$ of the CC-FBA-IB ($V_{DS} = 10\,\text{V}$, $I_{DSQ} = 156\,\text{mA}$) and CC-FBA-IG ($V_{DS} = 10\,\text{V}$, $I_{DSQ} = 240\,\text{mA}$) using a CSC and a VASC at $V_{VASC} = -6\,\text{V}$.

Noise Figure Results

Fig. 7.3.32 compares the measured *NF* of the CC-FBAs using a CSC and a VASC at a certain quiescent point of the CSS and the CGS (CC-FBAs-IB: $V_{DS} = 10\,\text{V}$, $I_{DSQ} = 156\,\text{mA}$, CC-FBAs-IG: $V_{DS} = 10\,\text{V}$, $I_{DSQ} = 240\,\text{mA}$) at $V_{VASC} = -6\,\text{V}$. Fig. 7.3.32a shows the *NF* of the CC-FBAs-IB using a CSC and a VASC which is about 4 dB in the frequency range of 1–13 GHz and increases up to 6 dB at 17 GHz. Although the VASC includes an additional active element, the corresponding *NF* of the CC-FBAs-IB using the VASC is slightly better compared to the CC-FBA-IB using a CSC. Fig. 7.3.32b shows in the lower and moderate frequency range a *NF* of $< 4\,\text{dB}$ and $< 6\,\text{dB}$ at the f_c of 12 GHz of the CC-FBAs-IB using a CSC and a VASC. The *NF* of the CC-FBA-IG using a CSC and the *NF* of the CC-FBA-IG-D2 is very similar to each other with the exception of the higher interfering signal with the noise measurement setup at 10 GHz.

(a) *NF* of CC-FBA-IB and CC-FBA-IB-(D1D/D1U/D2).

(b) *NF* of CC-FBA-IG and CC-FBA-IG-D2.
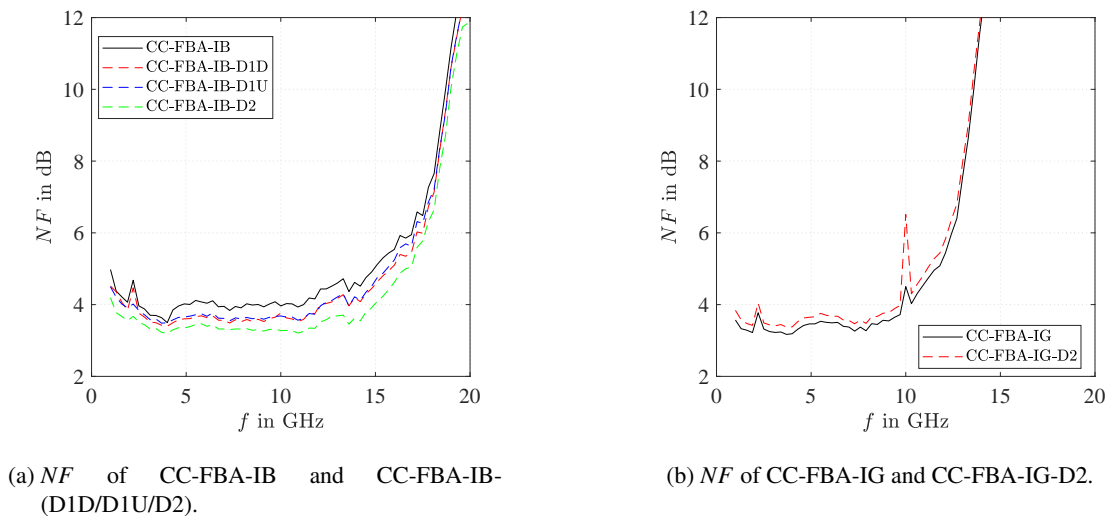
Figure 7.3.32: Comparison of measured *NF* of the CC-FBA-IB ($V_{DS} = 10\,\text{V}$, $I_{DSQ} = 156\,\text{mA}$) and CC-FBA-IG ($V_{DS} = 10\,\text{V}$, $I_{DSQ} = 240\,\text{mA}$) using a CSC and a VASC at $V_{VASC} = -6\,\text{V}$.

1-Tone Results

Fig. 7.3.33–Fig. 7.3.47 show the measured 1-Tone results of the CC-FBAs using a CSC and a VASC at a certain quiescent point of the CSS and the CGS (CC-FBA-IBs: $V_{DS} = 10\,V$, $I_{DSQ} = 156\,mA$, CC-FBA-IGs: $V_{DS} = 10\,V$, $I_{DSQ} = 240\,mA$) and a certain V_{VASC}. The V_{VASC} of the CC-FBA-(D1D/D1U/D2) is chosen between $-5\,V$ and $-9\,V$. Fig. 7.3.33 illustrates the $P_{out,max}$ of the CC-FBAs using a CSC and a VASC at $V_{VASC} = -6\,V$. For a $P_{DISS,MAX}$ of $7.28\,W$ ($\frac{P_{DISS,MAX}}{GP} = 7\,\frac{W}{mm}$) the CC-FBAs-IB using a CSC and a VASC achieve a $P_{out,max}$ at $1\,GHz$ of 30–$31\,dBm$ and at $17\,GHz \approx 27$–$28.5\,dBm$, shown in Fig. 7.3.33a. The $P_{out,max}$ of the CC-FBA-IB-D1D is slightly better at higher frequencies compared to the CC-FBA-IB using a CSC. The $P_{out,max}$ of the CC-FBAs-IB-(D1U/D2) is ≈ 0.5–$1\,dB$ worse over the complete bandwidth in contrast to the CC-FBA-IB using a CSC. Fig. 7.3.33b shows the $P_{out,max}$ of ≈ 27–$32\,dBm$ of the CC-FBAs-IG using a CSC and a VASC which are similar to each other.
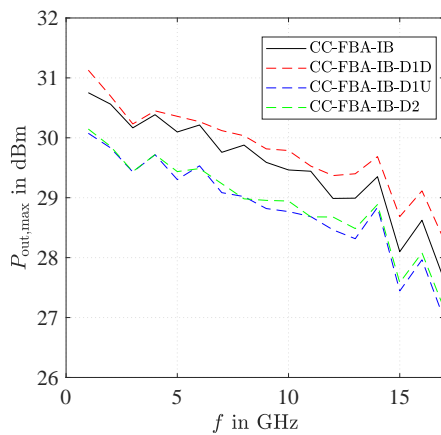
(a) $P_{out,max}$ vs. frequency of CC-FBA-IB and CC-FBA-IB-(D1D/D1U/D2).
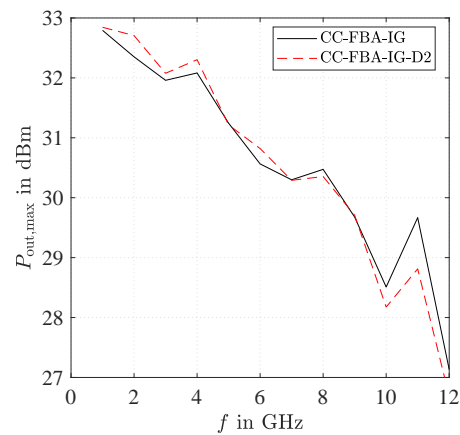
(b) $P_{out,max}$ vs. frequency of CC-FBA-IG and CC-FBA-IG-D2.

Figure 7.3.33: Comparison of measured $P_{out,max}$ vs. frequency of the CC-FBA-IB ($V_{DS} = 10\,V$, $I_{DSQ} = 156\,mA$) and CC-FBA-IG ($V_{DS} = 10\,V$, $I_{DSQ} = 240\,mA$) using a CSC and a VASC at $V_{VASC} = -6\,V$.
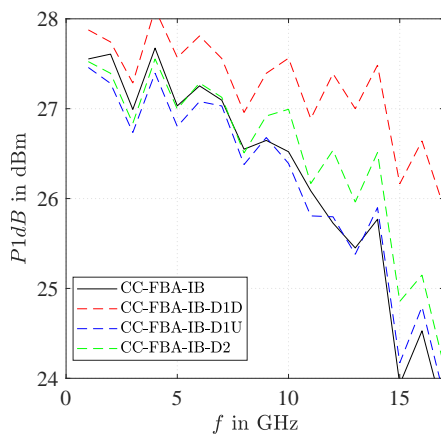
(a) $P1dB$ vs. frequency of CC-FBA-IB and CC-FBA-IB-(D1D/D1U/D2).
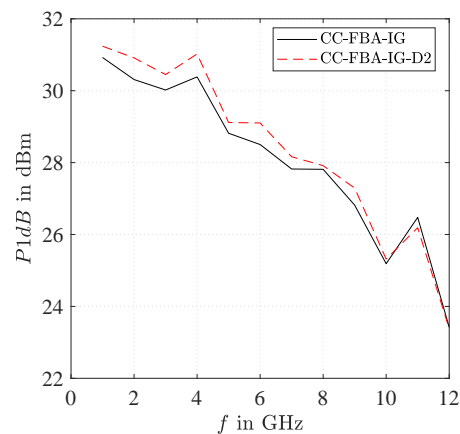
(b) $P1dB$ vs. frequency of CC-FBA-IG and CC-FBA-IG-D2.

Figure 7.3.34: Comparison of measured $P1dB$ vs. frequency of the CC-FBA-IB ($V_{DS} = 10\,V$, $I_{DSQ} = 156\,mA$) and CC-FBA-IG ($V_{DS} = 10\,V$, $I_{DSQ} = 240\,mA$) using a CSC and a VASC at $V_{VASC} = -6\,V$.

Fig. 7.3.34 compares the $P1dB$ of the CC-FBAs using a CSC and a VASC at $V_{\text{VASC}} = -6\,\text{V}$. A $P1dB$ of 24–28 dBm is achieved of the CC-FBAs-IB using CSC and a VASC, shown in Fig. 7.3.34a. The $P1dB$ of the CC-FBA-IB-D1U is almost equal to the CC-FBA-IB using a CSC. At higher frequencies the $P1dB$ is slightly increased by using the CC-FBAs-IB-D2. Comparing the $P1dB$ of the CC-FBA-IB-D1D and the CC-FBA-IB using a CSC, the $P1dB$ is significantly increased especially at higher frequencies using a VASC. The $P1dB$ of $\approx$ 24–31 dBm of the CC-FBAs-IG using a CSC and a VASC, shown in Fig. 7.3.34b, is very similar to each other.

Fig. 7.3.35–Fig. 7.3.38 show the harmonic distortion of the $HD2$ and $HD3$ versus frequency and versus P_{out} of the CC-FBA-IB-(D1D/D1U/D2) and of the CC-FBA-IG-D2 at $V_{\text{VASC}} = -5\,\text{V}$ and $V_{\text{VASC}} = -6\,\text{V}$. Depending on the realization structure of VASC the $HD2$ and $HD3$ can be improved in a certain P_{out} range by adjusting V_{VASC}.

(a) $HD2$ vs. frequency vs. P_{out} of CC-FBA-IB-D1D.

(b) $HD2$ vs. frequency vs. P_{out} of CC-FBA-IB-D1U.
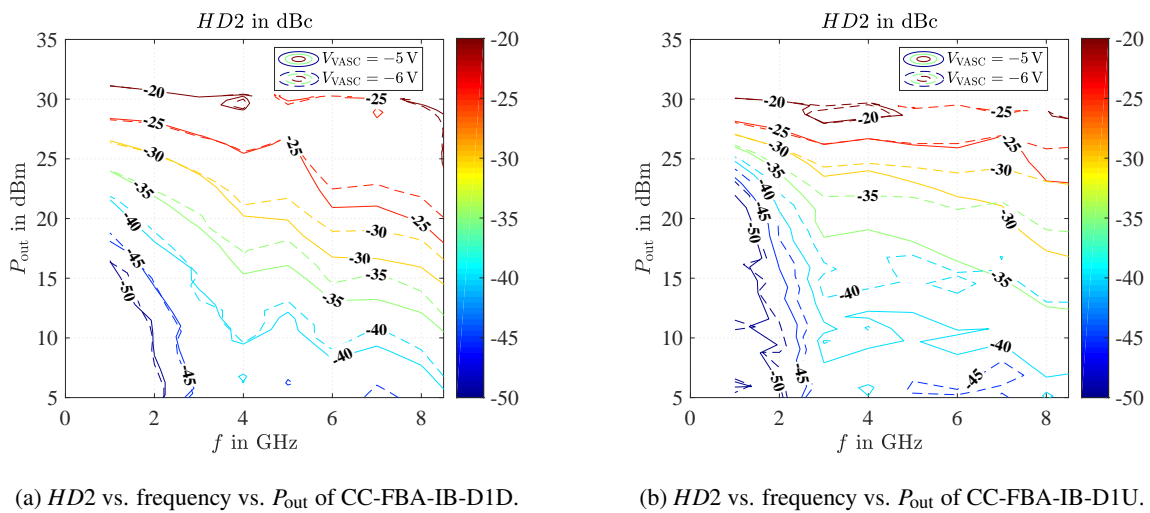
Figure 7.3.35: Measured $HD2$ vs. frequency vs. P_{out} of the CC-FBA-IB-D1D and CC-FBA-IB-D1U ($V_{\text{DS}} = 10\,\text{V}$, $I_{\text{DSQ}} = 156\,\text{mA}$) at $V_{\text{VASC}} = -5\,\text{V}$ and $V_{\text{VASC}} = -6\,\text{V}$.

(a) $HD2$ vs. frequency vs. P_{out} of CC-FBA-IB-D2.

(b) $HD2$ vs. frequency vs. P_{out} of CC-FBA-IG-D2.
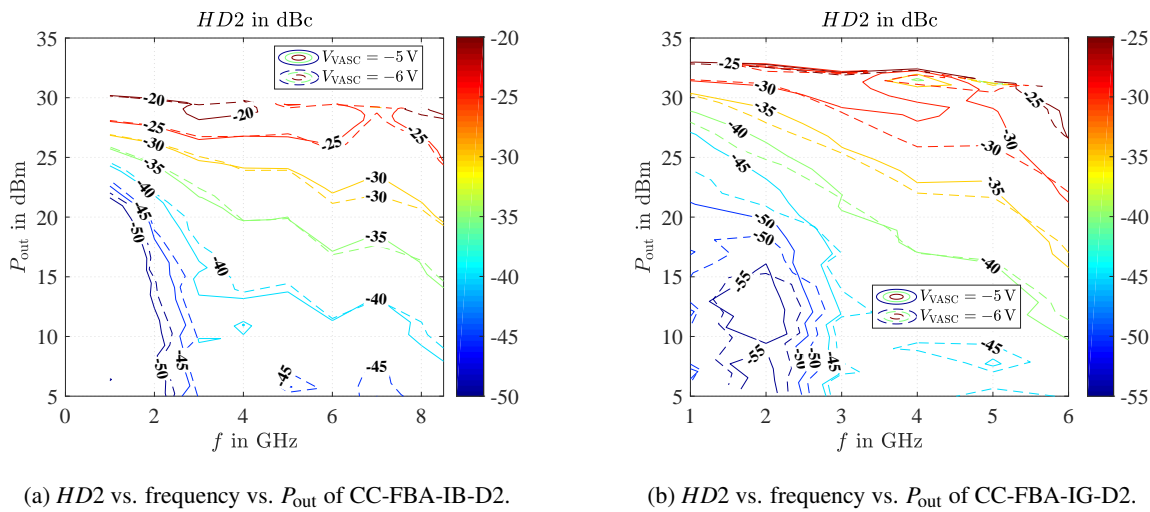
Figure 7.3.36: Measured $HD2$ vs. frequency vs. P_{out} of the CC-FBA-IB-D2 ($V_{\text{DS}} = 10\,\text{V}$, $I_{\text{DSQ}} = 156\,\text{mA}$) and CC-FBA-IG-D2 ($V_{\text{DS}} = 10\,\text{V}$, $I_{\text{DSQ}} = 240\,\text{mA}$) at $V_{\text{VASC}} = -5\,\text{V}$ and $V_{\text{VASC}} = -6\,\text{V}$.

(a) *HD*3 vs. frequency vs. P_{out} of CC-FBA-IB-D1D.

(b) *HD*3 vs. frequency vs. P_{out} of CC-FBA-IB-D1U.
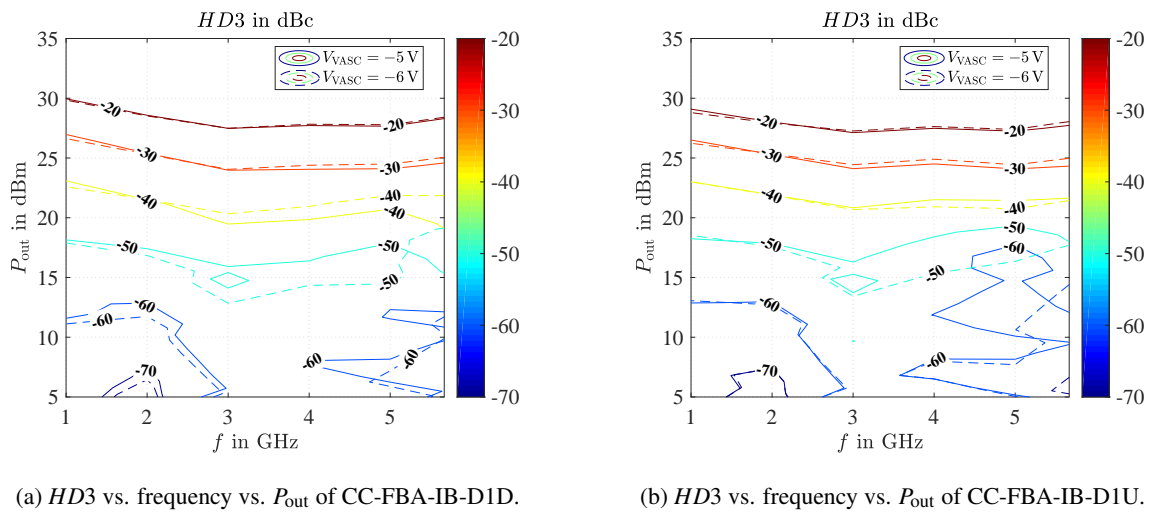
Figure 7.3.37: Measured *HD*3 vs. frequency vs. P_{out} of the CC-FBA-IB-D1D and CC-FBA-IB-D1U ($V_{DS} = 10\,V$, $I_{DSQ} = 156\,mA$) at $V_{VASC} = -5\,V$ and $V_{VASC} = -6\,V$.

(a) *HD*3 vs. frequency vs. P_{out} of CC-FBA-IB-D2.

(b) *HD*3 vs. frequency vs. P_{out} of CC-FBA-IG-D2.
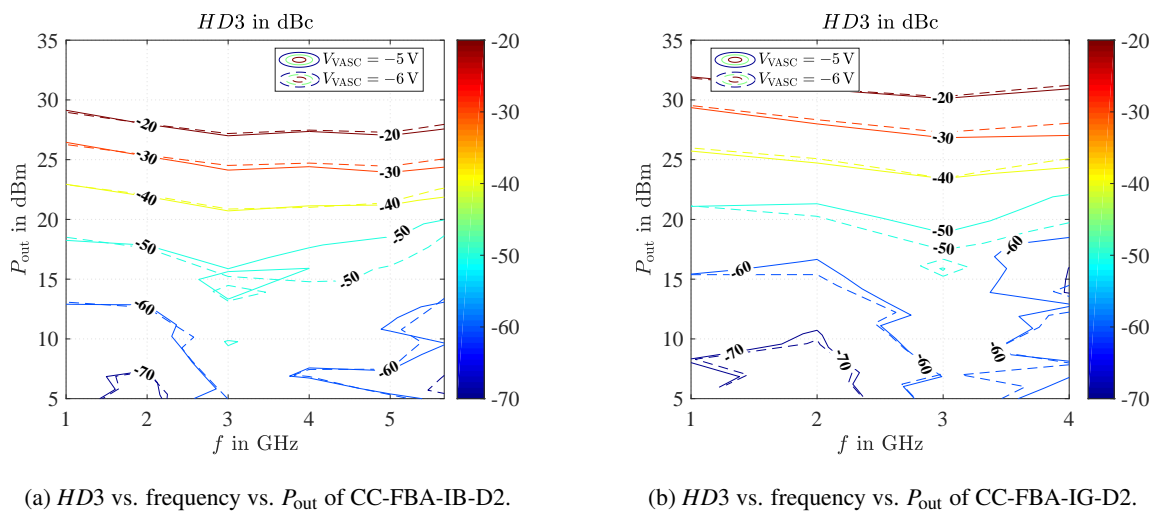
Figure 7.3.38: Measured *HD*3 vs. frequency vs. P_{out} of the CC-FBA-IB-D2 ($V_{DS} = 10\,V$, $I_{DSQ} = 156\,mA$) and CC-FBA-IG-D2 ($V_{DS} = 10\,V$, $I_{DSQ} = 240\,mA$) at $V_{VASC} = -5\,V$ and $V_{VASC} = -6\,V$.

At a P_{out} of 20 dBm, the Fig. 7.3.39 compares the *HD*2 of the CC-FBAs-IB using a CSC and a VASC at $V_{VASC} = -5\,V$ and $V_{VASC} = -6\,V$. The *HD*2 of the CC-FBA-IB using a CSC which is better than $-33\,$dBc, has a superior behavior at higher frequencies compared to the CC-FBAs-IB using a VASC. The *HD*2 increases by 3–14 dB at the f_c depending on the realization structure of the VASC and of the adjusted V_{VASC}. Using a lower V_{VASC} improves the *HD*2 slightly. At lower frequencies (1–4 GHz), the *HD*2 of the CC-FBA-IB can be improved by replacing the CSC by the VASC. At 1 GHz the *HD*2 can be enhanced up to 15 dB depending on the chosen realization of the VASC:

- The *HD*2 of the CC-FBA-IB-D1D is very similar at lower frequencies to the CC-FBA-IB using a CSC.
- The CC-FBA-IB-D2 shows the best *HD*2 performance compared to the other realizations of the VASC in the lower frequency range.
- The *HD*2 of the CC-FBA-IB-D1U is slightly worse than the CC-FBA-IB-D2, but significantly better in contrast to the CC-FBA-D1D.
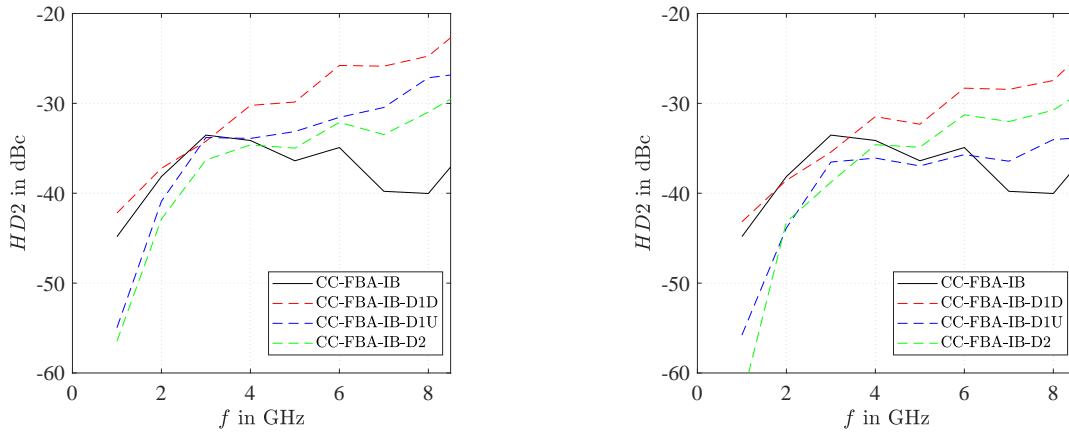
(a) *HD*2 vs. frequency of CC-FBA-IB and CC-FBA-IB-(D1D/D1U/D2) at $V_{\text{VASC}} = -5\,\text{V}$.

(b) *HD*2 vs. frequency of CC-FBA-IB and CC-FBA-IB-(D1D/D1U/D2) at $V_{\text{VASC}} = -6\,\text{V}$.

Figure 7.3.39: Comparison of measured *HD*2 vs. frequency of the CC-FBA-IB ($V_{\text{DS}} = 10\,\text{V}$, $I_{\text{DSQ}} = 156\,\text{mA}$) using a CSC and a VASC at a $P_{\text{out}} = 20\,\text{dBm}$ at different V_{VASC}.

Lowering the P_{out} by 5 dB to 15 dBm, the *HD*2 of the CC-FBAs-IB using a CSC and a VASC at $V_{\text{VASC}} = -5\,\text{V}$ and $V_{\text{VASC}} = -6\,\text{V}$ is compared in Fig. 7.3.40. Using a CSC, the *HD*2 of the CC-FBA-IB is better than $-36\,\text{dBc}$ and has the same characteristic as illustrated in Fig. 7.3.39. The *HD*2 of the CC-FBAs-IB using a VASC is still worse at a lower P_{out} at higher frequencies compared to the CC-FBA-IB using a CSC. At the f_{c}, the increase of the *HD*2 using the VASC instead of the CSC amounts to 2–11 dB. Furthermore, at lower frequencies the improvement of the *HD*2 of the CC-FBAs-IB-(D1U/D2) even degrades using the VASC at lower P_{out}.
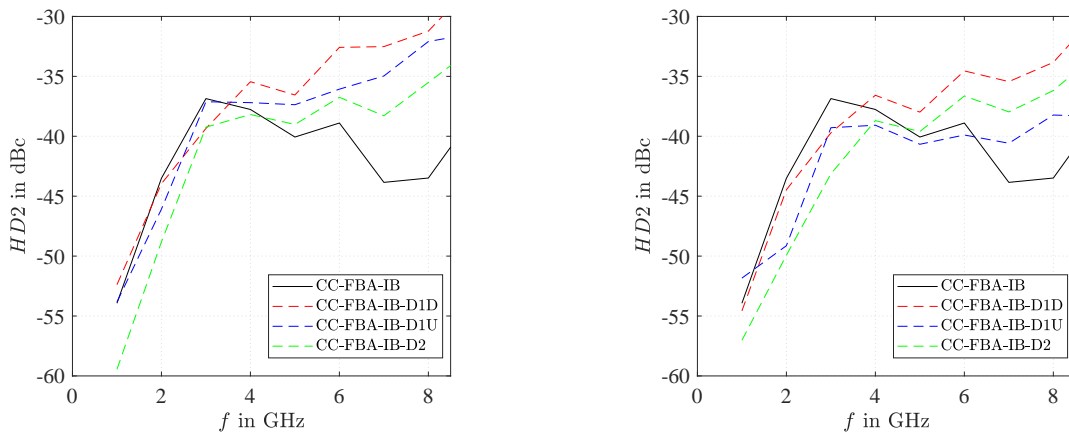
(a) *HD*2 vs. frequency of CC-FBA-IB and CC-FBA-IB-(D1D/D1U/D2) at $V_{\text{VASC}} = -5\,\text{V}$.

(b) *HD*2 vs. frequency of CC-FBA-IB and CC-FBA-IB-(D1D/D1U/D2) at $V_{\text{VASC}} = -6\,\text{V}$.

Figure 7.3.40: Comparison of measured *HD*2 vs. frequency of the CC-FBA-IB ($V_{\text{DS}} = 10\,\text{V}$, $I_{\text{DSQ}} = 156\,\text{mA}$) using a CSC and a VASC at a $P_{\text{out}} = 15\,\text{dBm}$ at different V_{VASC}.

Fig. 7.3.41 shows the *HD*3 of the CC-FBAs-IB using a CSC and a VASC at a P_{out} of 20 dBm for different V_{VASC} ($V_{\text{VASC}} = -5\,\text{V}$ and $V_{\text{VASC}} = -6\,\text{V}$). The *HD*3 of the CC-FBA-IB using a CSC is better than $-40\,\text{dBc}$. Replacing the CSC by a VASC, the *HD*3 can be improved depending on the realization structure of the VASC and the adjusted V_{VASC}:

- Adjusting V_{VASC} to $-6\,$V, the $HD3$ of the CC-FBA-IB-D1D is up to $2\,$dB better at higher frequencies compared to the CC-FBA-IB using a CSC, shown in Fig. 7.3.41b. At lower frequencies the improvement is rather negligible. However, increasing V_{VASC} to $-5\,$V increases the $HD3$ of the CC-FBA-IB-D1D which results even in a worse $HD3$ in a certain frequency range in contrast to the CC-FBA-IB using a CSC.
- Replacing the CSC by a VASC and adjusting V_{VASC} to $-5\,$V, the $HD3$ of the CC-FBAs-IB-(D1U/D2) is improved by $\approx 1\,$dB in the frequency range of 1–3 GHz, shown in Fig. 7.3.41a. At the f_c the best $HD3$ improvement up to $7\,$dB is achieved by the CC-FBA-IB-D2. However, the CC-FBA-IB-D1U shows the better average improvement of the $HD3$ compared to the CC-FBA-IB-D2 from $3\,$GHz to the f_c. Decreasing V_{VASC} to $-6\,$V, decreases the improvement of the $HD3$ of the CC-FBAs-IB-(D1U/D2).
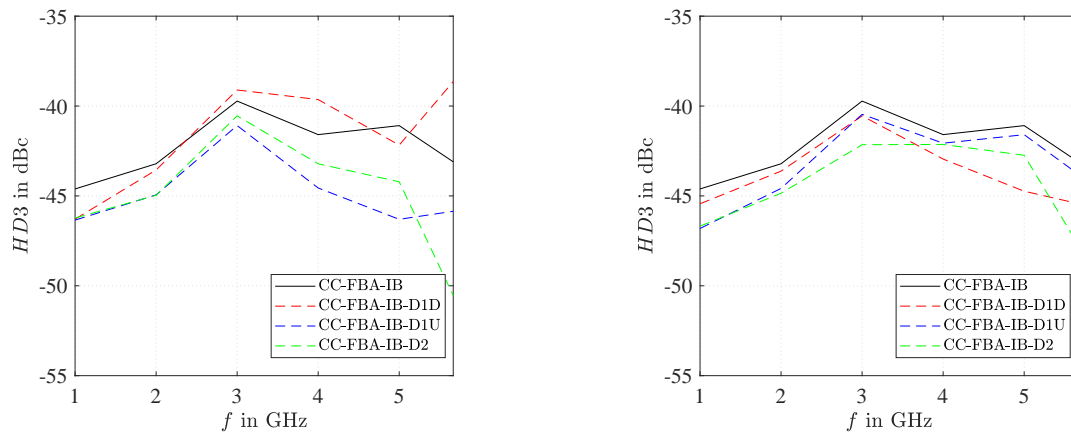
(a) $HD3$ vs. frequency of CC-FBA-IB and CC-FBA-IB-(D1D/D1U/D2) at $V_{VASC} = -5\,$V.

(b) $HD3$ vs. frequency of CC-FBA-IB and CC-FBA-IB-(D1D/D1U/D2) at $V_{VASC} = -6\,$V.

Figure 7.3.41: Comparison of measured $HD3$ vs. frequency of the CC-FBA-IB ($V_{DS} = 10\,$V, $I_{DSQ} = 156\,$mA) using a CSC and a VASC at a $P_{out} = 20\,$dBm at different V_{VASC}.
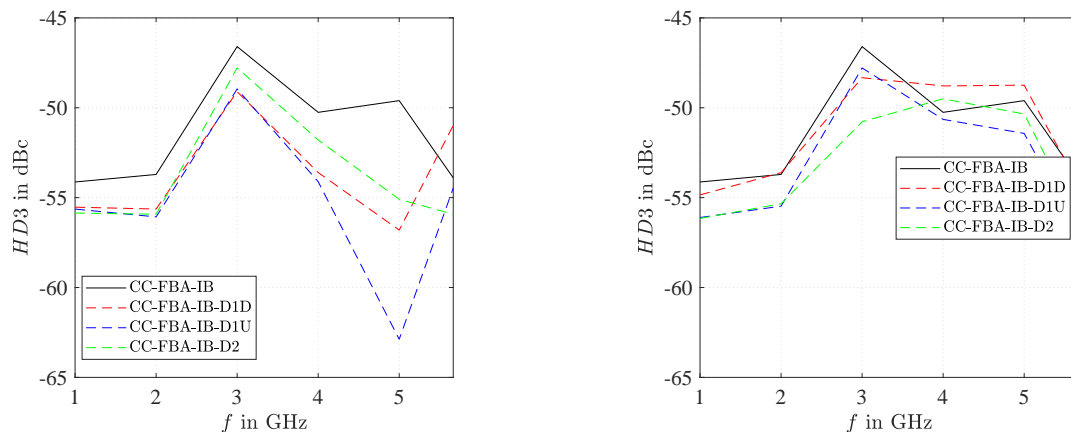
(a) $HD3$ vs. frequency of CC-FBA-IB and CC-FBA-IB-(D1D/D1U/D2) at $V_{VASC} = -5\,$V.

(b) $HD3$ vs. frequency of CC-FBA-IB and CC-FBA-IB-(D1D/D1U/D2) at $V_{VASC} = -6\,$V.

Figure 7.3.42: Comparison of measured $HD3$ vs. frequency of the CC-FBA-IB ($V_{DS} = 10\,$V, $I_{DSQ} = 156\,$mA) using a CSC and a VASC at a $P_{out} = 15\,$dBm at different V_{VASC}.

At a $P_{out} = 15\,$dBm, Fig. 7.3.42 compares the $HD3$ of the CC-FBAs-IB using a CSC and a VASC at $V_{VASC} = -5\,$V and $V_{VASC} = -6\,$V. Due to the lower P_{out}, the CC-FBA-IB using a CSC achieves a $HD3$ of better than $-46\,$dBc over the hole bandwidth. Furthermore, the $HD3$ improvement using a VASC

is even enhanced adjusting V_{VASC} to $-5\,\text{V}$. However, at $V_{\text{VASC}} = -6\,\text{V}$, the $HD3$ shows an increase at higher frequencies. As a result the $HD3$ of the CC-FBA-IB-D1D is worse in the higher frequency range compared to the CC-FBA-IB using a CSC.

Fig. 7.3.43 shows the $HD2$ of the CC-FBA-IG using a CSC and the CC-FBA-IG-D2 using a VASC at different P_{out} levels ($P_{\text{out}} = 20\,\text{dBm}$ and $P_{\text{out}} = 15\,\text{dBm}$) and different V_{VASC} ($V_{\text{VASC}} = -5\,\text{V}$ and $V_{\text{VASC}} = -6\,\text{V}$). At moderate and higher frequencies the $HD2$ of the CC-FBA-IG using a CSC is slightly better compared to the CC-FBA-IG-D2.
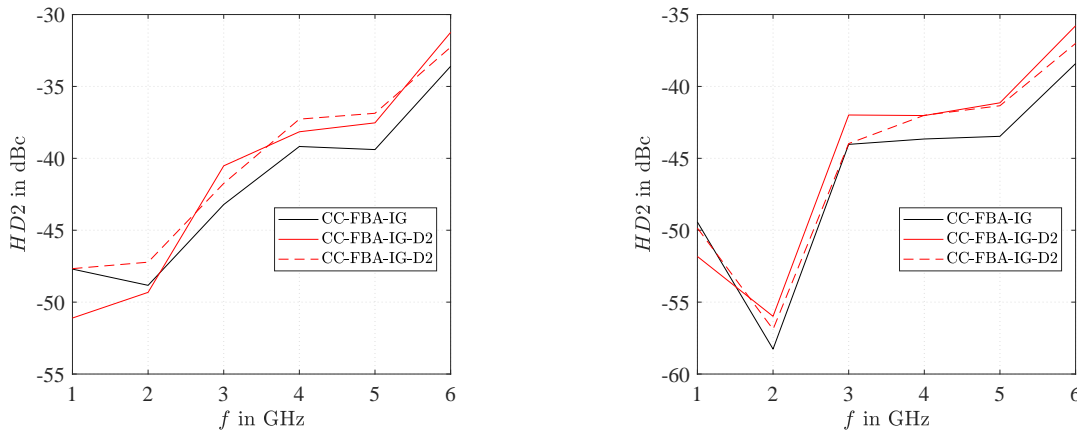
(a) $HD2$ vs. frequency of CC-FBA-IG and CC-FBA-IG-D2 at $P_{\text{out}} = 20\,\text{dBm}$.

(b) $HD2$ vs. frequency of CC-FBA-IG and CC-FBA-IG-D2 at $P_{\text{out}} = 15\,\text{dBm}$.

Figure 7.3.43: Comparison of measured $HD2$ vs. frequency of the CC-FBA-IG ($V_{\text{DS}} = 10\,\text{V}$, $I_{\text{DSQ}} = 240\,\text{mA}$) using a CSC and a VASC at different P_{out} at $V_{\text{VASC}} = -5\,\text{V}$ (solid line) and $V_{\text{VASC}} = -6\,\text{V}$ (dashed line).

Replacing the CSC of the CC-FBA-IG by a VASC, the improvement of the $HD3$ at different P_{out} levels ($P_{\text{out}} = 20\,\text{dBm}$ and $P_{\text{out}} = 15\,\text{dBm}$) and different V_{VASC} ($V_{\text{VASC}} = -5\,\text{V}$ and $V_{\text{VASC}} = -6\,\text{V}$) is illustrated in Fig. 7.3.44.
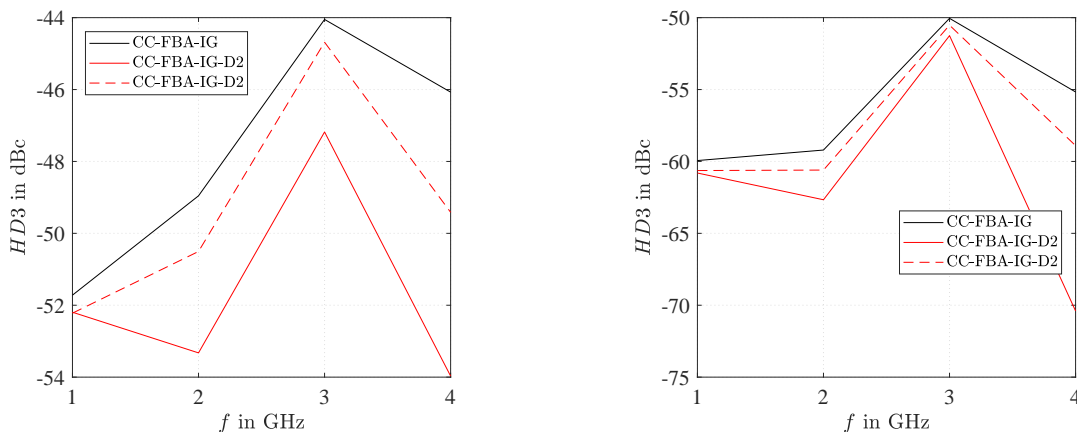
(a) $HD3$ vs. frequency of CC-FBA-IG and CC-FBA-IG-D2 at $P_{\text{out}} = 20\,\text{dBm}$.

(b) $HD3$ vs. frequency of CC-FBA-IG and CC-FBA-IG-D2 at $P_{\text{out}} = 15\,\text{dBm}$.

Figure 7.3.44: Comparison of measured $HD3$ vs. frequency of the CC-FBA-IG ($V_{\text{DS}} = 10\,\text{V}$, $I_{\text{DSQ}} = 240\,\text{mA}$) using a CSC and a VASC at different P_{out} at $V_{\text{VASC}} = -5\,\text{V}$ (solid line) and $V_{\text{VASC}} = -6\,\text{V}$ (dashed line).

At a P_{out} of 20 dBm and adjusting V_{VASC} to -5 V, a maximum $HD3$ improvement of 8 dB at 4 GHz, shown in Fig. 7.3.44a, is achieved. The improvement degrades at lower P_{out} as well as adjusting V_{VASC} to -6 V, but still show the superior behavior of the CC-FBA-IG-D2 compared to the CC-FBA-IG using a CSC at higher frequencies, illustrated in Fig. 7.3.44b. However, at lower frequencies the $HD3$ improvement using a VASC is rather negligible and expands to moderate frequencies at $P_{\text{out}} = 15$ dBm.

Fig. 7.3.45 compares the $HD2$ versus P_{out} at $f = 8$ GHz of the CC-FBAs-IB using a CSC and a VASC at different V_{VASC} ($V_{\text{VASC}} = -5$ V and $V_{\text{VASC}} = -6$ V). The $HD2$ of the CC-FBA-IB using a CSC shows a superior behavior over the hole P_{out} range in contrast to the CC-FBAs-IB using a VASC. Although, the $HD2$ of the CC-FBAs-IB using a VASC can be improved by decreasing the V_{VASC} from -5 V to -6 V, the $HD2$ is still 5–12 dB worse —depending on the realization structure of the VASC— than the CC-FBA-IB using a CSC.
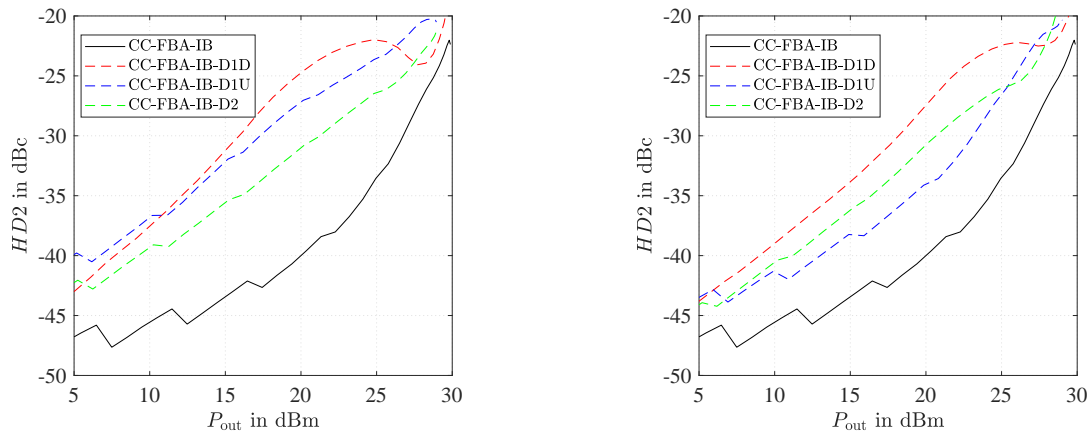
(a) $HD2$ vs. P_{out} of CC-FBA-IB and CC-FBA-IB-(D1D/D1U/D2) at $V_{\text{VASC}} = -5$ V.

(b) $HD2$ vs. P_{out} of CC-FBA-IB and CC-FBA-IB-(D1D/D1U/D2) at $V_{\text{VASC}} = -6$ V.

Figure 7.3.45: Comparison of measured $HD2$ vs. P_{out} of the CC-FBA-IB ($V_{\text{DS}} = 10$ V, $I_{\text{DSQ}} = 156$ mA) using a CSC and a VASC at $f = 8$ GHz at different V_{VASC}.

The $HD3$ versus P_{out} at $f = 5$ GHz of the CC-FBAs-IB using a CSC and a VASC at different V_{VASC} ($V_{\text{VASC}} = -5$ V and $V_{\text{VASC}} = -6$ V) is shown in Fig. 7.3.46. Comparing the $HD3$, the result is completely different to the $HD2$ comparison. Replacing the CSC by a VASC and adjusting V_{VASC} to -5 V, the $HD3$ can be improved up to 20 dB at a certain P_{out} level. At moderate P_{out} levels (10–21 dBm), the $HD3$ improvement of the CC-FBAs-IB using a VASC depends on the realization structure of the VASC, illustrated in Fig. 7.3.46a:

- The CC-FBA-IB-D1D and the CC-FBA-IB-D2 show as similar $HD3$ improvement up to ≈ 6 dB at a P_{out} of 16 dBm.
- The CC-FBA-IB-D1U shows the superior $HD3$ performance in contrast to the other realizations of the VASC.

At higher power levels the $HD3$ of the CC-FBAs-IB using a VASC is slightly worse than the CC-FBA-IB using a CSC. Furthermore, decreasing the V_{VASC} from -5 V to -6 V shifts the $HD3$ improvement to higher P_{out} levels using the VASC, shown in Fig. 7.3.46b. However, the advantage using the VASC regarding the $HD3$ decreases with lower V_{VASC}.

(a) *HD*3 vs. *P*out of CC-FBA-IB and CC-FBA-IB-(D1D/D1U/D2) at $V_{\mathrm{VASC}} = -5\,\mathrm{V}$.

(b) *HD*3 vs. *P*out of CC-FBA-IB and CC-FBA-IB-(D1D/D1U/D2) at $V_{\mathrm{VASC}} = -6\,\mathrm{V}$.
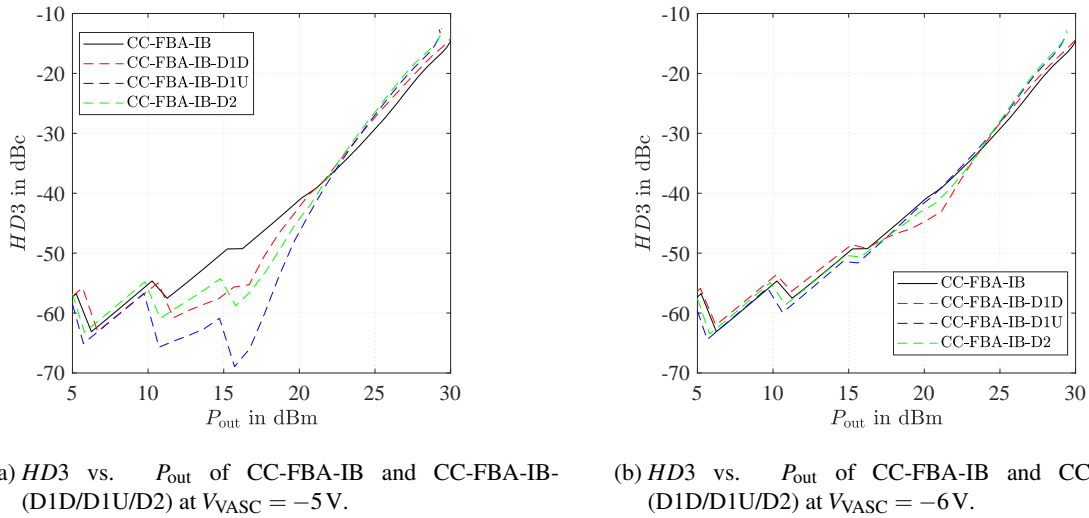
Figure 7.3.46: Comparison of measured *HD*3 vs. *P*out of the CC-FBA-IB ($V_{\mathrm{DS}} = 10\,\mathrm{V}$, $I_{\mathrm{DSQ}} = 156\,\mathrm{mA}$) using a CSC and a VASC at $f = 5\,\mathrm{GHz}$ at different V_{VASC}.

Fig. 7.3.47 compares the *HD*2 and *HD*3 versus *P*out at $f = 6\,\mathrm{GHz}$ and $f = 4\,\mathrm{GHz}$ of the CC-FBAs-IG using a CSC and a VASC at different V_{VASC} ($V_{\mathrm{VASC}} = -5\,\mathrm{V}$ and $V_{\mathrm{VASC}} = -6\,\mathrm{V}$). The *HD*2 and *HD*3 of the CC-FBAs-IG show a similar characteristic as the CC-FBAs-IB:

- The *HD*2 of the CC-FBA-IG-D2 is 1–3 dB worse compared to the CC-FBA-IG using a CSC, illustrated in Fig. 7.3.47a.
- At moderate *P*out levels (14–24 dBm) and adjusting V_{VASC} to $-5\,\mathrm{V}$, the *HD*3 improvement of the CC-FBA-IG-D2 amounts to 3–18 dB, shown in Fig. 7.3.47.

(a) *HD*2 vs. *P*out of CC-FBA-IG and CC-FBA-IG-D2 at $f = 6\,\mathrm{GHz}$.

(b) *HD*3 vs. *P*out of CC-FBA-IG and CC-FBA-IG-D2 at $f = 4\,\mathrm{GHz}$.
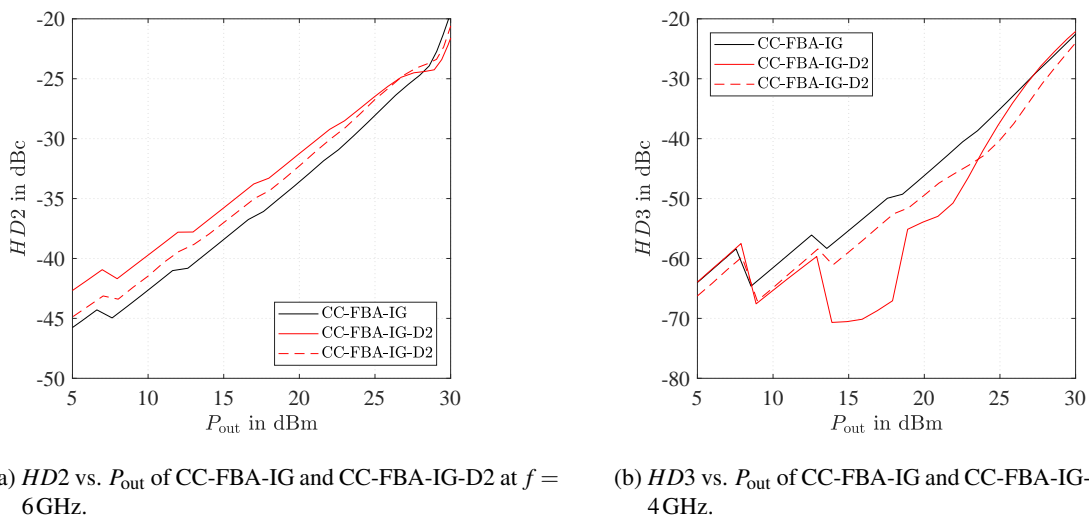
Figure 7.3.47: Comparison of measured *HD*2 and *HD*3 vs. *P*out of the CC-FBA-IG ($V_{\mathrm{DS}} = 10\,\mathrm{V}$, $I_{\mathrm{DSQ}} = 240\,\mathrm{mA}$) using a CSC and a VASC at different frequencies at $V_{\mathrm{VASC}} = -5\,\mathrm{V}$ (solid line) and $V_{\mathrm{VASC}} = -6\,\mathrm{V}$ (dashed line).

7.3.3 Conclusion

In Sec. 7.3 several designed CC-FBAs using the new concept with different realizations of the VASC with $C_{st,var}$ were presented to verify the theory set up in Ch. 6. The small-signal measurements (S-parameters and NF) and large-signal measurements (1-tone) of the CC-FBAs-(IB/IG) using a CSC and a VASC were compared with each other to highlight the advantages and to show the disadvantages of the different realizations of the VASC regarding three proposed applications of the new concept.

Key performance of the new concept as gain control mechanism in the CC-FBA:

- The $|\underline{S}_{21}|$ of the CC-FBAs using a VASC can be varied by 4–6 dB at the f_c. $|\underline{S}_{21}|$ of the CC-FBA-IB-D1U and the CC-FBA-IB-D2 are very similar and can be adjusted by 4 dB, whereas $\Delta |\underline{S}_{21}|$ of the CC-FBA-IB-D1D amounts to 6 dB which is the highest delta compared to the other realizations of the VASC.
- Due to the trade-off between stability and $\underline{S}_{21}$, the stability of the CC-FBAs using the new concept degrades with increasing adjusted $|\underline{S}_{21}|$. At a certain point of $|\underline{S}_{21}|$, the CC-FBA is no longer unconditionally stable, also due to the higher input and output reflection (higher $|\underline{S}_{11}|$ and $|\underline{S}_{22}|$) which can lead to an oscillation at the input and output of the CC-FBA.
- Furthermore, despite the VASC which includes at least one transistor as a diode, the corresponding NF was unchanged in contrast to the CC-FBAs using a CSC independent on the adjusted V_{VASC}.
- One of the key large-signal parameter $P_{out,max}$ of the CC-FBAs using a VASC was lower or similar to the CC-FBAs using a CSC depending on the realization structure of the VASC and of the adjusted V_{VASC}. While the CC-FBA-IB-D1D offered a similar $P_{out,max}$ compared to the CC-FBA-IB using a CSC, the $P_{out,max}$ of the CC-FBA-IB-D1U and the CC-FBA-IB-D2 were 1–2 dB lower than the $P_{out,max}$ of the CC-FBA-IB using a CSC.
- Comparing the harmonic distortion of the second order and third order of the CC-FBAs-IB using a VASC with the CC-FBA-IB using a CSC, two properties were exhibited. On the one hand the $HD2$, especially at higher frequencies was significantly deteriorated (up to 5–15 dB at 8.5 GHz) adjusting the V_{VASC} to -4 V to increase $|\underline{S}_{21}|$ comparing the CC-FBA-IB using a VASC. On the other hand the $HD3$ was improved using a certain realization structure of the VASC at $V_{VASC} = -4$ V. While the CC-FBA-IB-D1U improved the $HD3$ up to 10 dB at higher frequencies, the $HD3$ was slightly increased using the CC-FBA-IB-D2 at higher frequencies and even deteriorated by 15 dB using the CC-FBA-IB-D1D at the f_c.

Key performance of the new concept to improve the compression behavior of the CC-FBA:

- If the V_{VASC} is adjusted to -6 V, the S-parameters of the CC-FBAs-IB using a VASC showed a very similar behavior to the CC-FBA-IB using a CSC. As a result, the stability of the CC-FBA-IB using a VASC and a CSC was almost equal.
- Although the NF of the CC-FBAs-IB using a VASC showed an improvement of about 1 dB compared to the CC-FBA-IB using a CSC, this effect is believed to be rather related to process variations due to the fact that the VASC adds additional noise to the CC.
- Furthermore, regarding the large-signal performance, the $P_{out,max}$ of the CC-FBAs-IB using a VASC was up to 0.5 dB lower than the CC-FBA-IB using a CSC, independent on the realization structure of the VASC. However, comparing the CC-FBA-IG using a VASC and a CSC with each other, no $P_{out,max}$ degradation was detected.
- The gain compression improvement of the CC-FBAs-IB using a VASC depended significantly on the realization of the VASC and on the adjusted V_{VASC}. The CC-FBA-IB-D1D showed the best compression behavior in contrast to the other realization structures of the VASC. The $P1dB$ improvement amounted to 2.5 dB at higher frequencies adjusting V_{VASC} to -5 V. The $P0.1dB$ even showed an improvement of about 10 dB. The CC-FBA-IB-D1U and the CC-FBA-IB-D2 showed a similar compression improvement behavior adjusting V_{VASC} to -5 V. However, adjusting V_{VASC} to -6 V, the compression behavior of the CC-FBA-IB-D1U was worse than the CC-FBA-IB-D2.
- Additionally, as well as the gain compression, the $HD2$ and $HD3$ depended also on the realization structure of the VASC. Adjusting V_{VASC} to -6 V, the $HD2$ and $HD3$ of the CC-FBAs-IB using a

VASC were significantly improved —depending on the realization structure of the VASC— compared to the CC-FBA-IB using a CSC. Using two anti-parallel diodes as a VASC in the CC-FBA-IB-D2, the best $HD2$ and $HD3$ behavior were achieved comparing to the other realized structures of the VASC and to the CSC in the CC-FBA-IB. The improvement of the $HD2$ and the $HD3$ amounted to 2–6 dB and 1–4 dB, respectively. The $HD2$ of the CC-FBA-IB-D1D and the CC-FBA-IB-D1U behaved vice versa. The $HD2$ of the CC-FBA-IB-D1U was better in the low frequency range and the CC-FBA-IB-D1D was better at higher frequencies. However, the $HD3$ of the CC-FBA-IB-D1U showed a superior behavior over the complete frequency range compared to the CC-FBA-IB-D1D.

Key performance of the new concept to improve the linearity behavior of the CC-FBA:

- The S-Parameters as well as the NF of the CC-FBAs-IB using a VASC and a CSC were very similar to each other because the small-signal performance of the VASC —adjusting V_{VASC} to -6 V— and of the CSC were nearly equal. Moreover, due to the fact that the quiescent point of the CC-FBA to improve the compression behavior or to improve the linearity were not very far from each other, the small-signal results were very similar.
- Furthermore, the $P_{out,max}$ of the CC-FBA-IB-D1D was very similar using a VASC or a CSC. The $P_{out,max}$ of the CC-FBA-IB using a CSC was up to 0.5 dB higher than the CC-FBAs-IB-(D1U/D2) using a VASC.
- Additionally, comparing the $P1dB$ of the CC-FBA-IB-D1D and the CC-FBA-IB using a CSC, the $P1dB$ was improved by ≈ 2 dB at higher frequencies using a VASC. The CC-FBA-IB using a CSC and the CC-FBAs-IB-(D1U/D2) were similar to each other. At certain frequency points the CC-FBA-IB-D2 seemed to be slightly better than the CC-FBA-IB-D1U.
- Replacing the CSC by a VASC, the $HD2$ and the $HD3$ were improved in a certain frequency range and P_{out} range, depending on the adjusted V_{VASC} and on the realization structure of the VASC. The $HD2$ was mainly improved in the lower frequency range. However, at higher frequencies the CC-FBA-IB using a CSC showed a superior behavior in contrast to the CC-FBAs-IB using a VASC. The $HD2$ of the CC-FBA-D1D showed almost the worst behavior over the complete frequency range. The $HD3$ was improved using the VASC over a moderate power range and a wide frequency range, depending on the adjusted V_{VASC}. The CC-FBA-IB-D1U showed the best $HD3$ improvement which is up to 20 dB at $P_{out} = 16$ dBm. Decreasing V_{VASC} changed the power range improvement of the $HD3$ to higher power levels. However, the overall performance will degrade. The CC-FBAs-IB-(D1D/D2) showed a slightly worse $HD3$ behavior than the CC-FBA-IB-D1U, but still better than the CC-FBA-IB using a CSC in a wide frequency range and at moderate power levels.

7.4 Summary

In Sec. 7.1 the fundamentals of two types of amplifier structures to realize multi-decade PAs were shown and explained. Afterwards, in Sec. 7.2 and in Sec. 7.3 several designed FBAs, including small-signal measurements and large-signal measurements, were presented to verify the theoretical investigations in Ch. 4–Ch. 6 by highlighting the advantages and disadvantages of the CC topology in broadband PAs and to point out the superior RF performance using the new concept by replacing the CSC with C_{st} by the VASC with $C_{st,var}$. At the end of each section a conclusion was given to reveal a short overview of the insights. The most important key findings and trade-offs are summarized in Table 7.4.1 and Table 7.4.2.

Table 7.4.1 underlines the superior RF performance of the CC topology in contrast to the CS topology which matches with the presented theory in Ch. 4 and Ch. 5 with the exception of the improved noise behavior of the CC-FBA-IB (same P_{DISS} as CS-FBA). However, this effect can be traced back to the lower V_{DS} of the CC topology where the noise performance achieves its optimum.

Table 7.4.1: Key findings and trade-offs of the CC topology compared to the CS topology in FBAs.

			Improvement	Topology	Trade-Offs
RF-Parameters	Small-Signal	SSB	by 30%[*]	CC-FBA-IB	SSB versus $\lvert\underline{S}_{21}\rvert$, versus NF, versus P_{DISS} versus stability,
			by 40%		
		$\lvert\underline{S}_{21}\rvert$	by 1–2 dB	CC-FBA-IG	
		NF	by 2 dB @ low f		
	Large-Signal	LSB	due to higher $SS\text{-}B$	CC-FBA-IB	LSB versus $Gain$, versus $P_{out,max}$, versus Linearity, versus P_{DISS}
		$P_{out,max}$	by 3 dB @ low f	CC-FBA-IG	
		$P1dB$	by 4 dB @ low f	CC-FBA-IG	
			by 2 dB @ moderate f		
		$HD2$	by ≈ 1 dB[*]		
			by ≈ 2 dB[*]	CC-FBA-IB	
			by ≈ 5 dB	CC-FBA-IG	
		$HD3$	by ≈ 8–11 dB		

[*] same P_{DISS} of CS-FBA and CC-FBA otherwise same quiescent point for each active cell

Table 7.4.2 illustrates the improvement of the new concept regarding the different realizations of the VASC. As proposed in Ch. 6 all three realizations of the VASC should achieve a similar maximum dynamic range and as a result a similar $\lvert\underline{S}_{21}\rvert$ and bandwidth. However, the CC-FBA-IB-D1D achieved the highest dynamic range regarding the S-parameters. The improved dynamic behavior of $\lvert\underline{S}_{21}\rvert$ of the CC-FBA-IB-D1D could be explained by different multiple project wafer productions of the CC-FBAs using the VASC, due to the even slightly higher $\lvert\underline{S}_{21}\rvert$ at lower frequencies which is independent of the $C_{st,var}$. Furthermore, the CC-FBA-IB-D1D achieved the highest $P1dB$ improvement at higher frequencies compared to the other realization structures of the VASC which matches with the presented theory in Ch. 6. However, despite the higher $P1dB$ the P_{out} suffers a little bit using the VASC, which can be traced back to the higher mismatch at higher P_{out} levels at the output of the PA. The CC-FBA-IB-D2 achieved the best linearity behavior regarding $HD2$ and $HD3$ in a certain frequency and power range in contrast to the other realization structures of the VASC. Although the theory in Ch. 6 demonstrated a better linearity using a VASC as predistortion of the CGS or to improve the linearity of the $\underline{V}_{gs}$ at the CGS, in practice the VASC with its lowest non-linearity characteristic results overall in the best linearity behavior of PAs. Of course, this effect depends on the quiescent point of the FBA and the exact RF behavior of the VASC.

Table 7.4.2: Key findings and trade-offs of the new concept in CC-FBAs.

		CC-FBA-IB-(VASC)	Improvement due to the VASC			Key findings
			D1D	D1U	D2	
RF-Parameters	Small-Signal	SSB	↑	↑	↑	**D1D:** best small-signal performance
		$\lvert \underline{S}_{21} \rvert$	↑↑↑	↑↑	↑↑	
		NF	↓–0*	↓–0*	↓–0*	
	Large-Signal	LSB	↑	↑	↑	**D1D:** best $P_{\text{out,max}}$ and $P1dB$ performance **D2:** best linearity ($HD2$, $HD3$)
		$P_{\text{out,max}}$	0–↓*	↓↓	↓↓	
		$P1dB$	↑↑↑	↑↑ – ↑*	↑↑	
		$HD2$	↓↓–↑↑↑*	↓↓–↑↑*	↓↓↓–↑*	
		$HD3$	↓–0*	↓↓↓–0*	↓↓↓–0*	

* depends on the quiescent point of the CC-FBA and on the quiescent point of the VASC

In summary, the CC-FBA using the new concept has a superior small-signal and large-signal performance compared to the CS-FBA. Nevertheless, the new concept demonstrated its main advantages only in a certain frequency and power level range. Moreover, stability of PAs should be carefully investigated using the new concept especially at large-signal operation.

8 Conclusion and Outlook

The GaN-HEMT technology as state-of-the-art semiconductor is more and more employed to PA devices in high-end test and measurement equipment to offer high linearity and P_{out} over a wide frequency spectrum. Furthermore, replacing the CS topology by the CC topology in broadband PAs is a very beneficial solution to improve the RF performance of PAs.

Conclusion

The focus of this thesis consists of two main topics:

- The first focus of this thesis was the investigation and comparison of the CC topology with the CS topology in multi-decade PAs —using the GaN-HEMT technology— to highlight the advantages and disadvantages of the CC topology.
- The second main topic of this thesis comprised the development of a new concept to improve the RF performance of multi-decade PAs using the CC topology. Furthermore, different realization structures of the new concept were compared to each other with respect to their RF characteristic.

The thesis started with definitions of several important small-signal parameters, large-signal parameters and noise parameters to achieve a fundamental understanding how RF circuits can be described. Afterwards, the superior performance of the GaN-HEMT technology was highlighted, compared to other semiconductor technologies (i.e. Si-LDMOS, GaAs-HEMT) and an overview about modeling of GaN-HEMTs regarding small-signal, large-signal and noise behavior was given.

Subsequently, the first focus of this thesis was elaborated comprising the functionality of the CSS, the classical CC as well as the modified CC —more used nowadays using the GaN-HEMT technology— which were explained to give a fundamental understanding of both topologies. Moreover, several key small-signal and large-signal parameters were derived and their dependencies were investigated to point out the advantages and disadvantages of the CC topology. Fig. 8.0.1 illustrates the trade-offs of the advantages and disadvantages of the CC topology compared to the CS topology.
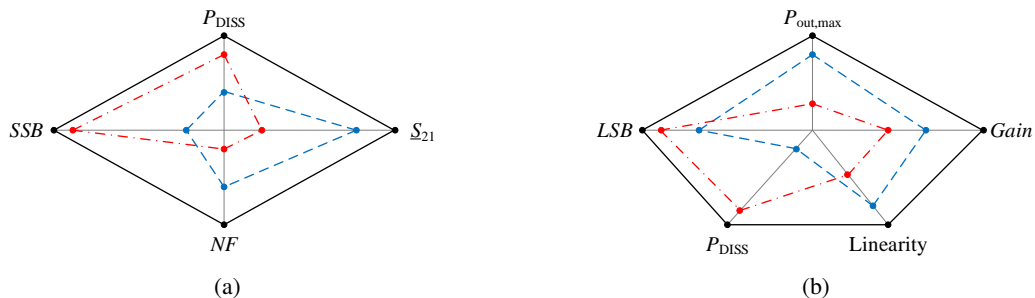
Figure 8.0.1: Trade-offs of the CC topology. (a) Small-signal trade-offs. (b) Large-signal trade-offs.

Afterwards, the second focus of this thesis was the development of a new CC topology by replacing the CSC with C_{st} —at the gate of the CGS— by a VASC with $C_{\text{st,var}}$. At the beginning the general principle of the proposed concept was explained to give a fundamental understanding of the new concept. Then, the implementation of the VASC were discussed, starting with the advantages and disadvantages of the VASC realized by a varactor diode or a transistor, followed by different structures —schematic and layout— of the VASC to achieve a different small-signal and large-signal RF behavior of the VASC. Additionally, the voltage dependency of $C_{\text{st,var}}$ of different VASC structures and the corresponding first

and second derivative are illustrated to highlight the different RF performances of the VASCs. Using two varactor diodes in parallel or in series offer much more flexibility to adjust the small-signal value of $C_{st,var}$ and the large-signal behavior compared to one varactor diode. Furthermore, improving certain key-parameters of broadband PAs using the new concept, the three applications

- gain control at higher frequencies ($\underline{S}_{21}$),
- compression improvement and
- linearity improvement

were discussed depending on different realizations of the VASC and with respect to complexity and flexibility. To achieve the best dynamic range to control the gain at higher frequencies in broadband PAs, one varactor diode as a VASC is the best candidate. However, the linearity of the VASC is worse compared to other realizations. Using two varactor diodes as a VASC shows the best compression improvement and maintaining a moderate non-linearity of the VASC itself. Also to increase the linearity of the CGS and as a result of the CC topology, two varactor diodes are very suited.

Subsequently, after shortly explaining the fundamentals of multi-decade PAs and giving an overview about state-of-the-art performance of multi-decade PAs using the GaN-HEMT technology, the two main focuses of this thesis and the related theory were verified by small-signal and large-signal measurements of several designed FBAs using the CS topology, the CC topology and the CC topology applying the new concept:

- CS-FBA ($V_{DS} = 20$ V, $I_{DSQ} = 156$ mA):
  A $|\underline{S}_{21}|$ of 13–15 dB was achieved with a maximum bandwidth of 12 GHz, while maintaining an input and output matching of better than -10 dB over the complete bandwidth. Furthermore, the minimum value of the NF was 4.5 dB and increased up to 7 dB at lower frequencies and 8 dB higher frequencies. Moreover, a $P_{out,max}$ of about 31.5 dBm and a maximum $P1dB$ of about 28 dBm were achieved. A minimum $HD2$ and $HD3$ of about -35 dBc and about -45 dBc, up to 6 GHz and 4 GHz respectively, were maintained at a P_{out} of 10 dB below the $P1dB$.
- CC-FBA-IB ($V_{DS} = 20$ V, $I_{DSQ} = 156$ mA):
  The main goal of the CC-FBA-IB was to improve the bandwidth and maintaining a similar $|\underline{S}_{21}|$ compared to the CS-FBA. While the input and output matching is better than -10 dB over the complete bandwidth, a gain of 13–14 dB was achieved with a maximum bandwidth of 17 GHz and maintaining a NF of 5–8 dB. As a result the bandwidth was improved by 40 % in contrast to the CS-FBA. However, the NF was slightly worse than the CS-FBA.
  Furthermore, a maximum P_{out} and $P1dB$ of about 31 dBm and 29 dBm were achieved which were similar to the CS-FBA up to the f_c of the CS-FBA. Moreover, the $HD2$ and $HD3$ of the CC-FBA-IB were also in the same range as the CS-FBA. At a P_{out} of 10 dB below the $P1dB$, the linearity reflected by $HD2$ and $HD3$ was between -35 dBc and -30 dBc and about -45 dBc, respectively.
- CC-FBA-IG ($V_{DS} = 20$ V, $I_{DSQ} = 240$ mA):
  While the CC-FBA-IB has the focus to increase the bandwidth compared to the CS-FBA, the maximum feasible GP of the CC was applied for the CC-FBA-IG to maintain the same bandwidth as the CS-FBA and to increase the $|\underline{S}_{21}|$ and P_{out}. As a result a gain of 15–17 dB was achieved with a maximum bandwidth of 12 GHz, while maintaining an input and output matching between -10 dB and -8 dB over the complete bandwidth. Therefore, the $|\underline{S}_{21}|$ is about 1–2 dB higher compared to the CS-FBA. Moreover, a NF of about 4.5 dB was achieved at lower and moderate frequencies —even slightly better than the CS-FBA— and increased up to 8 dB at the f_c.
  Due to the larger GP of the CC-FBA-IG compared to the CC-FBA-IB, the maximum P_{out} and $P1dB$ were significantly improved, amounted to 35 dBm and 33 dBm, respectively. Lowering the P_{out} down to $P1dB - 10$ dB, the $HD2$ and $HD3$ were still better than -35 dBc and -45 dBc.
- CC-FBA-IB (adapting the new concept):
  The new concept was adapted to the CC-FBA-IB using three different realization structures of the VASC, the CC-FBA-IB-D1D (one varactor diode: direction down), the CC-FBA-IB-D1U (one varactor diode: direction up) and the CC-FBA-IB-D2 (two varactor diodes: anti-parallel). If V_{VASC} had been

adjusted to $-6\,\text{V}$, the S-parameters of the CC-FBAs-IB using a VASC showed a very similar characteristic to the CC-FBA-IB using a CSC. Increasing the V_{VASC} to $-1\,\text{V}$, the CC-FBA-IB-D1D showed the best $|\underline{S}_{21}|$ improvement (up to $6\,\text{dB}$ at $V_{\text{DS}} = 10\,\text{V}$, $I_{\text{DSQ}} = 156\,\text{mA}$). However, as the $|\underline{S}_{21}|$ increases the stability decreases. Furthermore, the CC-FBA-IB-D1D had a superior large-signal performance —i.e. regarding the compression behavior— in contrast to the other realization structures of the VASC. Although, the theory suggested also two anti-parallel diodes to maximize the compression improvement (CC-FBA-IB-D2), the measurements did not confirm that statement. The CC-FBA-IB-D1D using a VASC improved the $P1dB$ by $\approx 2.5\,\text{dB}$ at higher frequencies compared to the CC-FBA-IB using a CSC. However, the CC-FBA-IB-D1U and the CC-FBA-IB-D2 showed a much better performance regarding the linearity of the PAs. Although, the CC-FBA-IB-D1U ($V_{\text{DS}} = 10\,\text{V}$, $I_{\text{DSQ}} = 156\,\text{mA}$) had the largest $HD3$ improvement of about $20\,\text{dB}$ at $P_{\text{out}} = 16\,\text{dBm}$, adjusting V_{VASC} to $-5\,\text{V}$, the CC-FBA-IB-D2 achieved overall the best $HD2$ and $HD3$ performance. Additionally, the CC-FBA-IB-D2 offered the possibility to change the linearity behavior of the VASC without changing the small-signal value $C_{\text{st,var}}$. Furthermore, the exact amount of improvement of the $P1dB$ and the $HD2$ and $HD3$ depended on the quiescent point of the amplifier and of the adjusted V_{VASC} of the VASC as well as on the frequency range. A negligible disadvantage of the VASC was the higher mismatch at the output at higher power levels of the PA to the $\underline{Z}_{\text{load}}$, which resulted in a slight degradation of the $P_{\text{out,max}}$.

- CC-FBA-IG (adapting the new concept):
  Furthermore, the new concept was also adapted to the CC-FBA-IG to show the superior performance of the new concept at lower frequencies. On the one hand the $|\underline{S}_{21}|$ of the CC-FBA-IG-D2 was improved by $4\,\text{dB}$ at $11\,\text{GHz}$, adjusting V_{VASC} to $-1\,\text{V}$. However, on the other hand the power compression was improved negligibly compared to the CC-FBA-IG using a CSC. This behavior was believed due to the much higher C_{st} of the CSC. Nevertheless, adjusting V_{VASC} to $-5\,\text{V}$, the $HD3$ was significantly improved in a moderate power range while the $HD2$ was only slightly degraded.

As stated, the new concept was able to improve certain key-parameters in multi-decade PAs using the CC topology. Although these improvements were not only frequency and power sweep spots, the performance of the new concept was limited to a certain frequency and power level range.

Synoptical, the main work of this thesis can be described by one sentence:

The thesis highlighted the trade-offs of the CC topology compared to the CS topology in multi-decade PAs and introduced a new concept to further improve the performance and lower some disadvantages of the CC topology verified by small-signal and large-signal measurements of several designed multi-decade PAs in feedback topology.

Outlook

In the near future, the new concept is planned to adapt to other multi-decade PA topologies, like the TWA topology. However, the proposed new concept can also be further implemented in octave-band or narrow-band PA topologies to improve certain RF properties.

Another very interesting topic is the VASC itself. In this thesis the different small-signal and large-signal characteristic possibilities were limited. The limitations are given on the one hand by the semiconductor process itself —i.e. maximum dynamic range of the realized VASC— and on the other hand by the implemented VASC. To determine the optimum small-signal and large-signal characteristic of the VASC would help to maximize the improvement of the new concept. Probably, the optimum behavior of the VASC differs, regarding the gain improvement, compression improvement and linearity improvement.

Furthermore, the idea of the new concept can also be used in input and output matching networks to adjust the matching networks in a way that the large-signal behavior of the networks improve i.e. the P_{out} or the linearity of a PA.

A Small-Signal Parameters of the Common-Source Stage

A.1 Y-Parameters

Using the SSM, shown in Fig. A.1.1, the Y-parameters of the CSS can be determined to

$$\underline{Y}_{11,\mathrm{CSS}} = \underline{Y}_{\mathrm{gs}} + \underline{Y}_{\mathrm{gd}} \tag{A.1.1}$$

$$\underline{Y}_{12,\mathrm{CSS}} = -\underline{Y}_{\mathrm{gd}} \tag{A.1.2}$$

$$\underline{Y}_{21,\mathrm{CSS}} = \underline{g}'_{\mathrm{m}} - \underline{Y}_{\mathrm{gd}} \tag{A.1.3}$$

$$\underline{Y}_{22,\mathrm{CSS}} = \underline{Y}_{\mathrm{ds}} + \underline{Y}_{\mathrm{gd}} \tag{A.1.4}$$

with

$$\underline{g}'_{\mathrm{m}} = \underline{g}_{\mathrm{m}} \frac{j \cdot \Im\left\{\underline{Z}_{\mathrm{gs}}\right\}}{\underline{Z}_{\mathrm{gs}}} \tag{A.1.5}$$

and

$$\underline{g}_{\mathrm{m}} = \left|\underline{g}_{\mathrm{m}}\right| \cdot e^{j\omega\tau} \; . \tag{A.1.6}$$
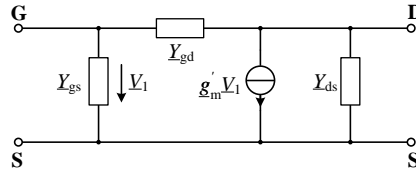
Figure A.1.1: General SSM of the CSS.

A.2 Maximum Stable Gain

The *MSG* of the CSS, using the simplified SSM, shown in Fig. 4.2.1, can be calculated to

$$MSG_{\mathrm{CSS}} = \left|\frac{\underline{Y}_{21,\mathrm{CSS}}}{\underline{Y}_{12,\mathrm{CSS}}}\right| \tag{A.2.1}$$

$$= \frac{g_{\mathrm{m}}}{\omega C_{\mathrm{gd}}}\left|1 + j\frac{f}{f_0}\right| \tag{A.2.2}$$

with

$$f_0 = -\frac{1}{2\pi} \cdot \frac{g_{\mathrm{m}}}{C_{\mathrm{gd}}} \; . \tag{A.2.3}$$

A.3 Short Circuit Current Gain

The $\underline{H}_{21}$ of the CSS, using the simplified SSM, shown in Fig. 4.2.1, can be calculated to

$$\underline{H}_{21,\text{CSS}} = \frac{\underline{Y}_{21,\text{CSS}}}{\underline{Y}_{11,\text{CSS}}} \tag{A.3.1}$$

$$= \frac{g_{\text{m}}}{j\omega\left(C_{\text{gs}} + C_{\text{gd}}\right)}\left(1 + j\frac{f}{f_0}\right) \tag{A.3.2}$$

with

$$f_0 = -\frac{1}{2\pi}\cdot\frac{g_{\text{m}}}{C_{\text{gd}}}\ . \tag{A.3.3}$$

A.4 Extraction of Intrinsic Elements

Using the intrinsic Y-parameters of the CSS the intrinsic elements, shown in Fig. A.4.1, can be calculated to

$$C_{\text{gs,CSS}} = -\frac{1}{\omega\cdot\Im\left\{\frac{1}{\underline{Y}_{11,\text{CSS}}+\underline{Y}_{12,\text{CSS}}}\right\}} \qquad r_{\text{gs,CSS}} = \Re\left\{\frac{1}{\underline{Y}_{11,\text{CSS}}+\underline{Y}_{12,\text{CSS}}}\right\} \tag{A.4.1}$$

$$C_{\text{gd,CSS}} = \frac{1}{\omega\cdot\Im\left\{\frac{1}{\underline{Y}_{12,\text{CSS}}}\right\}} \qquad r_{\text{gd,CSS}} = -\Re\left\{\frac{1}{\underline{Y}_{12,\text{CSS}}}\right\} \tag{A.4.2}$$

$$C_{\text{ds,CSS}} = \frac{\Im\left\{\underline{Y}_{22}+\underline{Y}_{12}\right\}}{\omega} \qquad r_{\text{ds,CSS}} = \frac{1}{\Re\left\{\underline{Y}_{22}+\underline{Y}_{12}\right\}} \tag{A.4.3}$$

and

$$\underline{g}_{\text{m,CSS}} = \left|\underline{g}_{\text{m,CSS}}\right|\cdot e^{j\omega\tau_{\text{CSS}}} \tag{A.4.4}$$

$$\left|\underline{g}_{\text{m,CSS}}\right| = \left|\left(1 + j\omega C_{\text{gs,CSS}}r_{\text{gs,CSS}}\right)\left(\underline{Y}_{21}-\underline{Y}_{12}\right)\right| \tag{A.4.5}$$

$$= \frac{\left|\underline{Y}_{11}+\underline{Y}_{12}\right|}{\left|\Im\left\{\underline{Y}_{11}+\underline{Y}_{12}\right\}\right|}\left|\underline{Y}_{21}-\underline{Y}_{12}\right| \tag{A.4.6}$$

$$\tau_{\text{CSS}} = \frac{1}{\omega}\cdot\arctan\left(\frac{\Im\left\{\left(1 + j\omega C_{\text{gs,CSS}}r_{\text{gs,CSS}}\right)\left(\underline{Y}_{21}-\underline{Y}_{12}\right)\right\}}{\Re\left\{\left(1 + j\omega C_{\text{gs,CSS}}r_{\text{gs,CSS}}\right)\left(\underline{Y}_{21}-\underline{Y}_{12}\right)\right\}}\right)\ . \tag{A.4.7}$$
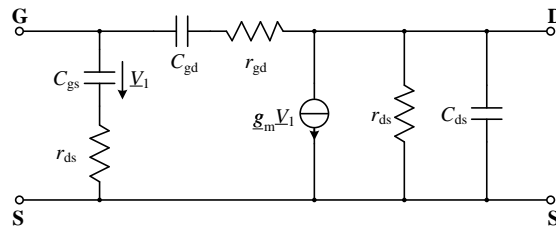
Figure A.4.1: Intrinsic SSM of the CSS.

B Small-Signal Parameters of the Common-Gate Stage

B.1 H-Parameters

B.1.1 H-Parameters of the Classical Common-Gate Stage

Using the SSM, shown in Fig. B.1.1, the H-parameters of the CGS can be determined to

$$\underline{H}_{11,\text{CGS}} = \frac{1}{\underline{g}'_m + \underline{Y}_{gs} + \underline{Y}_{ds}} \tag{B.1.1}$$

$$\underline{H}_{12,\text{CGS}} = \frac{\underline{Y}_{ds}}{\underline{g}'_m + \underline{Y}_{gs} + \underline{Y}_{ds}} \tag{B.1.2}$$

$$\underline{H}_{21,\text{CGS}} = -\frac{\underline{g}'_m + \underline{Y}_{ds}}{\underline{g}'_m + \underline{Y}_{gs} + \underline{Y}_{ds}} \tag{B.1.3}$$

$$\underline{H}_{22,\text{CGS}} = \underline{Y}_{gd} + \frac{\underline{Y}_{gs}\underline{Y}_{ds}}{\underline{g}'_m + \underline{Y}_{gs} + \underline{Y}_{ds}} \ . \tag{B.1.4}$$
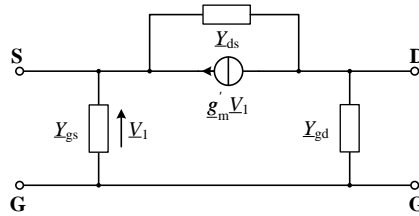
Figure B.1.1: General SSM of the classical CGS.

The H-parameters of the CGS using the simplified SSM, shown in Fig. 4.2.2, results to

$$\underline{H}_{11,\text{CGS}} = \frac{r_{ds}}{1 + g_m r_{ds}} \frac{1}{\left(1 + j\frac{f}{f_\infty}\right)} \tag{B.1.5}$$

$$\underline{H}_{12,\text{CGS}} = \frac{1}{1 + g_m r_{ds}} \frac{\left(1 + j\frac{f}{f_{01}}\right)}{\left(1 + j\frac{f}{f_\infty}\right)} \tag{B.1.6}$$

$$\underline{H}_{21,\text{CGS}} = -1 \frac{\left(1 + j\frac{f}{f_{02}}\right)}{\left(1 + j\frac{f}{f_\infty}\right)} \tag{B.1.7}$$

$$\underline{H}_{22,\text{CGS}} = j\omega C_{gd} + j\omega \left(\frac{C_{gs}}{1 + g_m r_{ds}}\right) \frac{\left(1 + j\frac{f}{f_{01}}\right)}{\left(1 + j\frac{f}{f_\infty}\right)} \tag{B.1.8}$$

with zeros and pole

$$f_{01} = \frac{1}{2\pi} \cdot \frac{1}{r_{ds}C_{ds}} \tag{B.1.9}$$

$$f_{02} = \frac{1}{2\pi} \cdot \frac{1 + g_m r_{ds}}{r_{ds}C_{ds}} \tag{B.1.10}$$

$$f_{\infty} = \frac{1}{2\pi} \cdot \frac{1 + g_m r_{ds}}{r_{ds}\left(C_{gs} + C_{ds}\right)} \, . \tag{B.1.11}$$

Relations between zeros and pole can be determined to

$$f_{01} < f_{\infty} < f_{02} \tag{B.1.12}$$

if the in-eq. (5.1.4) is valid. If the in-equation is not valid the relation between zeros and pole shifts to

$$f_{\infty} < f_{01} < f_{02} \, . \tag{B.1.13}$$

B.1.2 H-Parameters of the Modified Common-Gate Stage

Using the SSM, shown in Fig. B.1.2, the H-parameters of the modified CGS can be determined to

$$\underline{H}_{11,\text{CGS}} = \frac{\underline{Y}_{st} + \underline{Y}_{gd} + \underline{Y}_{gs}}{\underline{Y}_{ds}\left(\underline{Y}_{st} + \underline{Y}_{gd} + \underline{Y}_{gs}\right) + \left(\underline{Y}_{gs} + \underline{g}'_m\right)\left(\underline{Y}_{st} + \underline{Y}_{gd}\right)} \tag{B.1.14}$$

$$\underline{H}_{12,\text{CGS}} = \frac{\underline{Y}_{ds}\left(\underline{Y}_{st} + \underline{Y}_{gd} + \underline{Y}_{gs}\right) + \underline{Y}_{gd}\left(\underline{Y}_{gs} + \underline{g}'_m\right)}{\underline{Y}_{ds}\left(\underline{Y}_{st} + \underline{Y}_{gd} + \underline{Y}_{gs}\right) + \left(\underline{Y}_{gs} + \underline{g}'_m\right)\left(\underline{Y}_{st} + \underline{Y}_{gd}\right)} \tag{B.1.15}$$

$$\underline{H}_{21,\text{CGS}} = -\frac{\underline{Y}_{ds}\left(\underline{Y}_{st} + \underline{Y}_{gd} + \underline{Y}_{gs}\right) + \underline{g}'_m\left(\underline{Y}_{st} + \underline{Y}_{gd}\right) + \underline{Y}_{gd}\underline{Y}_{gs}}{\underline{Y}_{ds}\left(\underline{Y}_{st} + \underline{Y}_{gd} + \underline{Y}_{gs}\right) + \left(\underline{Y}_{gs} + \underline{g}'_m\right)\left(\underline{Y}_{st} + \underline{Y}_{gd}\right)} \tag{B.1.16}$$

$$\underline{H}_{22,\text{CGS}} = \frac{\underline{Y}_{st}\underline{Y}_{gd}\left(\underline{Y}_{st} + \underline{Y}_{gd} + \underline{Y}_{gs}\right) + \underline{Y}_{st}\underline{Y}_{ds}\underline{Y}_{gs}}{\underline{Y}_{ds}\left(\underline{Y}_{st} + \underline{Y}_{gd} + \underline{Y}_{gs}\right) + \left(\underline{Y}_{gs} + \underline{g}'_m\right)\left(\underline{Y}_{st} + \underline{Y}_{gd}\right)} \, . \tag{B.1.17}$$
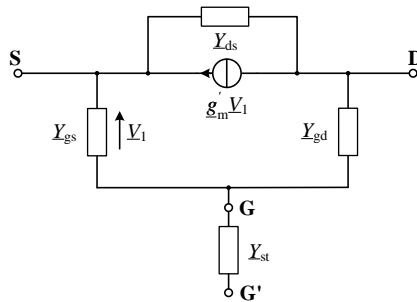
Figure B.1.2: General SSM of the modified CGS.

B.1.3 Dependency of H-Parameters on C_{st}

Table B.1.1 and Table B.1.2 shows the change of the H-parameters and the change of the ratio between f_∞ and f_{01}, f_{02}, f_{03} of the H-parameters lowering C_{st}.

Table B.1.1: Change of H-Parameters depending on C_{st}.

		$C_{\text{st}} \to 0$	Comment
$\underline{H}_{11,\text{CGS}}$	$\left\| \underline{H}_{11,\text{CGS}} \right\|$	↑	independent of process
	f_∞	↓	depend on process
$\underline{H}_{12,\text{CGS}}$	$\left\| \underline{H}_{12,\text{CGS}} \right\|$	↑	independent of process
	f_∞	↓	depend on process
	f_{01}	↑	depend on process
$\underline{H}_{21,\text{CGS}}$	$\left\| \underline{H}_{21,\text{CGS}} \right\|$	=	independent of process
	f_∞	↓	depend on process
	f_{02}	↓	independent of process
$\underline{H}_{22,\text{CGS}}$	$\left\| \underline{H}_{22,\text{CGS}} \right\|$	↓	independent of process
	f_∞	↓	depend on process
	f_{03}	=	independent of process

Table B.1.2: Change of ratio between f_∞ and f_{01}, f_{02}, f_{03} depending on C_{st}.

	$\infty \to C_{\text{st}} \to 0$			Comment
$\underline{H}_{12,\text{CGS}}$	$f_\infty > f_{01}$	↘		depend on process
			$f_\infty = f_{01}$	independent of process
$\underline{H}_{21,\text{CGS}}$	$f_\infty < f_{02}$	→	$f_\infty = f_{02}$	independent of process
$\underline{H}_{22,\text{CGS}}$	$f_\infty > f_{03}$	↘		depend on process
			$f_\infty = f_{03}$	independent of process

B.2 Maximum Stable Gain

The *MSG* of the classical CGS and the modified CGS, using the simplified SSM, shown in Fig. 4.2.2 and Fig. 4.2.3 respectively, can be calculated to

$$MSG_{\text{CGS}} = \left| \frac{\underline{H}_{21,\text{CGS}}}{\underline{H}_{12,\text{CGS}}} \right| \tag{B.2.1}$$

$$MSG_{\text{classical CGS}} = (1 + g_{\text{m}} r_{\text{ds}}) \left| \frac{1 + j\frac{f}{f_{01}}}{1 + j\frac{f}{f_{\infty 1}}} \right| \tag{B.2.2}$$

$$MSG_{\text{modified CGS}} = \frac{C_{\text{gs}} + (C_{\text{st}} + C_{\text{gd}})(1 + g_{\text{m}} r_{\text{ds}})}{C_{\text{st}} + C_{\text{gs}} + C_{\text{gd}}(1 + g_{\text{m}} r_{\text{ds}})} \left| \frac{1 + j\frac{f}{f_{02}}}{1 + j\frac{f}{f_{\infty 2}}} \right| \tag{B.2.3}$$

with

$$f_{01} = \frac{1}{2\pi} \cdot \frac{1 + g_m r_{ds}}{r_{ds} C_{ds}} \tag{B.2.4}$$

$$f_{02} = \frac{1}{2\pi} \cdot \frac{C_{gs} + (C_{st} + C_{gd})(1 + g_m r_{ds})}{r_{ds}(C_{ds}[C_{st} + C_{gs} + C_{gd}] + C_{gd}C_{gs})} \tag{B.2.5}$$

$$f_{\infty 1} = \frac{1}{2\pi} \cdot \frac{1}{r_{ds} C_{ds}} \tag{B.2.6}$$

$$f_{\infty 2} = \frac{1}{2\pi} \cdot \frac{C_{st} + C_{gs} + C_{gd}(1 + g_m r_{ds})}{r_{ds}(C_{ds}[C_{st} + C_{gs} + C_{gd}] + C_{gd}C_{gs})} \ . \tag{B.2.7}$$

B.3 Open Circuit Output Impedance

The real part of $\underline{H}_{22}$ of the classical CGS using the simplified SSM, shown in Fig. 4.2.2, can be determined to

$$\Re\{\underline{H}_{22}\} = \omega^2 r_{ds} \frac{C_{gs}(C_{gs} - C_{ds} g_m r_{ds})}{(1 + g_m r_{ds})^2} \frac{1}{\left(1 + \frac{f^2}{f_\infty^2}\right)} \tag{B.3.1}$$

with pole

$$f_\infty = \frac{1}{2\pi} \cdot \frac{1 + g_m r_{ds}}{r_{ds}(C_{gs} + C_{ds})} \ . \tag{B.3.2}$$

The sign of $\Re\{\underline{H}_{22}\}$ is given by $(C_{gs} - C_{ds} g_m r_{ds})$. Due to the fact that the result is usually negative using the GaN-HEMT technology ($g_m r_{ds} \approx 15$–60, $\frac{C_{gs}}{C_{ds}} \approx 4$–$6$), $\Re\{\underline{H}_{22}\}$ is also negative which leads often to an unstable behavior of the CGS.

The real part of $\underline{H}_{22}$ of the modified CGS using the simplified SSM, shown in Fig. 4.2.3a, which uses an additional stabilization capacitor with C_{st} and a stabilization resistor with R_{st} to improve the stability of the CGS, results to

$$\Re\{\underline{H}_{22}\} = \omega^2 \left(C_{st}^2 \frac{r_{ds} C_{gs}[C_{gs} - C_{ds} g_m r_{ds}] + R_{st}[C_{gs} + C_{gd}(1 + g_m r_{ds})]^2}{[C_{gs} + (C_{st} + C_{gd})(1 + g_m r_{ds})]^2} + \omega^2 \cdot \dots \right) \ . \tag{B.3.3}$$

Evaluating of eq. (B.3.3), $\Re\{\underline{H}_{22}\} > 0$ above a certain frequency which is given by

$$\omega > \frac{1}{r_{ds}(C_{ds}[C_{gs} + C_{gd}] + C_{gs}C_{gd})} \sqrt{\frac{r_{ds}}{R_{st}} C_{gs}(C_{ds} g_m r_{ds} - C_{gs}) - (C_{gs} + C_{gd}[1 + g_m r_{ds}])^2} \ . \tag{B.3.4}$$

$\Re\{\underline{H}_{22}\} > 0$ can be realized over the complete frequency range, if R_{st} is chosen large enough:

$$R_{st} > \frac{r_{ds} C_{gs}(C_{ds} g_m r_{ds} - C_{gs})}{(C_{gs} + C_{gd}[1 + g_m r_{ds}])^2} \ . \tag{B.3.5}$$

B.4 Extraction of Intrinsic Elements

Using the intrinsic Y-parameters of the CGS the intrinsic elements, shown in Fig. B.4.1, can be calculated to

$$C_{gs,CGS} = -\frac{1}{\omega \cdot \Im\left\{\frac{1}{\underline{Y}_{11} + \underline{Y}_{21}}\right\}} \qquad\qquad r_{gs,CGS} = \Re\left\{\frac{1}{\underline{Y}_{11} + \underline{Y}_{21}}\right\} \qquad (B.4.1)$$

$$C_{gd,CGS} = -\frac{1}{\omega \cdot \Im\left\{\frac{1}{\underline{Y}_{22} + \underline{Y}_{12}}\right\}} \qquad\qquad r_{gd,CGS} = \Re\left\{\frac{1}{\underline{Y}_{22} + \underline{Y}_{12}}\right\} \qquad (B.4.2)$$

$$C_{ds,CGS} = -\frac{\Im\{\underline{Y}_{12}\}}{\omega} \qquad\qquad r_{ds,CGS} = -\frac{1}{\Re\{\underline{Y}_{12}\}} \qquad (B.4.3)$$

and

$$\underline{g}_{m,CGS} = \left|\underline{g}_{m,CGS}\right| \cdot e^{j\omega\tau_{CGS}} \qquad (B.4.4)$$

$$\left|\underline{g}_{m,CGS}\right| = \left|(1 + j\omega C_{gs,CGS} r_{gs,CGS})(\underline{Y}_{21} - \underline{Y}_{12})\right| \qquad (B.4.5)$$

$$= \frac{|\underline{Y}_{11} + \underline{Y}_{21}|}{|\Im\{\underline{Y}_{11} + \underline{Y}_{21}\}|}|\underline{Y}_{21} - \underline{Y}_{12}| \qquad (B.4.6)$$

$$\tau_{CGS} = \frac{1}{\omega} \cdot \arctan\left(\frac{\Im\{(1 + j\omega C_{gs,CGS} r_{gs,CGS})(\underline{Y}_{21} - \underline{Y}_{12})\}}{\Re\{(1 + j\omega C_{gs,CGS} r_{gs,CGS})(\underline{Y}_{21} - \underline{Y}_{12})\}}\right). \qquad (B.4.7)$$
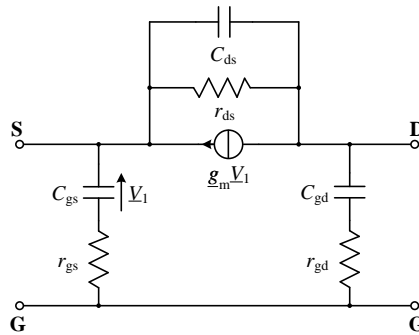
Figure B.4.1: Intrinsic SSM of the CGS.

C Small-Signal Parameters of the Cascode

C.1 Y-Parameters

C.1.1 Derivation of the Y-Parameters

To calculate the Y-Parameters of the CC a general valid relation can be used:

1. Transformation:
   - $\underline{\mathbf{Y}}_{\text{CSS}} \to \underline{\mathbf{A}}_{\text{CSS}}$
   - $\underline{\mathbf{H}}_{\text{CGS}} \to \underline{\mathbf{A}}_{\text{CGS}}$
2. Multiplication:
   - $\underline{\mathbf{A}}_{\text{CSS}} \cdot \underline{\mathbf{A}}_{\text{CGS}} = \underline{\mathbf{A}}_{\text{CC}}$
3. Transformation:
   - $\underline{\mathbf{A}}_{\text{CC}} \to \underline{\mathbf{Y}}_{\text{CC}}$

Y-parameters of the CC result to

$$\underline{Y}_{11,\text{CC}} = \underline{Y}_{11,\text{CSS}} - \frac{\underline{H}_{11,\text{CGS}}\underline{Y}_{12,\text{CSS}}\underline{Y}_{21,\text{CSS}}}{1 + \underline{Y}_{22,\text{CSS}}\underline{H}_{11,\text{CGS}}} \tag{C.1.1}$$

$$\underline{Y}_{12,\text{CC}} = \frac{\underline{Y}_{12,\text{CSS}}\underline{H}_{12,\text{CGS}}}{1 + \underline{Y}_{22,\text{CSS}}\underline{H}_{11,\text{CGS}}} \tag{C.1.2}$$

$$\underline{Y}_{21,\text{CC}} = -\frac{\underline{Y}_{21,\text{CSS}}\underline{H}_{21,\text{CGS}}}{1 + \underline{Y}_{22,\text{CSS}}\underline{H}_{11,\text{CGS}}} \tag{C.1.3}$$

$$\underline{Y}_{22,\text{CC}} = \underline{H}_{22,\text{CGS}} - \frac{\underline{Y}_{22,\text{CSS}}\underline{H}_{12,\text{CGS}}\underline{H}_{21,\text{CGS}}}{1 + \underline{Y}_{22,\text{CSS}}\underline{H}_{11,\text{CGS}}} \ . \tag{C.1.4}$$

C.1.2 Y-Parameters of the Classical Cascode

Using the SSM, shown in Fig. C.1.1, the Y-parameters of the CC can be determined to

$$\underline{Y}_{11,\text{CC}} = \underline{Y}_{\text{gs}} + \underline{Y}_{\text{gd}} + \frac{\underline{Y}_{\text{gd}}\left(\underline{g}'_{\text{m}} - \underline{Y}_{\text{gd}}\right)}{\underline{g}'_{\text{m}} + \underline{Y}_{\text{gs}} + 2 \cdot \underline{Y}_{\text{ds}} + \underline{Y}_{\text{gd}}} \tag{C.1.5}$$

$$\underline{Y}_{12,\text{CC}} = -\frac{\underline{Y}_{\text{gd}}\underline{Y}_{\text{ds}}}{\underline{g}'_{\text{m}} + \underline{Y}_{\text{gs}} + 2 \cdot \underline{Y}_{\text{ds}} + \underline{Y}_{\text{gd}}} \tag{C.1.6}$$

$$\underline{Y}_{21,\text{CC}} = \frac{\left(\underline{g}'_{\text{m}} - \underline{Y}_{\text{gd}}\right)\left(\underline{g}'_{\text{m}} + \underline{Y}_{\text{ds}}\right)}{\underline{g}'_{\text{m}} + \underline{Y}_{\text{gs}} + 2 \cdot \underline{Y}_{\text{ds}} + \underline{Y}_{\text{gd}}} \tag{C.1.7}$$

$$\underline{Y}_{22,\text{CC}} = \underline{Y}_{\text{gd}} + \frac{\underline{Y}_{\text{ds}}}{\underline{g}'_{\text{m}} + \underline{Y}_{\text{gs}} + \underline{Y}_{\text{ds}}}\left[\underline{Y}_{\text{gs}} + \frac{\left(\underline{g}'_{\text{m}} + \underline{Y}_{\text{ds}}\right)\left(\underline{Y}_{\text{ds}} + \underline{Y}_{\text{gd}}\right)}{\left(\underline{g}'_{\text{m}} + \underline{Y}_{\text{gs}} + 2 \cdot \underline{Y}_{\text{ds}} + \underline{Y}_{\text{gd}}\right)}\right] \ . \tag{C.1.8}$$
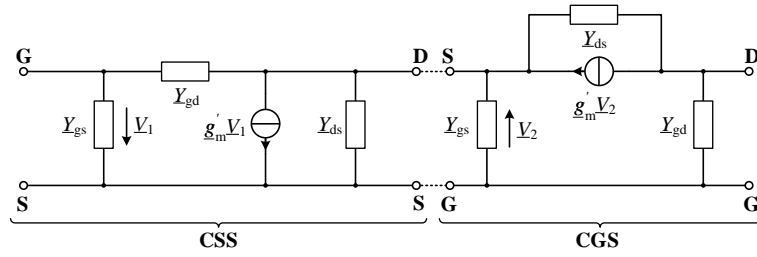
Figure C.1.1: General SSM of the classical CC.

Applying the simplified SSM, shown in Fig. 4.2.4, and assuming same *GP* for the CSS and the CGS, the Y-parameters of the CC results to

$$\underline{Y}_{11,\mathrm{CC}} = j\omega\left(C_{\mathrm{gs}}+C_{\mathrm{gd}}\right) + j\omega C_{\mathrm{gd}}\left(\frac{g_{\mathrm{m}}r_{\mathrm{ds}}}{2+g_{\mathrm{m}}r_{\mathrm{ds}}}\right)\frac{\left(1+j\frac{f}{f_{01}}\right)}{\left(1+j\frac{f}{f_{\infty}}\right)} \tag{C.1.9}$$

$$\underline{Y}_{12,\mathrm{CC}} = -j\omega C_{\mathrm{gd}}\frac{1}{(2+g_{\mathrm{m}}r_{\mathrm{ds}})}\frac{\left(1+j\frac{f}{f_{02}}\right)}{\left(1+j\frac{f}{f_{\infty}}\right)} \tag{C.1.10}$$

$$\underline{Y}_{21,\mathrm{CC}} = g_{\mathrm{m}}\left(\frac{1+g_{\mathrm{m}}r_{\mathrm{ds}}}{2+g_{\mathrm{m}}r_{\mathrm{ds}}}\right)\frac{\left(1+j\frac{f}{f_{03}}\right)\left(1+j\frac{f}{f_{01}}\right)}{\left(1+j\frac{f}{f_{\infty}}\right)} \tag{C.1.11}$$

and

$$\underline{Y}_{22,\mathrm{CC}} = j\omega C_{\mathrm{gd}} + j\omega\left(\frac{C_{\mathrm{gs}}}{1+g_{\mathrm{m}}r_{\mathrm{ds}}}\right)\frac{\left(1+j\frac{f}{f_{02}}\right)}{\left(1+j\frac{f}{f_{\infty2}}\right)}$$
$$+\frac{1}{r_{\mathrm{ds}}\left(2+g_{\mathrm{m}}r_{\mathrm{ds}}\right)}\frac{\left(1+j\frac{f}{f_{02}}\right)\left(1+j\frac{f}{f_{03}}\right)\left(1+j\frac{f}{f_{04}}\right)}{\left(1+j\frac{f}{f_{\infty1}}\right)\left(1+j\frac{f}{f_{\infty2}}\right)} \tag{C.1.12}$$

with zeros and poles

$$f_{01} = -\frac{1}{2\pi}\frac{g_{\mathrm{m}}}{C_{\mathrm{gd}}} \tag{C.1.13}$$

$$f_{02} = \frac{1}{2\pi}\frac{1}{r_{\mathrm{ds}}C_{\mathrm{ds}}} \tag{C.1.14}$$

$$f_{03} = \frac{1}{2\pi}\frac{(1+g_{\mathrm{m}}r_{\mathrm{ds}})}{r_{\mathrm{ds}}C_{\mathrm{ds}}} \tag{C.1.15}$$

$$f_{04} = \frac{1}{2\pi}\frac{1}{r_{\mathrm{ds}}\left(C_{\mathrm{ds}}+C_{\mathrm{gd}}\right)} \tag{C.1.16}$$

$$f_{\infty1} = \frac{1}{2\pi}\frac{(2+g_{\mathrm{m}}r_{\mathrm{ds}})}{r_{\mathrm{ds}}\left(C_{\mathrm{gs}}+2\cdot C_{\mathrm{ds}}+C_{\mathrm{gd}}\right)} \tag{C.1.17}$$

$$f_{\infty2} = \frac{1}{2\pi}\frac{1+g_{\mathrm{m}}r_{\mathrm{ds}}}{r_{\mathrm{ds}}\left(C_{\mathrm{gs}}+C_{\mathrm{ds}}\right)}\,. \tag{C.1.18}$$

Relations between poles and zeros can be determined to

$$f_{04} < f_{02} < f_{\infty1} < f_{\infty2} < f_{03} < f_{01} \tag{C.1.19}$$

if the in-equations

$$C_{gd} < C_{ds} \cdot g_m r_{ds} \tag{C.1.20}$$

$$C_{gd} < C_{ds} \cdot \frac{g_m r_{ds}}{1 + g_m r_{ds}} \tag{C.1.21}$$

$$C_{gs} + C_{gd} < C_{ds} \cdot g_m r_{ds} \tag{C.1.22}$$

$$C_{gs} < C_{gd} \left(1 + g_m r_{ds}\right) + C_{ds} \cdot g_m r_{ds} \tag{C.1.23}$$

are valid.

C.1.3 Y-Parameters of the Modified Cascode

Using the SSM, shown in Fig. C.1.2, the Y-parameters of the modified CC can be determined to

$$\underline{Y}_{11,CC} = \underline{Y}_{gs1} + \underline{Y}_{gd1} + \frac{\underline{Y}_{gd1}\left(\underline{g}'_{m1} - \underline{Y}_{gd1}\right)}{\underline{g}'_{m2,eff} + \underline{Y}_{gs2,eff} + \underline{Y}_{ds2,eff} + \underline{Y}_{ds1} + \underline{Y}_{gd1}} \tag{C.1.24}$$

$$\underline{Y}_{12,CC} = \frac{-\underline{Y}_{gd1}\underline{Y}_{ds2,eff}}{\underline{g}'_{m2,eff} + \underline{Y}_{gs2,eff} + \underline{Y}_{ds2,eff} + \underline{Y}_{ds1} + \underline{Y}_{gd1}} \tag{C.1.25}$$

$$\underline{Y}_{21,CC} = \frac{\left(\underline{g}'_{m1} - \underline{Y}_{gd1}\right)\left(\underline{g}'_{m2,eff} + \underline{Y}_{ds2,eff}\right)}{\underline{g}'_{m2,eff} + \underline{Y}_{gs2,eff} + \underline{Y}_{ds2,eff} + \underline{Y}_{ds1} + \underline{Y}_{gd1}} \tag{C.1.26}$$

and

$$\underline{Y}_{22,CC} = \underline{Y}_{gd2} + \frac{\underline{Y}_{ds2,eff}\underline{Y}_{gs2,eff}}{\underline{g}'_{m2,eff} + \underline{Y}_{gs2,eff} + \underline{Y}_{ds2,eff}} +$$
$$+ \frac{\underline{Y}_{ds2,eff}}{\left(\underline{g}'_{m2,eff} + \underline{Y}_{gs2,eff} + \underline{Y}_{ds2,eff}\right)} \frac{\left(\underline{g}'_{m2,eff} + \underline{Y}_{ds2,eff}\right)\left(\underline{Y}_{ds1} + \underline{Y}_{gd1}\right)}{\left(\underline{g}'_{m2,eff} + \underline{Y}_{gs2,eff} + \underline{Y}_{ds2,eff} + \underline{Y}_{ds1} + \underline{Y}_{gd1}\right)} \; . \tag{C.1.27}$$
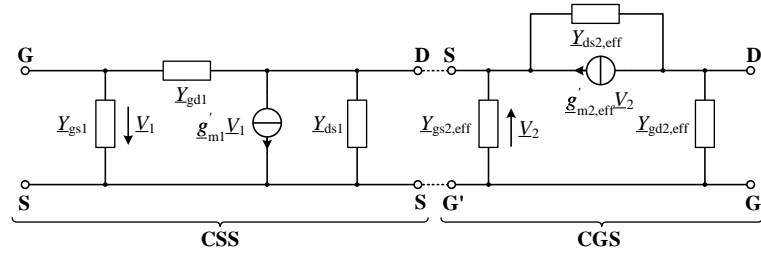
Figure C.1.2: General SSM of the recalculated modified CC (considering $\underline{Y}_{st}$).

Applying the simplified SSM, shown in Fig. 4.2.5, the Y-parameters of the modified CC results to

$$\underline{Y}_{11,CC} = j\omega\left(C_{gs1} + C_{gd1}\right) + j\omega C_{gd1}\left(\frac{g_{m1}\left[r_{ds1} \parallel r_{ds2,eff}\right]}{1 + g_{m2,eff}\left[r_{ds1} \parallel r_{ds2,eff}\right]}\right)\frac{\left(1 + j\frac{f}{f_{01}}\right)}{\left(1 + j\frac{f}{f_{\infty 1}}\right)} \tag{C.1.28}$$

$$\underline{Y}_{12,CC} = -j\omega C_{gd1}\frac{1}{\left(1 + \frac{r_{ds2,eff}}{r_{ds1}} + g_{m2,eff}r_{ds2,eff}\right)}\frac{\left(1 + j\frac{f}{f_{02}}\right)}{\left(1 + j\frac{f}{f_{\infty 1}}\right)} \tag{C.1.29}$$

$$\underline{Y}_{21,CC} = g_{m1}\frac{\left(1 + g_{m2,eff}r_{ds2,eff}\right)}{\left(1 + \frac{r_{ds2,eff}}{r_{ds1}} + g_{m2,eff}r_{ds2,eff}\right)}\frac{\left(1 + j\frac{f}{f_{03}}\right)\left(1 + j\frac{f}{f_{01}}\right)}{\left(1 + j\frac{f}{f_{\infty 1}}\right)} \tag{C.1.30}$$

and

$$\underline{Y}_{22,\text{CC}} = j\omega C_{\text{gd2}} + j\omega \left(\frac{C_{\text{gs2}}}{1 + g_{\text{m2,eff}} r_{\text{ds2,eff}}} \right) \frac{\left(1 + j\frac{f}{f_{02}}\right)}{\left(1 + j\frac{f}{f_{\infty 2}}\right)}$$

$$+ \frac{1}{(r_{\text{ds1}} + r_{\text{ds2,eff}})\left(1 + g_{\text{m2,eff}}\left[r_{\text{ds1}} \parallel r_{\text{ds2,eff}}\right]\right)} \frac{\left(1 + j\frac{f}{f_{02}}\right)\left(1 + j\frac{f}{f_{03}}\right)\left(1 + j\frac{f}{f_{04}}\right)}{\left(1 + j\frac{f}{f_{\infty 1}}\right)\left(1 + j\frac{f}{f_{\infty 2}}\right)} \quad \text{(C.1.31)}$$

with zeros and poles

$$f_{01} = -\frac{1}{2\pi} \frac{g_{\text{m1}}}{C_{\text{gd1}}} \tag{C.1.32}$$

$$f_{02} = \frac{1}{2\pi} \frac{1}{r_{\text{ds2,eff}} C_{\text{ds2,eff}}} \tag{C.1.33}$$

$$f_{03} = \frac{1}{2\pi} \frac{(1 + g_{\text{m2,eff}} r_{\text{ds2,eff}})}{r_{\text{ds2,eff}} C_{\text{ds2,eff}}} \tag{C.1.34}$$

$$f_{04} = \frac{1}{2\pi} \frac{1}{r_{\text{ds1}}\left(C_{\text{ds1}} + C_{\text{gd1}}\right)} \tag{C.1.35}$$

$$f_{\infty 1} = \frac{1}{2\pi} \frac{(1 + g_{\text{m2,eff}}\left[r_{\text{ds1}} \parallel r_{\text{ds2,eff}}\right])}{(r_{\text{ds1}} \parallel r_{\text{ds2,eff}})\left(C_{\text{ds1}} + C_{\text{ds2,eff}} + C_{\text{gs2,eff}} + C_{\text{gd1}}\right)} \tag{C.1.36}$$

$$f_{\infty 2} = \frac{1}{2\pi} \frac{1 + g_{\text{m2,eff}} r_{\text{ds2,eff}}}{r_{\text{ds2,eff}}\left(C_{\text{gs2,eff}} + C_{\text{ds2,eff}}\right)} \,. \tag{C.1.37}$$

C.2 Maximum Stable Gain

Using eq. (A.2.1) and eq. (B.2.1), the *MSG* of the classical CC and the modified CC can be expressed by

$$MSG_{\text{CC}} = MSG_{\text{CSS}} \cdot MSG_{\text{CGS}} \tag{C.2.1}$$

$$= \left| \frac{\underline{Y}_{21,\text{CSS}}}{\underline{Y}_{12,\text{CSS}}} \right| \cdot \left| \frac{\underline{H}_{21,\text{CGS}}}{\underline{H}_{12,\text{CGS}}} \right| \tag{C.2.2}$$

$$= \left| \frac{\underline{Y}_{21,\text{CC}}}{\underline{Y}_{12,\text{CC}}} \right| \,. \tag{C.2.3}$$

The *MSG* of the classical CC and the modified CC, using the simplified SSM, shown in Fig. 4.2.4 and Fig. 4.2.5 respectively, can be calculated to

$$MSG_{\text{classical CC}} = \frac{g_{\text{m1}}}{\omega C_{\text{gd1}}} \left(1 + g_{\text{m2}} r_{\text{ds2}}\right) \left| \frac{\left(1 + j\frac{f}{f_{01}}\right)\left(1 + j\frac{f}{f_{03}}\right)}{\left(1 + j\frac{f}{f_{\infty 1}}\right)} \right| \tag{C.2.4}$$

$$MSG_{\text{modified CC}} = \frac{g_{\text{m1}}}{\omega C_{\text{gd1}}} \left[\frac{C_{\text{gs2}} + (C_{\text{st}} + C_{\text{gd2}})(1 + g_{\text{m2}} r_{\text{ds2}})}{C_{\text{st}} + C_{\text{gs2}} + C_{\text{gd2}}(1 + g_{\text{m2}} r_{\text{ds2}})} \right] \left| \frac{\left(1 + j\frac{f}{f_{02}}\right)\left(1 + j\frac{f}{f_{03}}\right)}{\left(1 + j\frac{f}{f_{\infty 2}}\right)} \right| \tag{C.2.5}$$

with

$$f_{01} = \frac{1}{2\pi} \cdot \frac{1 + g_{m2}r_{ds2}}{r_{ds2}C_{ds2}} \tag{C.2.6}$$

$$f_{02} = \frac{1}{2\pi} \cdot \frac{C_{gs2} + (C_{st} + C_{gd2})(1 + g_{m2}r_{ds2})}{r_{ds}(C_{ds2}[C_{st} + C_{gs2} + C_{gd2}] + C_{gd2}C_{gs2})} \tag{C.2.7}$$

$$f_{03} = -\frac{1}{2\pi} \cdot \frac{g_{m1}}{C_{gd1}} \tag{C.2.8}$$

$$f_{\infty 1} = \frac{1}{2\pi} \cdot \frac{1}{r_{ds2}C_{ds2}} \tag{C.2.9}$$

$$f_{\infty 2} = \frac{1}{2\pi} \cdot \frac{C_{st} + C_{gs2} + C_{gd2}(1 + g_{m2}r_{ds2})}{r_{ds2}(C_{ds2}[C_{st} + C_{gs2} + C_{gd2}] + C_{gd2}C_{gs2})} \, . \tag{C.2.10}$$

C.3 Short Circuit Current Gain

The $\underline{H}_{21}$ of the classical CC and the modified CC, using the simplified SSM, shown in Fig. 4.2.4 and Fig. 4.2.5 respectively, can be calculated to

$$\underline{H}_{21,\text{classical CC}} = \frac{g_{m1}(r_{ds1} \parallel r_{ds2})(1 + g_{m2}r_{ds2})}{j\omega(C_{gs1} + C_{gd1})\left(1 + \left[g_{m2} + g_{m1}\left(\frac{C_{gd1}}{C_{gs1} + C_{gd1}}\right)\right][r_{ds1} \parallel r_{ds2}]\right)r_{ds2}} \cdot$$

$$\cdot \frac{\left(1 + j\frac{f}{f_{01}}\right)\left(1 + j\frac{f}{f_{02}}\right)}{\left(1 + j\frac{f}{f_{\infty 1}}\right)} \tag{C.3.1}$$

and

$$\underline{H}_{21,\text{modified CC}} = \frac{g_{m1}(r_{ds1} \parallel r_{ds2,\text{eff}})(1 + g_{m2,\text{eff}}r_{ds2,\text{eff}})}{j\omega(C_{gs1} + C_{gd1})\left(1 + \left[g_{m2,\text{eff}} + g_{m1}\left(\frac{C_{gd1}}{C_{gs1} + C_{gd1}}\right)\right][r_{ds1} \parallel r_{ds2,\text{eff}}]\right)r_{ds2,\text{eff}}} \cdot$$

$$\cdot \frac{\left(1 + j\frac{f}{f_{01}}\right)\left(1 + j\frac{f}{f_{03}}\right)}{\left(1 + j\frac{f}{f_{\infty 2}}\right)} \tag{C.3.2}$$

with

$$f_{01} = -\frac{1}{2\pi} \cdot \frac{g_{m1}}{C_{gd1}} \tag{C.3.3}$$

$$f_{02} = \frac{1}{2\pi} \cdot \frac{1 + g_{m2}r_{ds2}}{r_{ds2}C_{ds2}} \tag{C.3.4}$$

$$f_{03} = \frac{1}{2\pi} \cdot \frac{1 + g_{m2,\text{eff}}r_{ds2,\text{eff}}}{r_{ds2,\text{eff}}C_{ds2,\text{eff}}} \tag{C.3.5}$$

$$f_{\infty 1} = \frac{1}{2\pi} \cdot \frac{1 + \left(g_{m2} + g_{m1}\left[\frac{C_{gd1}}{C_{gs1} + C_{gd1}}\right]\right)(r_{ds1} \parallel r_{ds2})}{(r_{ds1} \parallel r_{ds2})\left(C_{gs2} + C_{ds2} + C_{ds1} + C_{gd1}\left[1 - \frac{C_{gd1}}{C_{gs1} + C_{gd1}}\right]\right)} \tag{C.3.6}$$

$$f_{\infty 2} = \frac{1}{2\pi} \cdot \frac{1 + \left(g_{m2,\text{eff}} + g_{m1}\left[\frac{C_{gd1}}{C_{gs1} + C_{gd1}}\right]\right)(r_{ds1} \parallel r_{ds2,\text{eff}})}{(r_{ds1} \parallel r_{ds2,\text{eff}})\left(C_{gs2,\text{eff}} + C_{ds2,\text{eff}} + C_{ds1} + C_{gd1}\left[1 - \frac{C_{gd1}}{C_{gs1} + C_{gd1}}\right]\right)} \, . \tag{C.3.7}$$

C.4 Unilateral Power Gain

Inserting the Y-parameters of the cascode —eq. (C.1.1)–eq. (C.1.4)— into eq. (2.2.11), the Mason's invariant U of the cascode can be determined to

$$U_{CC} = \frac{\left| \frac{\underline{Y}_{21}\underline{H}_{21} + \underline{Y}_{12}\underline{H}_{12}}{1 + \underline{Y}_{22}\underline{H}_{11}} \right|^2}{4 \cdot \left(\Re\left\{ \underline{Y}_{11} - \frac{\underline{Y}_{12}\underline{Y}_{21}\underline{H}_{11}}{1 + \underline{Y}_{22}\underline{H}_{11}} \right\} \Re\left\{ \underline{H}_{22} - \frac{\underline{H}_{12}\underline{H}_{21}\underline{Y}_{22}}{1 + \underline{Y}_{22}\underline{H}_{11}} \right\} - \Re\left\{ \frac{\underline{Y}_{12}\underline{H}_{12}}{1 + \underline{Y}_{22}\underline{H}_{11}} \right\} \Re\left\{ -\frac{\underline{Y}_{21}\underline{H}_{21}}{1 + \underline{Y}_{22}\underline{H}_{11}} \right\} \right)}, \tag{C.4.1}$$

where the Y-parameters are the small-signal parameters of the CSS and the H-parameters are the small-signal parameters of the CGS. Neglecting the feedback of the CSS ($\underline{Y}_{12,CSS} = 0$), U of the cascode results to

$$U_{CC} = \frac{\left| \frac{\underline{Y}_{21}\underline{H}_{21}}{1 + \underline{Y}_{22}\underline{H}_{11}} \right|^2}{4 \cdot \Re\{\underline{Y}_{11}\} \Re\left\{ \underline{H}_{22} - \frac{\underline{H}_{12}\underline{H}_{21}\underline{Y}_{22}}{1 + \underline{Y}_{22}\underline{H}_{11}} \right\}} . \tag{C.4.2}$$

If the mismatch between the CSS and the CGS is very high ($\left| \underline{Y}_{22,CS}\underline{H}_{11,CG} \right| \ll 1$), U_{CC} rather simplifies to

$$U_{CC} = \frac{\left| \underline{Y}_{21}\underline{H}_{21} \right|^2}{4 \cdot \Re\{\underline{Y}_{11}\} \Re\{\underline{H}_{22} - \underline{H}_{12}\underline{H}_{21}\underline{Y}_{22}\}} . \tag{C.4.3}$$

C.5 Equivalent Noise Representation

The following informations are obtained from [143].

The equivalent noise sources with $\underline{I}_{n1,CC}$ and $\underline{I}_{n2,CC}$ of the CC, shown in Fig. 5.1.6 can be determined by eq. (5.1.22) and eq. (5.1.23) and can be recalculated to equivalent input noise sources with $\underline{I}_n$ and $\underline{V}_n$. Using the general valid relationship

$$\underline{I}_{n,CC} = \frac{\underline{Y}_{11,CC}}{\underline{Y}_{21,CC}} \underline{I}_{n2,CC} - \underline{I}_{n1,CC} \tag{C.5.1}$$

$$= \frac{\underline{Y}_{11,CSS}}{\underline{Y}_{21,CSS}} \cdot \left(\frac{1 + \underline{H}_{11,CGS}\underline{H}_{22,CSS}}{-\underline{H}_{21,CGS}} \right) \underline{I}_{n2,CC} - \underline{I}_{n1,CC} \tag{C.5.2}$$

and

$$\underline{V}_{n,CC} = \frac{1}{\underline{Y}_{21,CC}} \underline{I}_{n2,CC} \tag{C.5.3}$$

$$= -\frac{1 + \underline{Y}_{22,CSS}\underline{H}_{11,CGS}}{\underline{Y}_{21,CSS}\underline{H}_{21,CGS}} \underline{I}_{n2,CC} \tag{C.5.4}$$

with

$$\underline{H}_{22,CSS} = \frac{\underline{Y}_{11,CSS}\underline{Y}_{22,CSS} - \underline{Y}_{12,CSS}\underline{Y}_{21,CSS}}{\underline{Y}_{11,CSS}} \tag{C.5.5}$$

$$= \frac{\det(\mathbf{\underline{Y}}_{CSS})}{\underline{Y}_{11,CSS}} \tag{C.5.6}$$

of the CC, the equivalent input noise sources with $\underline{I}_n$ and $\underline{V}_n$, shown in Fig. 2.4.3c can be expressed by

$$\underline{I}_{n,CC} = \underbrace{\frac{\underline{Y}_{11,CSS}}{\underline{Y}_{21,CSS}}\underline{I}_{n,d1} - \underline{I}_{n,g1}}_{\underline{I}_{n,CSS}} - \frac{\underline{Y}_{11,CSS}}{\underline{Y}_{21,CSS}}\left(\underline{I}_{n,g2} + \left[1 + \frac{1 + \underline{H}_{11,CGS}\underline{H}_{22,CSS}}{\underline{H}_{21,CGS}}\right]\underline{I}_{n,d2}\right) \tag{C.5.7}$$

$$\underline{V}_{n,CC} = \underbrace{\frac{1}{\underline{Y}_{21,CC}}\underline{I}_{n,d1}}_{\underline{V}_{n,CSS}} - \frac{1}{\underline{Y}_{21,CSS}}\left(\underline{I}_{n,g2} + \left[1 + \frac{1 + \underline{Y}_{22,CSS}\underline{H}_{11,CGS}}{\underline{H}_{21,CGS}}\right]\underline{I}_{n,d2}\right) \tag{C.5.8}$$

by inserting eq. (5.1.22) and eq. (5.1.23) into eq. (C.5.2) and eq. (C.5.4). However, eq. (5.1.22) and eq. (5.1.23) are only valid for the classical cascode (RF short at the gate of the CGS).

Using the simplified SSM for the CGS with the following properties

$$\begin{pmatrix} \underline{H}_{11,CGS} & \underline{H}_{12,CGS} \\ \underline{H}_{21,CGS} & \underline{H}_{22,CGS} \end{pmatrix} = \begin{pmatrix} 0 & 0 \\ -1 & 0 \end{pmatrix}, \tag{C.5.9}$$

the equivalent noise sources with $\underline{I}_{n1,CC}$ and $\underline{I}_{n2,CC}$ of the CC results to

$$\underline{I}_{n1,CC} = \underline{I}_{n,g1} \tag{C.5.10}$$

$$\underline{I}_{n2,CC} = \underline{I}_{n,d1} - \underline{I}_{n,g2} \tag{C.5.11}$$

and the correlation factor of the noise sources with $\underline{I}_{n1,CC}$ and $\underline{I}_{n2,CC}$ can be determined to

$$\underline{\gamma}_{CC} = \underbrace{\frac{\overline{\underline{I}_{n,g1}^{*}\underline{I}_{n,d1}}}{\sqrt{\overline{|\underline{I}_{n,g1}|^2} \cdot \overline{|\underline{I}_{n,d1}|^2}}}}_{\underline{\gamma}_{CSS}} \cdot \sqrt{\frac{\overline{|\underline{I}_{n,d1}|^2}}{\overline{|\underline{I}_{n,d1}|^2} + \overline{|\underline{I}_{n,g2}|^2}}} \cdot \tag{C.5.12}$$

The input noise sources with $\underline{I}_{n,CC}$ and $\underline{V}_{n,CC}$ are given by

$$\underline{I}_{n,CC} = \frac{\underline{Y}_{11,CSS}}{\underline{Y}_{21,CSS}}\left(\underline{I}_{n,d1} - \underline{I}_{n,g2}\right) - \underline{I}_{n,g1} \tag{C.5.13}$$

$$= \underline{I}_{n,CSS} - \frac{\underline{Y}_{11,CSS}}{\underline{Y}_{21,CSS}}\underline{I}_{n,g2} \tag{C.5.14}$$

and

$$\underline{V}_{n,CC} = \frac{1}{\underline{Y}_{21,CSS}}\left(\underline{I}_{n,d1} - \underline{I}_{n,g2}\right) \tag{C.5.15}$$

$$= \underline{V}_{n,CSS} - \frac{1}{\underline{Y}_{21,CSS}}\underline{I}_{n,g2} \cdot \tag{C.5.16}$$

References

[1] M. Seifart, *Analoge Schaltungen*. Berlin: Verlag Technik, 1988.

[2] J. G. Andrews, S. Buzzi, W. Choi, S. V. Hanly, A. Lozano, A. C. K. Soong, and J. C. Zhang, "What Will 5G Be?" *IEEE Journal on Selected Areas in Communications*, vol. 32, no. 6, pp. 1065–1082, Jun. 2014.

[3] "IEEE Standard Letter Designations for Radar-Frequency Bands," *IEEE Std 521-1976*, pp. 1–7, Nov. 1976.

[4] "IEEE Standard Letter Designations for Radar-Frequency Bands," *IEEE Std 521-1984*, pp. 1–8, Mar. 1984.

[5] "IEEE Standard Letter Designations for Radar-Frequency Bands," *IEEE Std 521-2002 (Revision of IEEE Std 521-1984)*, pp. 1–10, Jan. 2003.

[6] T. Huber, "Konzeptanalyse und Implementierung einer aktiven rauscharmen Impedanz in GaN zur Rauschminimierung in Traveling-Wave PAs," Master's thesis, Rosenheim University, Germany, 2013.

[7] F. V. Hunt and R. W. Hickman, "On Electronic Voltage Stabilizers," *Review of Scientific Instruments*, vol. 10, no. 1, pp. 6–21, Jan. 1939.

[8] H. Wallman, A. B. Macnee, and C. P. Gadsden, "A Low-Noise Amplifier," *Proceedings of the IRE*, vol. 36, no. 6, pp. 700–708, Jun. 1948.

[9] S. De Meyer, A. Philippon, M. Campovecchio, C. Charbonniaud, S. Piotrowicz, D. Floriot, and R. Quere, "Modeling of a 4-18GHz 6W Flip-Chip Integrated Power Amplifier based on GaN HEMTs Technology," in *2005 European Microwave Conference*, vol. 3, Oct. 2005, pp. 1603–1606.

[10] R. Santhakumar, Yi Pei, U. K. Mishra, and R. A. York, "Monolithic Millimeter-wave Distributed Amplifiers using AlGaN/GaN HEMTs," in *2008 IEEE MTT-S International Microwave Symposium Digest*, Jun. 2008, pp. 1063–1066.

[11] K. W. Kobayashi, YaoChung Chen, I. Smorchkova, B. Heying, Wen-Ben Luo, W. Sutton, M. Wojtowicz, and A. Oki, "Multi-Decade GaN HEMT Cascode-Distributed Power Amplifier with baseband Performance," in *2009 IEEE Radio Frequency Integrated Circuits Symposium*, Jun. 2009, pp. 369–372.

[12] P. Dennler, D. Schwantuschke, R. Quay, and O. Ambacher, "8–42 GHz GaN Non-Uniform Distributed Power Amplifier MMICs in Microstrip Technology," in *2012 IEEE/MTT-S International Microwave Symposium Digest*, Jun. 2012, pp. 1–3.

[13] K. W. Kobayashi, "An 8-W 250-MHz to 3-GHz Decade-Bandwidth Low-Noise GaN MMIC Feedback Amplifier With > +51-dBm OIP3," *IEEE Journal of Solid-State Circuits*, vol. 47, no. 10, pp. 2316–2326, Oct. 2012.

[14] P. Dennler, R. Quay, P. Brückner, M. Schlechtweg, and O. Ambacher, "Watt-Level Non-Uniform Distributed 6–37 GHz Power Amplifier MMIC with Dual-Gate Driver Stage in GaN technology," in *2014 IEEE Topical Conference on Power Amplifiers for Wireless and Radio Applications (PAWR)*, Jan. 2014, pp. 37–39.

[15] K. W. Kobayashi, D. Denninghoff, and D. Miller, "A Novel 100 MHz–45 GHz Input-Termination-Less Distributed Amplifier Design With Low-Frequency Low-Noise and High Linearity Implemented With A 6 Inch $0.15\,\mu$m GaN-SiC Wafer Process Technology," *IEEE Journal of Solid-State Circuits*, vol. 51, no. 9, pp. 2017–2026, Sep. 2016.

[16] T. Huber, R. Quay, and W. Bösch, "Multi-Decade GaN Feedback Power Amplifiers in Common-Source and Cascode Topology," in *2016 Asia-Pacific Microwave Conference (APMC)*, Dec. 2016, pp. 1–4.

[17] G. Nikandish, R. B. Staszewski, and A. Zhu, "The (R)evolution of Distributed Amplifiers: From Vacuum Tubes to Modern CMOS and GaN ICs," *IEEE Microwave Magazine*, vol. 19, no. 4, pp. 66–83, Jun. 2018.

[18] R. de L. Kronig, "On the Theory of Dispersion of X-Rays," *J. Opt. Soc. Am.*, vol. 12, no. 6, pp. 547–557, Jun. 1926.

[19] H. A. Kramers, "La diffusion de la lumière par les atomes," *Atti Cong. Intern. Fisica, (Transactions of Volta Centenary Congress) Como*, vol. 2, pp. 545–557, 1927.

[20] H. W. Bode, "Amplifier," U.S. Patent 2,123,178, Jul. 12, 1938.

[21] H. W. Bode, "Relations Between Attenuation and Phase in Feedback Amplifier Design," *The Bell System Technical Journal*, vol. 19, no. 3, pp. 421–454, Jul. 1940.

[22] H. W. Bode, *Network Analysis and Feedback Amplifier Design*, ser. Bell Telephone Laboratories series. Van Nostrand, 1945.

[23] R. M. Fano, "Theoretical Limitations on the Broadband Matching of Arbitrary Impedances," *Journal of the Franklin Institute*, vol. 249, no. 1, pp. 57–83, Jan. 1950.

[24] G. L. Matthaei, *Microwave Filters, Impedance-Matching Networks, and Coupling Structures*. McGraw-Hill, 1964, no. Bd. 1.

[25] J. Bechhoefer, "Kramers–Kronig, Bode, and the meaning of zero," *American Journal of Physics*, vol. 79, no. 10, pp. 1053–1059, Oct. 2011.

[26] C. A. Liechti, "Characteristics of Dual-Gate GaAs MESFETs," in *1974 4th European Microwave Conference*, Sep. 1974, pp. 87–91.

[27] C. A. Liechti, "Performance of Dual-Gate GaAs MESFET's as Gain-Controlled Low-Noise Amplifiers and High-Speed Modulators," *IEEE Transactions on Microwave Theory and Techniques*, vol. 23, no. 6, pp. 461–469, Jun. 1975.

[28] K. W. Kobayashi, "Linearized Darlington Amplifier," U.S. Patent 6,933,787, Aug. 23, 2005.

[29] K. W. Kobayashi, Y. Chen, I. Smorchkova, R. Tsai, M. Wojtowicz, and A. Oki, "1-Watt Conventional and Cascoded GaN-SiC Darlington MMIC Amplifiers to 18 GHz," in *2007 IEEE Radio Frequency Integrated Circuits (RFIC) Symposium*, Jun. 2007, pp. 585–588.

[30] E. Jutzi, *Charakterisierung und Modellierung von Aluminium-Galliumnitrid, Galliumnitrid-Heterostrukturfeldeffekttransistoren*, ser. Berichte aus der Elektrotechnik. Shaker, 2007.

[31] A. Van der Ziel, "Gate Noise in Field Effect Transistors at Moderately High Frequencies," *Proceedings of the IEEE*, vol. 51, no. 3, pp. 461–467, Mar. 1963.

[32] E. Bolinder, "Note on the Matrix Representation of Linear Two-Port Networks," *IRE Transactions on Circuit Theory*, vol. 4, no. 4, pp. 337–339, Dec. 1957.

[33] M. S. Gupta, "Power Gain in Feedback Amplifiers, a Classic Revisited," *IEEE Transactions on Microwave Theory and Techniques*, vol. 40, no. 5, pp. 864–879, May 1992.

[34] E. Bolinder, "Survey of Some Properties of Linear Networks," *IRE Transactions on Circuit Theory*, vol. 4, no. 3, pp. 70–78, Sep. 1957.

[35] E. Bolinder, "Correction to 'Survey of Some Properties of Linear Networks'," *IRE Transactions on Circuit Theory*, vol. 5, no. 2, pp. 139–139, Jun. 1958.

[36] W. Struble and A. Platzker, "Stability Analysis for RF and Microwave Circuit Design," 2015. [Online]. Available: https://www.microwaves101.com/uploads/Stability-Analysis-Presentation.pdf

[37] S. Venkateswaran, "An Invariant Stability Factor and its Physical Significance," *Proceedings of the IEE - Part C: Monographs*, vol. 109, no. 15, pp. 98–102, Mar. 1962.

[38] J. Rollett, "Stability and Power-Gain Invariants of Linear Twoports," *IRE Transactions on Circuit Theory*, vol. 9, no. 1, pp. 29–32, Mar. 1962.

[39] J. Rollett, "Correction to 'Stability and Power-Gain Invariants of Linear Twoports'," *IEEE Transactions on Circuit Theory*, vol. 10, no. 1, pp. 107–107, Mar. 1963.

[40] J. Linvill, "The Relationship of Transistor Parameters to Amplifier Performance," in *1955 IEEE International Solid-State Circuits Conference. Digest of Technical Papers*, Feb. 1955, pp. 8–8.

[41] J. G. Linvill and L. G. Schimpf, "The Design of Tetrode Transistor Amplifiers," *The Bell System Technical Journal*, vol. 35, no. 4, pp. 813–840, Jul. 1956.

[42] K. Kurokawa, "Power Waves and the Scattering Matrix," *IEEE Transactions on Microwave Theory and Techniques*, vol. 13, no. 2, pp. 194–202, Mar. 1965.

[43] M. L. Edwards and J. H. Sinsky, "A New Criterion for Linear 2-Port Stability Using a Single Geometrically Derived Parameter," *IEEE Transactions on Microwave Theory and Techniques*, vol. 40, no. 12, pp. 2303–2311, Dec. 1992.

[44] "IRE Standards on Electron Tubes: Definitions of Terms, 1957," *Proceedings of the IRE*, vol. 45, no. 7, pp. 983–1010, Jul. 1957.

[45] M. Karp, "Power Gain and Stability," *IRE Transactions on Circuit Theory*, vol. 4, no. 4, pp. 339–340, Dec. 1957.

[46] N. George, *Network Stability and Transistor Cascades*, Emerson Research Laboratories, TMS, May 1956.

[47] S. Mason, "Power Gain in Feedback Amplifier," *Transactions of the IRE Professional Group on Circuit Theory*, vol. CT-1, no. 2, pp. 20–25, Jun. 1954.

[48] W. H. Ku, "Unilateral Gain and Stability Criterion of Active Two-Ports in Terms of Scattering Parameters," *Proceedings of the IEEE*, vol. 54, no. 11, pp. 1617–1618, Nov. 1966.

[49] *Predictions Based on the Maximum Oscillator Frequency*, Feb. 1955.

[50] P. R. Drouilhet, "Predictions Based on the Maximum Oscillator Frequency of a Transistor," *IRE Transactions on Circuit Theory*, vol. 2, no. 2, pp. 178–183, Jun. 1955.

[51] R. L. Pritchard, "Two-Dimensional Current Flow in Junction Transistors at High Frequencies," *Proceedings of the IRE*, vol. 46, no. 6, pp. 1152–1160, Jun. 1958.

[52] J. Lindmayer and C. Y. Wrigley, "Beta Cutoff Frequencies of Junction Transistors," *Proceedings of the IRE*, vol. 50, no. 2, pp. 194–198, Feb. 1962.

[53] M. Golio and J. Golio, *RF and Microwave Circuits, Measurements, and Modeling*, ser. The RF and Microwave Handbook, Second Edition. CRC Press, 2007.

[54] S. C. Cripps, *RF Power Amplifiers for Wireless Communications*, ser. Artech House microwave library. Artech House, 2006.

[55] A. Van der Ziel, *Noise in Solid State Devices and Circuits*. Wiley, 1986.

[56] J. B. Johnson, "Thermal Agitation of Electricity in Conductors," *Phys. Rev.*, vol. 32, pp. 97–109, Jul. 1928.

[57] H. Nyquist, "Thermal Agitation of Electric Charge in Conductors," *Phys. Rev.*, vol. 32, pp. 110–113, Jul. 1928.

[58] W. Schottky, "Über spontane Stromschwankungen in verschiedenen Elektrizitätsleitern," *Annalen der Physik*, vol. 362, no. 23, pp. 541–567, Jul. 1918.

[59] J. B. Johnson, "The Schottky Effect in Low Frequency Circuits," *Phys. Rev.*, vol. 26, pp. 71–85, Jul. 1925.

[60] W. Schottky, "Small-Shot Effect and Flicker Effect," *Phys. Rev.*, vol. 28, pp. 74–103, Jul. 1926.

[61] A. Van der Ziel, "Flicker Noise in Electronic Devices," ser. Advances in Electronics and Electron Physics, L. Marton and C. Marton, Eds. Academic Press, 1979, vol. 49, pp. 225–297.

[62] H. Rothe and W. Dahlke, "Theory of Noisy Fourpoles," *Proceedings of the IRE*, vol. 44, no. 6, pp. 811–818, Jun. 1956.

[63] H. T. Friis, "Noise Figures of Radio Receivers," *Proceedings of the IRE*, vol. 32, no. 7, pp. 419–422, Jul. 1944.

[64] A. H. Jarndal, *Large Signal Modeling of GaN Device for High Power Amplifier Design*.   Kassel University Press, 2006.

[65] E. S. Mengistu, *Large-Signal Modeling of GaN HEMTs for Linear Power Amplifier Design*.   Kassel University Press, 2008.

[66] J. Olsson, N. Rorsman, L. Vestling, C. Fager, J. Ankarcrona, H. Zirath, and K.-H. Eklund, "1 W/mm RF Power Density at 3.2 GHz for a Dual-Layer RESURF LDMOS Transistor," *IEEE Electron Device Letters*, vol. 23, no. 4, pp. 206–208, Apr. 2002.

[67] S. J. C. H. Theeuwen, H. Mollee, R. Heeres, and F. Van Rijs, "LDMOS Technology for Power Amplifiers up to 12 GHz," in *2018 13th European Microwave Integrated Circuits Conference (EuMIC)*, Sep. 2018, pp. 162–165.

[68] E. Kohn, A. Aleksov, M. Kubovic, P. Schmid, J. Kusterer, M. Schreck, and M. Kasu, "Diamond A New Materials Base for Future Ultra High Power RF Electronics," in *2004 19th International Conference on Compound Semiconductor Manufacturing Technology*, May 2004, pp. 29–34.

[69] S. Koizumi, H. Umezawa, J. Pernot, and M. Suzuki, *Power Electronics Device Applications of Diamond Semiconductors*, ser. Woodhead Publishing Series in Electronic and Optical Materials. Elsevier Science, 2018.

[70] H. Morkoç, S. Strite, G. B. Gao, M. E. Lin, B. Sverdlov, and M. Burns, "Large-band-gap SiC, III-V nitride, and II-VI ZnSe-based semiconductor device technologies," *Journal of Applied Physics*, vol. 76, no. 3, pp. 1363–1398, Aug. 1994.

[71] A. A. Burk, M. J. O'Loughlin, R. R. Siergiej, A. K. Agarwal, S. Sriram, R. C. Clarke, M. F. MacMillan, V. Balakrishna, and C. D. Brandt, "SiC and GaN wide bandgap semiconductor materials and devices," *Solid-State Electronics*, vol. 43, no. 8, pp. 1459–1464, Aug. 1999.

[72] M. N. Yoder, "Wide Bandgap Semiconductor Materials and Devices," *IEEE Transactions on Electron Devices*, vol. 43, no. 10, pp. 1633–1636, Oct. 1996.

[73] B. Gil, *III-Nitride Semiconductors and their Modern Devices*, ser. Series on Semiconductor Science and Technology.   OUP Oxford, Aug. 2013.

[74] M. Levinshtein, S. Rumyantsev, and M. Shur, *Handbook Series on Semiconductor Parameters*. World Scientific, Nov. 1996, vol. 1.

[75] J. L. Hudgins, G. S. Simin, E. Santi, and M. A. Khan, "An Assessment of Wide Bandgap Semiconductors for Power Devices," *IEEE Transactions on Power Electronics*, vol. 18, no. 3, pp. 907–914, May 2003.

[76] E. J. Ryder, "Mobility of Holes and Electrons in High Electric Fields," *Phys. Rev.*, vol. 90, pp. 766–769, Jun. 1953.

[77] S. Montanari, "Fabrication and characterization of planar Gunn diodes for Monolithic Microwave Integrated Circuits," Ph.D. dissertation, RWTH Aachen University, Germany, Dec. 2004.

[78] R. J. Trew, "Wide Bandgap Semiconductor Transistors for Microwave Power Amplifiers," *IEEE Microwave Magazine*, vol. 1, no. 1, pp. 46–54, Mar. 2000.

[79] L. I. Berger, *Semiconductor Materials*.   Taylor & Francis, Dec. 1996.

[80] M. Bhatnagar and B. J. Baliga, "Comparison of 6H-SiC, 3C-SiC, and Si for Power Devices," *IEEE Transactions on Electron Devices*, vol. 40, no. 3, pp. 645–655, Mar. 1993.

[81] M. Ruff, H. Mitlehner, and R. Helbig, "SiC Devices: Physics and Numerical Simulation," *IEEE Transactions on Electron Devices*, vol. 41, no. 6, pp. 1040–1054, Jun. 1994.

[82] T. P. Chow and R. Tyagi, "Wide Bandgap Compound Semiconductors for Superior High-Voltage Unipolar Power Devices," *IEEE Transactions on Electron Devices*, vol. 41, no. 8, pp. 1481–1483, Aug. 1994.

[83] R. C. Marshall, J. W. Faust, and C. E. Ryan, Eds., *Silicon Carbide—1973*. Columbia, SC: University of South Carolina Press, 1974.

[84] L. Tolbert, B. Ozpineci, S. Islam, and M. Chinthavali, "Wide Bandgap Semiconductors for Utility Applications," *Proceedings of the IASTED Multi-Conference- Power and Energy Systems*, vol. 7, Jan. 2003.

[85] R. J. Kaplar, J. C. Neely, D. L. Huber, and L. J. Rashkin, "Generation-After-Next Power Electronics: Ultrawide-bandgap devices, high-temperature packaging, and magnetic nanocomposite materials," *IEEE Power Electronics Magazine*, vol. 4, no. 1, pp. 36–42, Mar. 2017.

[86] K. Shenai, R. S. Scott, and B. J. Baliga, "Optimum Semiconductors for High-Power Electronics," *IEEE Transactions on Electron Devices*, vol. 36, no. 9, pp. 1811–1823, Sep. 1989.

[87] S. M. Sze, *Physics of Semiconductor Devices*, 2nd ed., ser. Wiley international edition. Wiley-Interscience, Jan. 1969.

[88] O. Ambacher, "Growth and applications of Group III-nitrides," *Journal of Physics D: Applied Physics*, vol. 31, no. 20, pp. 2653–2710, Oct. 1998.

[89] H. Ibach and H. Lüth, *Solid-State Physics: An Introduction to Principles of Materials Science*, ser. Advanced texts in physics. Springer Berlin Heidelberg, Nov. 2009.

[90] R. L. Anderson, "Germanium-Gallium Arsenide Heterojunctions," *IBM Journal of Research and Development*, vol. 4, no. 3, pp. 283–287, Jul. 1960.

[91] R. L. Anderson, "Experiments on Ge-GaAs Heterojunctions," *IRE Transactions on Electron Devices*, vol. 9, no. 6, pp. 509–509, Nov. 1962.

[92] T. Mimura, S. Hiyamizu, T. Fujii, and K. Nanbu, "A New Field-Effect Transistor with Selectively Doped GaAs/n-Al$_x$Ga$_{1-x}$As Heterojunctions," *Japanese Journal of Applied Physics*, vol. 19, no. 5, pp. L225–L227, May 1980.

[93] O. Ambacher, J. Smart, J. R. Shealy, N. G. Weimann, K. Chu, M. Murphy, W. J. Schaff, L. F. Eastman, R. Dimitrov, L. Wittmer, M. Stutzmann, W. Rieger, and J. Hilsenbeck, "Two-dimensional electron gases induced by spontaneous and piezoelectric polarization charges in N- and Ga-face AlGaN/GaN heterostructures," *Journal of Applied Physics*, vol. 85, no. 6, pp. 3222–3233, Mar. 1999.

[94] P. Javorka, "Fabrication and Characterization of AlGaN/GaN High Electron Mobility Transistors," Ph.D. dissertation, RWTH Aachen University, Germany, Feb. 2004.

[95] M. S. Shur, *GaAs Devices and Circuits*, ser. Microdevices. Springer US, 2013.

[96] M. A. Khan, J. M. Van Hove, J. N. Kuznia, and D. T. Olson, "High electron mobility GaN/Al$_x$Ga$_{1-x}$N heterostructures grown by low-pressure metalorganic chemical vapor deposition," *Applied Physics Letters*, vol. 58, no. 21, pp. 2408–2410, May 1991.

[97] T. Egawa, N. Nakada, H. Ishikawa, and M. Umeno, "GaN MESFETs on (111) Si substrate grown by MOCVD," *Electronics Letters*, vol. 36, no. 21, pp. 1816–1818, Oct. 2000.

[98] T. Huber, "DissertantInnenseminar Informations- und Kommunikationstechnik (16S): GaN-Cascodes in Broadband Power Amplifiers," Apr. 2016, Institute of Microwave and Photonic Engineering, University Graz, Austria.

[99] A. Wood, W. Brakensick, C. Dragon, and W. Burger, "120 Watt, 2 GHz, Si LDMOS RF Power Transistor for PCS Base Station Applications," in *1998 IEEE MTT-S International Microwave Symposium Digest (Cat. No.98CH36192)*, vol. 2, Jun. 1998, pp. 707–710.

[100] C. T. Burns, A. Chang, and D. W. Runton, "A 900 MHz, 500 W Doherty Power Amplifier Using Optimized Output Matched Si LDMOS Power Transistors," in *2007 IEEE/MTT-S International Microwave Symposium*, Jun. 2007, pp. 1577–1580.

[101] D. Gruner, R. Sorge, O. Bengtsson, A. Z. Markos, and G. Boeck, "A 1 W Si-LDMOS Power Amplifier with 40 % Drain Efficiency for 6 GHz WLAN Applications," in *2010 IEEE MTT-S International Microwave Symposium*, May 2010, pp. 1–1.

[102] R. A. Sadler, S. T. Allen, W. L. Pribble, T. S. Alcorn, J. J. Sumakeris, and J. W. Palmour, "SiC MESFET Hybrid Amplifier with 30-W Output Power at 10 GHz," in *Proceedings 2000 IEEE/ Cornell Conference on High Performance Devices (Cat. No.00CH37122)*, Aug. 2000, pp. 173– 177.

[103] Y. Lee, M. Lee, S. Jung, and Y. Jeong, "A High-Efficiency SiC MESFET Power Amplifier Based on Class-F Configuration," in *2007 Asia-Pacific Microwave Conference*, Dec. 2007, pp. 1–4.

[104] V. Baranov, R. Zimin, A. Matveev, A. Kistchinsky, and D. Sukhanov, "Wideband L-S Band SiC Power Amplifiers," in *2009 19th International Crimean Conference Microwave Telecommunication Technology*, Sep. 2009, pp. 55–56.

[105] L. Wang, W. Chen, P. Wang, X. Xue, J. Dong, and Z. Feng, "A High Power SiC MESFET Class-E Power Amplifier With An Asymmetrical Spurline Resonator," in *2009 Asia Pacific Microwave Conference*, Dec. 2009, pp. 1120–1123.

[106] C. Shen, F. Huang, C. Lin, H. Chang, Y. Chan, and Y. Wang, "A Broadband Stacked Power Amplifier Using 2-μm GaAs HBT Process for *C*-Band Applications," in *2008 Asia-Pacific Microwave Conference*, Dec. 2008, pp. 1–4.

[107] D. Li, C. Wang, W. Huang, R. Krishna, S. Cho, B. Shrestha, G. I. Kyung, and N. Kim, "A High-Power Ka-Band Power Amplifier Design Based on GaAs P-HEMT Technology for VSAT ODU Applications," in *2009 3rd IEEE International Symposium on Microwave, Antenna, Propagation and EMC Technologies for Wireless Communications*, Oct. 2009, pp. 20–23.

[108] H. Shigematsu, Y. Inoue, A. Akasegawa, M. Yamada, S. Masuda, Y. Kamada, A. Yamada, M. Kanamura, T. Ohki, K. Makiyama, N. Okamoto, K. Imanishi, T. Kikkawa, K. Joshin, and N. Hara, "C-band 340-W and X-band 100-W GaN Power Amplifiers with Over 50-% PAE," in *2009 IEEE MTT-S International Microwave Symposium Digest*, Jun. 2009, pp. 1265–1268.

[109] K. Yamauchi, H. Noto, H. Nonomura, S. Kunugi, M. Nakayama, and Y. Hirano, "A 45% Power Added Efficiency, Ku-band 60W GaN Power Amplifier," in *2011 IEEE MTT-S International Microwave Symposium*, Jun. 2011, pp. 1–4.

[110] M. Micovic, A. Kurdoghlian, A. Margomenos, D. F. Brown, K. Shinohara, S. Burnham, I. Milosavljevic, R. Bowen, A. J. Williams, P. Hashimoto, R. Grabar, C. Butler, A. Schmitz, P. J. Willadsen, and D. H. Chow, "92-96 GHz GaN Power Amplifiers," in *2012 IEEE/MTT-S International Microwave Symposium Digest*, Jun. 2012, pp. 1–3.

[111] E. Ture, S. Leone, P. Brückner, R. Quay, and O. Ambacher, "High-Power (>2 W) E-Band PA MMIC Based on High Efficiency GaN-HEMTs with Optimized Buffer," in *2019 IEEE MTT-S International Microwave Symposium (IMS)*, Jun. 2019, pp. 1407–1410.

[112] M. Matloubian, A. S. Brown, L. D. Nguyen, M. A. Melendes, L. E. Larson, M. J. Delancey, J. E. Pence, R. A. Rhodes, M. A. Thompson, and J. A. Henige, "High-Power *V*-Band AlInAs/GaInAs on InP HEMTs," *IEEE Electron Device Letters*, vol. 14, no. 4, pp. 188–189, Apr. 1993.

[113] T. O'Sullivan, M. Le, P. Partyka, R. Milano, and P. M. Asbeck, "Design of a 70 GHz Power Amplifier using a Digital InP HBT Process," in *2007 IEEE Bipolar/BiCMOS Circuits and Technology Meeting*, Sep. 2007, pp. 214–217.

[114] T. O'Sullivan, M. Urteaga, R. Pierson, and P. M. Asbeck, "InP HBT Millimeter-wave Power Amplifier Implemented using Planar Radial Power Combiner," in *2008 IEEE MTT-S International Microwave Symposium Digest*, Jun. 2008, pp. 293–296.

[115] T. B. Reed, M. Rodwell, Z. Griffith, P. Rowell, A. Young, M. Urteaga, and M. Field, "A 220 GHz InP HBT Solid-State Power Amplifier MMIC with 90mW P$_{OUT}$ at 8.2dB Compressed Gain," in *2012 IEEE Compound Semiconductor Integrated Circuit Symposium (CSICS)*, Oct. 2012, pp. 1–4.

[116] Z. Griffith, M. Urteaga, and P. Rowell, "A 140-GHz 0.25-W PA and a 55-135 GHz 115-135 mW PA, High-Gain, Broadband Power Amplifier MMICs in 250-nm InP HBT," in *2019 IEEE MTT-S International Microwave Symposium (IMS)*, Jun. 2019, pp. 1245–1248.

[117] T. Shivan, M. Hossain, R. Doerner, S. Schulz, T. Johansen, S. Boppel, W. Heinrich, and V. Krozer, "A 175 GHz Bandwidth High Linearity Distributed Amplifier in 500 nm InP DHBT Technology," in *2019 IEEE MTT-S International Microwave Symposium (IMS)*, Jun. 2019, pp. 1253–1256.

[118] J. M. Golio, *Microwave MESFETs and HEMTs*, ser. Microwave Library.   Artech House, 1991.

[119] G. Dambrine, A. Cappy, F. Heliodore, and E. Playez, "A New Method for Determining the FET Small-Signal Equivalent Circuit," *IEEE Transactions on Microwave Theory and Techniques*, vol. 36, no. 7, pp. 1151–1159, Jul. 1988.

[120] E. Chigaeva, W. Walthes, D. Wiegner, M. Grozing, F. Schaich, N. Wieser, M. Berroth, O. Breitschadel, L. Kley, B. Kuhn, F. Scholz, H. Schweizer, O. Ambacher, and J. Hilsenbeck, "Determination of Small-Signal Parameters of GaN-based HEMTs," in *Proceedings 2000 IEEE/ Cornell Conference on High Performance Devices (Cat. No.00CH37122)*, Aug. 2000, pp. 115–122.

[121] M. Berroth and R. Bosch, "High-Frequency Equivalent Circuit of GaAs FET's for Large-Signal Applications," *IEEE Transactions on Microwave Theory and Techniques*, vol. 39, no. 2, pp. 224–229, Feb. 1991.

[122] M. Berroth and R. Bosch, "Broad-Band Determination of the FET Small-Signal Equivalent Circuit," *IEEE Transactions on Microwave Theory and Techniques*, vol. 38, no. 7, pp. 891–895, Jul. 1990.

[123] C. A. Liechti, "Microwave Field-Effect Transistors—1976," *IEEE Transactions on Microwave Theory and Techniques*, vol. 24, no. 6, pp. 279–300, Jun. 1976.

[124] A. Van der Ziel, "Thermal Noise in Field-Effect Transistors," *Proceedings of the IRE*, vol. 50, no. 8, pp. 1808–1812, Aug. 1962.

[125] F. M. Klaassen, "On the Influence of Hot Carrier Effects on the Thermal Noise of Field-Eeffect Transistors," *IEEE Transactions on Electron Devices*, vol. 17, no. 10, pp. 858–862, Oct. 1970.

[126] W. Baechtold, "Noise Behavior of Schottky Barrier Gate Field-Eeffect Transistors at Microwave Frequencies," *IEEE Transactions on Electron Devices*, vol. 18, no. 2, pp. 97–104, Feb. 1971.

[127] W. Baechtold, "Noise Behavior of GaAs Field-Eeffect Transistors with Short Gate Lengths," *IEEE Transactions on Electron Devices*, vol. 19, no. 5, pp. 674–680, May 1972.

[128] A. Van der Ziel, "Thermal Noise in the Hot Electron Regime in FETs," *IEEE Transactions on Electron Devices*, vol. 18, no. 10, pp. 977–977, Oct. 1971.

[129] H. Statz, H. A. Haus, and R. A. Pucel, "Noise Characteristics of Gallium Arsenide Field-Eeffect Transistors," *IEEE Transactions on Electron Devices*, vol. 21, no. 9, pp. 549–562, Sep. 1974.

[130] R. A. Pucel, H. A. Haus, and H. Statz, "Signal and Noise Properties of Gallium Arsenide Microwave Field-Effect Transistors," ser. Advances in Electronics and Electron Physics, L. Marton, Ed.   Academic Press, 1975, vol. 38, pp. 195–265.

[131] M. W. Pospieszalski, "Modeling of Noise Parameters of MESFET's and MODFET's and Their Frequency and Temperature Dependence," *IEEE Transactions on Microwave Theory and Techniques*, vol. 37, no. 9, pp. 1340–1350, Sep. 1989.

[132] H. Fukui, "Optimal Noise Figure of Microwave GaAs MESFET's," *IEEE Transactions on Electron Devices*, vol. 26, no. 7, pp. 1032–1037, Jul. 1979.

[133] A. F. Podell, "A Functional GaAs FET Noise Model," *IEEE Transactions on Electron Devices*, vol. 28, no. 5, pp. 511–517, May 1981.

[134] L. Klapproth, A. Schaefer, and G. Boeck, "A Bias Dependent HEMT Noise Model," in *1997 IEEE MTT-S International Microwave Symposium Digest*, vol. 2, Jun. 1997, pp. 881–884.

[135] F. Danneville, G. Dambrine, H. Happy, and A. Cappy, "Influence of the Gate Leakage Current on the Noise Performance of MESFETs and MODFETs," in *ESSDERC '93: 23rd European solid State Device Research Conference*, Sep. 1993, pp. 47–50.

[136] A. Nalli, A. Raffo, G. Crupi, S. D'Angelo, D. Resca, F. Scappaviva, G. Salvo, A. Caddemi, and G. Vannini, "GaN HEMT Modelling Through 50-Ω NF Measurements," in *2015 Integrated Nonlinear Microwave and Millimetre-wave Circuits Workshop (INMMiC)*, Oct. 2015, pp. 1–3.

[137] J. M. Miller, *Dependence of the Input Impedance of a Three-Electrode Vacuum Tube Upon the Load in the Plate Circuit*, ser. Scientific papers of the Bureau of Standards.   U.S. Government Printing Office, Nov. 1919, vol. 15, no. 351.

[138] J. P. Fraysse, J. P. Viaud, M. Campovecchio, P. Auxemery, and R. Quere, "A 2 W, High Efficiency, 2-8 GHz, Cascode HBT MMIC Power Distributed Amplifier," in *2000 IEEE MTT-S International Microwave Symposium Digest (Cat. No.00CH37017)*, vol. 1, Jun. 2000, pp. 529–532.

[139] S. Asai, F. Murai, and H. Kodera, "GaAs Dual-Gate Schottky-Barrier FET's for Microwave Frequencies," *IEEE Transactions on Electron Devices*, vol. 22, no. 10, pp. 897–904, Oct. 1975.

[140] C.-H. Chen, K. Krishnamurthy, S. Keller, G. Parish, M. Rodwell, U. K. Mishra, and Y.-F. Wu, "AlGaN/GaN dual-gate modulation-doped field-effect transistors," *Electronics Letters*, vol. 35, no. 11, pp. 933–935, May 1999.

[141] B. M. Green, K. K. Chu, J. A. Smart, V. Tilak, Hyungtak Kim, J. R. Shealy, and L. F. Eastman, "Cascode Connected AlGaN/GaN HEMT's on SiC Substrates," *IEEE Microwave and Guided Wave Letters*, vol. 10, no. 8, pp. 316–318, Aug. 2000.

[142] A. Chen, J. Hutchby, V. Zhirnov, and G. Bourianoff, *Emerging Nanoelectronic Devices*.   Wiley, 2015.

[143] T. Huber, R. Quay, and W. Bösch, "Noise Degradation of Cascodes in Broadband Power Amplifiers," in *2017 Integrated Nonlinear Microwave and Millimetre-wave Circuits Workshop (INMMiC)*, Apr. 2017, pp. 1–3.

[144] S. Lee, B. Green, K. Chu, K. J. Webb, and L. F. Eastman, "Demonstration of a High Efficiency Nonuniform Monolithic Gallium-Nitride Distributed Amplifier," in *2000 IEEE MTT-S International Microwave Symposium Digest (Cat. No.00CH37017)*, vol. 1, Jun. 2000, pp. 549–552.

[145] K. Krishnamurthy, S. Keller, U. K. Mishra, M. J. W. Rodwell, and S. I. Long, "Broad-band Microwave Power Amplifiers in GaN Technology," in *GaAs IC Symposium. IEEE Gallium Arsenide Integrated Circuits Symposium. 22nd Annual Technical Digest 2000. (Cat. No.00CH37084)*, Nov. 2000, pp. 33–36.

[146] B. M. Green, V. Tilak, Sungjae Lee, Hyungtak Kim, J. A. Smart, K. J. Webb, J. R. Shealy, and L. F. Eastman, "High-Power Broadband AlGaN/GaN HEMT MMICs on SiC Substrates," in *2001 IEEE MTT-S International Microwave Sympsoium Digest (Cat. No.01CH37157)*, vol. 2, May 2001, pp. 1059–1062.

[147] B. M. Green, V. Tilak, S. Lee, H. Kim, J. A. Smart, K. J. Webb, J. R. Shealy, and L. F. Eastman, "High-Power Broad-Band AlGaN/GaN HEMT MMICs on SiC Substrates," *IEEE Transactions on Microwave Theory and Techniques*, vol. 49, no. 12, pp. 2486–2493, Dec. 2001.

[148] Avago Technologies, "AMMC5024: 30 KHz – 40 GHz Traveling Wave Amplifier," Sep. 2008, Datasheet. [Online]. Available: https://docs.broadcom.com/docs/AV02-0632EN

[149] Analog Devices, "HMC1022: GaAs pHEMT MMIC, 0.25 WATT POWER AMPLIFIER, DC – 48 GHz," Jan. 2017, Datasheet. [Online]. Available: https://www.analog.com/media/en/technical-documentation/data-sheets/hmc1022.pdf

[150] MACOM, "MAAM-011275: Wideband Distributed Amplifier, 30 kHz – 40 GHz," Aug. 2019, Datasheet. [Online]. Available: https://cdn.macom.com/datasheets/MAAM-011275-DIE.pdf

[151] K. W. Kobayashi, Y. Chen, I. Smorchkova, B. Heying, W. Luo, W. Sutton, M. Wojtowicz, and A. Oki, "A Cool, Sub-0.2 dB Noise Figure GaN HEMT Power Amplifier With 2-Watt Output Power," *IEEE Journal of Solid-State Circuits*, vol. 44, no. 10, pp. 2648–2654, Oct. 2009.

[152] R. Amirpour, D. Schwantuschke, P. Brueckner, R. Quay, and O. Ambacher, "High-Q Anti-Series AlGaN/GaN High Electron-Mobility Varactor," in *2019 IEEE MTT-S International Microwave Symposium (IMS)*, Jun. 2019, pp. 599–602.

[153] M. Coers and W. Bösch, "DC to 6.5 GHz Highly Linear Low-Noise AlGaN/GaN Traveling Wave Amplifier with Diode Predistortion," in *2014 IEEE MTT-S International Microwave Symposium (IMS2014)*, Jun. 2014, pp. 1–4.

[154] Northrop Grumman, "Process Technology Overview." [Online]. Available: https://www.northropgrumman.com/businessventures/microelectronics/pages/foundryservices.aspx

[155] K. K. Samanta, "Designing and Packaging Wide-Band PAs: Wideband PA and Packaging, History, and Recent Advances," *IEEE Microwave Magazine*, vol. 17, no. 10, pp. 35–45, Oct. 2016.

[156] A. Ghavidel, F. Tamjid, A. Fathy, and A. Kheirdoost, "GaN Widening Possibilties for PAs: Wideband GaN Power Amplifiers Utilize the Technology's Special Properties," *IEEE Microwave Magazine*, vol. 18, no. 4, pp. 46–55, Jun. 2017.

[157] W. S. Percival, "Improvements in and relating to thermionic valve circuits," United Kingdom Patent 460,562, Jan. 25, 1937.

[158] C. F. Campbell, "Evolution of the Nonuniform Distributed Power Amplifier: A Distinguished Microwave Lecture," *IEEE Microwave Magazine*, vol. 20, no. 1, pp. 18–27, Jan. 2019.

[159] C. Campbell, C. Lee, V. Williams, M. Kao, H. Tserng, P. Saunier, and T. Balisteri, "A Wideband Power Amplifier MMIC Utilizing GaN on SiC HEMT Technology," *IEEE Journal of Solid-State Circuits*, vol. 44, no. 10, pp. 2640–2647, Oct. 2009.

[160] E. Reese, D. Allen, C. Lee, and T. Nguyen, "Wideband Power Amplifier MMICs Utilizing GaN on SiC," in *2010 IEEE MTT-S International Microwave Symposium*, May 2010, pp. 1230–1233.

[161] S. Masuda, A. Akasegawa, T. Ohki, K. Makiyama, N. Okamoto, K. Imanishi, T. Kikkawa, and H. Shigematsu, "Over 10W C-Ku Band GaN MMIC Non-uniform Distributed Power Amplifier with Broadband Couplers," in *2010 IEEE MTT-S International Microwave Symposium*, May 2010, pp. 1–1.

[162] R. Santhakumar, B. Thibeault, M. Higashiwaki, S. Keller, Z. Chen, U. K. Mishra, and R. A. York, "Two-Stage High-Gain High-Power Distributed Amplifier Using Dual-Gate GaN HEMTs," *IEEE Transactions on Microwave Theory and Techniques*, vol. 59, no. 8, pp. 2059–2063, Aug. 2011.

[163] J. J. Komiak, K. Chu, and P. C. Chao, "Decade Bandwidth 2 to 20 GHz GaN HEMT Power Amplifier MMICs in DFP and No FP Technology," in *2011 IEEE MTT-S International Microwave Symposium*, Jun. 2011, pp. 1–4.

[164] W. Ciccognani, E. Limiti, P. E. Longhi, C. Mitrano, A. Nanni, and M. Peroni, "An Ultra-Broadband Robust LNA for Defence Applications in AlGaN/GaN Technology," in *2010 IEEE MTT-S International Microwave Symposium*, May 2010, pp. 493–496.

[165] C. F. Campbell, M. D. Roberg, J. Fain, and S. Nayak, "A 1-8GHz Gallium Nitride Distributed Power Amplifier MMIC Utilizing a Trifilar Transformer," in *2016 11th European Microwave Integrated Circuits Conference (EuMIC)*, Oct. 2016, pp. 217–220.

[166] C. F. Campbell, S. Nayak, Ming-Yih Kao, and Shuoqi Chen, "Design and Performance of 16-40GHz GaN Distributed Power Amplifier MMICs Utilizing an Advanced 0.15μm GaN Process," in *2016 IEEE MTT-S International Microwave Symposium (IMS)*, May 2016, pp. 1–4.

[167] K. W. Kobayashi, D. Denninghoff, and D. Miller, "A Novel 0.1-44 GHz Linear Common-Drain-Cascode 0.15um GaN Distributed Amplifier Architecture with Improved IP3-BW," in *2016 IEEE Compound Semiconductor Integrated Circuit Symposium (CSICS)*, Oct. 2016, pp. 1–4.

[168] K. W. Kobayashi, D. Denninghoff, and D. Miller, "A Novel 100 MHz-45 GHz GaN HEMT Low Noise Non-Gate-Terminated Distributed Amplifier Based on a 6-Inch 0.15μm GaN-SiC mm-Wave Process Technology," in *2015 IEEE Compound Semiconductor Integrated Circuit Symposium (CSICS)*, Oct. 2015, pp. 1–4.

[169] J. M. Schellenberg, "A 2-W W-Band GaN Traveling-Wave Amplifier With 25-GHz Bandwidth," *IEEE Transactions on Microwave Theory and Techniques*, vol. 63, no. 9, pp. 2833–2840, Sep. 2015.

[170] H. S. Black, "Stabilized Feedback Amplifiers," *The Bell System Technical Journal*, vol. 13, no. 1, pp. 1–18, Jan. 1934.

[171] T. Huber, "DissertantInnenseminar Informations- und Kommunikationstechnik (16W): GaN-Cascodes in Broadband Power Amplifiers," Nov. 2016, Institute of Microwave and Photonic Engineering, University Graz, Austria.

[172] K. W. Kobayashi, "An 8-Watt 250-3000 MHz Low Noise GaN MMIC Feedback Amplifier with > +50 dBm OIP3," in *2011 IEEE Compound Semiconductor Integrated Circuit Symposium (CSICS)*, Oct. 2011, pp. 1–4.

[173] K. W. Kobayashi, "Bias Optimized IP2 & IP3 Linearity and NF of a Decade-Bandwidth GaN MMIC Feedback Amplifier," in *2012 IEEE Radio Frequency Integrated Circuits Symposium*, Jun. 2012, pp. 479–482.

[174] J. P. Conlon, N. Zhang, M. J. Poulton, J. B. Shealy, R. Vetury, D. S. Green, J. D. Brown, and S. Gibb, "GaN Wide Band Power Integrated Circuits," in *2006 IEEE Compound Semiconductor Integrated Circuit Symposium*, Nov. 2006, pp. 85–88.

[175] S. E. Shih, W. R. Deal, W. E. Sutton, Y. C. Chen, I. Smorchkova, B. Heying, M. Wojtowicz, and M. Siddiqui, "Broadband GaN Dual-Gate HEMT Low Noise Amplifier," in *2007 IEEE Compound Semiconductor Integrated Circuits Symposium*, Oct. 2007, pp. 1–4.

[176] K. W. Kobayashi, Y. Chen, I. Smorchkova, R. Tsai, M. Wojtowicz, and A. Oki, "A 2 Watt, Sub-dB Noise Figure GaN MMIC LNA-PA Amplifier with Multi-octave Bandwidth from 0.2-8 GHz," in *2007 IEEE/MTT-S International Microwave Symposium*, Jun. 2007, pp. 619–622.

[177] M. V. Aust, A. K. Sharma, Y. Chen, and M. Wojtowicz, "Wideband Dual-Gate GaN HEMT Low Noise Amplifier for Front-End Receiver Electronics," in *2006 IEEE Compound Semiconductor Integrated Circuit Symposium*, Nov. 2006, pp. 89–92.

[178] T. Huber, R. Quay, and W. Bösch, "New Concept for Power Compression Improvement of GaN Cascodes in Broadband Power Amplifiers," *IEEE Microwave and Wireless Components Letters*, vol. 27, no. 6, pp. 590–592, Jun. 2017.

[179] T. Huber, R. Quay, and W. Bösch, "New Concept to Control the Gain of GaN-Cascodes in Broadband Power Amplifiers," in *2017 12th European Microwave Integrated Circuits Conference (EuMIC)*, Oct. 2017, pp. 184–187.

[180] S. E. Shih, W. R. Deal, D. Yamauchi, W. E. Sutton, Y. C. Chen, I. Smorchkova, B. Heying, M. Wojtowicz, and M. Siddiqui, "Design and Analysis of Ultra Wideband GaN Dual-Gate HEMT Low Noise Amplifiers," in *2009 IEEE MTT-S International Microwave Symposium Digest*, Jun. 2009, pp. 669–672.

[181] M. Chen, W. Sutton, I. Smorchkova, B. Heying, W. Luo, V. Gambin, F. Oshita, R. Tsai, M. Wojtowicz, R. Kagiwada, A. Oki, and J. Lin, "A 1–25 GHz GaN HEMT MMIC Low-Noise Amplifier," *IEEE Microwave and Wireless Components Letters*, vol. 20, no. 10, pp. 563–565, Oct. 2010.

Publications

T. Huber, R. Quay, and W. Bösch, "Multi-Decade GaN Feedback Power Amplifiers in Common-Source and Cascode Topology," in *2016 Asia-Pacific Microwave Conference (APMC)*, Dec. 2016, pp. 1–4.

T. Huber, R. Quay, and W. Bösch, "Noise Degradation of Cascodes in Broadband Power Amplifiers," in *2017 Integrated Nonlinear Microwave and Millimetre-wave Circuits Workshop (INMMiC)*, Apr. 2017, pp. 1–3.

T. Huber, R. Quay, and W. Bösch, "New Concept for Power Compression Improvement of GaN Cascodes in Broadband Power Amplifiers," *IEEE Microwave and Wireless Components Letters*, vol. 27, no. 6, pp. 590–592, Jun. 2017.

T. Huber, R. Quay, and W. Bösch, "New Concept to Control the Gain of GaN-Cascodes in Broadband Power Amplifiers," in *2017 12th European Microwave Integrated Circuits Conference (EuMIC)*, Oct. 2017, pp. 184–187.